Ductility of RC beams with FRP reinforcing bars.

By Miguel Angel Dávila Sänhdars

Corrigenda

Page 62 line 9

The compressive resultant, C_c, is the summation of all the forces …

Page 63 line 12

In order to make it clearer it should be stated that in the procedure for the segmental analysis, values of the curvature and the depth to the neutral axis are initially guessed. Equilibrium (static) is checked and if not satisfied, the depth to the neutral axis is adjusted iteratively until static is satisfied, subject to boundary conditions of maximum strains induced in the beam components.

Page 69 line 14

variation of ψ is shown as from 1^{-6} to 100^{-6}.

Page 79 line 3

goes up and keeps rising until the top fiber of concrete crushes and then it drops down until the collapse of beam.

Page 85 figure 3.6

The horizontal scale should be 10^{-6}.

Page 86.

Figure 3.7 should be for beam 3 as follow

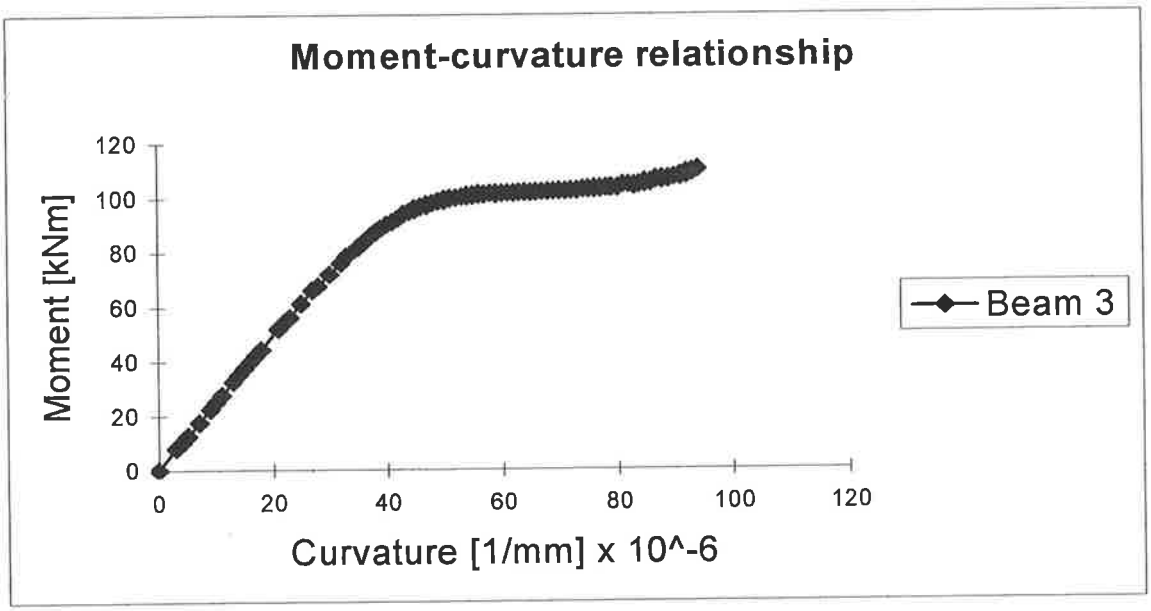

Figure 3.7. – Moment-curvature relationship of beam 3.

Page 260 line 13

Accordingly, beam 3 behaved very ductile. The deflection reduced after the beam was unloaded as can be seen in figure 9.3.

THE UNIVERSITY OF ADELAIDE
Department of Civil and Environmental Engineering

DUCTILITY OF RC BEAMS WITH FRP REINFORCING BARS

A Thesis
by

Miguel Angel Dávila Sänhdars

B. Sc. in Civil Engineering (University of El Salvador)

Submitted to the Research and Graduate Studies Branch
for the Degree of **Master of Engineering Science**

August, 1998.

To my children:

MIGUEL ANGEL,

ROSALÍA,

RAQUEL MESALINA,

GABRIEL ANGEL,

JANET

AND

YURI ALEXEI.

Ductility of RC beams with FRP rebars (Synopsis)

Concrete structures with steel reinforcing bars are vulnerable to damage by corrosion most of all in coastal areas. A very common practice has been, for many years, to increase the amount of concrete covering, in order to protect the reinforcing bars against corrosion. Increasing the concrete covering, not only increases the structure's weight, but also the cost. RC beams with FRP rebars are a very good solution, with regard to the corrosion problem. The behaviour of RC beams with glass FRP reinforcing bars is studied in this research.

The Young's modulus of glass FRP rebars is significantly lower than steel rebars causing, therefore, the problem of large deflections. Over reinforcing the beams with FRP rebars, guarantee stiffness, however, the beams also become brittle. Brittle failure can be prevented with the addition of FRP compressive reinforcement to the beam which is the subject of this thesis.

Beam specimens, with different combinations of longitudinal reinforcement, have been tested. It was found that, RC beams, with compressive reinforcement have a very good ductile behaviour. The beams were designed using a segmental analysis, and a mathematical model has been developed to facilitate the design by hand of ductile RC beams with FRP reinforcing bars.

Statement of originality

This work contains no material which has been accepted for the award of any other degree or diploma in any university or other tertiary institution and, on the best of my knowledge and belief, contains no material previously published or written by another person, except where due reference has been made in the text.

I give my consent to this copy of my thesis, when deposited in the University Library, being available for loan and photocopying.

Signature: ..Date: 25/8/98.

Acknowledgments

The project was supervised by Dr. Deric J. Oehler, Senior Lecturer in the Department of Civil and Environmental Engineering, the University of Adelaide. His advice, assistance and encouragement to accomplish the project are gratefully acknowledged. I express my deepest gratitude to him for his excellent guidance and enthusiastic supervision and for his review of the thesis.

I would like to thank Mr. David Hale, Laboratory Technician for his advice and enormous help during the experimental work. Also I appreciate the enthusiastic help given by Mr. Jeffrey Hiorns during the experimental test procedure.

I am also thankful to the academics and staff for their help and assistance during my postgraduate candidature. Especial thanks to both Ms. Bernice Golledge for her secretarial help and Ms. Diane Keable for her help and high concern about my own safety during my postgraduate candidature.

The FRP reinforcing bars were provided by Mr. Peter Hastwell, which is gratefully acknowledged.

I am very grateful to my son Miguel Angel for his strong support and encouragement to go ahead with this research.

Table of contents

Content *Page No.*

Top2FRP = 2 FRP rebars at the top of the beam;

UCAM = Universal Computer Aid Measurement;

Y.M. = Young's modulus;

15T-FRP = FRP of 15 Tonnes nominal strength;

30T-FRP = FRP of 30 Tonnes nominal strength.

Notation

A_a, B_a, C_a, D_a = Coefficients of the concrete Wang's equation for the ascending branch;

A_c = Area of reinforcement in compression either steel or FRP rebars;

A_d, B_d, C_d, D_d = Coefficients of the concrete Wang's equation for the descending branch;

A_{fc} = Area of FRP reinforcing bars in compression;

A_{ft} = Area of FRP reinforcing bars in tension;

A_t = Area of reinforcement in tension either steel or FRP rebars;

b = width of the beam's cross-section;

BM = Bending moment;

C_c = Concrete force;

C_{cj} = Variable concrete force along the cross-section of the beam for an individual curvature ψ;

C_f = Force of the FRP rebars in compression;

d = Effective depth of the beam's cross-section;

D = Nominal bar diameter; Concrete cylinder diameter;

d_1 = Distance between the top fiber of concrete and the centroid of the reinforcing bars in compression;

E_c = Concrete Young's modulus; Secant modulus of elasticity at $0.45f_c$;

E_{co} = Secant modulus of elasticity at f_c;

E_{com} = Young's moduli of reinforcement in compression either steel or FRP rebars;

E_f = Young's modulus of the FRP rebars in general;

E_{fc} = Young's modulus of the FRP rebars in compression;

E_s = Young's modulus of the steel rebars;

E_{ten} = Young's moduli of reinforcement in tension either steel or FRP rebars;

f_c = Concrete strength;

FRP_{20} = FRP rebar of 20-mm diameter;

h = Depth of the beam's cross-section;

j = Counter variable along the depth of the beam;

L = Length;

l_e = Embedment length;

M_{fc} = Internal moment provided by the FRP rebars in compression;

M_n = Internal moment of the RC beams;

M_{nc} = Resultant moment of the concrete;

M_{ncj} = Elemental moment of the concrete;

MR = Modulus of rupture;

n = Neutral axis depth;

na = Neutral axis of the beam;

P = Concentrated load;

P_u = Ultimate concentrated load;

T_f = Force of the FRP rebars in tension;

V_f = Volume of fiber;

W_f = Weight of fiber;

X = Normalized concrete strain;

Y = Normalized concrete stress;

Y_{20} = Steel rebar of 20-mm diameter;

z = Lever arm;

ΔA = Segment of area in the beam's cross-section;

Δh = Increment of depth in the beam's cross-section;

$\Delta\varepsilon_c$ = Increment of concrete strain;

γ = Reduction factor of the neutral axis depth of the beam;

ε_c = Concrete strain;

ε_{ci} = Concrete strain at σ_{ci};

ε_{cj} = Variation of the concrete strain for a particular curvature ψ;

ε_{co} = Concrete strain at the concrete strength;

ε_{cu} = Concrete ultimate strain;

ε_{fc} = Strain of the FRP rebars in compression;

ε_{fcu} = Ultimate strain capacity of the FRP rebars in compression;

ε_{ft} = Strain of FRP rebars in tension;

ε_{ftu} = Ultimate strain capacity of the FRP rebars in tension;

σ_c = Concrete stress;

σ_{ci} = Concrete stress at the inflection point of the descending branch of the stress-strain curve;

σ_{cj} = Variable concrete stress for particular curvature ψ;

σ_{com} = Stress of the compressive reinforcement either steel or FRP rebars;

σ_{fc} = Stress of the FRP rebars in compression;

σ_{fcu} = Strength of FRP rebars in compression;

σ_{ft} = Stress of the FRP rebars in tension;

σ_{ftu} = Strength of FRP rebars in tension;

σ_{ten} = Stress of the tensile reinforcement either steel or FRP rebars;

ψ = Curvature of the beam.

Chapter 1
General introduction

1.1 Introduction.

Corrosion of steel reinforcing bars in concrete structures represents a very deep concern in the construction industry most of all in coastal regions where the concrete structures are exposed to seawater. The cost of maintenance of concrete structures attacked by salt corrosion represents a huge amount of money every year. In addition, if the repair of the concrete structures is not carried out in due time, the whole structure has to be replaced. Alternative materials are being investigated to replace steel reinforcing bars in concrete structures to prevent corrosion damage and therefore to prolong the service life of such structures.

This research represents a valuable contribution in the investigation of alternative materials to replace steel reinforcement in concrete structures where necessary. The investigation is focused on the ductility of RC beams with FRP reinforcing bars.

1.2 Disposition of the thesis.

This thesis is divided into ten chapters including this one. An extensive literature review is presented in chapter 2, where historical development of plastic materials studied

by prominent researcher is brought to the reader. Methods of manufacture and different types of plastic material are included as well as structural applications in the strengthening of existent structures. Bond strength, flexural strength and shear strength of reinforced concrete structures with FRP rebars, are also included in chapter 2.

Chapter 3 deals with a segmental analysis method in analyzing the cross-section of an RC beam that includes the mathematical algorithm of the analysis to be solved using a computer program. Computer simulations are done for different combinations of material properties and amount of reinforcing bars to visualize the ductility of RC beams with FRP reinforcing bars.

Rectangular block of stresses analysis is described in chapter 4. A mathematical model is developed for analyzing by hand, over reinforced concrete beams with FRP reinforcing bars. The mathematical model is applicable for both singly reinforced concrete beams and doubly reinforced concrete beams.

Chapter 5 presents a comparison between the segmental analysis method and the rectangular block of stresses analysis method. Emphasis is made on both the magnitude and position of the force exerted by the compressive concrete in the beam. Graphs are available to visualize the influence of the concrete's force beyond the concrete's ultimate strain capacity in the evaluation of the internal moment of the beam.

A parametric study of the influence of materials' properties is carried out in chapter 6. The amount of reinforcement, combination of types of materials and cross-sections' dimensions, are considered as significant parameters affecting the mechanical behavior of RC beams with FRP reinforcing bars. Graphs are available to visualize the influence of the variations of these parameters.

Design and manufacture of the beam specimens are in chapter 7. This chapter includes the design of five concrete beam specimens with different combinations of reinforcement. The combination of reinforcement is about not only the amount of reinforcement but also the type of reinforcement. Photographs are available to show the layout of the reinforcement cages.

Experimental work is explained in chapter 8 covering from the test rig and instrumentation up to the test procedure and processed data. A large number of photographs are available to follow in a step by step basis the testing procedure of the beam specimens. In these photographs can be seen clearly the mode of failure of the beam specimens as well as the mode of failure of the reinforcing bars. In addition is explained the test program of the concrete cylinders for both compressive and tensile strength. Flexural strength of plain concrete beams is also studied in chapter 8. FRP and steel coupons were tested to investigate the actual mechanical properties of the reinforcing bars and the mode of failure of them. The results of the tests of the reinforcing bars are summarized in tables and graphs in chapter 8.

Chapter 9 explains the methodology followed in the analysis of the test results. Ductility behavior of the beams is analyzed through the experimental moment-deflection relationship. Ductility behavior involves the plateau length as well as the changes of moment between the moment at the concrete crushing and the moment at ultimate failure of the beams. A comparison is made between the values of moment predicted in the design of the specimens and the values of moment obtained through the experimental work. Also in chapter 9 is calculated the flexural rigidity of the beams to investigate the effects of the amount of FRP reinforcing bars at the bottom of the beams.

Chapter 10 presents a list of the more relevant conclusions with regard to both the theoretical study and the experimental work.

Chapter 2
Literature review

2.1 Introduction.

A literature review is one the most important parts of a scientific research because it allows us to know about the historic developments regarding the topic being investigated, from the beginning until the present day. In doing so, all the relevant aspects regarding fiber reinforced plastic (FRP) materials have been covered herein. The literature review starts with the historical development and methods of manufacture of FRP materials as well as the identification of different types of FRP materials. There is included a review of the use of FRP sheets in retrofitting pultruded beams and pultruded columns as well as the retrofitting of reinforced concrete structures. After that, our attention is focused in the analysis and use of FRP reinforcing bars in concrete structures. Bond stress and bond test

methods are covered herein as well as the flexural and shear strength of RC beams with FRP rebars and FRP stirrups. Finally, we review the stress-strain relationship of normal concrete and select one of these properties to be used later in the computer simulations that have been developed in this research project.

2.2 Review of the development of the FRP materials.

The development of FRP materials is reviewed herein from its appearance in the plastic industry up to the present time. A historical review of the most significant findings and applications of plastic materials as well as the most common methods of manufacture is described. In addition, the most popular types of FRP materials are described.

2.2.1 Historical development.

Concrete structures with steel reinforcing bars are very weak under corrosion attack. The problem of corrosion brings about the degradation of the reinforcing bars. Therefore, the solution of this problem is to find a substitute material that not only has good strength but also good corrosion resistance.

The corrosion problem was detected many years ago. However, the lack of technical and scientific information available caused a delay in the development of materials with high corrosion resistance and suitable structural properties, such as plastic materials. At the beginning, the first steps in designing with plastics were merely through empirical procedures (Schwartz and Schwartz) [1].

Plastics have several features to attract architects and structural engineers to use it in the housing industry. The main features are: high-strength/weight ratios; attractive appearance; exceedingly good corrosion resistance; easy prefabrication; and a high

degree of built in thermal insulation. The family of plastics can be divided into two main groups: thermoplastic materials and thermosetting materials. Thermosetting materials are more resistant to heat than thermoplastic materials.

Polyvinylchloride (PVC) and polymethylmetacrylate (acrylics) are examples of thermoplastic materials for light structural elements. Fabrication of these plastic elements can be done by moulding or injection methods. Polyester, epoxide, phenolic, and silicone resins are examples of thermosetting plastic materials. Thermosetting resins for structural elements must be used with reinforcing fibers like carbon fiber or glass fiber (Benjamin) [2].

The first steps taken in the development of fiber reinforced plastic materials were mainly in the military industry. The attention was focused, most of all, in shell laminated elements for aircraft parts and missile parts. In doing so, strength and elasticity modulus of glass fiber reinforced plastic shell laminated elements was studied by Tsai [3], Pickett [4], and Leissa and Clausen [5]. It was found that the layout of the reinforcing fiber in the composite elements affects directly the strength and elasticity modulus of such elements. Measurements of inter-laminar shear strength in short beam flexural tests, and compressive strength associated with parallel splitting to the fibers of a parallel filament of glass fiber reinforced plastic was carried out by Corten [6]. The research was focused to investigate the propagation of cracks from internal voids and linear elastic fracture mechanics. Wendt [7] investigated properties and constitutive relations of composite materials, specially the internal stresses and deformations as well as failure modes. He found that glass-epoxy material performed better than aluminium at high strength requirements.

Buckling of laminated plates, and stability of unidirectional and bi-directional composite fibers in laminate elements was studied by Whitney [8]. It was found that the critical buckling load is a function of the elastic coefficient of the plate, resin modulus, fiber modulus and, most of all, the volume percentage of fiber content in the composite element.

Procedures used in the design, fabrication, and test of the F-111 horizontal tail aircraft, utilising a boron fiber-epoxy pre-impregnated laminate, were developed by Rogers [9]. It was found that in addition to good strength and stiffness in the structure, the fiber reinforced plastic composite materials offer the advantage of less weight than the traditional aluminium structures. The weight of the F-111 aircraft was 230 kilograms lighter using FRP materials than when using aluminium. This means that the structure becomes not only stronger and stiffer but also lightweight when using fiber composite materials. In addition, the overheating problem due to air friction also disappears.

One of the best contributions, perhaps, in the manipulation of glass fiber is that made by Guzzetta [10]. He came across the difficulty in forming continuos glass filaments due to sensitiveness to self-abrasion of the glass fibers. One way of reducing the sensitivity to abrasion, and decreasing resultant damage, is with a lubricant. Many types of lubricant are in use, but the type that is substantive to the glass surface should be permanent. In addition, if designed correctly, should afford a lubricating finish for the glass fibers most efficiently. A lubricant once absorbed by the glass fibers and incorporated into a reinforced plastic composite, will be located at the glass-resin interface and may affect the gross physical properties of the composite. The difference between the lubricant and coupling agent is that lubricant protects the fibers from self-abrasion and severe damage in processing, while the coupling agent locates itself at the interface between the resin

and the glass. Consequently, the coupling agents improve the properties of the glass-resin composite. This is a very important finding, because it is very helpful for the fabrication of continuous filaments of glass fibers, without damaging for self-abrasion and, therefore, the fabrication of fiber composite elements and materials.

Fiber composite elements are the combination of fiber reinforcement and binding resin. Therefore, it is necessary to know not only the mechanical properties of the reinforcing fiber but also the mechanical properties of the binding resins as well as the interrelation between the reinforcing fibers and the resin matrix. Patrick and Layne [11], Wong [12], and Sterman and Marsden [13], studied the modulus of rupture, bond strength, and shear strength of fiber composites. They investigated the bond strength between the resin and fibers, and the bond strength between layers of the same resin. To generate adhesion between glass fibers and resin, they used coupling agents such as vinyltrichlorosilane and methacrylatochromic chloride. Coupling agents are materials capable of reacting with and forming covalent chemical bonds with both the organic polymer and the inorganic glass. They found that with the above-mentioned coupling agents, the bond strength between the reinforcing glass-fiber and the resin matrix is substantially good.

Glass fiber paved the way for reinforced resin structural materials in the late 1930s. Since that time, steady improvement and continuos market growth have taken place. Glass fiber continues to be the most widely used reinforcement for plastics because of its high strength, ready availability to known specifications, low density, and low cost, according to Gill [14]. However, a couple of decades ago, composite plastic materials were used only for aerospace purpose, and for the fabrication of car body parts. The requirements were for stiff materials with high strength. Carbon fiber possesses more

stiffness than glass fiber. In addition, carbon fiber can reach a high strength with less strain than glass fiber, which makes it the preferred material for aerospace and car industry. Therefore, researchers put their attention into the investigation of carbon FRP composite materials. Later, in this chapter, are compared the stress-strain relationship of the main plastic materials currently in use. The production of carbon fiber commenced in Japan around 1959, but the main progress in production has been in the early 80s. Carbon fiber is the result of overheating cellulose materials. The first researcher to obtain carbon filaments by overheating cellulose resin, was Thomas Alba Edison in the last century, according to Gill [14]. In such a way, Edison discovered a suitable material for making lamp resistances.

2.2.2 Methods of manufacture.

Reinforced plastic material is a compound of filament fibers bound by a binding matrix. The manufacturing methods can be the moulding method, filament winding method or pultrusion method according to Ballinger [15]. Furthemore, there is the layout method.

a) Moulding process.

The moulding process is used for shell laminated or non-continuous elements like car body parts, aircraft parts, and missile parts. The fibers can be carbon fiber or glass fiber. The fibers are arranged prior to moulding, by placing alternated layers at a required angle θ between their directions. The reinforcing fibers are placed by handfuls, then impregnated with resin matrix, and finally moulded to get the desired shape.

b) Winding process.

The winding process is used for FRP braided continuos elements such as FRP rods and FRP tendons. Figure 2.1 shows schematically the winding process where: (a) represents the creel containing fibers packages; (b) is the winding machine; (c) is the resin impregnation tank; (d) is the curing die; (e) is the haul-off mechanism and (f) is the cut-off saw. The winding process starts when the fibers come from the creel (a) into the winding machine (b). The braided rods are impregnate with resin in the resin impregnation tank (c) and then treated in the curing die (d). The haul-off mechanism (e) pulls-out the rods and finally the rods are cut-off at the required length.

c) Pultrusion process.

The pultrusion process shown in figure 2.2 is for continuous elements such as rods, cables, bars, boxed and flanged beams, and boxed and flanged columns. Pultrusion is a continuous process of pulling fibers or fabrics from the creel of fibers or fabric packages through a resin bath, and then through a heated die to produce constant cross-section of structural shapes. The reinforcing fibers of the continuos elements made through the pultrusion process are all in a parallel array with respect to the axis of the element.

Let us have a look at the pultrusion process shown schematically in figure 2.2 from left to right. The process starts from the creel or basket, at the left hand side shown in figure 2.2a, containing fiber spools or packages of fabric rolls or mat rolls. Let us assume, for instance, the manufacture of FRP bars. The threads of glass fiber are pulled by the haul off mechanism (pultrusion) into the resin impregnation tank (figure 2.2b) where the fibers are bound together by the resin matrix. Resin may be epoxy resin, polyester resin or the like. After passing through the impregnation tank, the bound fibers go through the

pre-forming die (figure 2.2c), where the section of the element takes the desired constant shape, such as cylindrical or square. After forming, the continuous element it is dried in the curing die chamber (figure 2.2d). The haul off mechanism (figure 2.2e) is in charge of pulling the endless element and transporting it out of the process. The saw at the end of the process (figure 2.2f) is for cutting off the elements at the desired length.

d) Layout method.

The layout method consists of placing pre-impregnated parts of fiber reinforced plastic material in such a way as to configure the required element, such as superimpose configurations of woven mats. Figures 2.3 shows the layout of two layers of straps, one superimposed at 90^0 over the another one. Meanwhile, figure 2.4 shows an FRP element with a woven layout. The component pre-impregnated parts can be straps or tapes. One example of the layout method is the repair, by wrapping with FRP tapes or straps, of damaged RC columns. Another example is gluing an FRP tape along the soffit of an RC beam for strengthening or stiffening.

2.2.3 Types of FRP materials.

There are several types of FRP materials in the market. Plastic materials range from the raw fibers up to FRP material elements fabricated through the construction methods described above. Examples of raw fibers are, for instance, glass fiber and carbon fiber.

There are FRP sheets of two kinds with regard to the orientation of the reinforcing fibers. One sort of FRP sheet is the one with reinforcing fibers parallel to the length of the sheet, as shown in figure 2.5. Another sort of FRP sheet is the one with the reinforcing fibers non parallel to the length of the sheet, as shown in figure 2.6.

Continuous FRP pultruded elements are available in the form of deformed reinforcing bars and tendons as shown in figure 2.7. In this figure, it can be seen that the FRP reinforcing bar has transverse deformations to carry bond stress. However, the FRP tendon shows a smooth surface to avoid counteraction against post-tensioning forces.

In figure 2.8, plotted by Gueritse [16], the reader can see the tensile stress-strain relationship curves of filaments with different Young's moduli. The vertical axis of figure 2.8, is given in MPa; meanwhile, the horizontal axis, is given in percentage strain (strain %). The nylon filament has the lowest Young's modulus of 400 MPa followed by the polypropylene. Aramid HM, aramid standard and S-glass fiber have a high Young's modulus and high strength, compared with polypropylene and nylon. These three sorts of fibers are stronger than prestressing steel, but have a relatively low Young's modulus. Carbon fibers are in two categories: carbon fibers of higher Young's modulus (HM); and the carbon fibers of higher strength (HS). Notice that the Young's modulus of the carbon fibers is very similar to the Young's modulus of the prestressing steel. Also in this figure can be seen the different behavior of the FRP materials with respect to the steel. The stress-strain relationship of the FRP materials is linear; meanwhile the stress-strain relationship of the steel shows a non-linear trend.

In figure 2.9 we can see the stress-strain relationship of both glass-FRP reinforcing bars and steel rebars [17]. Here, we can see clearly that the Young's modulus of the FRP rebars is constant, ie the FRP rebars behave elastically at all times.

FRP continuous elements can be pultruded beams or pultruded columns like those shown in figures 2.10 and 2.11. The elements in figure 2.10 can be used as either beams or columns; however, the elements in figure 2.11 are specifically for beams.

2.3 FRP strengthening sheets and composite beams and column.

Composite FRP materials are developed in several shapes to suit the requirements for a better design and construction of structural elements. The necessity of finding new alternative materials for the construction industry has encouraged researchers to create new combinations of existing raw materials along with new geometric configurations. Examples are pultruded plastic beams reinforced with carbon sheets in the tensile zone as in figure 2.11b, and pultruded plastic beams reinforced with carbon sheets in the tensile zone and concrete in the compressive zone as in figure 2.11d. Deskovic and Triantafillou [18] and Deskovic and Triantafillou [19] investigated hybrid beams with a cross-section shown in figure 2.12. The pultruded beams were made of GFRP material and later a double layer of CFRP material was glued to the tension zone. At the top of the pultruded beams was cast a 53-mm thick concrete layer. Table 2.1 shows the geometric properties of the FRP materials involved in the manufacturing of the three beam specimens. When testing the beams, it was found that the carbon sheet failed first prior to the failure of the glass FRP flange which caused the collapse of the whole beam. Hence, initial failure of the carbon sheet was a warning of imminent failure. The early failure of the carbon sheet, with respect to the failure of the glass fiber flange of the beams, is understandable because the failure strain of the carbon fiber is much less than the failure strain of the glass fiber, as can be seen in figure 2.8.

Figure 2.13 shows the load-deflection relationship of beam 1 in table 2.1. The behavior of the beam was linear up to fracture of the CFRP reinforcing sheet, and then the bottom flange of GFRP took over up to the failure of the beam due to debonding. To prevent debonding between the concrete layer and the pultruded beam, the concrete layer was bolted to the top flange of the beam soon after the concrete was cast. The outcome

was excellent given that failure of the beams was due to concrete crushing instead of debonding, as shown in figures 2.14 and 2.15. Beam 3 with 21 mm^2 of CFRP reached larger deflections at failure than beam 1 with 25 mm^2 of CFRP.

Table 2.1. – Geometric properties of hybrid beams.

Beam (1)	GFRP flange thickness (mm) (2)	GFRP web thickness (mm) (3)	CFRP area (mm^2) (4)
1	5.8	3.8	21
2	4.9	3.0	20
3	5.2	2.9	25

Carbon sheets are used for strengthening and retrofitting deck slabs in existing bridges. Figure 2.16 shows a deck slab strengthened with a unidirectional CFRP reinforcing sheet. Kobayashi et al [20] found that after gluing a CFRP reinforcing sheet to the tension zone of the slab the deflection of the slab reduced by 15 to 20 per cent. The aim was to increase the loading capacity of the bridge. Carbon sheets take over the tensile stress of the old steel, improving considerably the loading capacity and, therefore, prolonging the service life of bridges.

Bridges are prone to damage not only at the superstructure level but also near the column-footing joints. Bridge columns damaged due to severe earthquake can be repaired using FRP straps (see figure 2.17). RC columns manufactured with conventional steel reinforcement have been loaded until failure, by means of a simulated earthquake. After removing the spalled concrete and reshaping the columns, the damaged columns were

wrapped with FRP straps that were concentrated around the zones of the plastic hinges of the columns. Three different types of FRP straps were tested by Saadatmanesh et al [21] which had the mechanical properties shown in table 2.2 and in figure 2.18. The test results of the repaired columns, according to the above researchers, were all satisfactory. The columns kept very good stiffness and appropriate ductility. The repair of columns, not only in bridges but also in buildings, is feasible using FRP straps because they represent low cost in both materials and work force.

There is another procedure which goes a bit further than repairing damaged columns (Mirmiran and Shahawy) [22]. Such a procedure consists of the manufacture of RC columns confined with FRP reinforcing straps instead of internal steel confining stirrups. It was emphasised that the design criterion must not follow the same criterion followed in the design of RC columns confined with steel hoops. Because using available confinement models that were calibrated for steel, may prove unsafe for fiber-wrapped FRP-encased concrete columns.

Table 2.2. – Properties of the FRP composite straps.

Fiber volume ratio	$V_f = 25.4$ %	$V_f = 50.2$ %	$V_f = 74.0$ %
Tensile strength MPa	281	532	814
Young's modulus MPa	9074	17755	29056
Ultimate strain mm/mm	0.031	0.03	0.028

Concrete beams can also be repaired using carbon FRP sheets for strengthening in tension and shear. Norris et al [23] investigated the use of CFRP sheets that were epoxy

bonded to both the tension face and web of concrete beams, to enhance their flexural and shear strengths. Figure 2.19 shows four different types of external reinforcement with CFRP sheets. The effect of CFRP sheets on the strength and stiffness of the beams is considered for various orientations of the fibers with respect to the axis of the beam. For instance, figure 2.19a shows a reinforced concrete beam with a unidirectional CFRP sheet parallel to the axis of the beam. The CFRP sheet is bonded at the tensile zone and at both sides of the web.

The beam shown in figure 2.19b has been bonded with a two-direction CFRP sheet; one direction of the sheet is parallel and the another one is transverse to the axis of the beam. The beam shown in figure 2.19c is bonded with a two directional CFRP sheet at 45° about the axis of the beam. Meanwhile, the beam shown in figure 2.19d has a CFRP sheet along the tensile zone, however, the sheet bonded at both sides of the web is placed near the ends only. Different modes of failure and gains in the ultimate strength were observed, depending on the orientation of the fibers. Muszynski and Sierakowski [24] in addition to investigating the mechanical behavior of RC beams with CFRP tape in the tension zone, also investigated the environmental behavior of the composite tape. It was found that CFRP tape is not vulnerable to freeze-thaw cycles and hot water immersion. However, CFRP tape is vulnerable to the exposure of rainwater and the ultraviolet energy sunlight. Also Saadatmanesh and Ehsani [25] investigated the static strength of reinforced concrete beams strengthened by gluing glass FRP plates, instead of CFRP, to their tension flanges as can be seen in figure 2.20. It was found that gluing GFRP plates to the tension face could significantly increase the flexural strength of RC beams. In addition, the epoxy bonded plate improved the cracking behavior of the beams by delaying the formation of visible cracks, and reduced crack widths at high load levels. The only problem is that the

GFRP plates reduced the original ductility of RC beams. The beams become stronger, however, the mode failure is without warning, which represents lack of safety.

2.4 FRP reinforcing bars in concrete structures.

The use of FRP reinforcing bars in concrete structures requires the knowledge of their fundamental properties. Within the main properties of FRP reinforcing bars, we need to know for instance, their tensile strength and bond strength. In addition, in this part of the chapter, is reviewed the bond strength as well as the most usual methods of bond testing. Later, the flexural strength of RC beams with FRP reinforcing bars is reviewed and then the shear strength of RC beams with FRP stirrups.

2.4.1 Bond strength and bond tests.

Bond strength in reinforced concrete structures is the ability of the reinforcing materials to work together with the concrete as far as possible without showing slip. Bond failure is one of the main concerns in the construction industry. In the early years of the concrete construction industry, the bond strength depended only on the chemical reaction of the cement surrounding the reinforcing bars because of the smooth surface of such rebars. Investigations carried out in recent decades led to the conclusion that protruded deformations of the reinforcing bars along with an appropriate confinement around the concrete improved considerably the bond strength.

Although good guidelines exist for the design of concrete structures reinforced with steel rebars, these guidelines do not apply for concrete structures reinforced with FRP rebars. The constituent materials of the FRP rebars are far different from the steel rebars, therefore, the design guidelines have to be different as well.

Let us have a look of some details of bond tests for FRP reinforcing bars in concrete structures. There are several bond test methods available and we will discuss four of them, which we will call pullout tests, confinement tests, flexural tests, and pre-tensioned tests.

a) Pullout test.

Firstly, the pullout testing, which is the more commonly used. Tests for both steel and FRP rebars have been done by Larralde and Silva [17]. Figure 2.21 shows schematically the set-up for the pullout test procedure. The bar coupon is embedded into the concrete cylinder at an embedment length l_e. The bar coupon is then pulled-out with a force P. Two things may happen, one of them is that the coupon fails and another one is that the coupon slips leaving behind the concrete cylinder.

Let us analyse the bond test results in table 2.3. Column 2 shows the diameter of the bar specimen and column 3 shows the embedment length of the coupon. Column 4 is the average normal-strength in MPa and column 5 the average bond-strength in kPa. The slippage is in column 6. Pairs of similar bars are marked with the same subscript. For example, $(FRP)_a$ and $(Steel)_a$ means FRP bar and Steel bar of 9.5-mm diameter and 76.2 mm of embedment length. For each pair of bars (FRP and steel), the bond strength is quite similar, however, the slippage of the FRP bars is four times the slippage of the similar steel bar.

Figure 2.22 represents the normal-strength/slip relationship plotted for the bar specimens, in table 2.3. The curve $(FRP)_a$ is representative of a FRP coupon of 9.5-mm diameter and 76.2 mm of embedment length. The curve $(FRP)_b$ is representative of a FRP coupon of 9.5-mm diameter and 152.4 mm of embedment length. The curve $(FRP)_c$ is

representative of a FRP coupon of 15.9-mm diameter and 76.2 mm of embedment length. Finally, the curve $(FRP)_d$ is representative of a FRP coupon of 15.9-mm diameter and 152.4 mm of embedment length. Perhaps of more importance is the comparison in figure 2.23, which shows the normal-strength/slip relationships of a steel coupon and an FRP coupon for a particular bond test.

Table 2.3. – Average values of bond test results of FRP and steel rebars.

Type of rebar (1)	Bar Diameter (mm) (2)	Embedment length (mm) (3)	Average normal strength (MPa) (4)	Average bond strength (kPa) (5)	Slip (mm) (6)
$(FRP)_a$	9.5	76.2	318.6	9,956	4.24
$(Steel)_a$	9.5	76.2	372.7	11,610	0.81
$(FRP)_b$	9.5	152.4	595.8	9,308	7.92
$(Steel)_b$	9.5	152.4	622.6	9,687	1.78
$(FRP)_c$	15.9	76.2	128.3	6,683	1.75
$(Steel)_c$	15.9	76.2	138.1	8,599	0.69
$(FRP)_d$	15.9	152.4	226.8	5,905	2.54
$(Steel)_d$	15.9	152.4	258.8	8,054	0.84

Note: Normal strength means the pullout strength at the specimen's failure.

The diameter and embedment length of both coupons is 9.5 mm and 76.2 mm respectively in figure 2.23. In this figure, can be seen the difference between the bond properties of FRP rebars and steel rebars. The steel coupon reaches a larger normal

strength with a shorter slippage than the FRP coupon. Figure 2.24 shows the normal-strength/slip relationship of a steel coupon and an FRP coupon, with a diameter of 9.5 mm and an embedment length of 152.4 mm. The specimens reach practically the same normal strength, however, the FRP bar reaches its strength at a much larger slippage than the steel bar.

b) Bond test with confinement.

A second method of bond testing might be called 'bond test with confinement' (Malvar) [26]. The specimen used is shown in figure 2.26. The specimen consists of a 76-mm diameter and 102-mm long concrete cylinder surrounding an FRP bar. Only 67 mm of the bar is in contact with concrete, contact being prevented in the rest of the specimen via silicone rubber spacer. A split, threaded steel pipe, which carries the pullout force via shear stresses, surrounds the outer concrete surface. The pipe is split into eight strips to offer no lateral resistance. The concrete cylinder is cast in place against the pipe threads. Casting is carried out with the specimen placed vertically. The interior of the steel ring is of an uneven surface to restrict movement of the concrete cylinder, when the pullout force is applied, generating a shearing force between the steel ring and the concrete cylinder.

The concrete cylinder is pre-cracked prior to the test by setting a surface pressure of 3.4 MPa in the radial direction and then unloaded. The bar is pulled on until longitudinal splitting occurs between the concrete and the bar. The first bar is tested under a radial pressure of 3.4 MPa, and the corresponding curve is labelled A in figure 2.25. The second one tested under a radial pressure of 10.3 MPa, and the corresponding curve is labelled B in figure 2.25. The third one is tested under a radial pressure of 17.2 MPa, and the

corresponding curve is labelled C in figure 2.25. The fourth one tested under the radial pressure of 24.1 MPa, and the corresponding curve is labelled D in figure 2.25. Finally, the fifth bar tested under the radial pressure of 31.0 MPa, and the corresponding curve labelled E in figure 2.25. Notice in figure 2.25 that only the bar under the radial pressure of 31.0 MPa breaks, that is denoted by the symbol x.

c) *Flexural bond test.*

A third method of bond testing is the 'flexural bond test'. Figure 2.27 shows schematically the set up of the flexural bond test. The flexural bond test consists of a reinforced concrete beam with a reinforcing bar in the tensile zone. In figure 2.27 can be seen also the cross-section of the beam specimen. The reinforcing bar passes through the recess notches in the side view of the beam. At the free ends of the beam, steel sleeves impede the contact between the reinforcing bar and the concrete to avoid shearing effects between the concrete and the reinforcing bar. The reinforcing bar makes contact with the concrete only between the two recess notches as well as along the shear span. The shear span is of different lengths for each beam specimen, because it represents the embedment length of the FRP bar.

Dial gauges are placed at the free ends of the steel sleeves to measure the displacements at the ends of the FRP bar and strain gauges are attached to the rebars between the recess notches (Daniali) [27]. First, were tested FRP coupons in tension, to determine the tensile strength and Young's modulus of the FRP bars. The tensile specimens were FRP bars of 9.52 mm, 12.7 mm, 19.05 mm and 25.4 mm diameter with a 60% to 70% of glass fiber content by weight. The results of the tensile test are in table 2.4

below. The low tensile strength and Young's modulus of the bar of 9.52-mm diameter is attributed to low content of glass fiber by weight.

The concrete for the manufacture of the beam specimens was 29 MPa strength. Table 2.5 shows the diameter and embedment length of the coupons as well as the bond test results. The failure of the bars of 12.7-mm diameter is due to tension for the three different embedment lengths shown in column 2 of table 2.5. The failure of the bars of 19.05-mm diameter was in three different ways that is bond, cover splitting and tension. Notice that the tension failure occurs for longer embedment length in contrast with the results obtained by Larralde and Silva [17] using the pullout test method. The bar of 25.4-mm diameter failed only for bond and cover splitting even at the embedment length of 762 mm, which means that to reach tensile failure, the embedment length must be larger than 762 mm.

Table 2.4. – Results from the tensile test.

Bar diameter [mm] (1)	Average tensile strength [MPa] (2)	Average Young's modulus [MPa] (3)	Ultimate strain (4)
9.52	286	21000	0.010
12.7	741	48000	0.014
19.05	527	40000	0.012
25.4	475	38000	0.012

A very interesting finding is the mode of failure at the interface between the reinforcing bars and the surrounding concrete with regard to the slippage. It was found in

this experimental work that in the pullout test the surrounding concrete shears the FRP rebars in contrast to testing steel rebars which shear the surrounding concrete. The shear effect between the concrete and the bars can be seen in figure 2.28. For instance, in figure 2.28a the shear occurs over the ribs of the steel bar, meanwhile in figures 2.28b and 2.28c the bond shear occurs in the deeper surface of the bar peeling off the outer deformations.

Table 2.5. – Test results from the flexural bond method.

Bar diameter [mm^2] (1)	Embedment length [mm] (2)	Free end slip [mm] (3)	Mode of failure (4)
12.7	203	0.7366	tensile
12.7	305	0.0500	tensile
12.7	406	0.0500	tensile
19.05	305	1.0160	bond
19.05	457	1.0160	cover splitting
19.05	610	0.0500	tensile
25.4	508	2.5146	bond
25.4	635	0.4874	bond
25.4	762	0.2540	bond and cover splitting

d) Pre-tensioning bond test.

A fourth method of bond testing consists of pre-tensioning an FRP bar and then casting the concrete block with two different strengths as in figure 2.29b. Such a method could be named as 'pre-tensioning bond test'. Along with the pre-tensioned method is

also made a one side pullout test to compare results (see figure 2.29a). Shima and Suga [28] used this bond testing method with the following materials properties: Braided aramid FRP bars of 14-mm diameter with 1.25 GPa strength and 68 GPa of Young's modulus. The concrete strength and setting up details are all in table 2.6. Where l_e is the embedded length; D is the nominal bar diameter; and σ_{ftu} is the strength of the FRP bars.

Figure 2.30 shows the bond stress-slip relationship of the test results from not only the pre-stressed bond test but also the pullout one side bond test. The bond strength is larger and the slip is shorter using the pre-stressing method than that obtained using the pullout test. In figure 2.30, it can be seen that the curves plotted from the pre-stressing test show bond strength of around 15 MPa and 20 MPa. The bond slip is near 1 mm. Meanwhile, the curves from the pullout test show bond strength between 7 MPa and 8 MPa with a bond slip of near 3.0 mm. Comparing the test results of the pre-stressed tests, it can be seen that the bond stress is proportional to the concrete strength.

Table 2.6. – Set up details of the pre-stress bond test.

Condition N°	Test method	Concrete strength [MPa]	l_e / D	Pre-stress of FRP bar $0.6\sigma_{ftu}$ [MPa]
1	Pullout test	40	80	
2		56	80	
3		84	80	
4	Pre-tensioned test	35	56.25	750
5		67	56.25	

2.4.2 Flexural strength of RC beam with FRP reinforcing bars.

RC beams with FRP reinforcing bars behave quite different from RC beams with steel rebars. The reason is that the FRP reinforcing bars possess a different behavior than the steel rebars (see figure 2.9). FRP reinforcing bars do not yield as steel rebars do. Hence, beams reinforced with steel rebars are designed as under reinforced to ensure not only flexural strength but also ductility, however, beams reinforced with FRP rebars must be designed as over reinforced. If an RC beam with FRP rebars is designed as under reinforced then the FRP bars fracture prematurely before the concrete reaches its compressive strength, and as a consequence the beam collapses without warning (Benmokrane et al) [29]. However, if the beam is designed as over reinforced one, then failure of the beam is due to failure of the compressive concrete. Failure of the RC beam with FRP rebars by crushing the compressive concrete means that the FRP reinforcing bars do not reach their tensile strength (Brown and Bartholomew) [30]. The brittle failure of the beam is present in both circumstances.

Let us look closely at brittle failure of the beam. Once the FRP rebars break, the beam fails because the tensile reinforcement no longer exists, therefore, the collapse of the beam is inevitable. The curve B of figure 2.31 shows, schematically, the moment-curvature relationship of an under reinforced concrete beam with FRP reinforcing bars. Note that the moment-curvature relationship is linear owing to the fact that the beam fails by fracture of the tensile reinforcement, in which the stress-strain relationship is linear. Once the concrete starts crushing, the collapse of the beam is also inevitable because the compressive strength of the concrete reduces. The curve A in figure 2.31 shows, schematically, the typical moment-curvature relationship of an over reinforced concrete beam with FRP reinforcing bars. The curve of the moment-curvature relationship is non-

linear because the beam fails as the compressive concrete crushes, and the stress-strain relationship of the concrete is non-linear.

Until now, good results have been found regarding to the strength of RC beams with FRP rebars. It only remains to add ductility to the beams. Ductility is an essential property of an RC structure that is required for earthquake resistence to give early warning of failure and is also required for moment redistribution. However, we cannot assume yielding of the FRP rebars because the stress-strain relationship is fully linear (see figure 2.9). Ductility of RC beams with FRP reinforcing bars is a major concern not only for structural designers but also structural researchers, therefore, some proposals have to be made to achieve ductility. Suggestions such as 'Since FRP reinforcing bars do not yield as the steel rebars do, there should be the explicit provision that failure be controlled by concrete crushing, as opposed to tensile reinforcement rupture' (Nanni) [31]. Another suggestion is the use of hybrid FRP reinforcement made of fibers with different elongation to obtain a progressive failure of the rebars to obtain ductility. Others suggestions are for example, the use of FRP confinement embedded in the zone of concrete compression as well as staggered tensile reinforcement. In addition, it has been suggested that partial debonding of the tensile reinforcing bars would achieve ductility of the RC beams with FRP reinforcing bars. All of the above suggestions only reflect the high concern about ductility of the RC beams with FRP reinforcing bars.

2.4.3 **Shear strength of RC beams with FRP stirrups.**

Closed-loop FRP stirrups have been used in laboratory tests of RC beams with steel rebars. FRP stirrups of 10-mm diameter were placed at 75-mm intervals along the beams and none of the beams showed shear failure. Conversely, the beams failed due to flexure.

These results are an indication that FRP stirrups resist the shear forces in the entire beam (Saadatmanesh and Ehsani) [32].

2.5 Stress-strain relationship of normal concrete.

Many equations exist, for obtaining the stress-strain relationship of the concrete (Popovic) [33], (Popovic) [34], (Hognestad) [35] and (Desayi) [36]. Many of these equations have some shortcomings which make them unacceptable for use in actual structural design. However, the most acceptable equation, which fits properly with experimental results, is Wang's equation (Wang et al) [37]. The stress-strain relationship using Wang's equation covers the ascending branch as well as the falling branch trending to infinity when the concrete strength trends to zero (Wee) [38] and (Holkmann) [39] (see figure 2.32). Wang et al found that the following expressions give the most acceptable fit to the stress-strain curves of normal concrete:

$$Y = \begin{cases} \dfrac{A_a * X + B_a * X^2}{1 + C_a * X + D_a * X^2} \; ; \; 0 \le X \le 1 \quad \text{(Ascending branch)} \\ \dfrac{A_d * X + B_d * X^2}{1 + C_d * X + D_d * X^2} \; ; \; X > 1 \quad \text{(Descending branch)} \end{cases} \qquad \ldots\ldots\ldots\ldots 2.1$$

Where $Y = \dfrac{\sigma_c}{f_c}$ 2.2

and $X = \dfrac{\varepsilon_c}{\varepsilon_{co}}$ 2.3

where σ_c and ε_c are stress and strain in general; f_c and ε_{co} are the concrete strength, and the corresponding strain. A_a, B_a, C_a, and D_a are coefficients for the ascending branch of the stress-strain curve; A_d, B_d, C_d, and D_d are coefficients for the descending branch of the stress-strain curve.

For the ascending branch of the stress-strain curve, the values of the four coefficients are established from the following four boundary conditions:

Boundary condition number one for the ascending branch

$$\frac{dY}{dX} = \frac{E_c}{E_{co}}, \quad \text{when } (Y = 0,\ X = 0) \qquad \ldots\ldots 2.4$$

Where E_c represents the secant modulus of elasticity at $0.45 f_c$, and E_{co} represents the secant modulus of elasticity at f_c.

Boundary condition number two for the ascending branch

$$Y = 0.45 \quad \text{for} \quad X = \frac{0.45}{E_c / E_{co}} \qquad \ldots\ldots 2.5$$

Boundary condition number three for the ascending branch

$$Y = 1 \text{ for } X = 1 \qquad \ldots\ldots 2.6$$

Boundary condition number four for the ascending branch

$$\frac{dY}{dX} = 0 \quad \text{for} \quad (Y = 1 \text{ and } X = 1) \qquad \ldots\ldots 2.7$$

For the descending branch of the stress-strain curve, the values of the four coefficients are established from the following four boundary conditions:

Boundary condition number one for the falling branch

$$Y = 1 \text{ for } X = 1 \qquad \ldots\ldots 2.8$$

Boundary condition number two for the falling branch

$$\frac{dY}{dX} = 0 \quad \text{for} \quad (Y = 1 \text{ and } X = 1) \qquad \ldots\ldots 2.9$$

Boundary condition number three for the falling branch

$$Y = \frac{\sigma_{ci}}{f_c} \quad \text{for} \quad X = \frac{\varepsilon_{ci}}{\varepsilon_{co}} \qquad \ldots\ldots 2.10$$

Where σ_{ci} is the concrete stress and ε_{ci} is the concrete strain at the inflection point i of the descending branch of the stress-strain curve.

Boundary condition number four for the falling branch

$Y \to 0$ for $X \to \infty$ 2.11

With this approach, an analytical stress-strain curve can be generated from the knowledge of three essential points of the experimental curve.

The three essential points, are the following:

1) Stress and strain, at the concrete strength point f_c.

2) Stress and strain at 0.45 f_c (ascending branch of the curve).

3) Stress and strain at the inflection point i (descending branch of the curve). The inflection point i is at $0.35f_c$ in the falling branch of stress-strain curve where stress-strain curve changes from being convex to become concave.

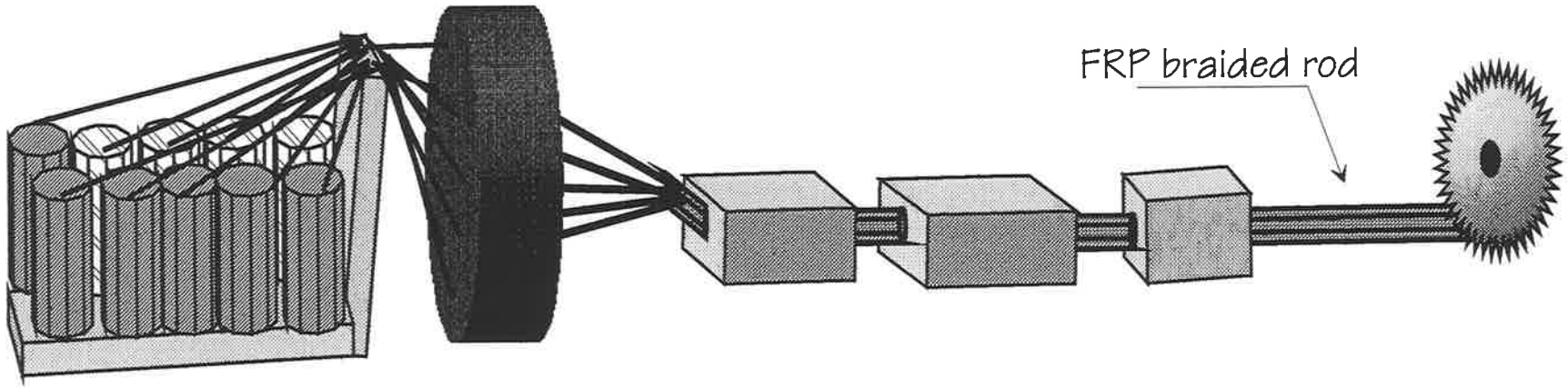

Figure 2.1 . - Schematic diagram of the winding process.

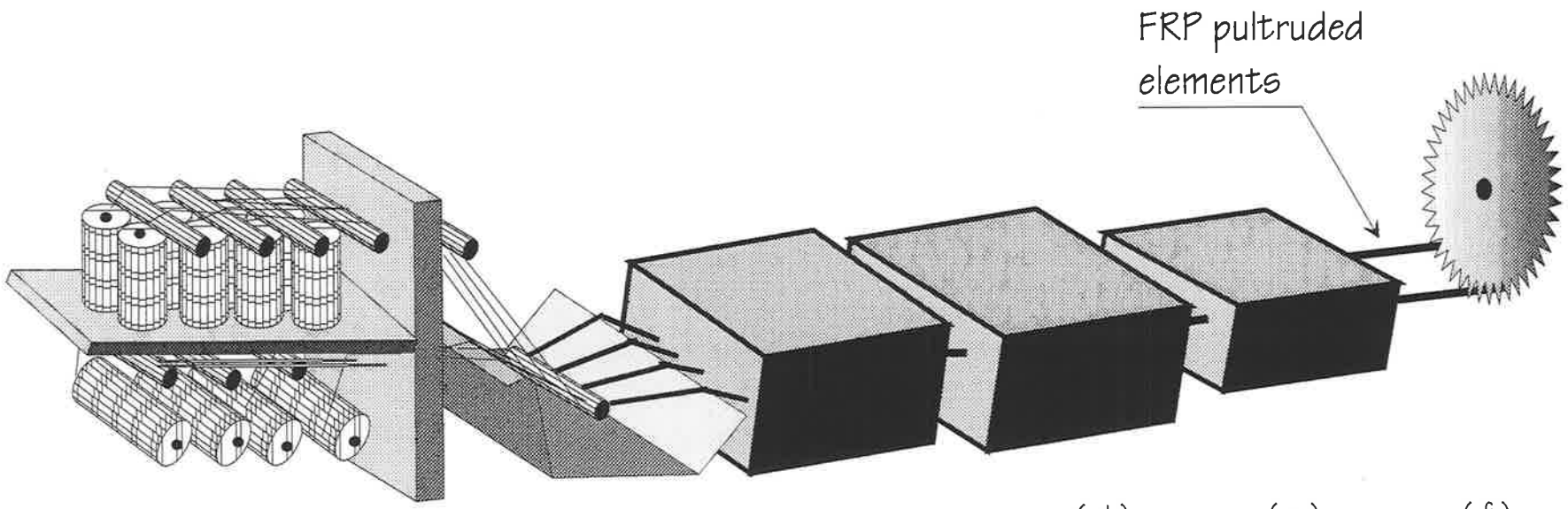

Figure 2.2 -. Schematic diagram of the pultrusion process.

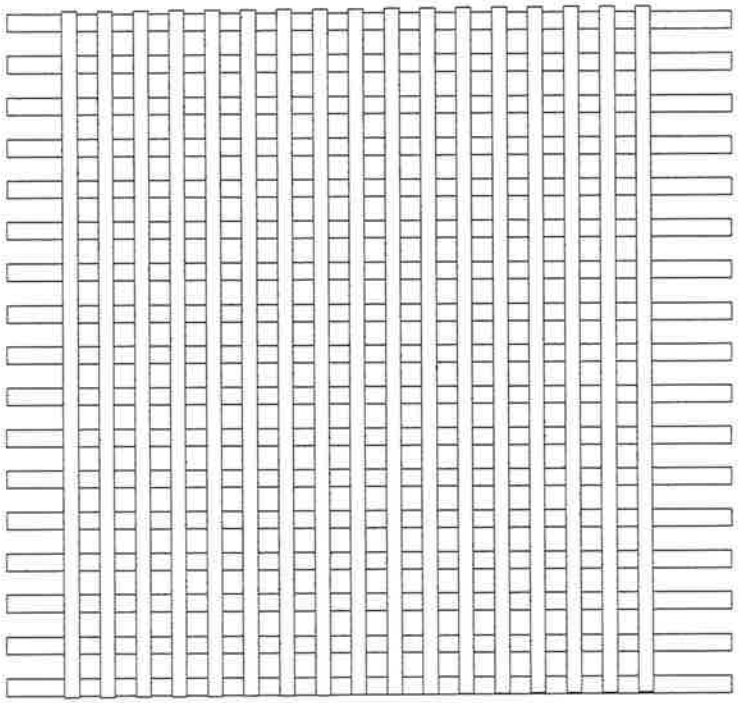

Figure 2.3. - Schematic repreesntation of FRP sheets with normal layout.

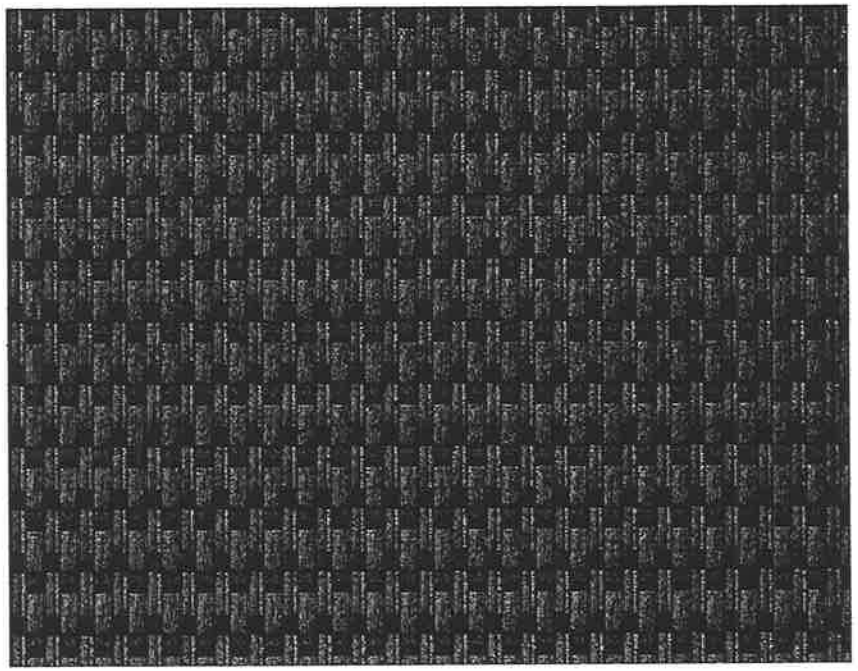

Figure 2.4. - Schematic representation of FRP woven sheets layout.

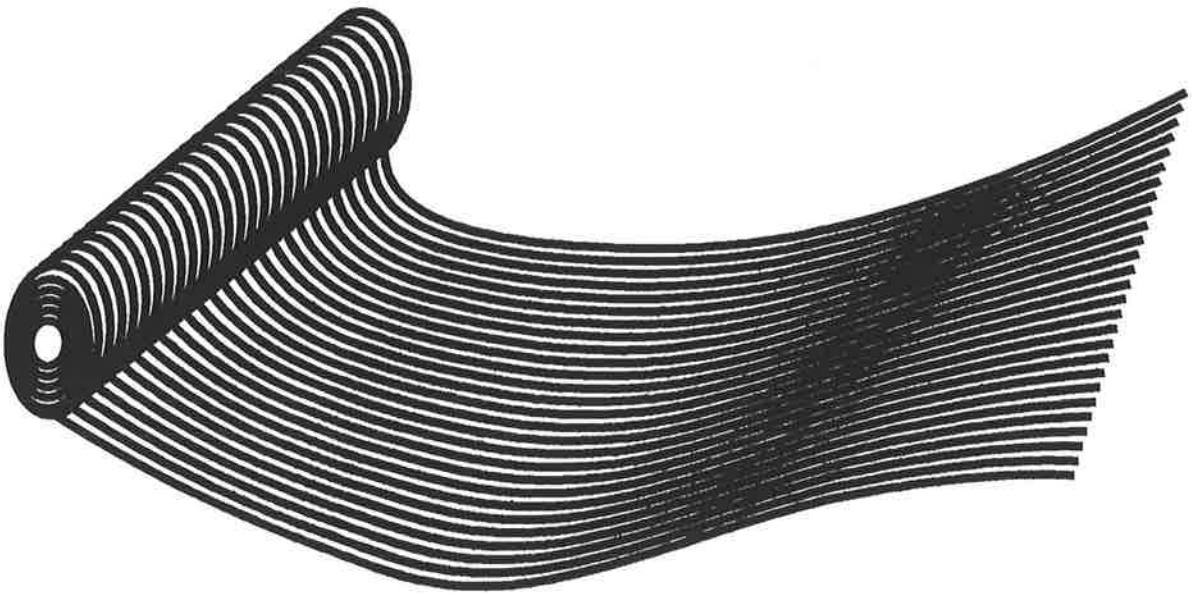

Figure 2..5. - FRP unidirectional sheet

Figure 2.6. - FRP bidirectional sheet..

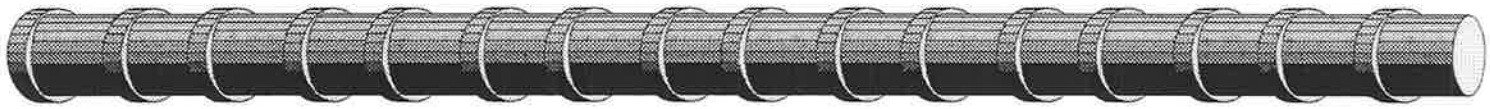

(a)
Reinforcing bar

(b)
Braided tendon

Fibure 2.7. - Schematic representation of FRP reinforcing bar and FRP tendon.

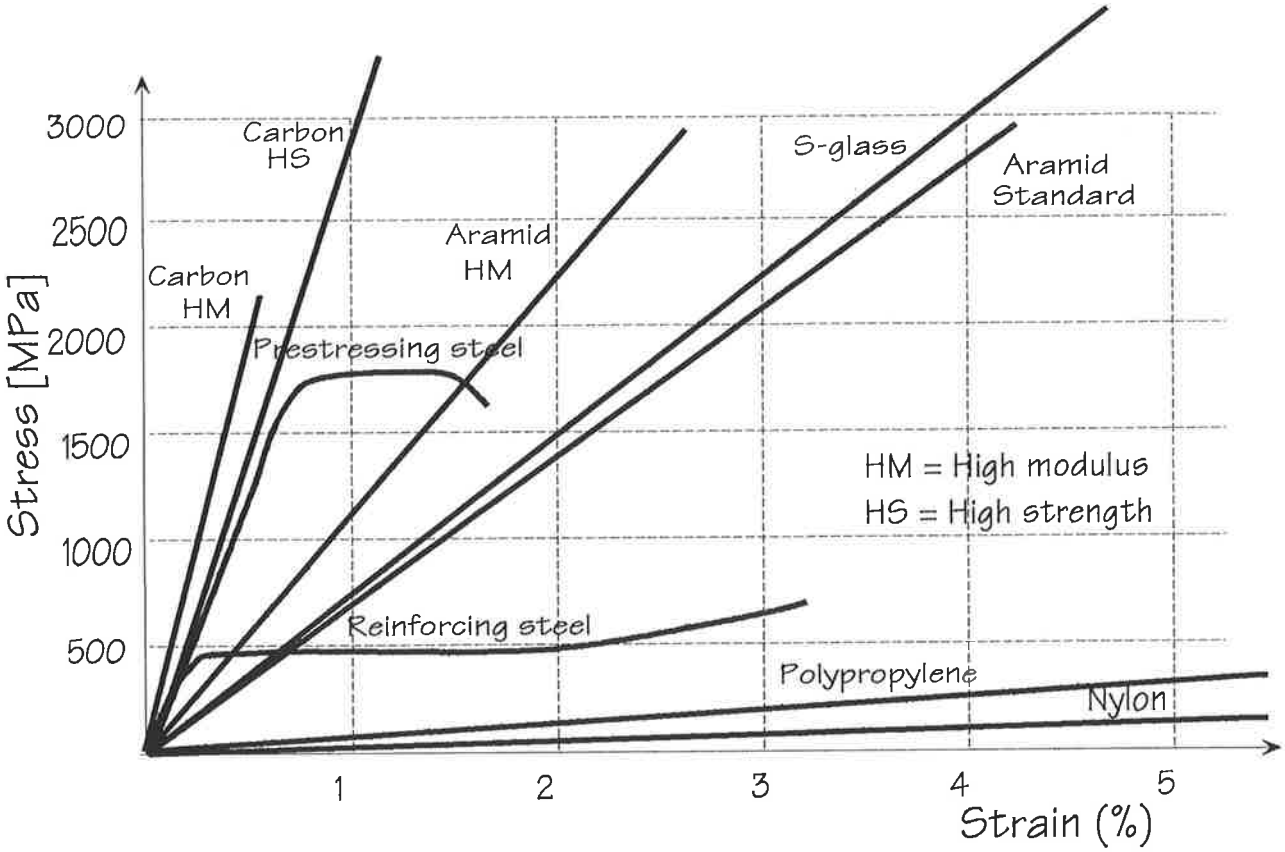

Figure 2.8. - Stress-strain relationship of FRP and steel materials

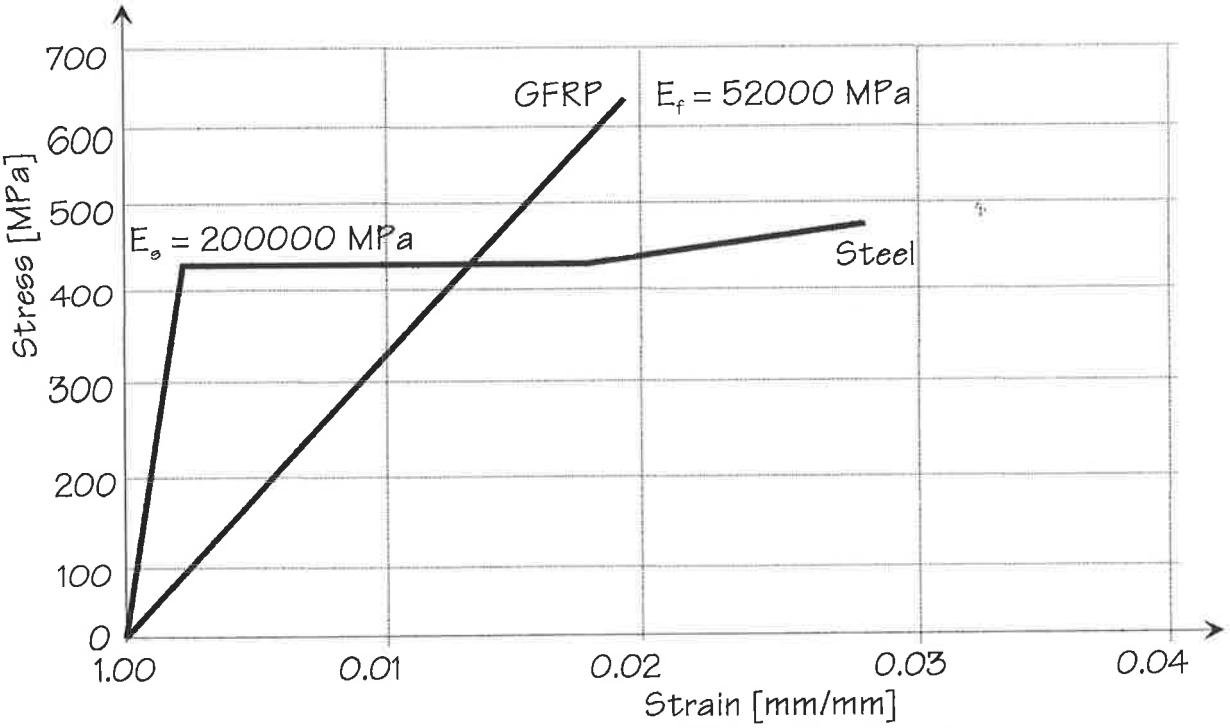

Figure 2.9.-Stress-strain relationship of FRP and steel rebars.

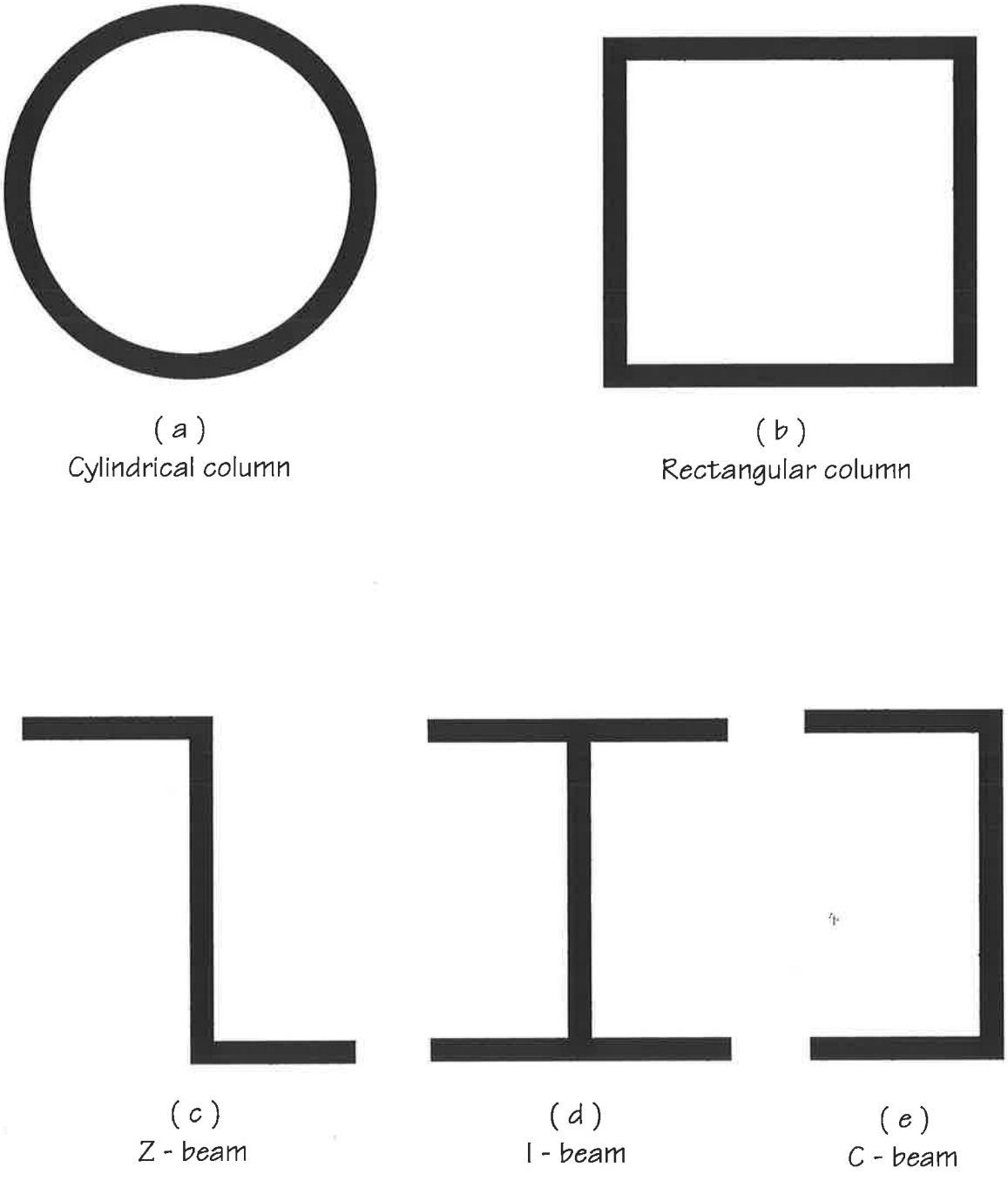

Figure 2.10. - Cross-sections of pultruded beams and columns.

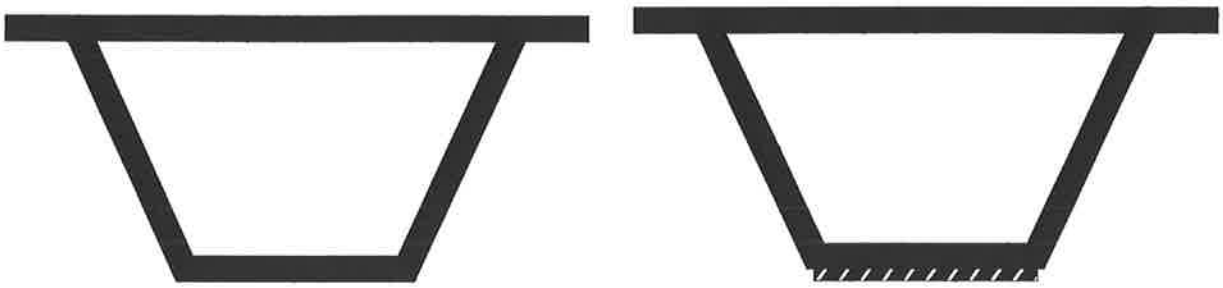

(a)
Trapezoidal boxed beam

(b)
Composite trapezoidal boxed beam

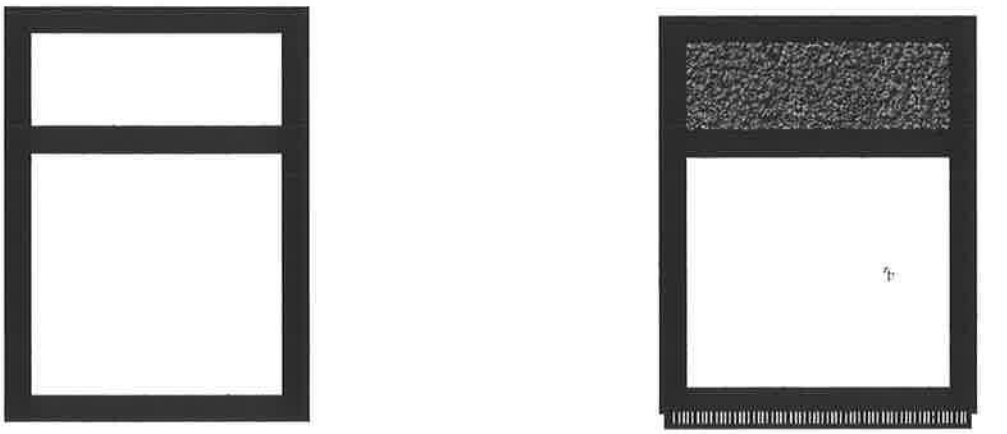

(c)
Rectangular boxed beam

(d)
Composite rectangular boxed beam

Figure 2.11. - FRP boxed beams.

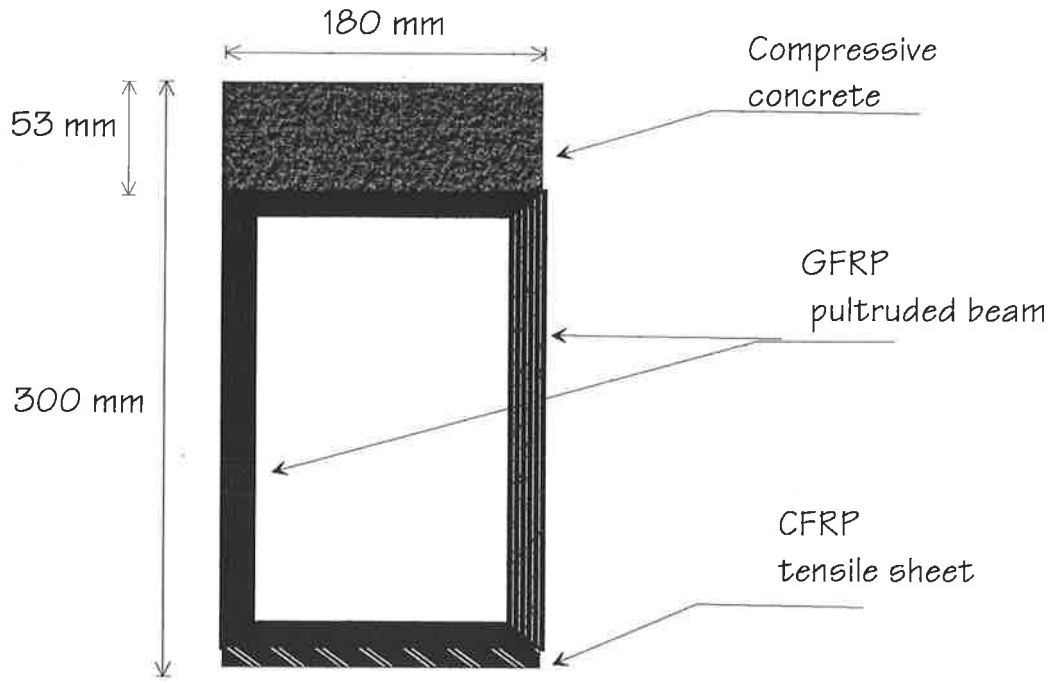

Figure 2.12. Cross-section of a hybrid beam.

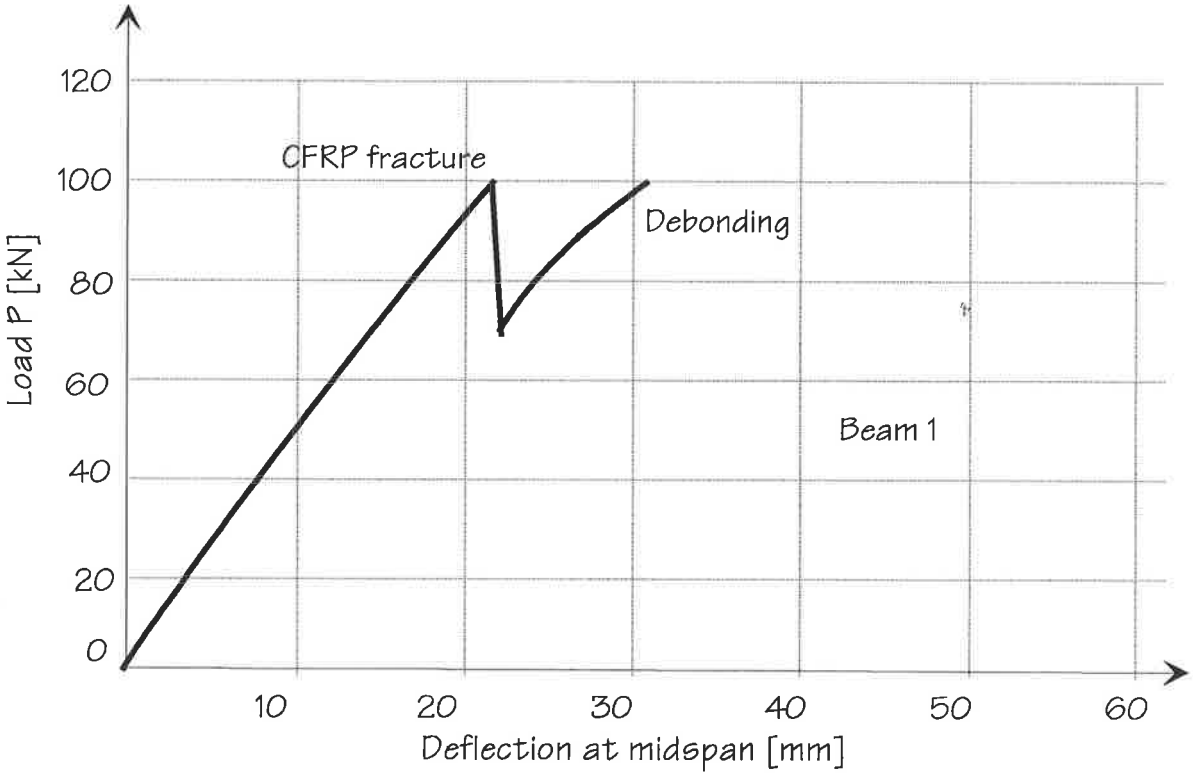

Figure 2.13.- Load-deflection relationship of beam 1.

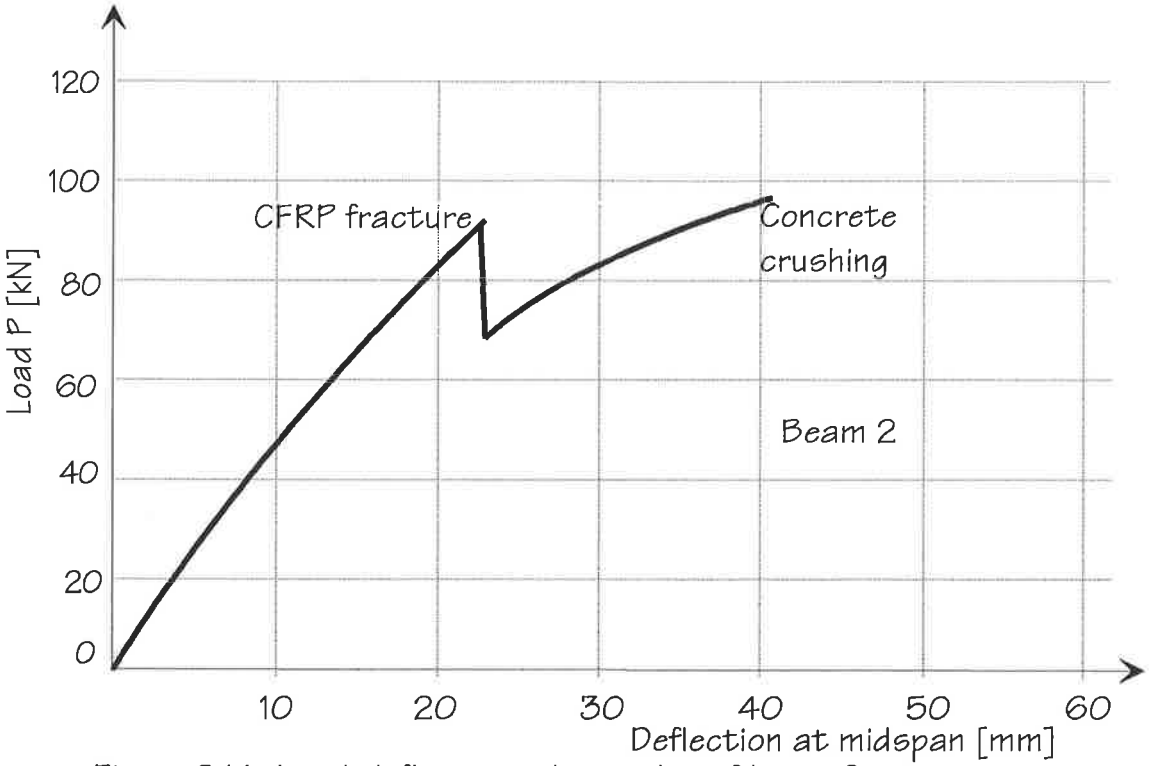

Figure 2.14.-Load-deflection relationship of beam 2.

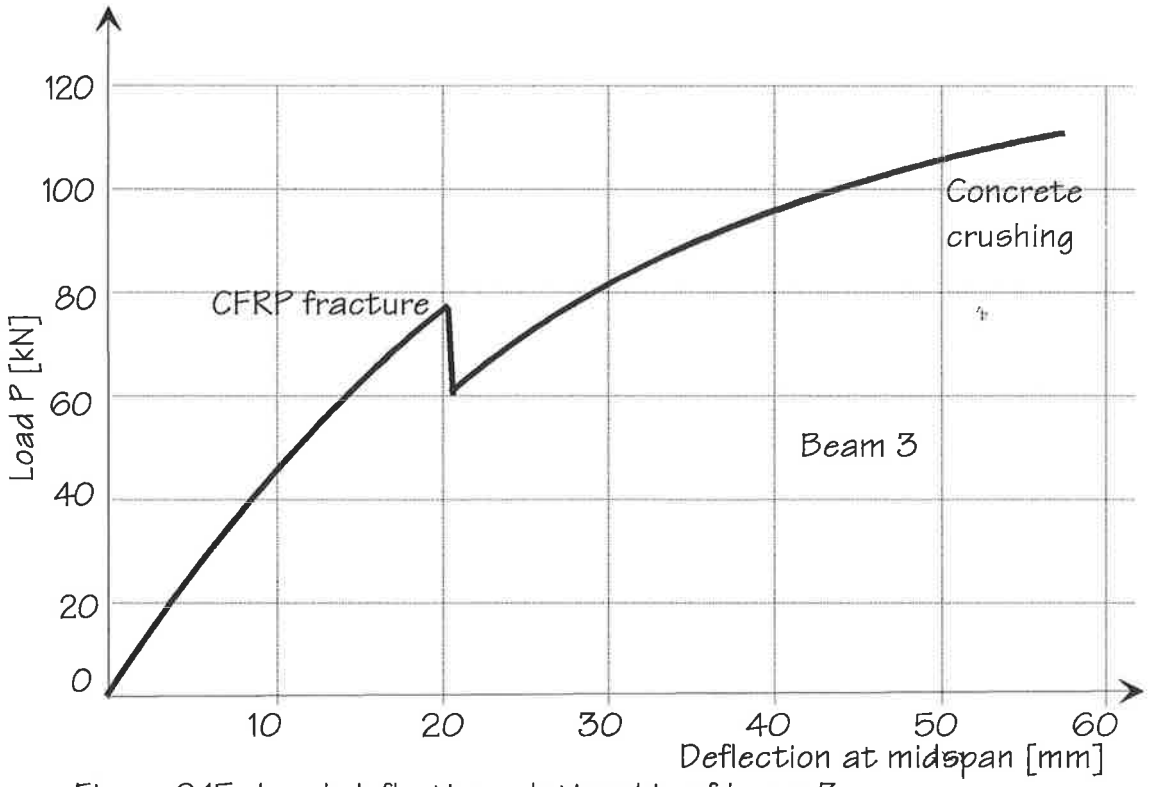

Figure 2.15.-Load-deflrction relationship of beam 3.

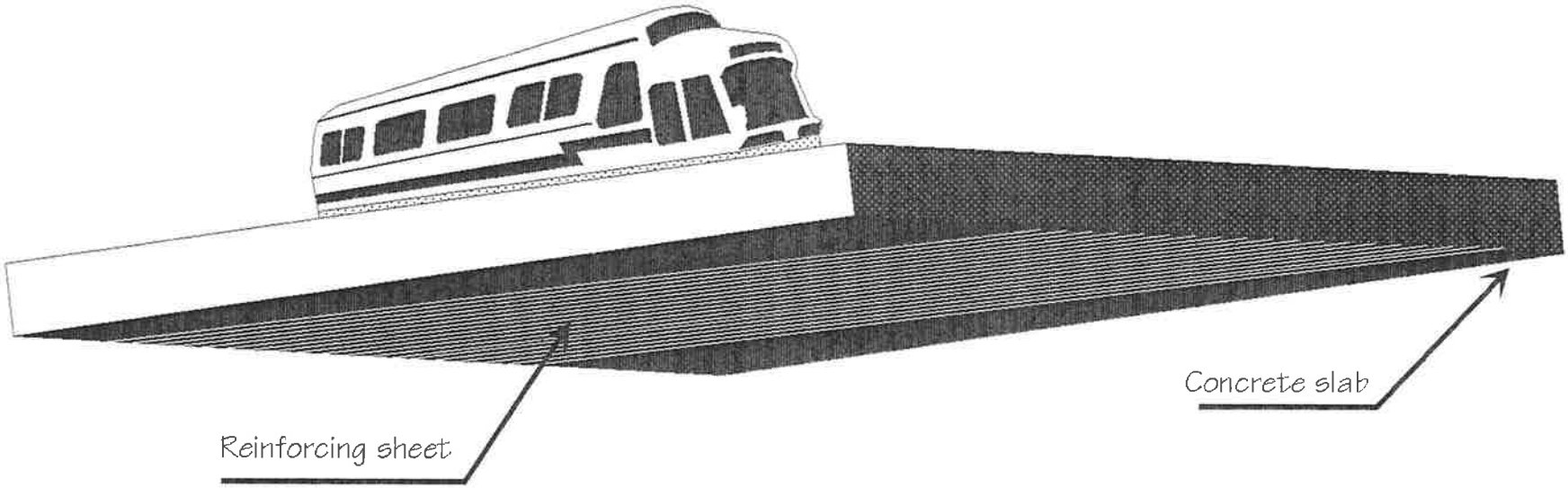

Figure 2.16. - CFRP reinforcing sheet to improve bridge capacity.

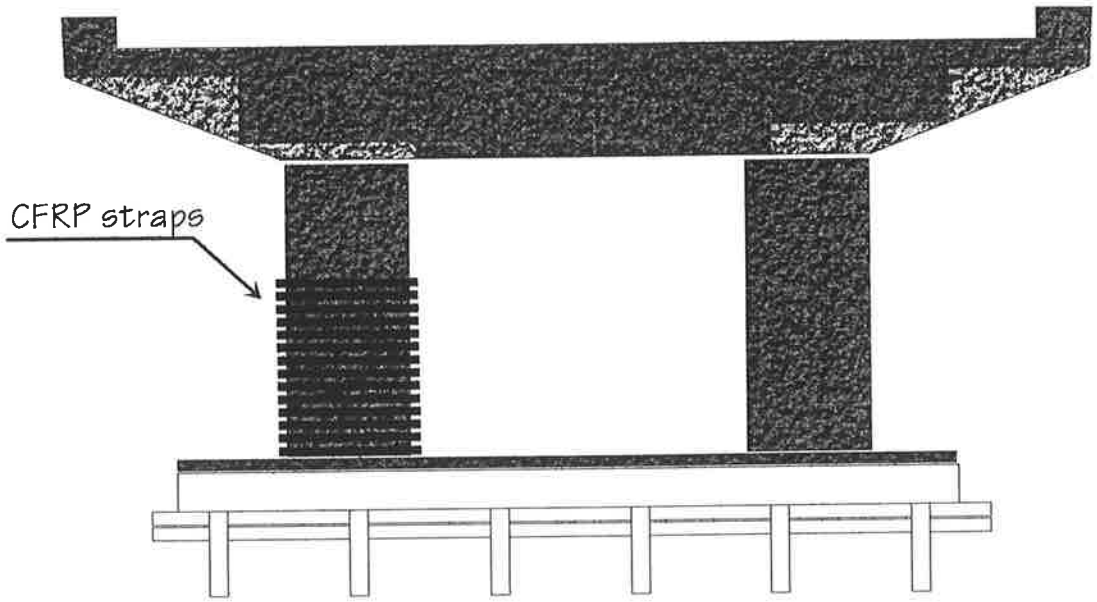

Figure 2.17. - Retrofitted and unretrofitted concrete bridge columns.

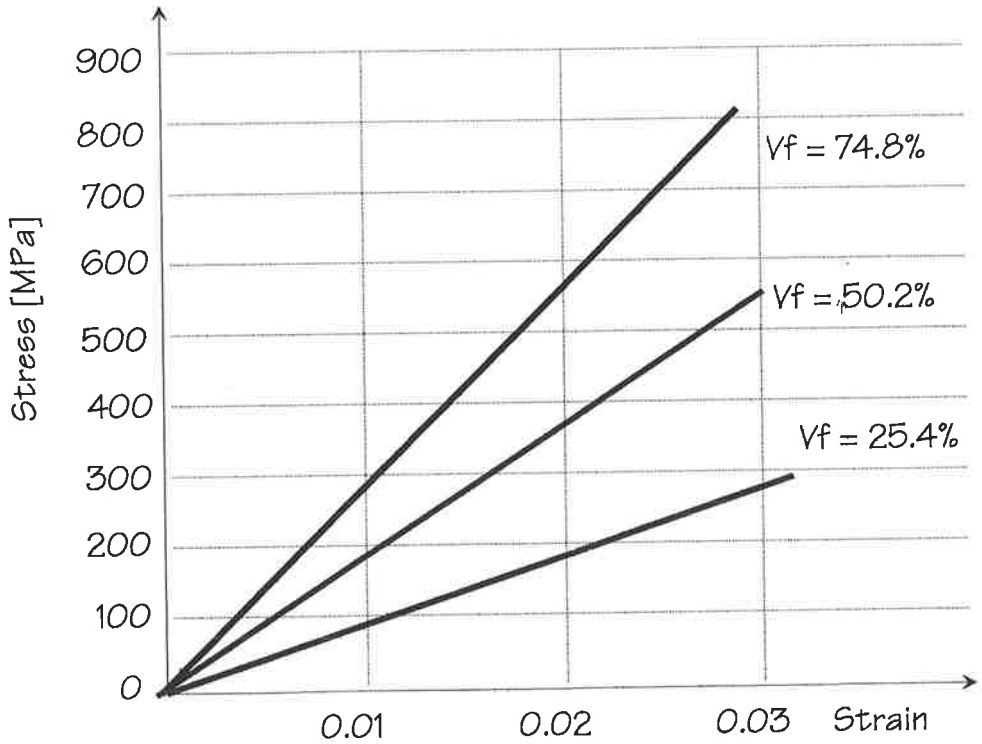

Figure 2.18. - Stress-strain relationship of FRP straps.

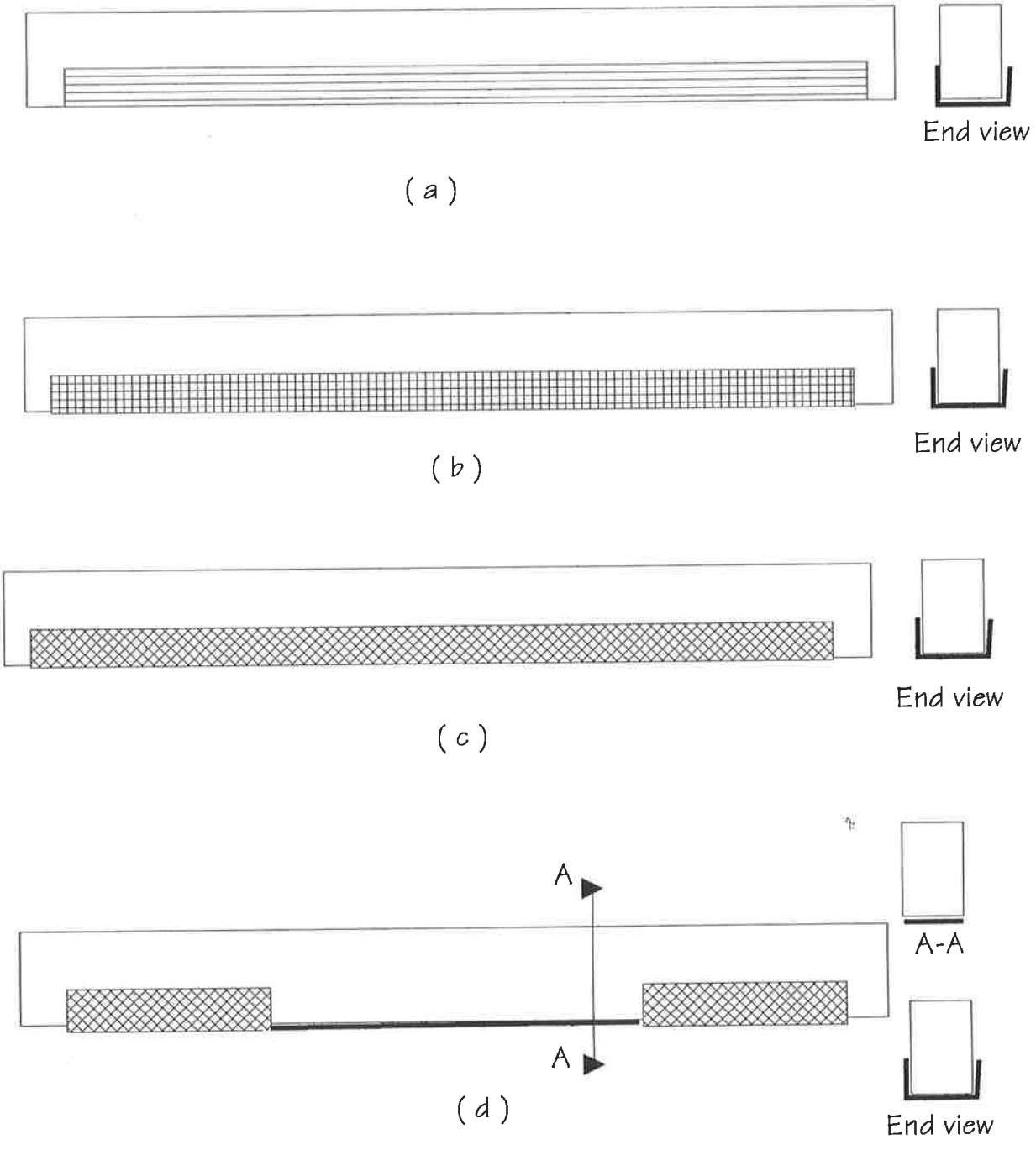

Figure 2.19. - Strengthened concrete beams with carbon fiber sheets.

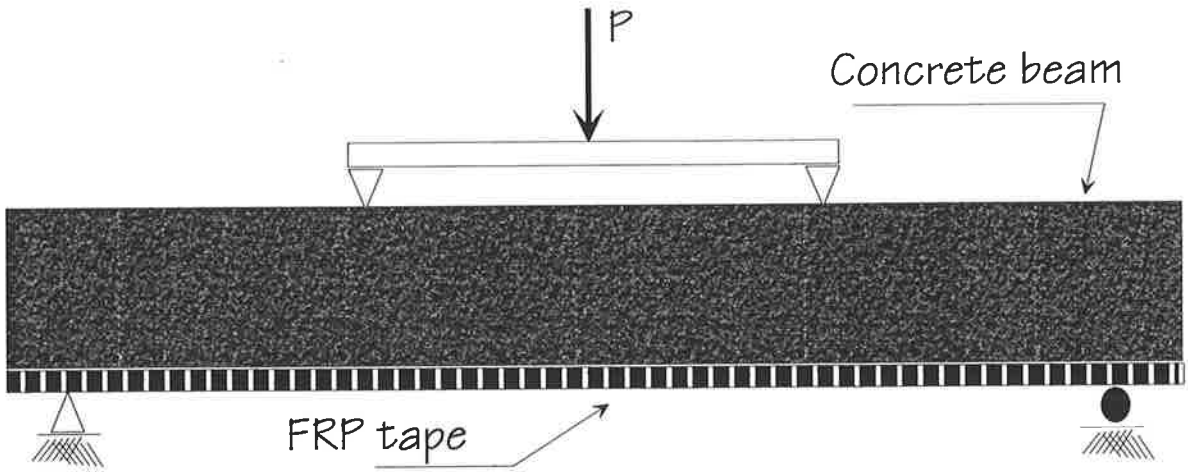

Figure 2.20. - Concrete beam with CFRP sheet as an external reinforcement.

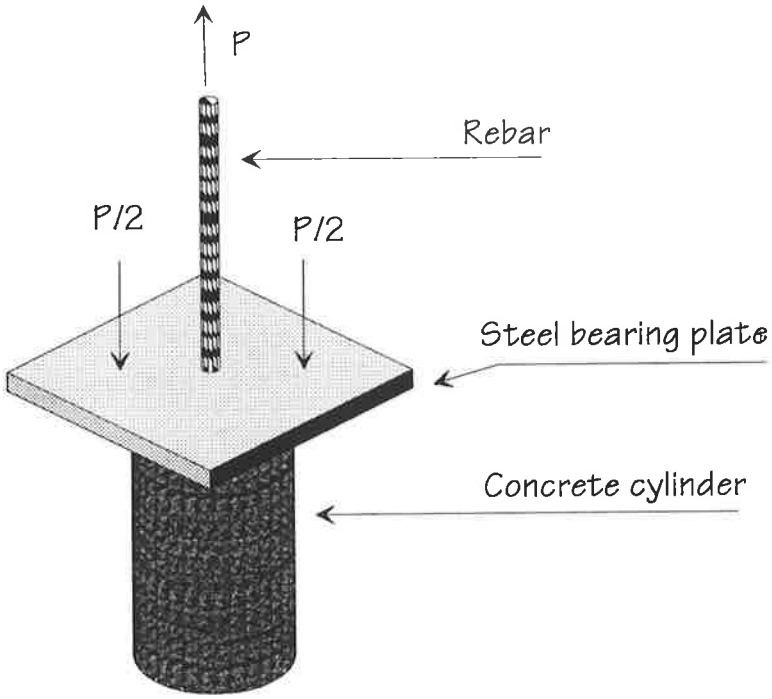

Figure 2.21. - Schematical Pullout test.

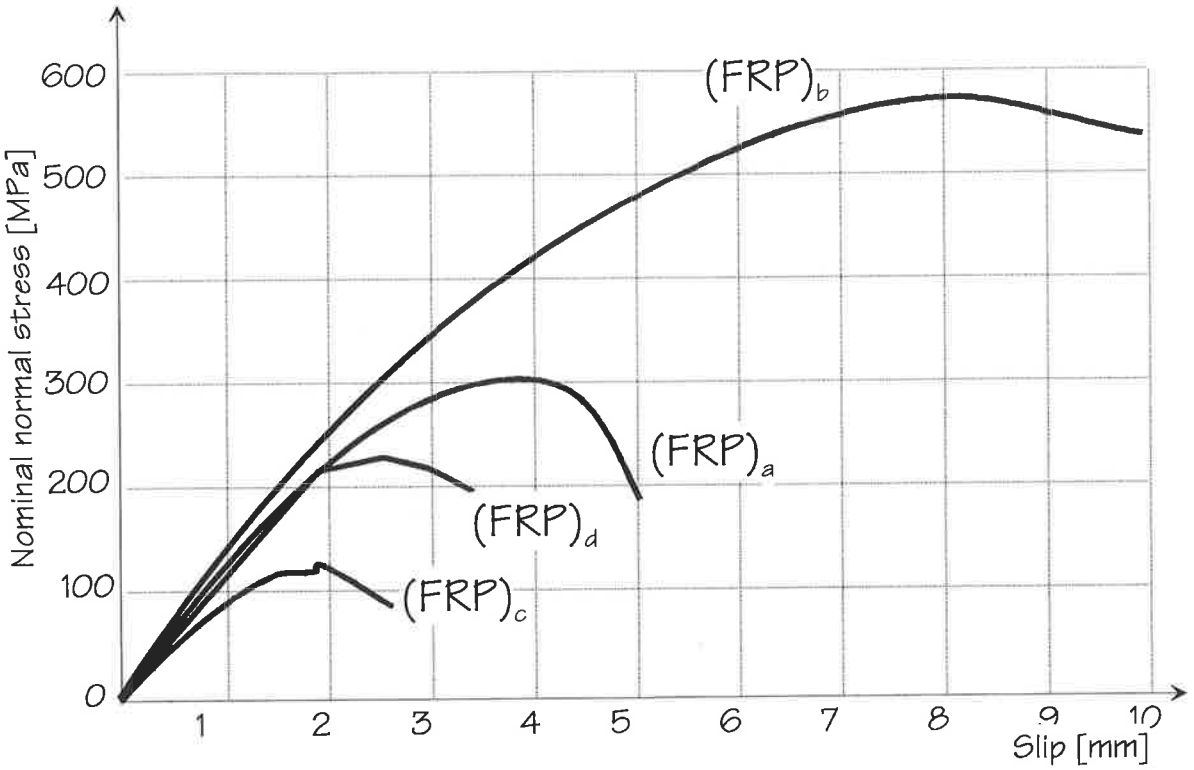

Figure 2.22. - Normal stress-slip relationship of FRP rebars from table 2.3.

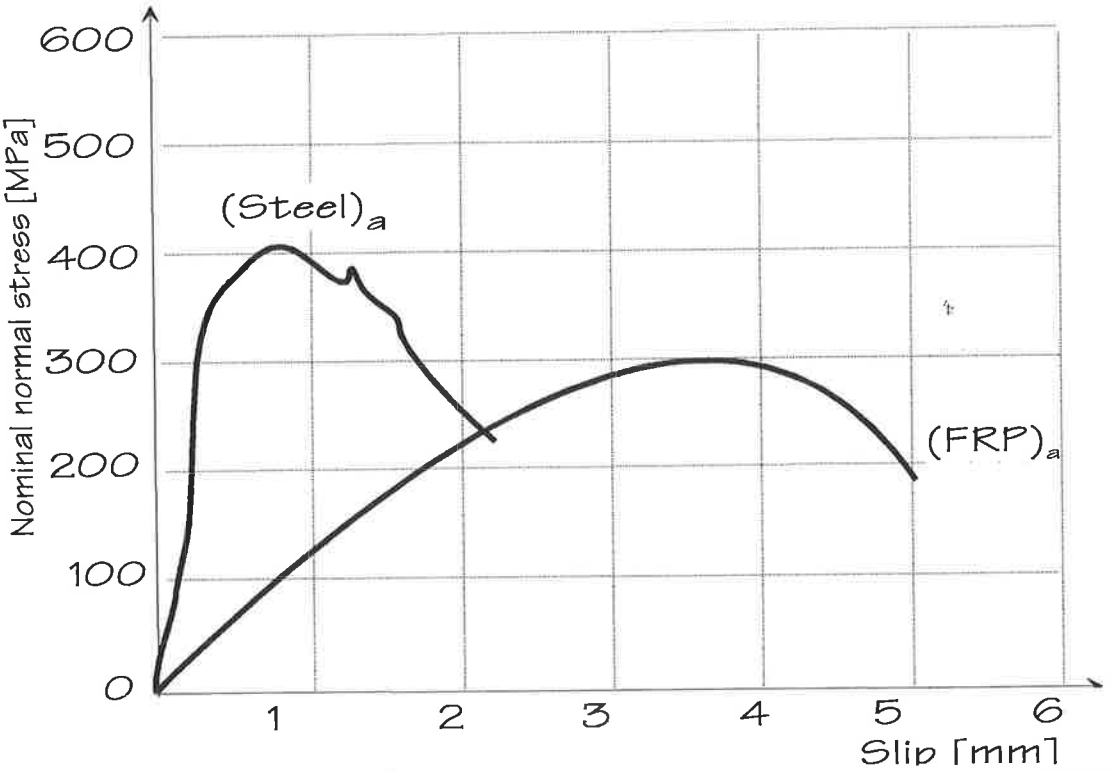

Figure 2.23. - Normal stress-slip relationship of FRP and steel rebars from table 2.3.

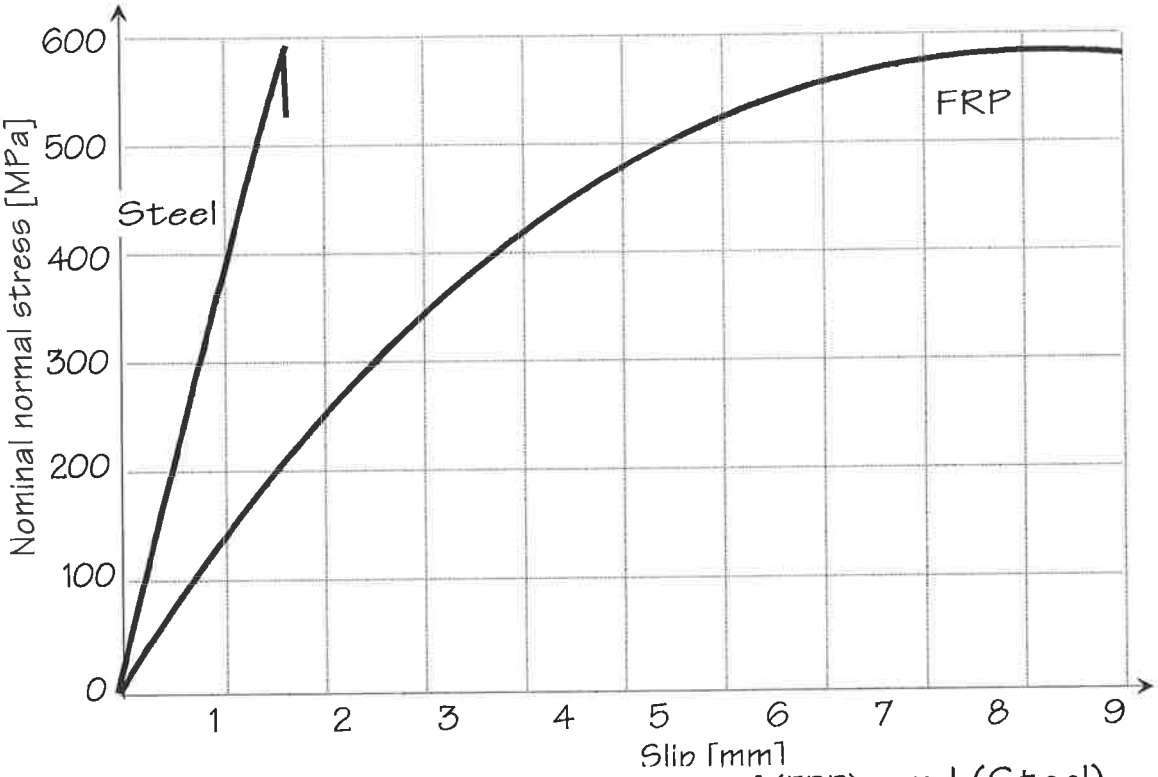

Figure 2.24. - Normal stress-slip relationship of $(FRP)_b$ and $(Steel)_b$ from table 2.3.

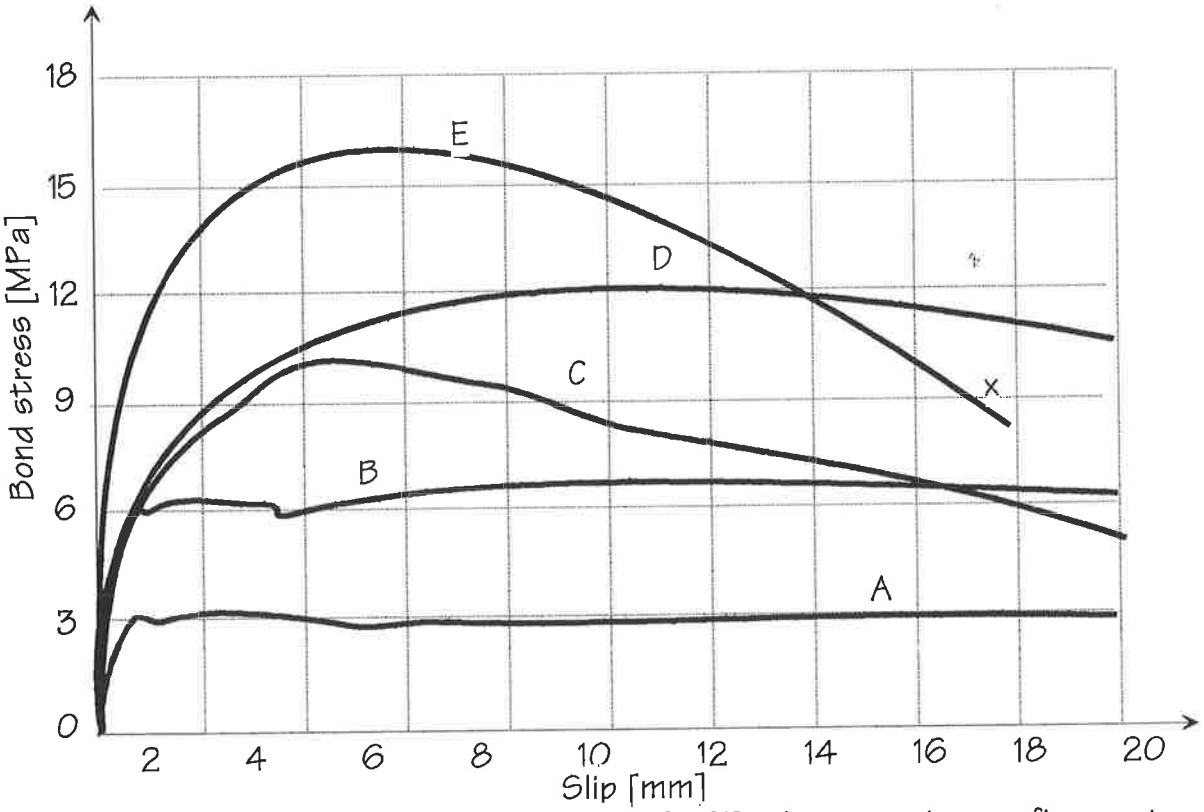

Figure 2.25. - Bond-stress-slip relationship of FRP rebars varying confinement.

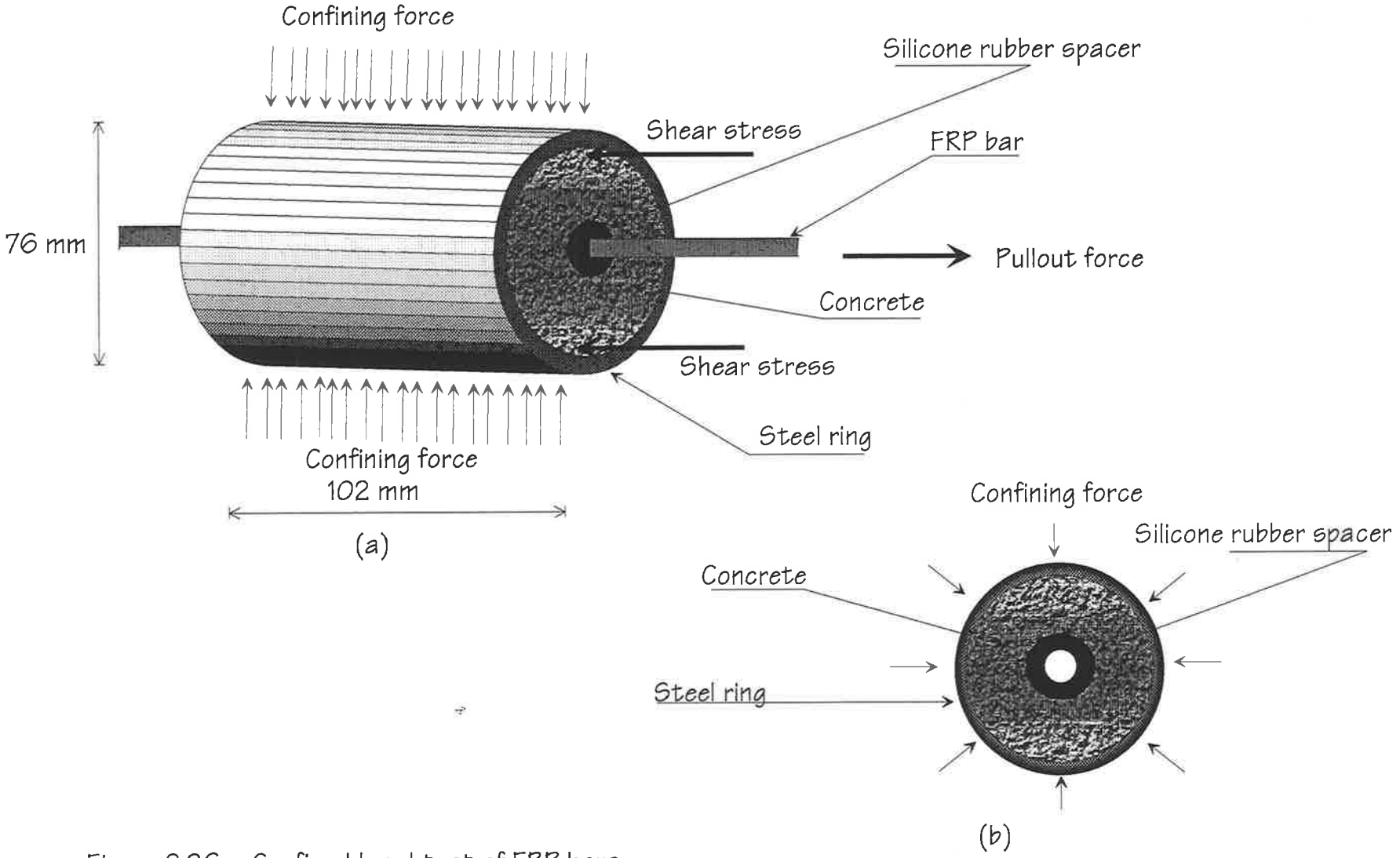

Figure 2.26. - Confined bond test of FRP bars.

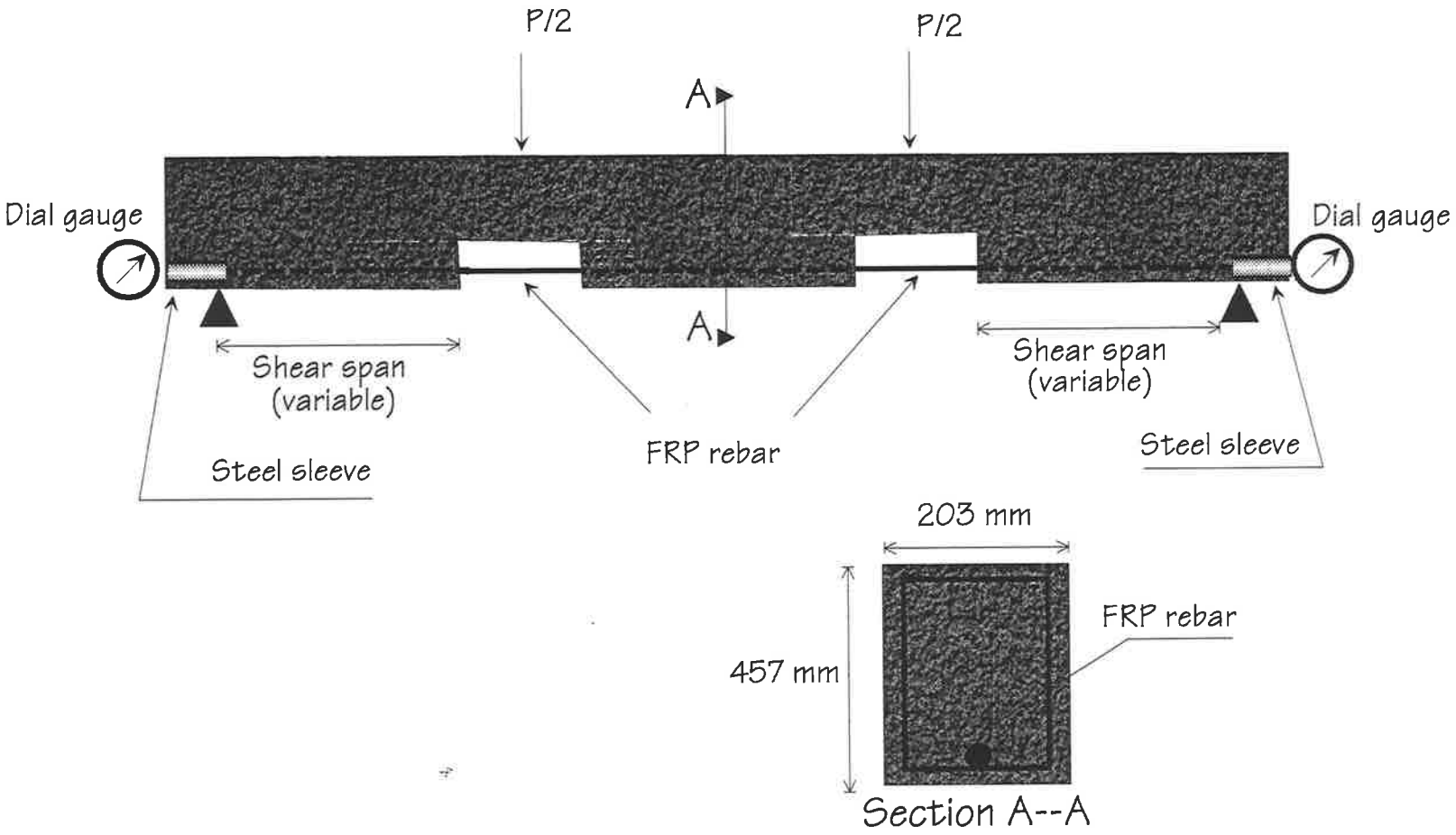

Figure 2.27. - Tensile bond test.

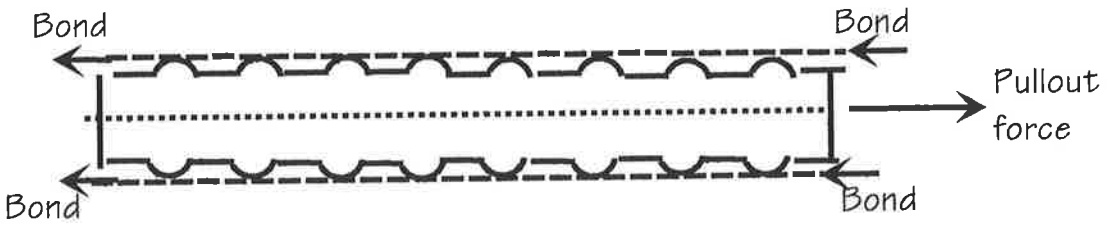

(a) Steel bar

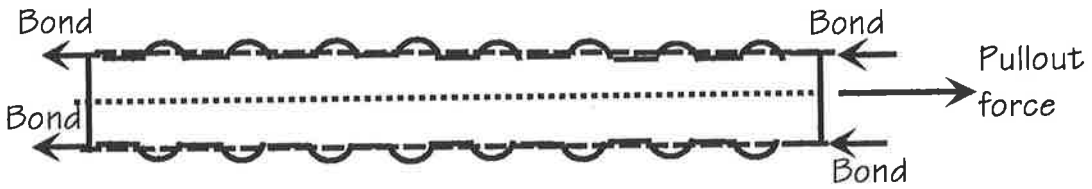

(b) FRP bar with outer deformations

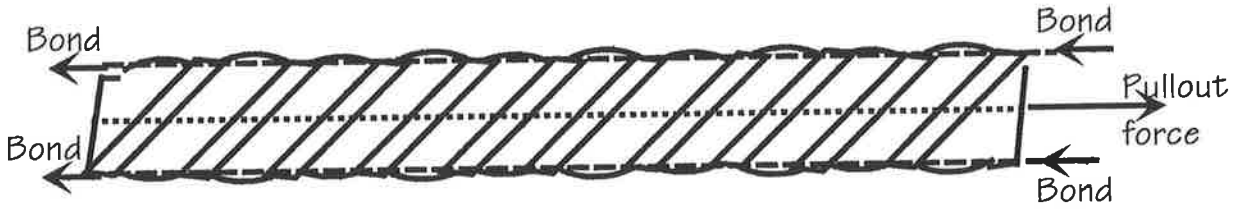

(c) FRP bar with swallow deformations

Figure 2.28. - Shear failure at pullout test.

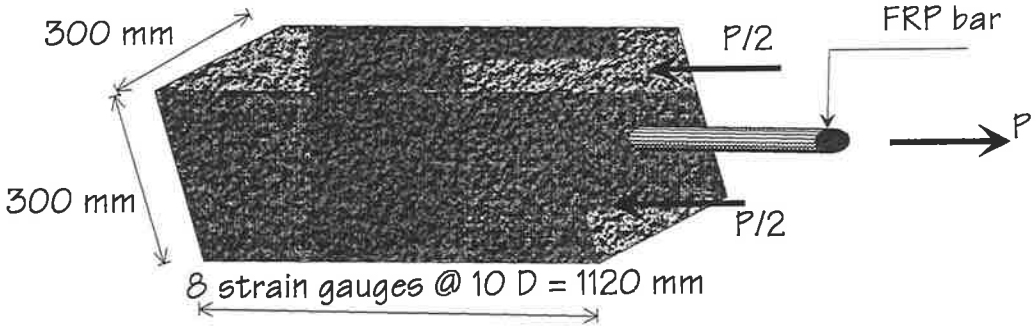

(a) One end pullout test specimen

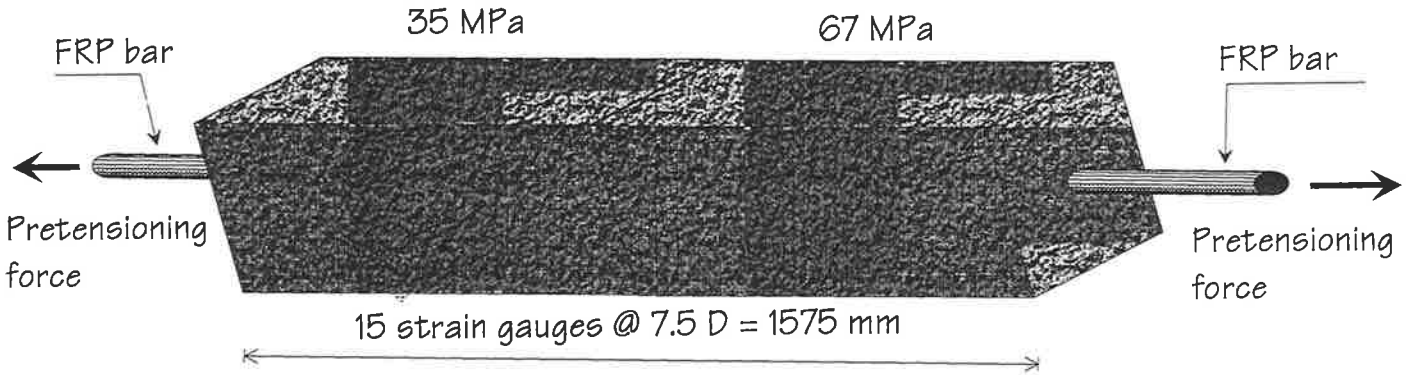

(b) Pre-stressed specimen

Figure 2.29. - Pre-tensioned bond test.

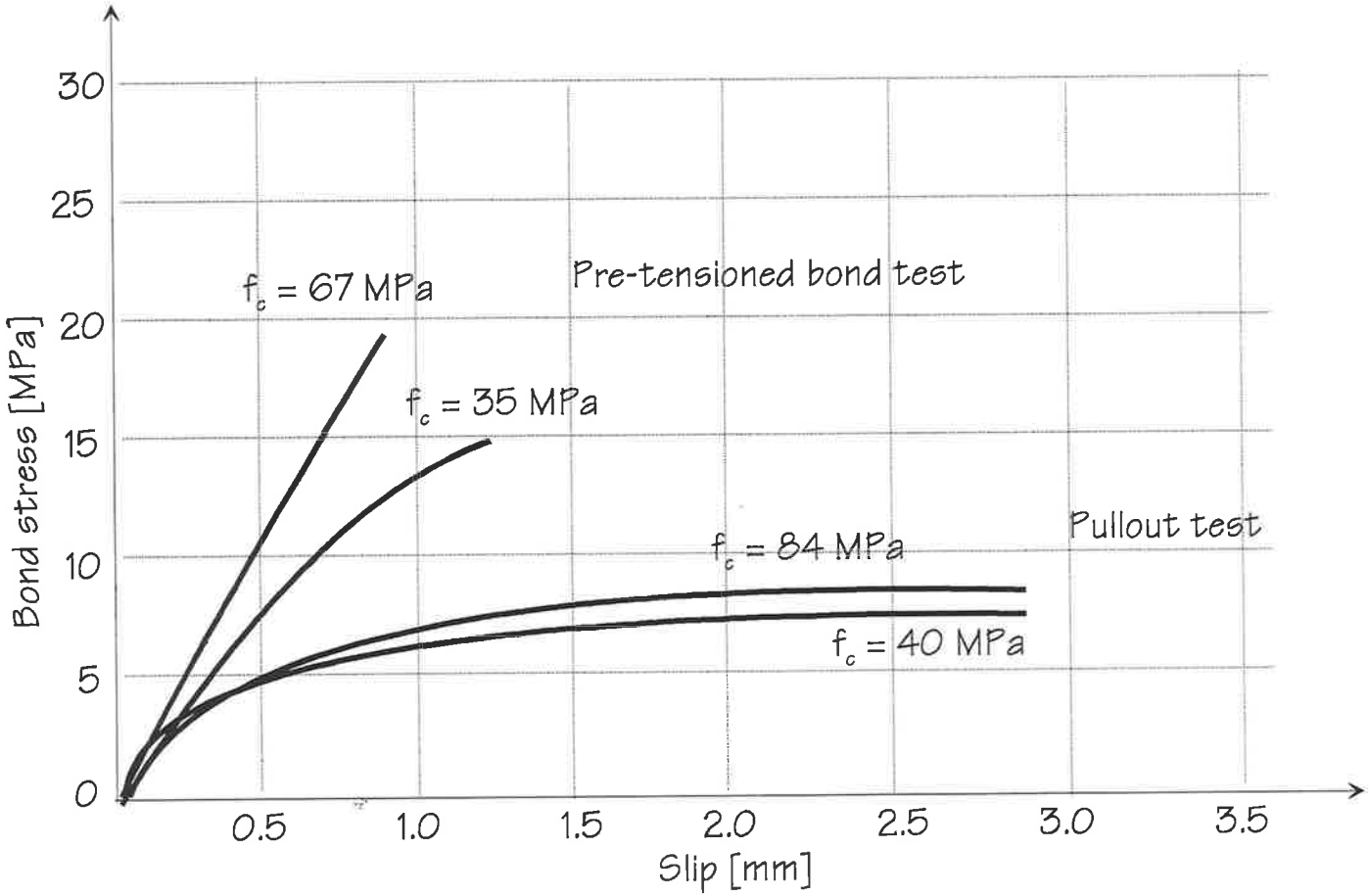

Figure 2.30. - Bond stress-slip relationship of FRP rebars.

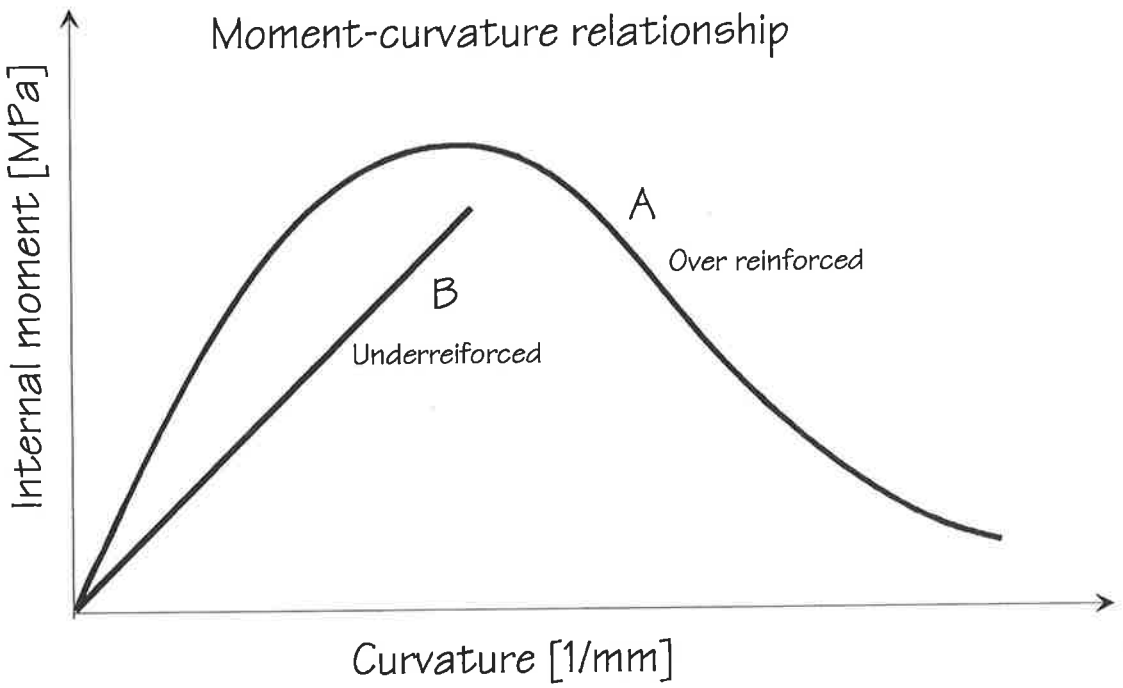

Figure 2.31. - Typical moment-curvature relationships of RC beams with FRP rebars.

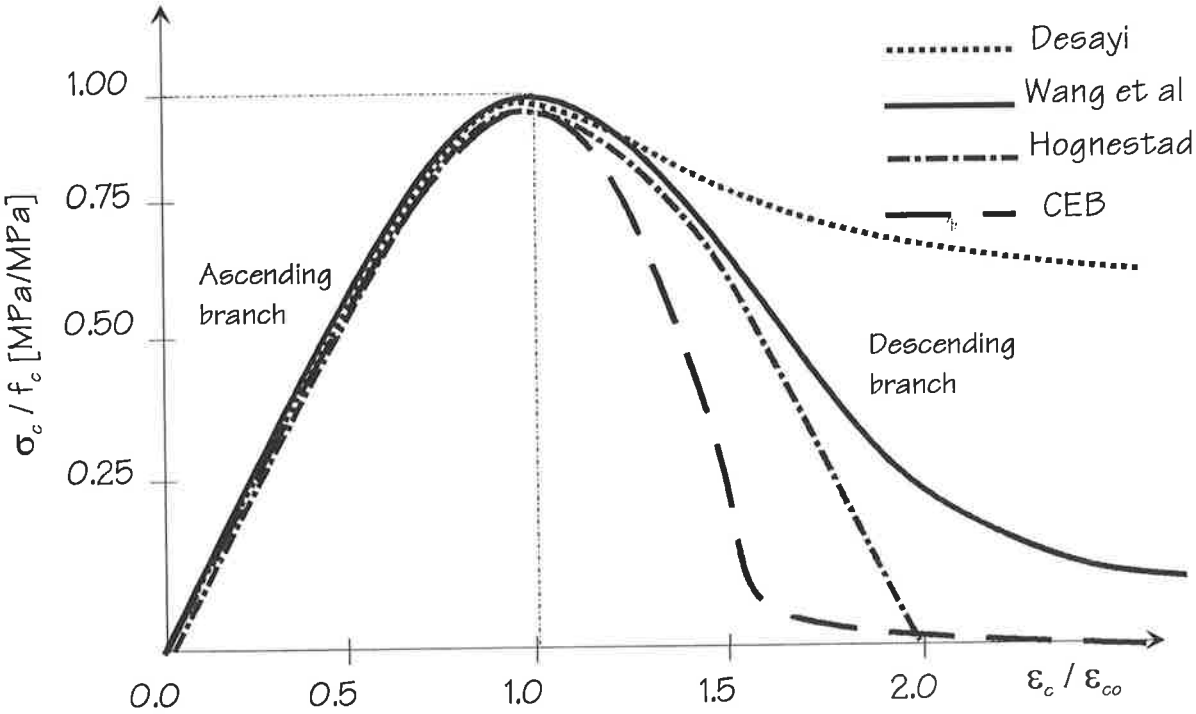

Figure 2.32. - Comparative graphics of stress-strain relationship of normal concrete.

Chapter 3

Segmental analysis

3.1 Introduction

This chapter is about the segmental analysis method applied to simply supported concrete beams. Segmental analysis can be used to design not only singly reinforced concrete beams but also doubly reinforced concrete beams. Furthermore, the type of reinforcement can be either FRP rebars or steel rebars or a combination of both. Firstly, the reader can find herein a description of what segmental analysis is about. Next is the analysis of RC beams with FRP reinforcing bars at the bottom only, which is used to explain in a step by step basis the use of segmental analysis. After

explaining the analysing procedure on beams with FRP reinforcing bars at the bottom only, is explained the analysed procedure for doubly reinforced concrete beams in order to describe the effects of the compressive reinforcement.

The procedure used in the analysis of the beams is organised into a mathematical algorithm that is used in a computer program, which is thoroughly described using a flowchart. Finally, the reader can see the results of the analysis of seven beams with different amounts and types of longitudinal reinforcement. In addition, there is a set of figures containing the moment-curvature relationship of two or three beams for making comparisons between them.

3.2 Segmental analysis

Ductility of reinforced concrete beams is measured either in terms of the load-deflection relationship from test data or in terms of the moment-curvature relationship, through a numerical analysis method. However, the design of the beams must be carried out through a numerical analysis method. The calculation of the moment-curvature relationship of the beams allows us to know not only the flexural strength of the beam but also the degree of ductility of the beams.

The analysis method, proposed in this thesis, is the segmental analysis method. Firstly, let us analyse a reinforced concrete beam with FRP reinforcing bars as a tensile reinforcement only. This is to make easy the understanding about the segmental analysis methodology. Later on is

analysed a reinforced concrete beam with both tensile FRP reinforcing bars, and compressive FRP reinforcing bars to get a deeper understanding about the segmental analysis method. The segmental analysis method is very helpful to evaluate both the actual flexural strength of the beams and their degree of ductility. The segmental analysis method is applicable to analysing RC beams with FRP reinforcing bars as well as RC beams with steel reinforcing bars.

3.2.1 RC beam with tensile reinforcement only.

Before starting with the calculation procedure, let us look at figure 3.1 as a whole and then, one by one, the subfigures marked from (a) to (d). Figure 3.1a shows the segmented cross-section of a beam with tensile reinforcement only, where b is the cross-section's width; h is the cross-section's depth; and d is the cross-section's effective depth; A_{ft} is the amount of FRP longitudinal reinforcement at the tensile zone; and ΔA is a segment of area in the cross-section of the beam. Figure 3.1b represents the strain profile, where n is the neutral axis depth in millimetres and ψ is the curvature in inverse of millimetres. The concrete strain at the top is ε_c and the strain of the tensile reinforcement is ε_{ft}. Figure 3.1c represents the stress profile; where σ_c is the concrete stress distribution, and σ_{ft} is the stress in the FRP tensile reinforcement. Figure 3.1d represents the distribution of forces along the cross-section, and the corresponding distances z of each component force, about the level of the tensile force T_f.

The calculation process starts with the division of the cross-sectional area of the beam into segmental areas ΔA which have a depth Δh and width b. In addition, for each segment of area ΔA, there is a strain ε_{cj} at its half depth Δh in figure 3.1b.

Let ψ be the curvature caused by a load P acting at the midspan of the concrete beam. Also, let us assume that the deformations along the cross-section of the beam are all small enough. If we add the usual assumption that the deformations are all proportional to their respective distances to the neutral axis of the beam, then we have two similar triangles in figure 3.1b. In that way, we are able to express the curvature ψ in terms of each strain and its respective distance to the neutral axis of the beam. Let ε_c be the concrete strain at the middle depth of the top segment of area ΔA (see figure 3.1a). The distance of ε_c to the neutral axis is the neutral axis depth n minus one half of the depth Δh. Therefore, the curvature ψ can be expressed in terms of the strain ε_c and its distance ($n - \Delta h/2$) to the neutral axis of the beam (see equation 3.1).

$$\psi = \frac{\varepsilon_c}{n - \frac{\Delta h}{2}} \qquad \text{3.1}$$

Solving for ε_c in equation 3.1, gives equation 3.2.

$$\varepsilon_c = \psi\left(n - \frac{\Delta h}{2}\right) \quad \ldots\ldots\ldots\ldots\ldots\ldots\ldots\ldots\ldots\ldots\ldots\ldots\ldots\ldots\ldots\ldots\ldots\ldots\ldots\ldots\ldots\ldots\ldots\ldots 3.2$$

Now, looking at figure 3.1b from top to bottom, we can see that for each segment of area, there is a corresponding strain. On the other side, each one of these strains over the neutral axis of the beam, is Δh closer than the upper one to the neutral axis of the beam. However, the strains below the neutral axis are Δh further away than the upper one from the neutral axis of the beam. The top concrete strain is named ε_c, next let us name it ε_{c1} the strain below ε_c. The strain below ε_{c1} would be ε_{c2} and so on until the lowest one named ε_{ch}.

With this approach, we can write down equations for each strain in figure 3.1 in terms of the curvature ψ and its distance to the neutral axis of the beam. For instance, the strain of the top segment of area ΔA is at a distance (n - Δh/2) from the neutral axis of the beam. Consequently, ε_{c1} is at the distance (n - 3Δh/2) and the strain ε_{c2} at the distance (n - 5Δh/2). Following this procedure, we can deduce that the distance between the strain at the bottom of the cross-section of the beam is (n – (2j – 1)Δh/2); where j is a countering number countering number also used in the numeric subscript of the corresponding strain ε_{cj}.

Let us look at equations 3.3 to 3.7.

$$\varepsilon_c = \psi\left(n - \frac{\Delta h}{2}\right) = \psi\left(n - \frac{(2\times 1 - 1)\Delta h}{2}\right) \quad \ldots\ldots\ldots\ldots\ldots\ldots\ldots\ldots\ldots\ldots\ldots\ldots\ldots\ldots 3.3$$

$$\varepsilon_{c1} = \psi\left(n - \frac{3\Delta h}{2}\right) = \psi\left(n - \frac{(2\times 2-1)\Delta h}{2}\right) \quad \ldots\ldots 3.4$$

$$\varepsilon_{c2} = \psi\left(n - \frac{5\Delta h}{2}\right) = \psi\left(n - \frac{(2\times 3-1)\Delta h}{2}\right) \quad \ldots\ldots 3.5$$

$$\varepsilon_{c3} = \psi\left(n - \frac{7\Delta h}{2}\right) = \psi\left(n - \frac{(2\times 4-1)\Delta h}{2}\right) \quad \ldots\ldots 3.6$$

which can be written as the following general expression

$$\varepsilon_{cj} = \psi\left(n - \frac{(2j-1)\Delta h}{2}\right) \quad \ldots\ldots 3.7$$

In addition, the strains upwards from the neutral axis are in compression and the strains downwards from the neutral axis are in tension. The strain ε_{ft} in the tensile reinforcement is calculated using the similarity of triangles as follows:

$$\frac{\varepsilon_c}{n - \frac{(\Delta h)}{2}} = \frac{\varepsilon_{ft}}{d-n} \quad \ldots\ldots 3.8$$

Solving for ε_{ft} in equation 3.8 gives equation 3.9 which can be used to calculate the strain ε_{ft} of the tensile reinforcement of the beam.

$$\varepsilon_{ft} = \frac{2\varepsilon_c(d-n)}{2n-\Delta h} \qquad \text{..........} 3.9$$

where d is the effective depth of the cross-section of the beam, n is the neutral axis depth, and Δh is the depth of the segment of area ΔA. The strain of the top segment of area in the cross-section is ε_c.

With the knowledge of the entire strain distribution for a particular curvature ψ, we are able to calculate the stress distribution in figure 3.1c. In doing so, we use equations from 2.1 to 2.3 (see section 2.5 in chapter 2) to evaluate the stress distribution.

Equation 2.1:

$$\left\{ \begin{array}{ll} Y = \dfrac{A_aX + B_aX^2}{1 + C_aX + D_aX^2} & \text{(for the ascending branch)} \\ \\ Y = \dfrac{A_dX + B_dX^2}{1 + C_dX + D_dX^2} & \text{(for the descending branch)} \end{array} \right\}$$

Where Y is the ratio of concrete stress σ_c and the concrete strength f_c in MPa indicated in equation 2.2 of chapter 2. Furthermore, X is the ratio of the general strain ε_c and the strain ε_{co} at the concrete strength as in equation 2.3 of chapter 2.

Equation 2.2:

$$Y = \frac{\sigma_c}{f_c}$$

Equation 2.2 becomes equation 3.10 after replacing σ_c by σ_{cj}.

$$Y = \frac{\sigma_{cj}}{f_c} \quad \ldots\ldots 3.10$$

Equation 2.3:

$$X = \frac{\varepsilon_c}{\varepsilon_{co}}$$

Here, we substitute ε_c of equation 2.3 by ε_{cj} so that equation 2.3 becomes equation 3.11. The reason for substituting the strain's symbols is that we identified ε_{cj} as the variation of strains in the cross-section of the beam for an individual curvature ψ. Meanwhile, the symbol ε_c is reserved, herein, for the strain of the segment of area at the top of the cross-section of the beam. In addition, the subscript 'a' stands for 'ascending' and the subscript 'd' stands for 'descending' in equation 2.1.

$$X = \frac{\varepsilon_{cj}}{\varepsilon_{co}} \quad \ldots\ldots 3.11$$

The next step is to calculate the force distribution along the cross-section of the beam. The internal force C_{cj} (in kN) for each segment of area ΔA is ΔA times the stress σ_{cj} at the level of that area as in equation 3.12.

$$C_{cj} = (\Delta A)\sigma_{cj} \qquad \text{3.12}$$

The segment of area ΔA is Δh times the width b of the cross-section of the beam and it is expressed in equation 3.13 (see figure 3.1a).

$$\Delta A = b\Delta h \qquad \text{3.13}$$

The resultant of the compressive forces C_c is the summation of all the forces C_{cj} using equation 3.14.

$$C_c = \sum_0^h C_{cj} \qquad \text{3.14}$$

Now, to review the equilibrium of forces, we calculate the tensile force T_f of the FRP rebars to compare it with C_c (see figure 3.1d). We start from the knowledge of the mechanical properties of the FRP rebars such as the strength σ_{ftu} (in MPa) and its Young's modulus E_{ft} (in MPa). The stress σ_{ft} of the FRP rebars is the strain ε_{ft} (see equation 3.9) times its Young's modulus E_{ft} as in equation 3.15. Care must be taken regarding the strain

of the tensile reinforcement to ensure that it does not exceed its ultimate strain ε_{ftu}.

$$\sigma_{ft} = \varepsilon_{ft} E_{ft} \quad \text{...} 3.15$$

The internal force T_f (in kN) of the tensile reinforcement is the stress σ_{ft} times the cross-sectional area A_{ft} of the reinforcing bar as in equation 3.16.

$$T = \sigma_{ft} A_{ft} \quad \text{...} 3.16$$

The structural element is in stable equilibrium if and only if the compressive force C_c equals the tensile one T_f. This equality is expressed in equation 3.17.

$$T_f = C_c \quad \text{...} 3.17$$

If equation 3.17 is not satisfied, then n is changed and the procedure repeated until equilibrium is achieved.

After checking the equilibrium of forces through equation 3.17, we then calculate the internal moment M_n of the beam. The internal moment M_n is the summation of all the elemental moments M_{ncj}. The moment M_{ncj}

for each force C_{cj} is the force C_{cj} times its distance z to the level of the tensile force T_f.

$$M_{ncj} = z\,C_{cj} \quad \ldots\ldots 3.18$$

Consequently, the internal moment M_n of the beam becomes the summation of all the moments M_{ncj} as in equation 3.19.

$$M_{nc} = \sum_{0}^{h} M_{ncj} \quad \ldots\ldots 3.19$$

The curvature ψ was a guessed at the beginning of the procedure, therefore, we know one point of the moment-curvature relationship. That point could be defined as (ψ_1, M_{n1}), for instance.

3.2.2 Doubly reinforced concrete beam.

The analysis of RC beams with tensile reinforcement only paved the way to understanding the analysis of doubly reinforced concrete beams without any difficulty. It is only just a matter of adding the mechanical effects of the compressive reinforcement.

Let us look at figure 3.2 of a doubly reinforced concrete beam. Figure 3.2 shows the cross-section, strain profile, stresses and forces for two different values of curvature ψ_1 and ψ_2. A load P acting over the beam

generates the curvature ψ_1. Therefore, as the load P is incremented, it generates the curvature ψ_2.

Figure 3.2a is the cross-section of the beam in which can be seen the amount of compressive reinforcement labelled A_{fc} and the amount of tensile reinforcement labelled A_{ft}. Figure 3.2b is the strain distribution where ε_{fc} is the strain of the compressive reinforcement. In the calculation of the moment M_{fc} provided by the compressive reinforcement, we start by calculating the strain ε_{fc}. In that calculation, we use the similarity of triangles method (see equation 3.20). Then, solving for ε_{fc} gives equation 3.21. The strain ε_c is the strain of the segment at the top of the cross-section of the beam and d_1 is the concrete cover plus one half of the diameter of the rebar at the top.

$$\frac{\varepsilon_{fc}}{n-d_1}=\frac{\varepsilon_c}{n-\frac{\Delta h}{2}} \qquad \ldots\ldots 3.20$$

$$\varepsilon_{fc}=\frac{2\varepsilon_c(n-d_1)}{2n-\Delta h} \qquad \ldots\ldots 3.21$$

The strain ε_{fc} must not be greater the ultimate strain ε_{fcu}. The stress σ_{fc} of the compressive reinforcement is the strain ε_{fc} times the Young's modulus E_{fc} of the compressive FRP rebars as in equation 3.22.

$$\sigma_{fc}=\varepsilon_{fc}E_{fc} \qquad \ldots\ldots 3.22$$

The force C_f of the compressive FRP rebars is the stress σ_{fc} times the amount of FRP reinforcement A_{fc} as in equation 3.23.

$$C_f = \sigma_{fc} A_{fc} \quad \ldots\ldots 3.23$$

Finally, the moment M_{fc} provided by the compressive reinforcement is the force C_f times the distance of compressive reinforcement to the level of the tensile force T_f as in equation 3.24.

$$M_{fc} = C_f (d - d_1) \quad \ldots\ldots 3.24$$

The calculation of the moment for the curvature ψ_1 of the doubly reinforced concrete beam is carried out following the same procedure as that described in section 3.2.1 for the beam with tensile reinforcement only. The new thing in this case is the incorporation of the compressive force C_f (see equation 3.23) into the equilibrium of forces as in equation 3.25.

$$C_c + C_f = T_f \quad \ldots\ldots 3.25$$

Then, the internal moment M_n is the sum of the moment M_{nc} and the moment M_{fc} as in equation 3.26.

$$M_n = M_{nc} + M_{fc} \quad \ldots\ldots\ldots\ldots\ldots\ldots\ldots\ldots\ldots\ldots\ldots\ldots\ldots\ldots\ldots\ldots\ldots\ldots\ldots\ldots 3.26$$

So far, we have a point (ψ_1, M_{n1}) in the moment-curvature relationship.

Now let us look at figure 3.2e. This is the strain distribution for the curvature ψ_2. Notice in this figure that as the curvature increases from ψ_1 to ψ_2, the neutral axis of the beam drops downwards. The neutral axis na_2 is lower than the neutral axis na_1. In addition, the strain of the top fiber of concrete becomes larger. Nonetheless, the evaluation of the strain distribution, the stresses and force distribution follows the same procedure as for the curvature at ψ_1. The equilibrium of forces is expressed equating the sum of the compressive forces with the tensile one as in equation 3.27.

$$C_c + C_f = T_f \quad \ldots\ldots\ldots\ldots\ldots\ldots\ldots\ldots\ldots\ldots\ldots\ldots\ldots\ldots\ldots\ldots\ldots\ldots\ldots\ldots 3.27$$

Therefore, we have another point (ψ_2, M_{n2}) in the curve of the moment-curvature relationship.

The evaluation of the moment-curvature relationship is extended up to any desired value of curvature ψ, as it will be seen later.

3.3 Computer program

The algorithm of the computer program is visualised throughout the flowchart in figure 3.3. The algorithm is broken into four main parts

which are: identification of the problem; input variables; core algorithm; and output results. The identification of the problem, is located in block number 2 of the flowchart. It tells us, that the computer program is about to solve for a doubly reinforced concrete beam through the segmental analysis.

The input variables are in block number 3 of the flowchart and they are the coefficients of the concrete stress equation (see equation 2.1) not only for the ascending branch but also for the descending branch. The variable h and the variable b are the dimensions of the cross-section of the beam. The variable d is the effective depth of the cross-section, and d_1 is the concrete covering plus one half of diameter of the rebars at the top. The variable ε_{co} is the strain at the concrete strength f_c. X_t is the ratio of concrete strains at the tensile range, and ΔA is the segmental area in the cross-section of the beam.

The variables X and Y are from of equation 2.1. The areas A_{ft} and A_{fc} represent the amount of tensile reinforcement and the amount of compressive reinforcement respectively. The strengths σ_{ftu} and σ_{fcu} represent the strength of the FRP tensile reinforcement and the strength of the FRP compressive reinforcement respectively. The material stiffnesses E_{fc} and E_{ft} are the Young's modulus of both the FRP compressive reinforcement and the FRP tensile reinforcement respectively. The variable n is the neutral axis depth of the cross-section of the beam. Finally, the variable ψ is the curvature caused by the load acting over the concrete beam. In the event that the programmer wish to analyse RC

beams with steel reinforcing bars, then the variables related to steel bars, have to be include in the block of variables declaration.

The core algorithm comprises three loops. The inner loop is for the variation of the counter j, from 0 to h by 1 mm at a time to evaluate the strains distribution along the cross-section of the beam for a particular value of curvature ψ. The value of 1 mm was chosen for Δh in this program, however, the programmer is free to adopt any other value. The other loop is for the variation of the neutral axis depth n from 1 to h, which uses a trial and error procedure until equilibrium of forces in the cross-section of the beam is achieved. The variation of n is 1 mm at a time, for compatibility with the variation of the counter j. Finally, the outermost loop is for the variation of curvature ψ from 1 up to the last one proposed by the programmer herself / himself. In the flowchart, the variation of ψ is shown as from 1 to 100.

Also in the same algorithm, there are three well-defined routines, which are the routines to evaluate strains, stresses, forces and the internal moment provided by the compressive concrete. The output results are in block 28, which are the neutral axis depth of the beam, the curvature ψ and the internal moment of the beam.

Having now defined the input variables and having given an overview of the whole algorithm, let us get through the algorithm in full detail. Let ψ be the first value of curvature 1 in block 4, and also let the neutral axis depth n be 1 in block 5 to start the computer program. Until now, we have opened two loops, the ψ loop and the n loop. Now let us open the third

loop in block 6 pertaining to the counter j along the cross-section of the beam. The strain ε_c corresponding to the top segment of concrete area is evaluated in block 7. Here, we start running the routine of the counter j for the curvature 1 and the neutral axis 1.

The computer program evaluates the strain distribution in block 9 for the values of j from 0 to h. The ratio of concrete strains is calculated in block 10 (see equation 3.11). The computer program verifies in block 13 whether of not the ratio X of the concrete strain is running in the range of X_t and 1. X_t is the ratio of the tensile strength of the concrete. If the conditional statement in the block 13 is true, then the computer program goes to block 14 and carries out the calculation of the ascending branch of the stress-strain curve. Otherwise, the computer program goes to block 15 and calculates the descending branch of the stress-strain curve (see equation 2.1).

The variable Y_a is for the ascending branch and the variable Y_d is for the descending or falling branch of the stress-strain relationship of the concrete. In addition, Y_a and Y_d represent the ratio of the concrete stresses along the stress-strain curve (see equation 3.10). In block 18, the computer program solves for σ_{cj} (see equation 3.10) to evaluate the concrete stress distribution. In addition, in block 18 the computer program evaluates the concrete forces distribution C_{cj} (see equation 3.12) and the resultant of concrete force C_c (see equation 3.14). The moments distribution M_{ncj} (see equation 3.18) and internal resultant moment M_{nc}

(see equation 3.19) in the compressive concrete are also evaluated in block 18.

Now, let us go through the routine of the compressive reinforcement. From block 7, the computer program takes the strain ε_c into block 11 to calculate the strain ε_{fc} of the compressive reinforcement (see figure 3.2b). The strain ε_{fc} is compared against the ultimate strain ε_{fcu} from block 8 to verify whether ε_{fc} is not greater than ε_{fcu}. Therefore, if ε_{fc} is greater than ε_{fcu} then the computer program goes to block 19 and calculate the stress σ_{fc} of the compressive reinforcement (see figure 3.2c). Otherwise, it goes to block 20 and makes σ_{fc} equal to zero, which in turn means that compressive reinforcement breaks. The force C_f and the moment M_{fc} are calculated in block 23.

At this stage, we have C_c, M_{nc}, C_f and M_{fc}. Therefore, it is only left to look into the calculation of the tensile reinforcement. Let us go through the routine related to the tensile reinforcement. In block 12 is calculated the strain ε_{ft} of the tensile reinforcement using the concrete strain from block 7. Then, in block 17 is verified whether the strain ε_{ft} is less than or equal to the ultimate strain ε_{ftu} from block 8. If the statement in block 17 is true, then the computer program goes to block 21 and calculates the stress σ_{ft} of the tensile reinforcement. Otherwise, it goes to block 22 and makes the stress σ_{ft} equal to zero, which means that the tensile reinforcement breaks. The force of the tensile reinforcement is calculated in block 24.

Figure 3.2d shows the forces profile where the reader can see the forces C_c, C_f and T_f. The computer program adds up the compressive forces C_c and C_f yielding the resultant force CF in block 25. The force CF is checked out in block 26 to determine how close is it to the tensile force T_f. The extent of similarity between CF and T_f, depends most all on the criterion of the programmer. Therefore, if the statement in block 26 satisfies the programmer's criterion, then the computer program adds up together the moments M_{nc} and M_{fc} to yield the internal moment BM of the beam.

Finally, the computer program prints out the neutral axis n, the curvature ψ and the internal moment BM. At this stage, the computer program has run for just one value of curvature ψ. After printing out the results in block 28, the computer program goes back to block 4 to pick up the next value of curvature ψ. However, if the statement in block 26 is not true, then the computer program goes to block 5 and tries with another value of neutral axis n until the condition in block 26 is true. The program stop runnings after the last value of curvature ψ entered by the programmer.

3.4 Illustration

Seven RC beams with simulated mechanical properties are analysed herein. Table 3.1 summarises the idealised mechanical properties of such beams. Column 1 of table 3.1 represents the identification of the beams from 1 to 7. Column 2 indicates the amount of rebars at the top of the

beams as well as the type and the size of the rebars. FRP for plastic bars and Y for steel bars indicate the type of the rebars. A number behind the types of rebars indicates the amount of rebars. The subscript 20 in front of the types of rebars indicates the size of the rebars (20-mm diameter). For instance, $1FRP_{20}$ indicates 1 FRP rebar of 20-mm diameter.

Column 3 of table 3.1 indicates the amount, types of rebars and size of rebars at the bottom of the cross-section of the beam. Columns 4 and 5 indicate the strength of the rebars at the top and bottom of the cross-section respectively. The Young's moduli (Y.M.) of the rebars at the top and bottom of the beams are in columns 6 and 7. Finally, the concrete strength is in column 8.

The reason for analysing these seven beams is to compare their mechanical behaviour under a variety of combinations of reinforcement. The combinations compare not only the amount of reinforcement but also the type of reinforcing bars. Furthermore, the size of rebars for all the beams is 20-mm diameter. The cross-sections of the beams described in table 3.1 are all in figure 3.4. The reader can see in figure 3.4, that the size of the reinforcing bars for both FRP and steel are all 20-mm diameter. In addition, the concrete covering for protecting the rebars is 20 mm thick.

By running the computer program described in the flowchart of figure 3.3, for the beams described in table 3.1 and in figure 3.4, we obtain the moment-curvature relationships in figures 3.5 to 3.11. In the figures from

3.12 to 3.15, we have sets of curves for comparing the flexural behavior between the beams with different amounts and types of reinforcement.

Let us analyse the moment-curvature relationship of beam 1 in figure 3.5. Beam 1, according to table 3.1 and figure 3.4, has three FRP reinforcing bars of 20-mm diameter and 624 MPa strength in the tensile zone. No compressive reinforcement is in beam 1. However, as beam 1 is an over reinforced one, its failure occurs when the compressive concrete crushes. That is the reason why the curve declines after the beam reaches its flexural strength at the curvature ψ of 45×10^{-6} mm^{-1}. In addition, the concrete strain ε_c at the flexural strength BM of the beam is 0.00423.

Let us analyse the moment-curvature relationship of beam 2 in figure 3.6. According to table 3.1 and figure 3.4, beam 2 has one FRP rebar of 20-mm diameter and 437 MPa strength at the top, and three FRP rebars of 20-mm diameter and 624 MPa strength at the bottom. The fracture of the FRP rebars at the top causes the failure of the beam. In addition, the reader can see that the falling branch of beam 2 is less steep than the falling branch of beam 1. This means that the compressive FRP rebar takes over from the crushed concrete pushing up the falling branch of the moment-curvature relationship.

The moment-curvature relationship of beam 3 is in figure 3.7. According to table 3.1 and figure 3.4 it has 2 FRP rebars of 20-mm diameter and 437 MPa strength at the top, and 3 FRP rebars of 20-mm diameter and 624 MPa strength at the bottom. The fracture of the reinforcing FRP rebars at the top causes the failure of the beam. In

addition, the falling branch of the moment-curvature relationship describes an interesting plateau after crushing the compressive concrete delaying the failure of the beam. The failure of beam 3 occurs at a larger curvature than that of beam 2. Furthermore, the strength and ductility of the beam increases with the addition of one more FRP rebar at the top.

The moment-curvature of the beam 4 is in figure 3.8. This beam has one steel rebar of 20-mm diameter and 410 MPa of yield strength at the top, and three FRP rebars of 20-mm diameter and 624 MPa strength at the bottom. Beam 4 fails soon after the concrete crushes in a similar fashion to beam 1. Only the difference with regard to beam 1 is that the onset of the concrete crushing is delayed to a larger curvature ψ.

The moment-curvature of beam 5 is in figure 3.9. Beam 5 has one FRP rebar of 20-mm diameter and 624 MPa strength at the top, and 5 FRP rebars of 20-mm and 624 MPa strength at the bottom. The fracture of the rebar at the top causes the failure of the beam. The moment-curvature relationship of beam 5 looks quite similar to the moment-curvature relationship of beam 2 with regard to their falling branch.

The moment-curvature of the beam 6 is in figure 3.10. Beam 6 has 2 steel bars of 20-mm diameter and 410 MPa yield strength at the bottom. No reinforcement is available at the top of the beam. The plateau of this beam is very noticeable. The length of the plateau of the curve is due to the steel rebars yielding.

The moment-curvature of the beam 7 is in figure 3.11. Beam 7 has 3 steel rebars of 20-mm diameter and 410 MPa yield strength at the bottom,

and not rebars at the top. As this beam has more steel at the tensile zone than beam 6, it becomes less ductile as well. The reader can see the declination of the falling branch of the moment-curvature curve as soon as the compressive concrete crushes. The plateau is much shorter than the plateau of the moment-curvature curve of beam 6.

After analysing the moment-curvature of the beams on an individual basis, let us have a look on the moment-curvature relationship of the beams not individually but by sets of beams. For instance, the set of curves in figure 3.12 shows the moment-curvature for the beams 1, 2 and 3. The aim of analysing this set of curves is to observe the influence of the compressive reinforcement to the flexural strength and ductility of the beams. The three beams have 3 FRP rebars of 20-mm diameter and 624 MPa strength at the bottom.

The difference between the beams in figure 3.12 is the amount of compressive reinforcement at the top. Beam 1 has not reinforcement at the top, meanwhile beam 2 has one FRP rebar of 20-mm diameter and 437 MPa strength at the top. Beam 3 has 2 FRP rebars of 437 MPa at the top. Notice that beam 1 fails as soon as the compressive concrete crushes showing a steep falling branch. However, the falling branch of the curve of beam 2 is further up showing an early warning of failure of the beam. The best shape of the moment-curvature relationship is that of beam 3, which describes an extended plateau from the onset of the concrete crushing until the fracture of the compressive rebars.

Figure 3.13 shows the moment-curvature relationship of beams 1, 2 and 4. The common parameter of these three beams is the reinforcement at the bottom, three FRP of 624 MPa strength. The difference between them is the reinforcement at the top. Beam 1 has no reinforcement at the top. Beam 2 has 1 FRP rebar of 437 MPa strength at the top, and beam 4 has 1 steel rebar of 410 MPa yield strength at the top. Beam 1 does not show ductility at all. Beam 2 shows ductility. Beam 4 is stronger than beam 1 and beam 2 but it is as brittle as beam 1. What happens is that once the steel rebar at the top of beam 4 yields its force remain constant (see figure 2.9) increasing therefore only the strength of the beam. This means that steel rebars at the top of the concrete beams do not help to provide ductility in the beams.

The contrary happen with FRP rebars. When the concrete crushes, the increase in the force of the FRP rebars compensates for the reduced strength of the concrete. This causes the declining branch of the curve to turn up. In other words, the negative slope of the declining curve, is compensated with the positive slope of the FRP force (see figure 2.9) due to the FRP rebars no yielding. In summary, we can say that the steel rebars as a compressive reinforcement give more strength to the beams but do not increase the ductility.

Figure 3.14 shows the moment-curvature relationship of beams 2 and 5. The common parameter in these two beams is the amount of reinforcement at the top, one FRP rebar. The difference between them is that the FRP rebar at the top of beam 2 is 437 MPa strength, and the FRP rebar at the

top of beam 5 is 624 MPa strength. Furthermore, beam 2 has three FRP rebars of 624 MPa strength at the bottom and beam 5 has five FRP of 624 MPa strength at the bottom. Beam 5 is a little bit stronger than beam 2, however, it is less ductile than beam 2. Practically, the increment in the tensile reinforcement in beam 5 only contributes to the flexural stiffness of the beam. Beam 5 is stiffer than beam 2.

Figure 3.15 shows the moment-curvature relationship of beams 1, 6 and 7. The common parameter of these three beams is that none of them has reinforcement at the top. The difference between them is that beam 1 has three FRP rebars of 624 MPa strength at the bottom. Beam 6 has two steel rebars of 410 MPa yield strength at the bottom, and beam 7 has three steel rebars of 410 MPa yield strength at the bottom. Beam 1 has no ductility at all. Beam 6 is less strong however it is ductile. Beam 7 is the stronger one however it is less ductile than beam 6.

Using the computer program described above, we can investigate not only the flexural strength and ductility of the beams but also other aspects of the beams such as the variation of the neutral axis depth. Figure 3.16 shows the variation of the neutral axis depth n in terms of the curvature ψ of beams 1 and 6. Neither beam 1 nor beam 6 has compressive reinforcement. Beam 1 has three FRP rebars of 624 MPa strength at the bottom and beam 6 has two steel rebars of 410 MPa yield strength at the bottom. It can be seen in figure 3.16 that the neutral axis depth of beam 1 starts in a higher position and, as the load over the beam is incremented, the neutral axis depth drops down considerably. In contrast, the neutral

axis depth of beam 6, which has two steel rebars, starts at a lower level.

However as the load upon the beam is incremented, the neutral axis depth goes up and keeps rising until ~~the beam is close to failure.~~ top fibre of concrete crushes and then it drops down until the collapse of the beam.

Table 3.1. – General properties of simulated RC beams.

Beam number (1)	Top rebars (2)	Bottom rebars (3)	Strength top rebars [MPa] (4)	Strength bottom rebars [MPa] (5)	Top rebars Y. M. [MPa] (6)	Bottom rebars Y. M. [MPa] (7)	Concrete strength [MPa] (8)
B1	–	$3FRP_{20}$	–	624	–	51482	30
B2	$1FRP_{20}$	$3FRP_{20}$	437	624	37191	51482	30
B3	$2FRP_{20}$	$3FRP_{20}$	437	624	37191	51482	30
B4	$1Y_{20}$	$3FRP_{20}$	410	624	200000	51482	30
B5	$1FRP_{20}$	$5FRP_{20}$	624	624	51482	51482	30
B6	–	$2Y_{20}$	–	410	–	200000	30
B7	–	$3Y_{20}$	–	410	–	200000	30

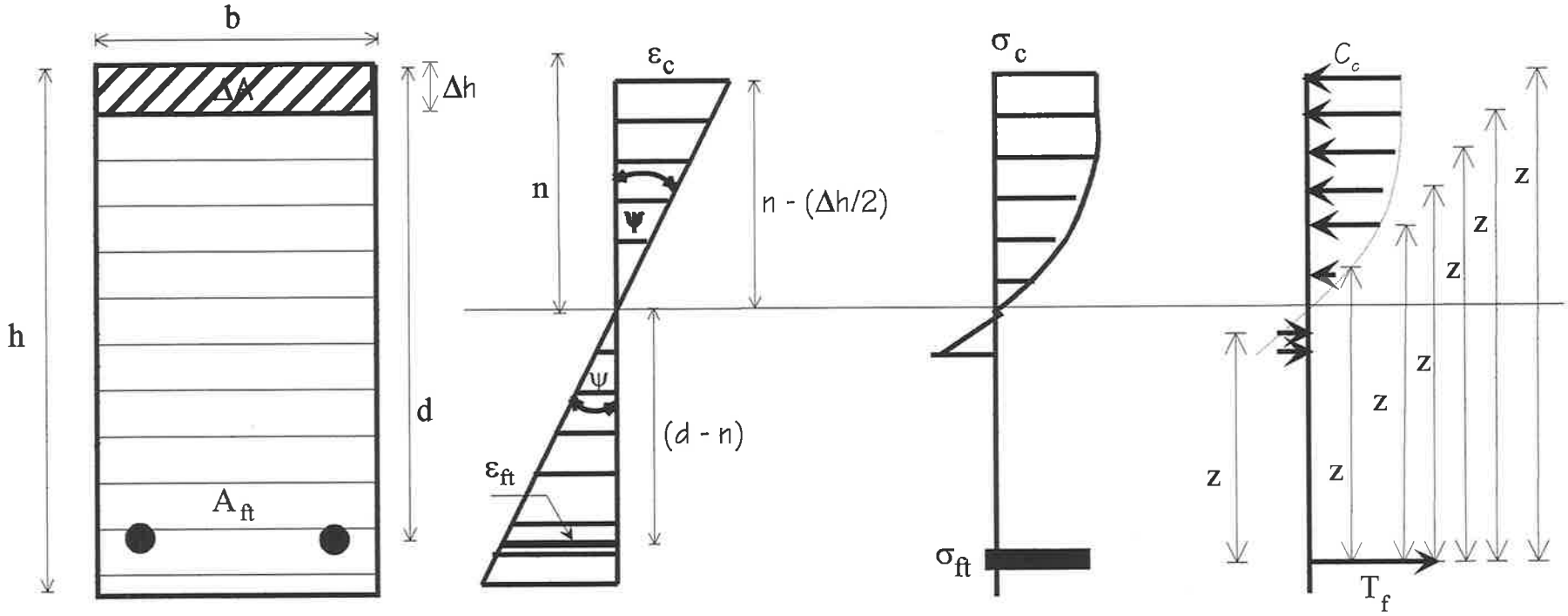

Figure 3.1. - Schematic representation of a segmented beam's cross-section.

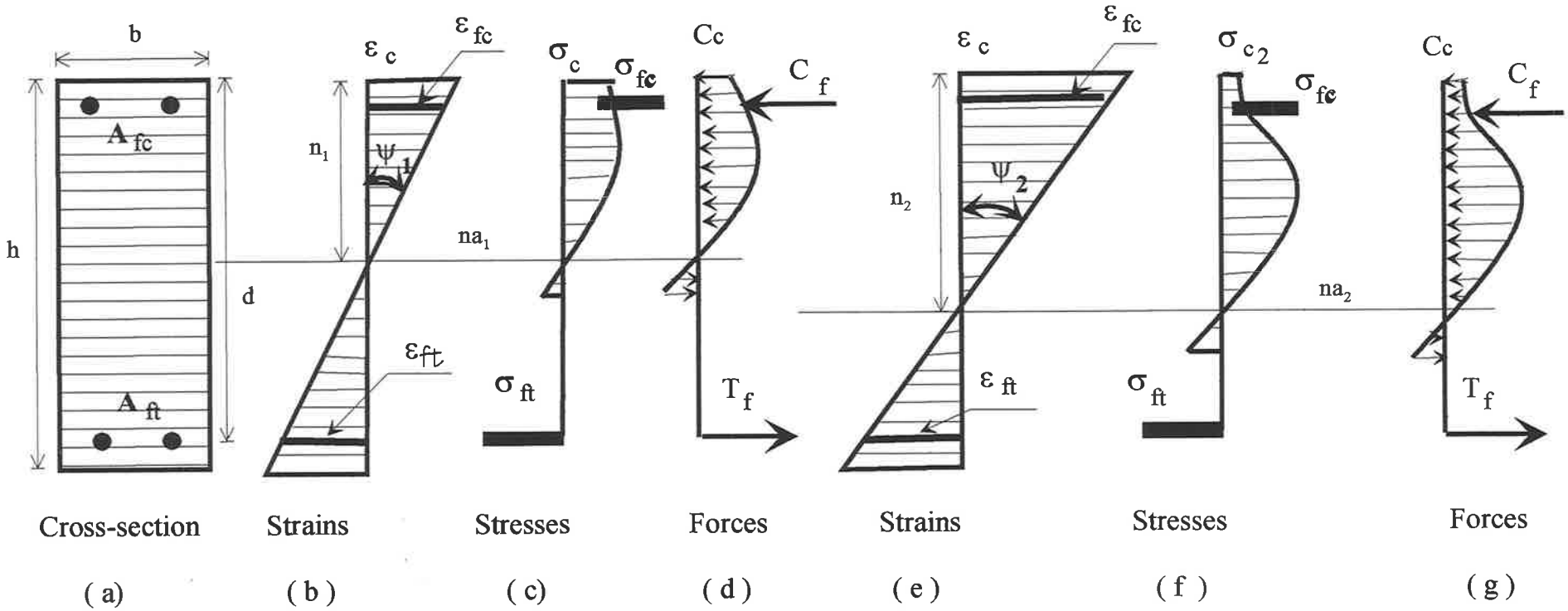

Figure 3.2. - Doubly reinforced concrete beam.

Figure 3- 3. – Flowchart of the segmental algorithm for the computer program.

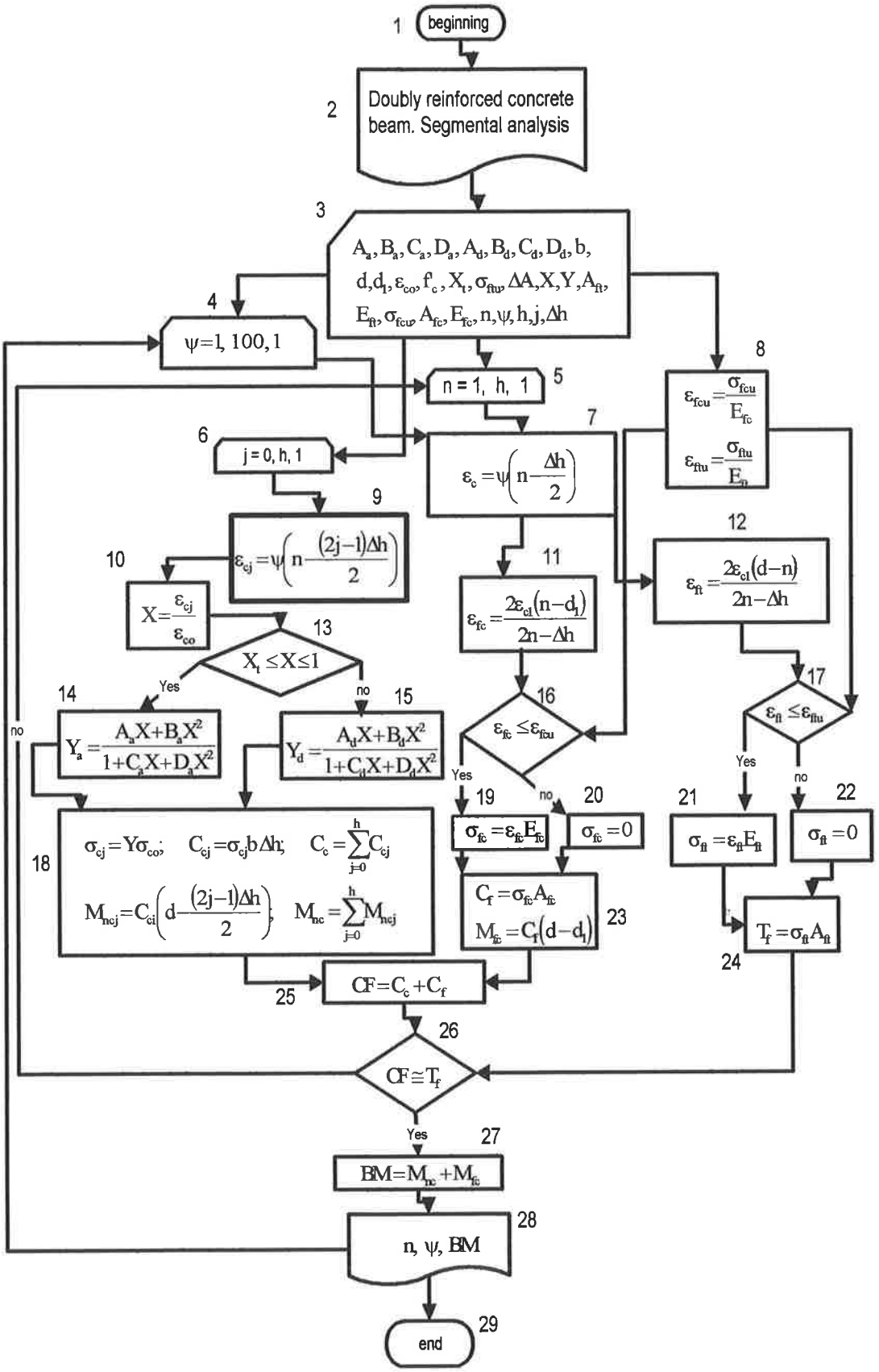

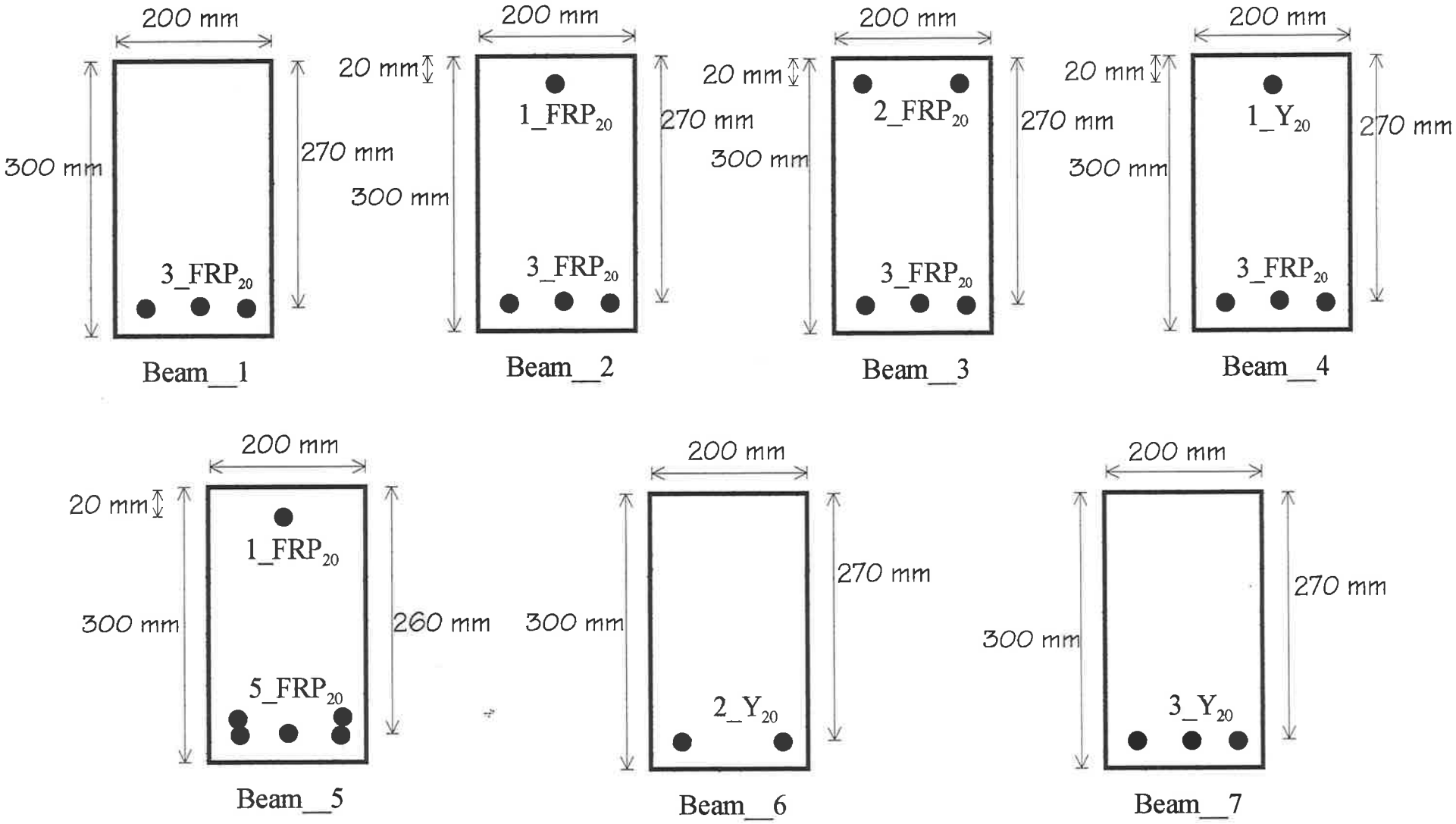

Figure 3.4. - Cross-sections of simulated RC beams.

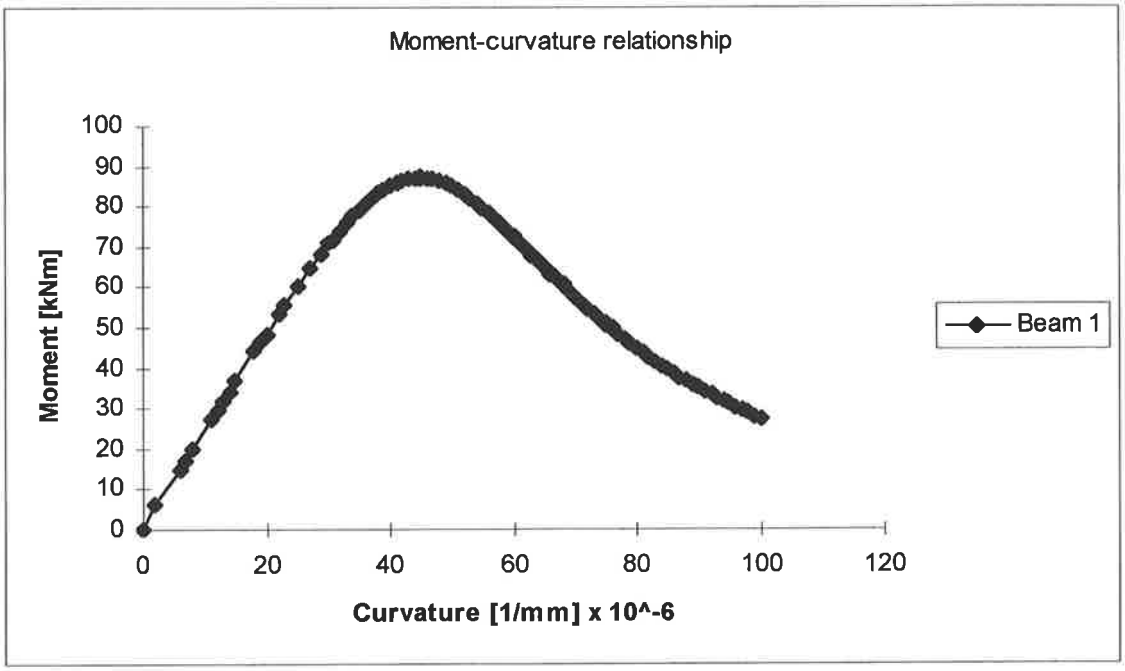

Figure 3.5. – Moment-curvature relationship of beam 1.

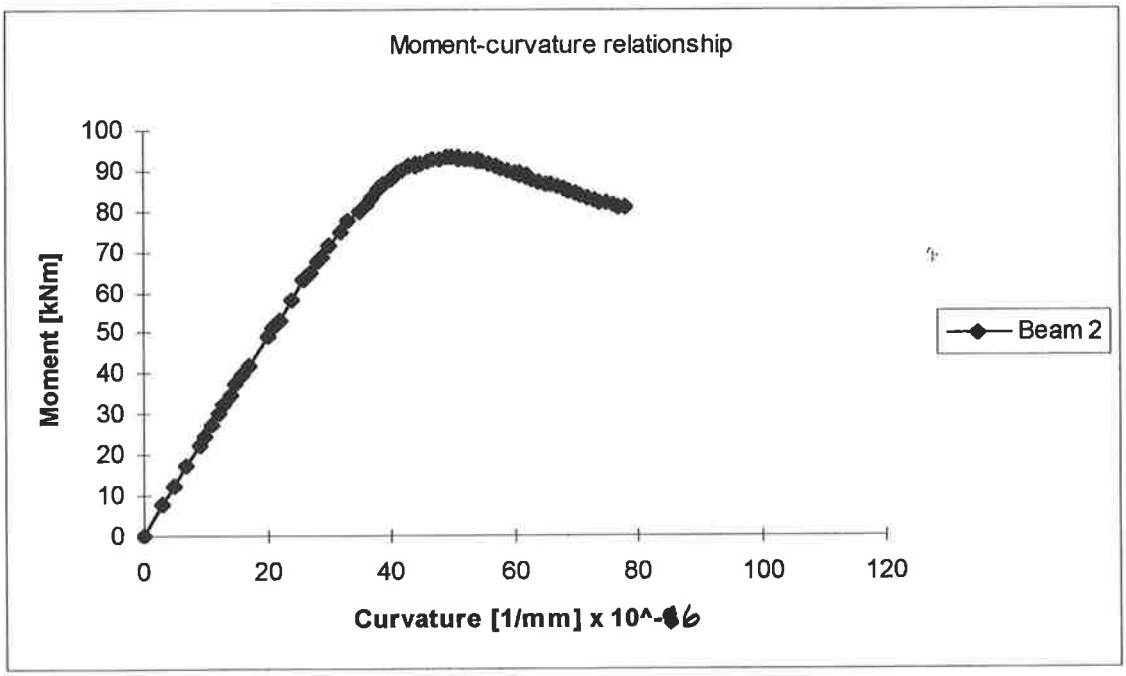

Figure 3.6. – Moment-curvature relationship of beam 2.

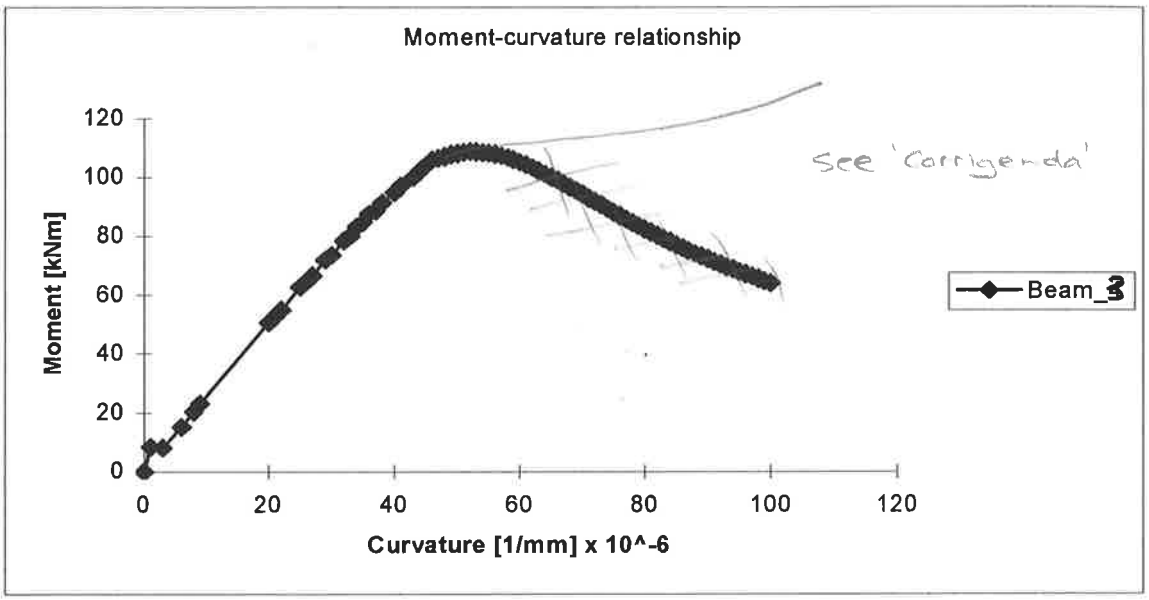

Figure 3.7. – Moment-curvature relationship of beam 3.

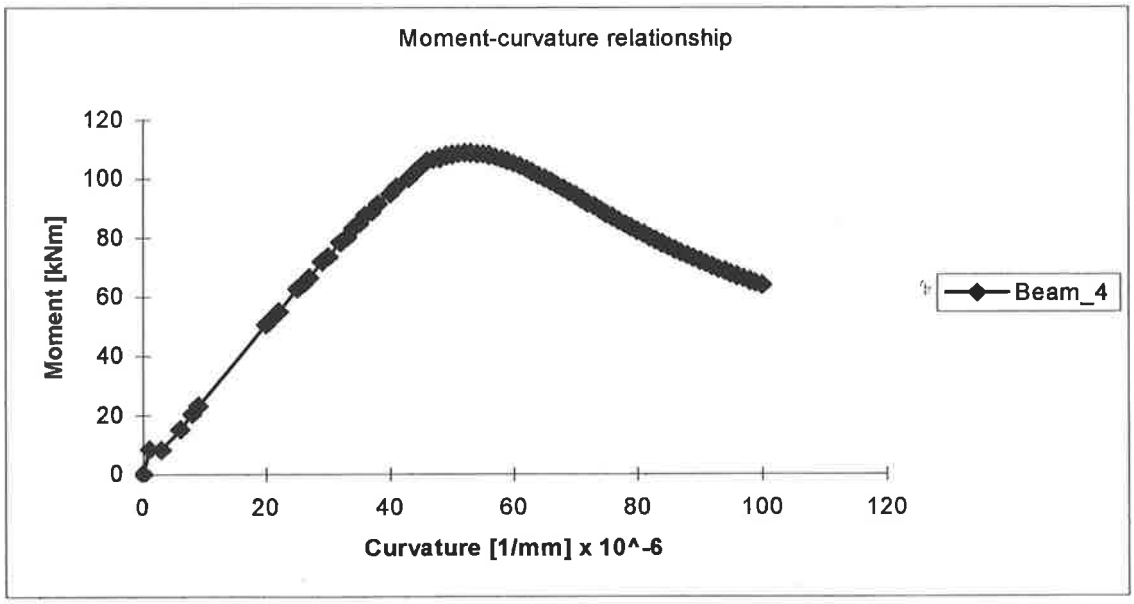

Figure 3.8. – Moment-curvature relationship of beam 4.

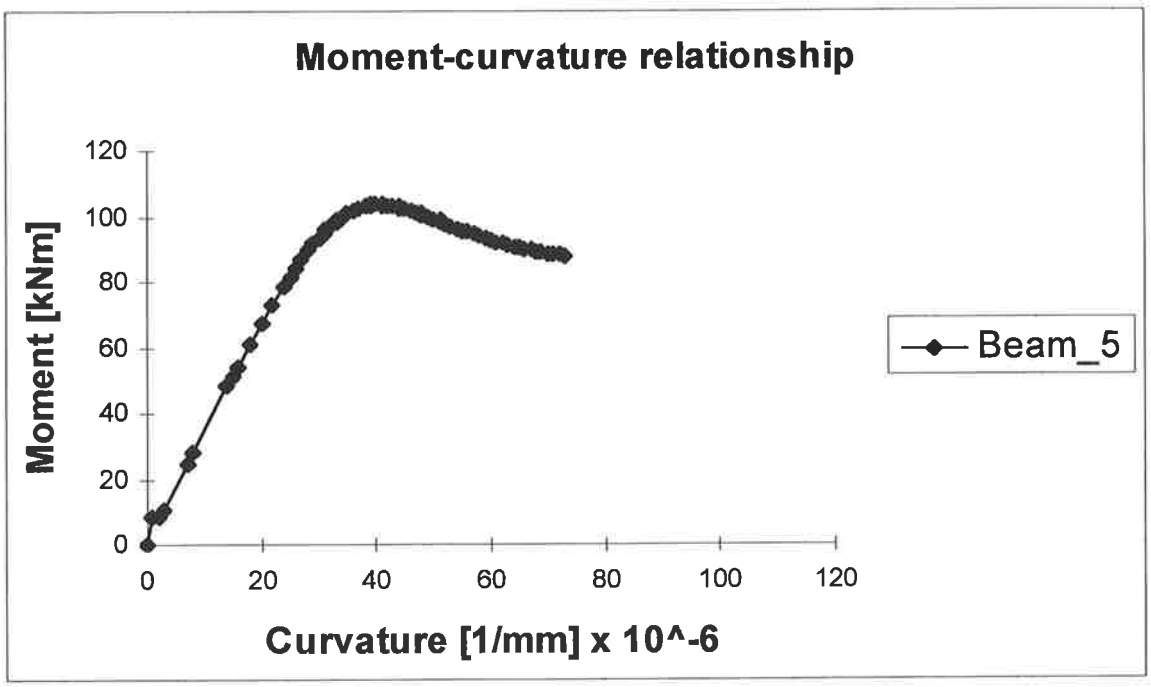

Figure 3.9. – Moment-curvature relationship of beam 5.

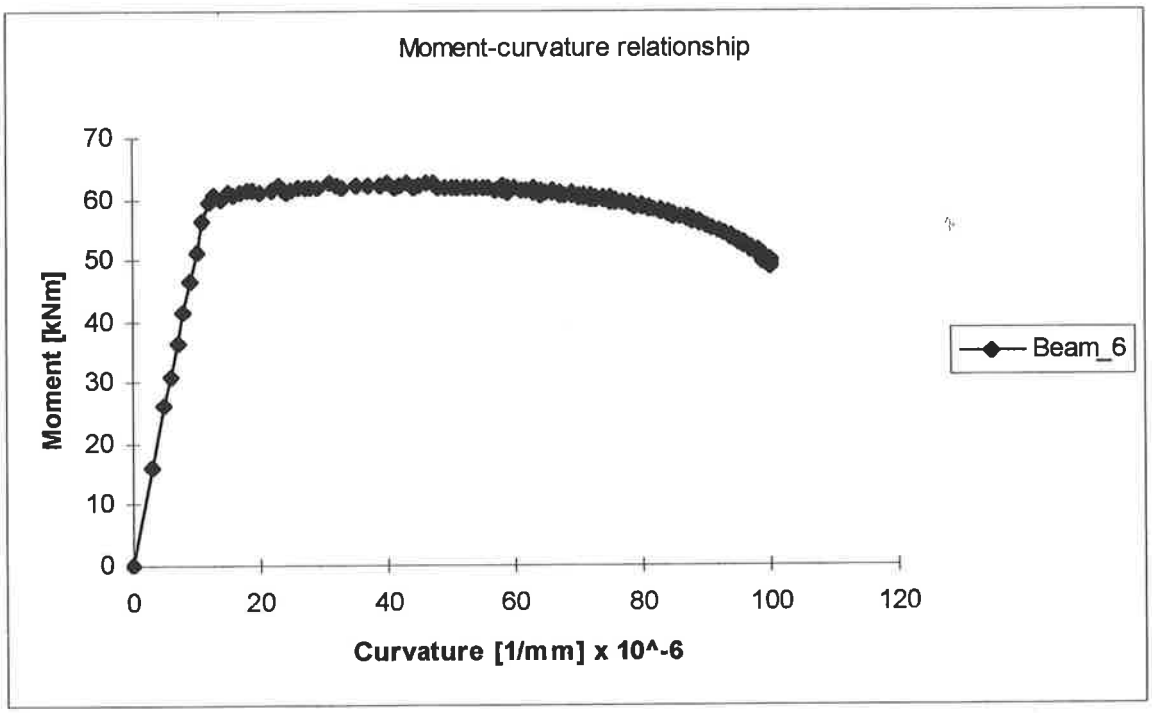

Figure 3.10. – Moment-curvature relationship of beam 6.

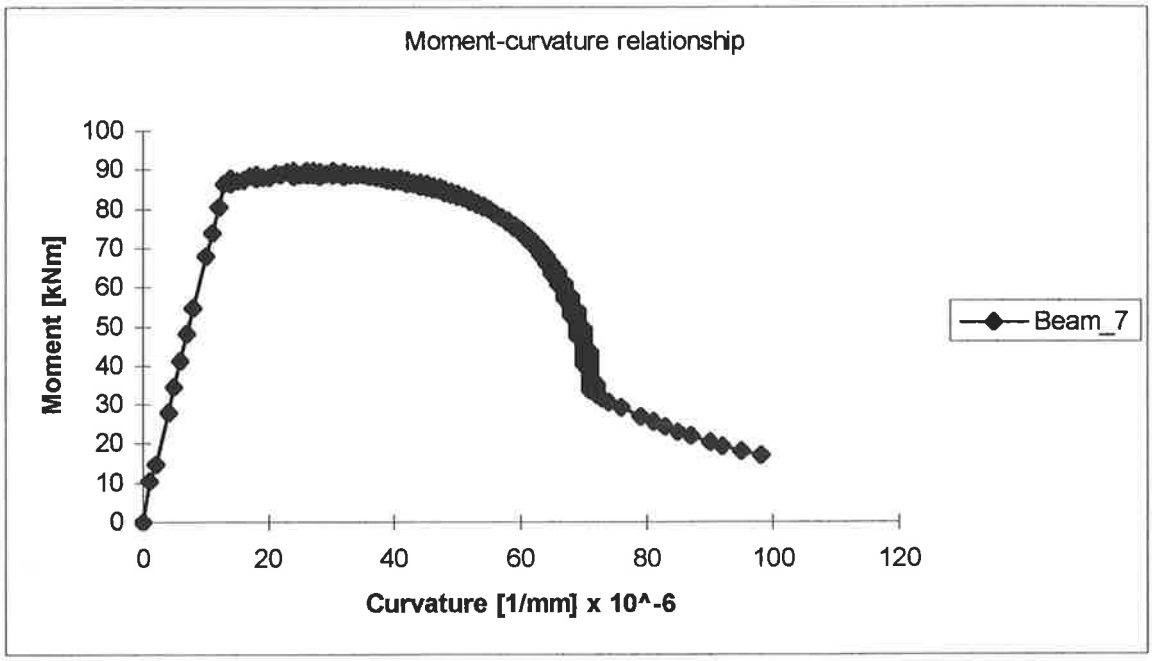

Figure 3.11. – Moment-curvature relationship of beam 7.

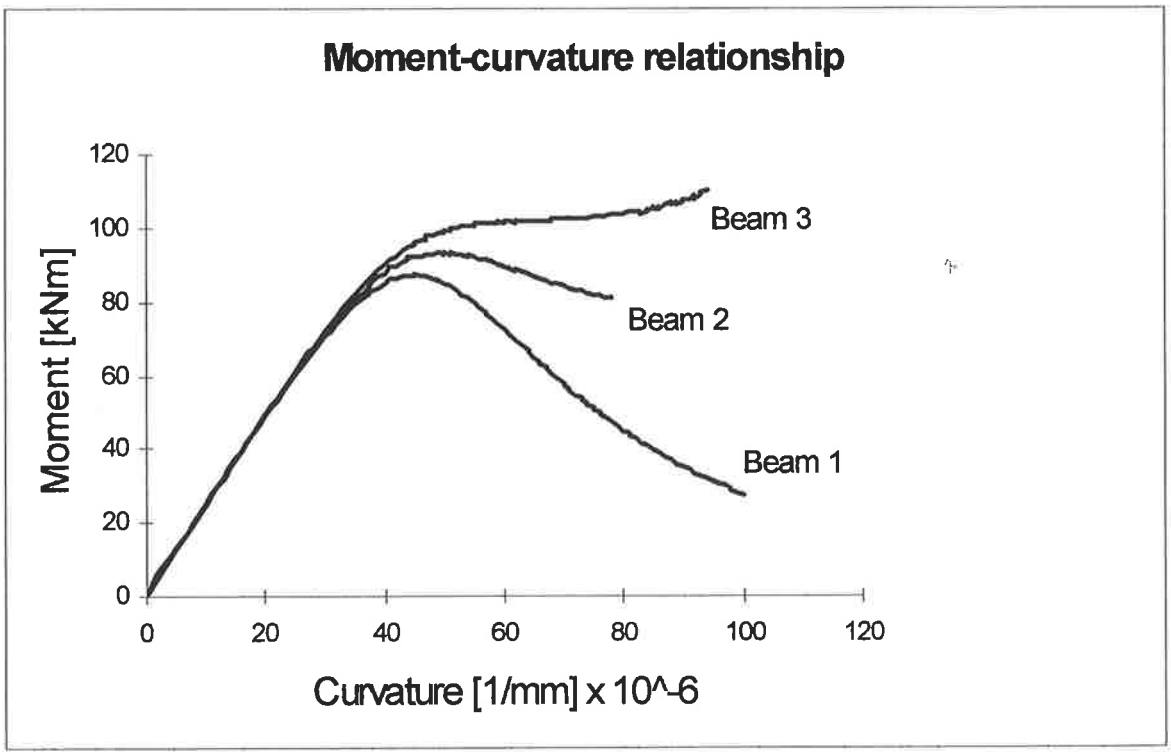

Figure 3.12. – Moment-curvature relationships of beams 1, 2 and 3.

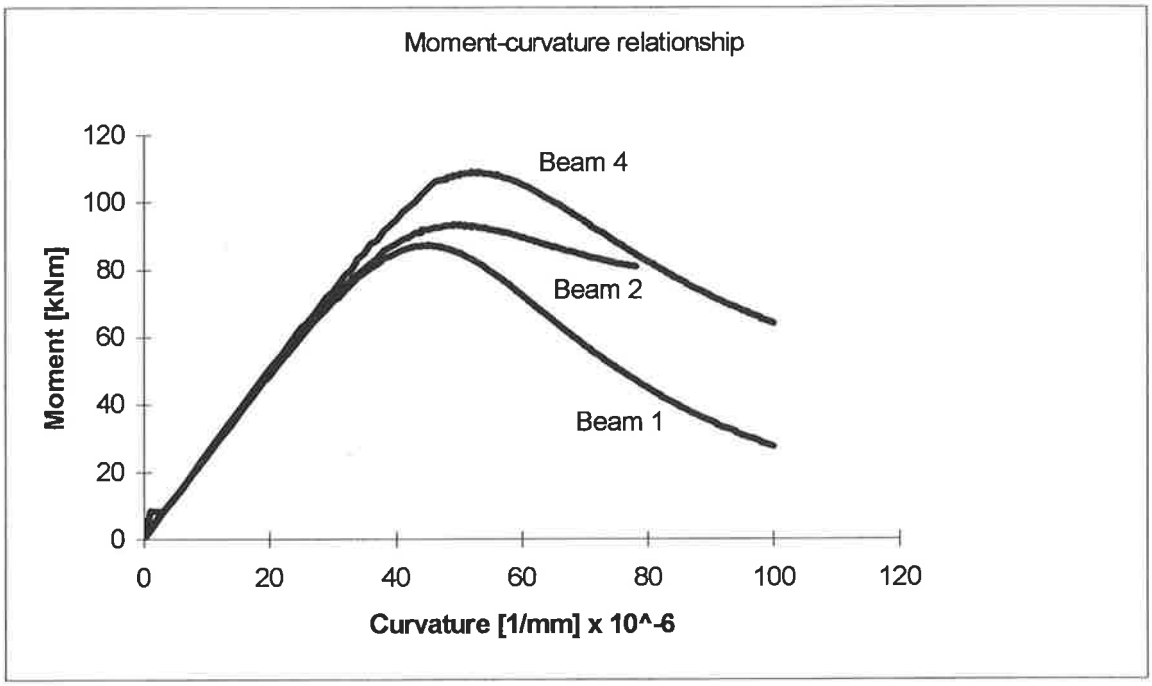

Figure 3.13. – Moment-curvature relationship of beams 1, 2 and 4.

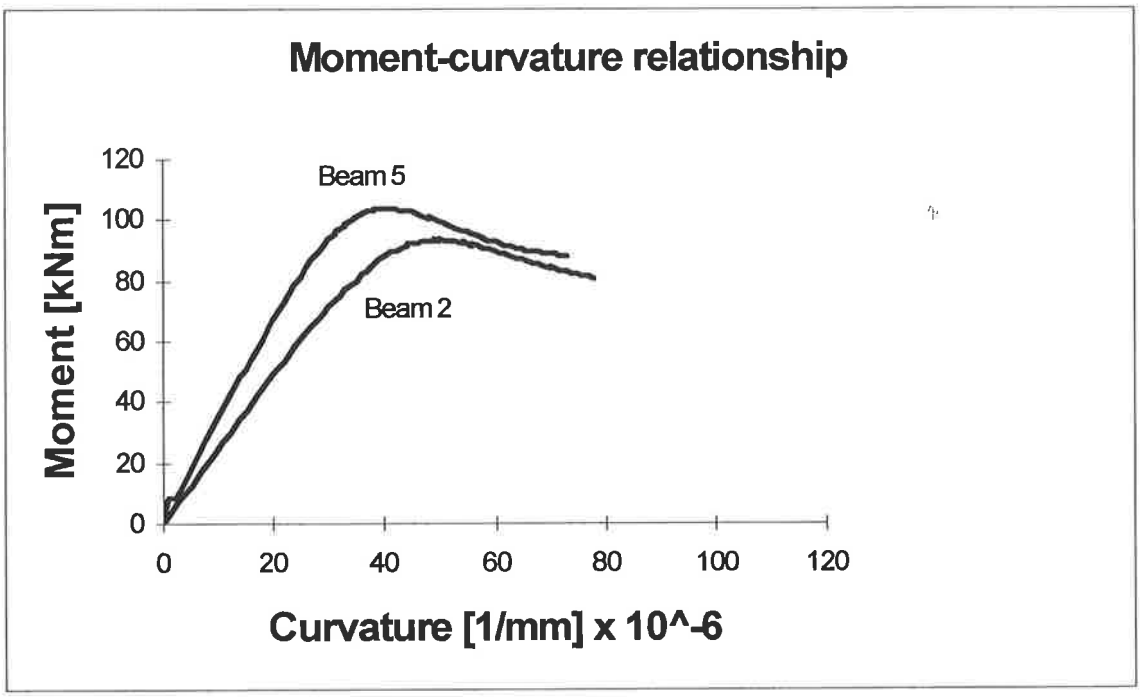

Figure 3.14. – Moment-curvature relationship of beams 2 and 5.

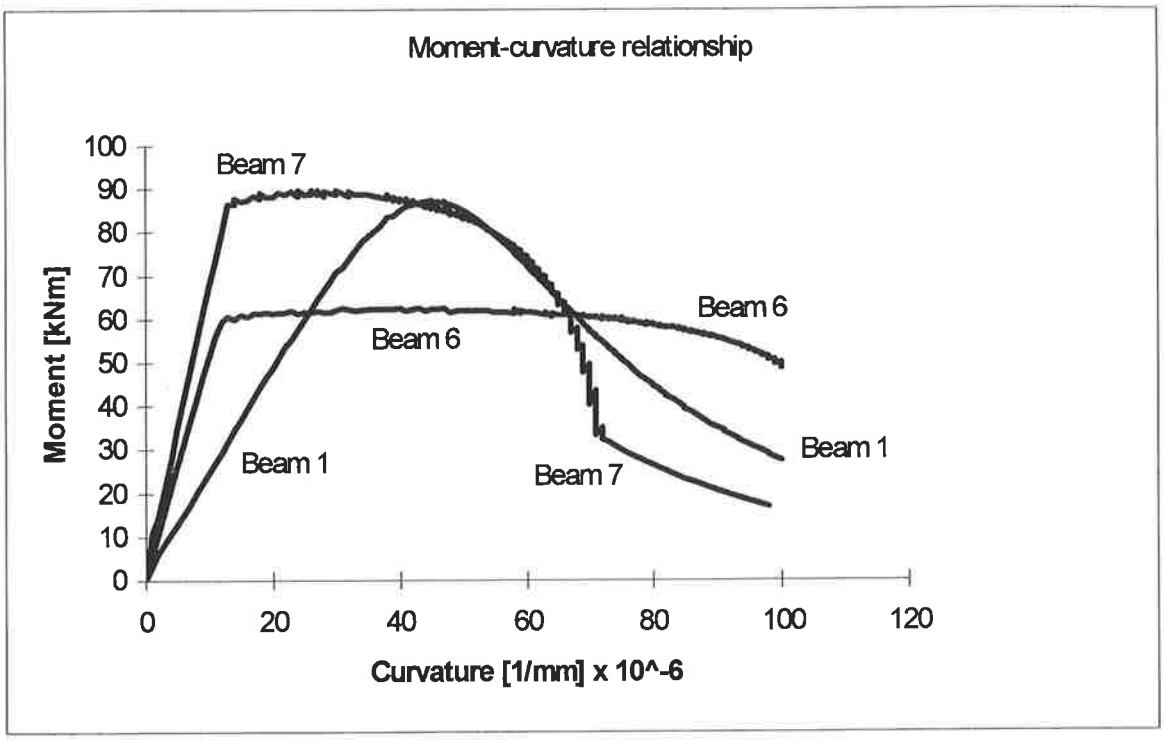

Figure 3.15. – Moment-curvature relationship of beams 1, 6 and 7.

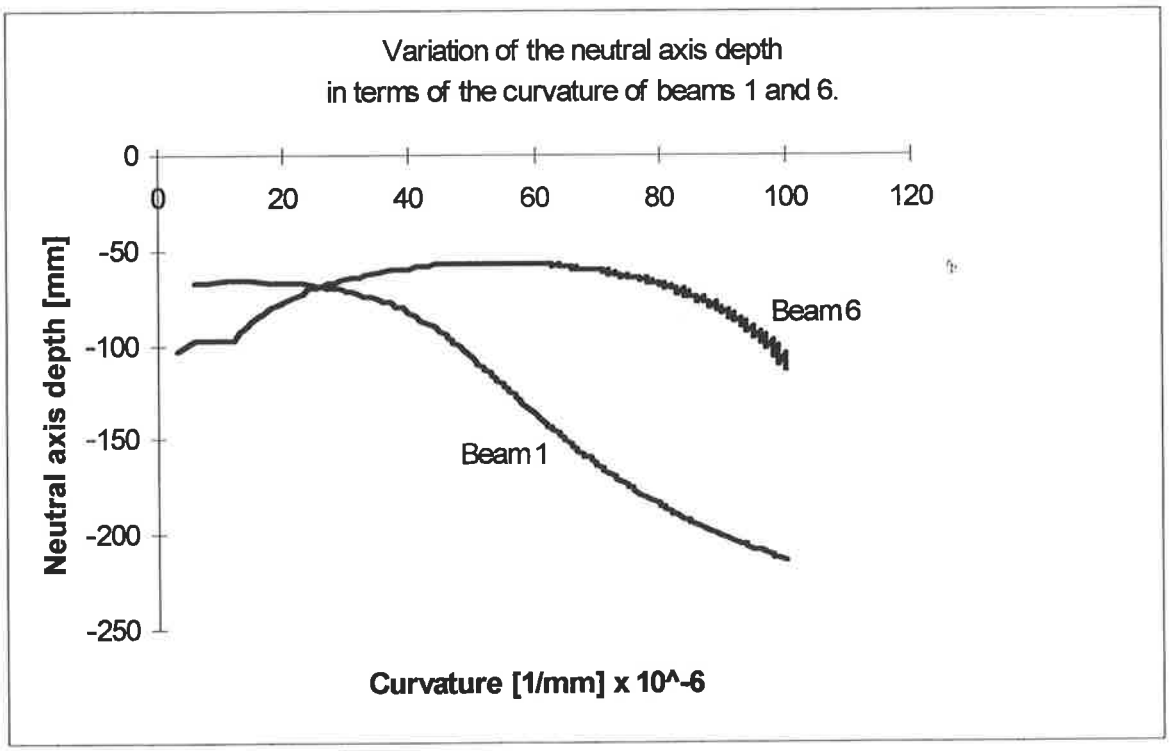

Figure 3.16. – Variation of the neutral axis depth in terms of the curvature of beams 1 and 6.

Chapter 4

Rectangular block of stresses analysis

4.1 Introduction

The aim of this chapter is to present a mathematical model that uses the rectangular block of stresses, which allows the design, by hand, of over reinforced concrete beams with FRP reinforcing bars.

In doing so, a mathematical model is first developed for singly reinforced concrete beams, in order to study the trend of the falling branch of the moment-curvature relationship. Later, doubly reinforced concrete beams are analysed. Finally, there is a

comparison of the results from the two beams to evaluate the benefits of the compressive reinforcement in providing ductility to the concrete beams.

4.2 RC beam with tensile reinforcement of FRP reinforcing bars only

4.2.1 Overview

The rectangular block of stresses analysis is carried out considering a uniformly distributed concrete stress, equivalent to 85% of the concrete strength f_c, that acts over a rectangular area of the beam's cross-section, called 'the compression zone'. The hatched area in figure 4.1a represents the compression zone for the curvature ψ_1; b is the width of the beam's cross-section; h is the depth of the concrete beam; d is the effective depth of the beam's cross-section; A_{ft} is the amount of tensile reinforcement of FRP reinforcing bars; and the neutral axis depth of the beam is n_1 in figure 4.1b.

The present analysis is developed for curvatures, which generate concrete strains greater than or equal to the ultimate strain capacity ε_{cu} of the concrete. In figure 4.1b can be seen the strain distribution, where the top fiber of concrete has already reached its ultimate strain capacity ε_{cu}. At the bottom of the strain distribution is the strain ε_{ft1} of the tensile reinforcement of FRP reinforcing bars. Figure 4.1c shows the stress profile where: $0.85f_c$ is the concrete stress; and the height of the block of stresses is $n_1\gamma$, in which γ is a reduction factor of the neutral axis depth to define the height of the rectangular block of stresses (Australian Standards) [40]; and σ_{ft1} is the stress of the tensile reinforcement. Figure 4.1d represents the forces, where C_{c1} is the concrete's force and T_{f1} is the force of the tensile reinforcement. The position of the compressive force is defined by its corresponding lever arm z_1.

Increasing the curvature from ψ_1 in figure 4.1b to ψ_2 in figure 4.1e modifies the profiles of strain, stress and forces because the beam's neutral axis drops down to the depth n_2.

4.2.2 Mathematical model for an RC beam with FRP reinforcing bars at the bottom only.

A beam's cross-section with 3 FRP reinforcing bars of 20-mm diameter in the tension zone, is shown in figure 4.1a. The aim is to evaluate the falling branch of the moment-curvature relationship. Therefore, our attention is focused primarily, on the calculation of both the internal moment M_{n1} and the corresponding curvature ψ_1, soon after the top fiber of concrete crushes. In doing so, let ψ_1 be the curvature generated by a load applied to the beam. Furthermore, the applied load is of such an intensity that it brings the top fiber of concrete into the crushing state with an ultimate strain ε_{cu}. The dimensions of the cross-section of the beam and the amount of reinforcement A_{ft} are all already known. In addition, let it be assumed that we know the strength σ_{ftu} of the FRP reinforcing bars, the Young's modulus E_{ft} of the FRP reinforcing bars, the amount of tensile reinforcement A_{ft}, and the concrete strength f_c.

4.2.2.1 Initial concrete crushing

The internal moment M_{n1} is the concrete force C_{c1} times the lever arm z_1, as shown in figure 4.1d.

$$M_{n1} = C_{c1} z_1 \qquad \ldots\ldots 4.1$$

The lever arm in equation 4.1 is the distance between the centroid of the tensile reinforcement and the centroid of the rectangular block of stresses (see figure 4.1d). This distance can be expressed as follow:

$$z_1 = d - \frac{n_1 \gamma}{2} \qquad \ldots\ldots 4.2$$

where d is the effective depth of the beam's cross-section; n_1 is the beam's neutral axis depth; and γ is a reduction factor of the neutral axis depth. The reduction factor γ is calculated using equation 4.3 as follows:

$$\gamma = 0.85 - 0.007(f_c - 28) \qquad \ldots\ldots 4.3$$

where f_c is the concrete strength in MPa.

Equation 4.1 can be modified by replacing the lever arm z_1 by its equivalent in equation 4.2. Therefore, equation 4.1 is transformed into equation 4.4.

$$M_{n1} = C_{c1}\left(d - \frac{n_1 \gamma}{2}\right) \qquad \ldots\ldots 4.4$$

Before calculating the internal moment M_{n1}, we must be sure that the beam is in stable equilibrium. A single reinforced concrete beam is in stable equilibrium if and only if the magnitude of the compressive force C_{c1} in figure 4.1d set equal to the tensile force T_{f1}. This condition is expressed as follow:

$$C_{c1} = T_{f1} \quad \ldots\ldots 4.5$$

The compressive force C_{c1} can be expressed in terms of the concrete strength f_c, the width b of the beam's cross-section, the neutral axis depth n_1 and the reduction factor γ of the neutral axis depth, as shown in equation 4.6. Meanwhile, the tensile force T_{f1} is shown in equation 4.7, in terms of the tensile stress σ_{ft1} and the amount of tensile reinforcement A_{ft}.

$$C_{c1} = 0.85 f_c b n_1 \gamma \quad \ldots\ldots 4.6$$

$$T_{f1} = \sigma_{ft1} A_{ft} \quad \ldots\ldots 4.7$$

In equation 4.6, the neutral axis n_1 is unknown. Furthermore, in equation 4.7, the stress σ_{ft1} of the tensile reinforcement is also unknown. These two unknowns are related in the strain profile in figure 4.1b, as we will see next.

Let us combine equations 4.5, 4.6 and 4.7 in such a way that the equivalent of the compressive force C_{c1} is equal to the equivalent of the tensile force T_{f1}, as follows:

$$0.85 f_c b n_1 \gamma = \sigma_{ft1} A_{ft} \quad \ldots\ldots 4.8$$

Notice that in the left-hand side is the unknown n_1, and in the right-hand side is the unknown σ_{ft1}. Solving for n_1 in equation 4.8 gives equation 4.9 below,

$$n_1 = \frac{\sigma_{ft1} A_{ft}}{0.85 f_c b \gamma} \qquad \ldots\ldots 4.9$$

Let us have a look for another compatible expression involving n_1, which will allow us to combine it with equation 4.9 in such a way as to obtain an expression with only one unknown.

Let us make the usual assumption that plane section remains plane for any curvature. With this assumption, all the strains in figure 4.1b are proportional to their distances from the neutral axis of the beam. Thus for geometric compatibility, we can write down equation 4.10, which reflects the proportionality of the strains.

$$\frac{\varepsilon_{cu}}{n_1} = \frac{\varepsilon_{ft1}}{d - n_1} = \psi_1 \qquad \ldots\ldots 4.10$$

Then, solving for n_1, gives equation 4.11.

$$n_1 = \frac{\varepsilon_{cu} d}{\varepsilon_{ft1} + \varepsilon_{cu}} \qquad \ldots\ldots 4.11$$

Equation 4.11 is congruent with equation 4.9; therefore, both can be compared as in equation 4.12.

$$\frac{\sigma_{ftu} A_{ft}}{0.85 f_c b \gamma} = \frac{\varepsilon_{cu} d}{\varepsilon_{ft1} + \varepsilon_{cu}} \qquad \ldots\ldots 4.12$$

It is observed that in equation 4.12 there is now only one unknown, which can be either the stress σ_{ftl} or the strain ε_{ftl} of the tensile reinforcement which are related by:

$$\sigma_{ftl} = \varepsilon_{ftl} E_{ft} \quad \ldots\ldots 4.13$$

Inserting σ_{ftl} from equation 4.13 into equation 4.12 and solving for ε_{ftl}, gives the second order equation 4.14 in terms of the ε_{ftl}.

$$(\varepsilon_{ftl})^2 + \varepsilon_{cu}\varepsilon_{ftl} - \frac{0.85 f_c b \gamma \varepsilon_{cu} d}{E_{ft} A_{ft}} = 0 \quad \ldots\ldots 4.14$$

It can be observed that apart from the strain ε_{ftl} of the tensile reinforcement, everything else is already known. However, it is still necessary to verify that the strain ε_{ftl} is not greater than the ultimate strain ε_{ftu} of the FRP reinforcement. This can be done using the following equation:

$$\varepsilon_{ftu} = \frac{\sigma_{ftu}}{E_{ft}} \quad \ldots\ldots 4.15$$

where σ_{ftu} is the tensile strength of the FRP reinforcing bars; and E_{ft} is the Young's modulus of the FRP reinforcing bars. If the strain ε_{ftl} is less than or equal to ε_{ftu}, then the calculation can be continued otherwise, the amount of reinforcement A_{ft} must be increased or the size of the beam's cross-section be reduced in order to prevent a brittle catastrophic failure due to fracture of the tensile reinforcing bars.

The neutral axis depth n_1 can now be calculated using either equation 4.9 or equation 4.11, soon after calculating ε_{ft1} in equation 4.14. Let us calculate the concrete force C_{c1} by just inserting the neutral axis depth n_1, into equation 4.6. We can now calculate the internal moment of the beam, using equation 4.4, where all the parameters involved in that equation, are now known. The corresponding curvature ψ_1 at the concrete crushing can be calculated using equation 4.16 below.

$$\psi_1 = \frac{\varepsilon_{cu}}{n_1} \qquad \ldots\ldots 4.16$$

So far, we have the first co-ordinates (ψ_1, M_{n1}) in the falling branch of the moment-curvature relationship. This point of the moment-curvature relationship corresponds to that point where the top fiber of concrete reaches its ultimate strain ε_{cu}; which in turn means the start of the falling branch of the moment-curvature relationship.

4.2.2.2 Falling branch

Next, let us calculate a second point in the falling branch of the moment-curvature relationship. We can start by assuming that the displacement applied to the beam has been increased, inflicting a larger deflection to the beam and, therefore, increasing the curvature ψ of the beam. Let us assume a curvature ψ_2 greater than ψ_1, and calculate the corresponding internal moment M_{n2} for this specific curvature ψ_2.

The second point (ψ_2, M_{n2}) of the moment-curvature relationship is calculated using figures 4.1e, 4.1f and 4.1g. Looking at figure 4.1g, the internal moment M_{n2} is the compressive concrete force C_{c2} times the lever arm z_2, as given in equation 4.17.

$$M_{n2} = C_{c2} z_2 \quad \ldots\ldots 4.17$$

The lever arm z_2 is found through equation 4.18, where n_2 is the distance between the already crushed top fiber of concrete and the neutral axis; and n_3 is the new neutral axis depth with respect to the fiber of concrete at the ultimate strain ε_{cu}.

$$z_2 = d - n_2 + n_3 - \frac{n_3 \gamma}{2} \quad \ldots\ldots 4.18$$

Let us take a look as to how to calculate the length of the lever arm z_2 in figure 4.1g. As has been mentioned above, the curvature ψ_2 in figure 4.1e is greater that the initial curvature ψ_1 in figure 4.1b. As a consequence, the neutral axis of the beam, drops down which can be seen in figure 4.1e. The strain ε_c at the top fiber of the beam has gone beyond the ultimate crushing strain ε_{cu} and also the neutral axis depth n_2, with respect to the already crushed top fiber of concrete, becomes deeper than n_1 in figure 4.1b. Furthermore, the level of the ultimate strain ε_{cu} is further down with respect to the initial level, in figure 4.1b, and the neutral axis depth with respect to ε_{cu} becomes n_3.

Now, to get the lever arm z_2 in figure 4.1g from the level of the FRP tensile reinforcement, we do the following: from the effective depth d of the beam's cross-section, we subtract n_2 to determine the distance from the FRP tensile reinforcement to the new neutral axis of the beam; from here, we add the new neutral axis depth n_3 measured from the level of the neutral axis to reach the distance to the level of the ultimate strain ε_{cu}. Reaching the ultimate strain ε_{cu} in figure 4.1e is equivalent to reaching the top side of the rectangular block of stresses in figure 4.1f. Being on the

topside of the block of stresses, we can get the centroid of the block, by just stepping down one half of the height $n_3\gamma$ of the rectangular block of stresses. The distance between the centroid of the rectangular block of stresses and the level of the tensile force T_{f2} is the length of the lever arm z_2. Equation 4.18 shows by itself the mathematical process to get the length of the lever arm z_2; nevertheless, the neutral axis depth n_3 as well as n_2 remain unknown. These unknown variables are calculated later.

For geometric compatibility, we can see in the figure 4.1e the following relationship:

$$\frac{\varepsilon_c}{n_2} = \frac{\varepsilon_{cu}}{n_3} = \frac{\varepsilon_{ft2}}{d - n_2} = \psi_2 \qquad \text{.....4. 19}$$

From this relationship, let us take out the relation that involve the ultimate strain ε_{cu}, the guessed curvature ψ_2 and, therefore, the unknown n_3, to pose equation 4.20 below.

$$\psi_2 = \frac{\varepsilon_{cu}}{n_3} \qquad \text{.....4. 20}$$

which can be written as

$$n_3 = \frac{\varepsilon_{cu}}{\psi_2} \qquad \text{.....4. 20}$$

The new neutral axis depth n_3 can also be used to calculate the concrete compressive force C_{c2} in equation 4.22 below.

$$C_{c2} = 0.85 f_c b n_3 \gamma \quad \ldots\ldots 4.21$$

The concrete beam is in stable equilibrium if and only if the compressive force C_{c2} is equal to the tensile one T_{f2}, as established in equation 4.22.

$$C_{c2} = T_{f2} \quad \ldots\ldots 4.22$$

This means that T_{f2} takes the value of C_{c2} as shown in equation 4.23

$$T_{f2} = 0.85 f_c b \gamma n_3 \quad \ldots\ldots 4.23$$

Hence, the stress σ_{ft2} can be calculated from the equation 4.24, because the amount of tensile reinforcement A_{ft} is already known.

$$\sigma_{ft2} = \frac{T_{f2}}{A_{ft}} \quad \ldots\ldots 4.24$$

The strain ε_{ft2} is calculated from equation 4.25 as follow

$$\varepsilon_{ft2} = \frac{\sigma_{ft2}}{E_{ft}} \quad \ldots\ldots 4.25$$

At this stage, it is only left to calculate the distance n_2 between the level of ε_c and the neutral axis (see figure 4.1e) to include it in equation 4.18 for the calculation of the lever

arm z_2. Extracting equation 4.27 from equations 4.19 and then solving for n_2 in equation 4.28 gives.

$$\frac{\varepsilon_{cu}}{n_3} = \frac{\varepsilon_{ft2}}{d - n_2} \qquad \ldots\ldots 4.26$$

$$n_2 = \frac{\varepsilon_{cu} d - n_3 \varepsilon_{ft2}}{\varepsilon_{cu}} \qquad \ldots\ldots 4.27$$

Finally, the internal moment is the concrete force C_{c2} times the lever arm z_2, in equation 4.28. The expression in brackets is the lever arm of the concrete force C_{c2} (see equation 4.18) about the level of the tensile force T_{f2}.

$$M_{n2} = C_{c2}\left(d - n_2 + n_3 - \frac{n_3 \gamma}{2}\right) \qquad \ldots\ldots 4.28$$

As the curvature ψ_2 was assumed before hand, we have the co-ordinates $(\psi_2,\ M_{n2})$ for the second point in the falling branch of the moment-curvature relationship. Therefore, for any other point $(\psi_i,\ M_{ni})$ of the falling branch of the moment-curvature relationship, it is only a matter of assuming a new curvature ψ_i and following the same procedure.

Illustration

Calculation of the falling branch of the moment-curvature relationship of the RC beam shown in figure 4.1. The properties of the concrete beam are as follow:

Beam properties

b = 200 mm

d = 300 mm

f_c = 30 MPa

A_{ft} = 942 mm^2

σ_{ftu} = 624 MPa

E_{ft} = 51482 MPa

a) Initial concrete crushing.

Let us start by calculating the first point (ψ_1, M_{n1}) of the moment-curvature relationship of the falling branch. In doing so, let us assume that crushing of the top fiber of concrete occurs at the strain ε_{cu} of 0.004.

Looking at all the of above equations, we can see the feasibility of using equation 4.14 to evaluate the strain ε_{ft1} of the FRP tensile reinforcement, which occurs at the same time as when the top fiber of concrete crushes. One can easily realise that the parameters involved in equation 4.14 are all already known, except the strain ε_{ft1} and the reduction factor γ of the neutral axis depth. Therefore in this equation, we can substitute all those known parameters plus the factor γ, and solve for ε_{ft1}. The factor γ is calculated using equation 4.3.

To start with the calculation, let us go through equation 4.14, to firstly obtain the strain ε_{ft1} of the tensile reinforcement.

Equation 4.14:

$$(\varepsilon_{ft1})^2 + \varepsilon_{cu}\varepsilon_{ft1} - \frac{0.85f_c'b\gamma\varepsilon_{cu}d}{E_{ft}A_{ft}} = 0$$

We need to know the factor γ to include it into equation 4.14, which can be calculated using equation 4.3.

Equation 4.3:

$$\gamma = 0.85 - 0.007(f_c - 28)$$

$$\gamma = 0.85 - 0.007(30 - 28) = 0.836$$

Once all the parameters are known, they are included into equation 4.14 to obtain the strain ε_{ft1}.

$$\varepsilon_{ft1}^2 + 0.004\varepsilon_{ft1} - \frac{0.85 \times 30 \times 10^6 \times 0.2 \times 0.836 \times 0.004 \times 0.27}{51482 \times 10^6 \times 942 \times 10^{-6}} = 0$$

Hence $\varepsilon_{ft1} = 0.00795$

Now let us calculate the stress σ_{ft1} of the FRP reinforcement using the equation 4.13.

Equation 4.13:

$\sigma_{ft1} = \varepsilon_{ft1} E_{ft}$

$\sigma_{ft1} = 0.00794 \times 51482 = 409$ MPa

This result is satisfactory because the stress σ_{ft1} of the tensile FRP rebars is less than the strength σ_{ftu}, that is the bar has not fractured.

The tensile force T_{f1} is calculated using equation 4.7 as follow:

Equation 4.7:

$T_{f1} = \sigma_{ft1} A_{ft}$

$T_{f1} = 408.77 \times 10^{6} \times 942 \times 10^{-6} = 385$ kN

At this point, the strain ε_{ft1} is known; therefore, the neutral axis depth n_1 can be evaluated using equation 4.11.

Equation 4.11:

$$n_1 = \frac{\varepsilon_{cu} d}{\varepsilon_{ft1} + \varepsilon_{cu}}$$

$$n_1 = \frac{0.004 \times 270}{0.00794 + .004} = 90.45 \text{ mm}$$

The internal moment M_{n1} is evaluated using equation 4.4.

Equation 4.4:

$$M_{n1} = C_{c1}\left(d - \frac{n_1\gamma}{2}\right)$$

$$M_{n1} = 385\left(0.27 - \frac{0.09045 \times 0.836}{2}\right) = 89.39 \text{ kNm}$$

Finally, the curvature ψ_1 is calculated using equation 4.16, as follow:

Equation 4.16:

$$\psi_1 = \frac{\varepsilon_{cu}}{n_1}$$

$$\psi_1 = \frac{0.004}{90.45} = 44.22 \text{ x } 10^{-6} \text{ mm}^{-1}$$

So far, we have derived the first point (ψ_1, M_{n1}) of the falling branch of the moment-curvature relationship.

$$(\psi_1, M_{n1}) = (44.22 \text{ x } 10^{-6}, 89.39)$$

b) Falling branch.

For the calculation of a second point of the moment-curvature relationship, instead of knowing the strain ε_c of the top fiber of concrete, we guess any curvature ψ_2 greater than

ψ_1. As ψ_2 is greater than ψ_1, then most of the top concrete is already crushed. Hence, the neutral axis drops further down than the previous one and consequently, the strain drops down with respect to the ε_{cu} in figure 4.1b. All of these comments can be verified in figure 4.1e. In such a figure, it can be seen clearly that the neutral axis for the curvature ψ_2 is in a lower position than the neutral axis for the curvature ψ_1. Also that the strain ε_c of the top fiber of concrete is larger than the ultimate strain ε_{cu}. The configuration represented by figure 4.1e happens because the beam is an over reinforced one and hence, the tensile reinforcement of FRP does not fracture. To start with the calculation of the second point of the falling branch of the moment-curvature relationship, let the curvature ψ_2 be 80 x 10^{-6} mm^{-1}, hence we can derive the neutral axis depth n_3 in figure 4.1e, using equation 4.20.

Equation 4.20:

$$n_3 = \frac{\varepsilon_{cu}}{\psi_2}$$

$$n_3 = \frac{0.004}{80 \times 10^{-6}} = 50 \text{ mm}$$

Now, let us insert n_3 into equation 4.21 of the concrete force, where γ is 0.836.

Equation 4.21:

$$C_{c2} = 0.85 f_c b n_3 \gamma$$

$C_{c2} = 0.85 \times 30 \times 10^6 \times 200 \times 50 \times 0.836 \times 10^{-6} = 213.18$ kN

For equilibrium conditions, the compressive force C_{c2} is set equal to the tensile force T_{f2}; thus,

Equation 4.22:

$$C_{c2} = T_{f2}$$

therefore,

$T_{f2} = 213.18$ kN

With this magnitude of the tensile force, we can calculate the stress σ_{ft2} of the tensile reinforcement, using equation 4.24.

Equation 4.24:

$$\sigma_{ft2} = \frac{T_{f2}}{A_{ft}}$$

$$\sigma_{ft2} = \frac{213.18 \times 10^3}{942 \times 10^{-6}} = 226.3 \text{ MPa}$$

The strain ε_{ft2} is calculated using equation 4.25.

Equation 4.25:

$$\varepsilon_{ft2} = \frac{\sigma_{ft2}}{E_{ft}}$$

$$\varepsilon_{ft2} = \frac{226.3 \times 10^6}{51482 \times 10^6} = 0.004395$$

The distance n_2 from the top of the beam to the neutral axis is calculated using equation 4.27.

Equation 4.27:

$$n_2 = \frac{\varepsilon_{cu} d - n_3 \varepsilon_{ft2}}{\varepsilon_{cu}}$$

$$n_2 = \frac{0.004 \times 270 - 50 \times 0.004395}{0.004} = 215 \text{ mm}$$

Notice that n_2 is the distance between the top of the cross-section and the neutral axis of the beam (see figure4.1e).

Knowing n_2 and n_3, and inserting them into the equation 4.18, gives the lever arm z_2, which can be inserted into equation 4.17 to calculate the bending moment as follow:

Equation 4.18:

$$z_2 = d - n_2 + n_3 - \frac{n_3 \gamma}{2}$$

$$z_2 = 270 - 215 + 50 - \frac{50 \times 0.836}{2} = 84.1 \text{ mm}$$

Substituting z_2 in the equation 4.17, gives the internal moment M_{n2}.

Equation 4.17:

$$M_{n2} = C_{c2} z_2$$

$$M_{n2} = 213.18 \text{ x } 84.1 \text{ x } 10^{-3} = 17.92 \text{ kNm}$$

Alternatively, n_2 and n_3 can be used in equation 4.28 to get the internal moment of the beam.

Equation 4.28:

$$M_{n2} = C_{c2}\left(d - n_2 + n_3 - \frac{n_3 \gamma}{2}\right)$$

$$M_{n2} = 213.18\left(0.27 - 0.215 + 0.05 - \frac{0.05 \times 0.836}{2}\right) = 17.93 \text{ kNm}$$

As the curvature ψ_2 was assumed before hand, we already have a second point in the moment-curvature relationship as given below.

$$\left(\psi_2,\ M_{n2}\right) = \left(80 \times 10^{-6},\ 17.93\right)$$

Results

Following the same procedure, two additional points have been calculated to define the trend of the curve, and they are included in table 4.1.

Table 4. 1.– *Results for a singly reinforced concrete beam.*

Curvature ψ [mm^{-1}]	Internal moment M_n [kNm]
44.22×10^{-6}	89.3
60×10^{-6}	38.8
70×10^{-6}	25.3
80×10^{-6}	17.9

Figure 4.5 shows the falling branch of the moment-curvature relationship using the results in table 4.1.

4.2.2.3 Alternative approach for the calculation of the falling branch of a singly reinforced concrete beam.

In addition to the above described procedure, can be derived a general equation of the moment-curvature relationship, assuming a variation of the equivalent effective depth d of the cross-section of the beam in terms of the variation of the curvature ψ. Hence, as

the curvature ψ increases, the equivalent effective depth d decreases and, consequently, the block of stresses moves downwards (see figure 4.2i). In addition, the character 'a' in the equation numbers below stands for 'alternative approach'.

From figure 4.2 i, we get the compatibility equation 1a.

$$\psi_2 = \frac{\varepsilon_{cu}}{n_3} = \frac{\varepsilon_{ft2}}{d - n_3} \qquad \ldots\ldots 1a$$

From equation 1a and solving for n_3 gives equation 2a.

$$n_3 = \frac{\varepsilon_{cu}}{\psi_2} = \text{constant} \qquad \ldots\ldots 2a$$

The force of the compressive concrete is calculated using equation 3a and the force of the tensile reinforcement is calculated using equation 4a.

$$C_{c2} = 0.85 f_c b \gamma n_3 = 0.85 f_c \, b \gamma \left(\frac{\varepsilon_{cu}}{\psi_2} \right) \qquad \ldots\ldots 3a$$

$$T_{f2} = A_{ft} E_{ft} \varepsilon_{ft2} \qquad \ldots\ldots 4a$$

From the compatibility equation 1a and solving for ε_{ft2} gives equation 5a.

$$\varepsilon_{ft2} = \frac{\varepsilon_{cu}(d_2 - n_3)}{n_3} \quad \text{.....5a}$$

As the beam is in equilibrium for every value of curvature ψ, then it is valid to write down equation 6a.

$$T_{f2} = A_{ft}E_{ft}\psi_2(d_2 - n_3) = 0.85f_c b\gamma\left(\frac{\varepsilon_{cu}}{\psi_2}\right) \quad \text{.....6a}$$

Rearranging equation 6a and solving for d_2 gives equation 7a.

$$d_2 = \frac{\varepsilon_{cu}}{\psi_2}\left(\frac{0.85f_c b\gamma}{A_{ft}E_{ft}\psi_2} + 1\right) \quad \text{.....7a}$$

The lever arm of the force C_{c2} can be written as follow:

$$z_2 = d_2 - \frac{\gamma n_3}{2} = d_2 - \frac{\gamma\varepsilon_{cu}}{2\psi_2} \quad \text{.....8a}$$

The internal moment of the beam is expressed in equation 9a.

$$M_{n2} = C_{c2}z_2 \quad \text{.....9a}$$

Substituting C_{c2} from equation 3a and z_2 from equation 8a gives equation 10a.

$$M_{n2} = 0.85 f_c b \gamma \left(\frac{\varepsilon_{cu}}{\psi_2}\right)\left(d_2 - \frac{\varepsilon_{cu}}{2\psi_2}\right) \quad \ldots\ldots\ldots\ldots\ldots\ldots\ldots\ldots\ldots\ldots\ldots\ldots\ldots\ldots\ldots\ldots 10a$$

Substituting d_2 from equation 7a in equation 10a gives equation 11a.

$$M_{n2} = 0.85 f_c b \gamma \left(\frac{\varepsilon_{cu}}{\psi_2}\right)\left(\frac{\varepsilon_{cu}}{\psi_2}\left(\frac{0.85 f_c b \gamma}{A_{fl} E_{fl} \psi_2} + 1\right) - \frac{\gamma \varepsilon_{cu}}{2\psi_2}\right) \quad \ldots\ldots\ldots\ldots\ldots\ldots\ldots\ldots\ldots\ldots\ldots\ldots 11a$$

Finally rearranging equation 11a gives the general equation 12a of the internal moment of the beam for a particular curvature ψ greater than the curvature ψ_1 at which the top fiber of concrete crushes.

$$M_{n2} = 0.85 f_c b \gamma \left(\frac{\varepsilon_{cu}}{\psi_2}\right)^2 \left(\frac{0.85 f_c b \gamma}{A_{fl} E_{fl} \psi_2} - \frac{\gamma}{2} + 1\right) \quad \ldots\ldots\ldots\ldots\ldots\ldots\ldots\ldots\ldots\ldots\ldots\ldots 12a$$

for $\psi_2 \geq \psi_1$

Example

Evaluation of the falling branch of the moment-curvature relationship of the beam in figure 4.1 using equations of the alternative approach derived from figure 4.2.

Evaluation at the curvature ψ of 60×10^{-6}.

Equation 12a:

$$M_{n2} = 0.85 f_c b \gamma \left(\frac{\varepsilon_{cu}}{\psi_2}\right)^2 \left(\frac{0.85 f_c b \gamma}{A_{ft} E_{ft} \psi_2} - \frac{\gamma}{2} + 1\right)$$

$$M_n = 0.85 \times 30 \times 200 \times 0.836 \left(\frac{0.004}{60 \times 10^{-6}}\right)^2 \left(\frac{0.85 \times 30 \times 200 \times 0.836}{942 \times 51482 \times 60 \times 10^{-6}} - \frac{0.836}{2} + 1\right) \times 10^{-6}$$

$M_n = 38.79$ kNm

which is the same value of internal moment M_n in table 4.1 calculated using the step by step procedure above. The same procedure is used for the calculation of the remaining values of internal moment in table 4.1.

4.3 RC beams with FRP reinforcing bars at the top and at the bottom.

4.3.1 Overview

Let us look at figure 4.3 to find out what is going on when the concrete beam is carrying FRP reinforcing bars that are in the compressive zone. The analysis is based on figure 4.3a which represents the cross-section of the beam where: b and h are the cross-section's dimensions; d is the effective depth of the cross-section; d_1' is the distance between the top of the beam's cross-section and the centroid of the compressive bars; A_{fc} is the amount of compressive reinforcement; and A_{ft} is the amount of tensile reinforcement.

With the application of load upon the beam, is generated the curvature ψ_1 which brings about the strains distribution shown in figure 4.3b; where ε_{cu} is the concrete ultimate strain capacity; ε_{fc1} is the strain in the compressive reinforcement; ε_{ft1} is the strain in the tensile reinforcement; and n_1 the neutral axis. Figure 4.3c shows the stress

distribution where: $0.85f_c$ is the concrete stress; σ_{fc1} is the stress in the compressive reinforcement; and σ_{ft1} is the stress in the tensile reinforcement. Notice in figure 4.3c that the stress σ_{fc1} of the compressive reinforcement is acting in conjunction with the concrete stress $0.85f_c$. The forces are shown in figure 4.3d where: C_{f1} is the force of the compressive reinforcement; C_{c1} is the concrete's force; T_{f1} is the force of the tensile reinforcement; and z_c and z_f are the lever arms of the compressive forces about the level of the tensile force T_{f1}.

As the displacement upon the concrete beam is increased, the curvature also increases from ψ_1 to ψ_2 bringing about the internal response of the beam shown in figures 4.3e, 4.3f and 4.3g. In figure 4.3e: ε_c is the strain of the top fiber of concrete; ε_{fc2} is the strain of the compressive reinforcement; ε_{cu} is the concrete ultimate strain; ε_{ft2} is the strain of the tensile reinforcement; n_2 is a notional neutral axis depth; and n_3 is the actual neutral axis depth. Figure 4.3f describes the stress distribution where: σ_{fc2} is the stress in the compressive reinforcement; $0.85f_c$ is the concrete stress; $n_3\gamma$ is the height of the block of stress; and σ_{ft2} is the stress in the tensile reinforcement. Notice that the block of concrete stress is further down in figure 4.3f than in figure 4.3c. Figure 4.3g represents the forces and their respective positions where z_c and z_f are the lever arms of the compressive forces with respect to the level of the tensile force T_{f2}.

4.3.2 **Mathematical model for a doubly reinforced concrete beam with FRP reinforcing bars.**

The mathematical model is based on figure 4.4 which shows the beam's cross-section, the strain distribution, the stress distribution and the force distribution. In figure

4.4a can be seen a doubly hatched area at the top, which represents the already failed concrete, whereas, the singly hatched area represents the concrete compression zone. Figure 4.4b shows the strains distribution. In the strain distribution, can be seen from top to bottom: the strain ε_c of the top fiber of concrete which has already failed; the strain ε_{fc} of the compressive reinforcement; the concrete ultimate strain ε_{cu}; the curvature ψ; and the strain ε_{ft} of the tensile reinforcement. Also, there are two neutral axis depths: a notional neutral axis depth n_1; and an actual neutral axis depth n_2.

To get through the mathematical model, the following properties will be assumed to be known: the Young's modulus E_{ft} of the FRP tensile reinforcement; the Young's modulus E_{fc} of the FRP compressive reinforcement; the strength σ_{ftu} of the FRP tensile reinforcement; the strength σ_{fcu} of the FRP compressive reinforcement; the concrete strength f_c; the dimensions d and b of the beam's cross-section; the distance d_1 between the top fiber of concrete and the centroid of the compressive reinforcement; and the curvature ψ. It will be assumed that the unknown parameter is n_1, the distance between the top fiber of concrete and the neutral axis of beam's cross-section.

From figure 4.4b and for geometric compatibility, we can get the following mathematical expression:

$$\frac{\varepsilon_c}{n_1} = \frac{\varepsilon_{fc}}{n_1 - d_1} = \frac{\varepsilon_{cu}}{n_2} = \frac{\varepsilon_{ft}}{d - n_1} = \psi \qquad \text{.....4. 29}$$

Also from the figure 4.5d, the following equation of equilibrium of forces is true.

$$C_f + C_c = T_f \qquad \text{.....4. 30}$$

where C_f is the force of the compressive reinforcement; C_c is the concrete force; and T_f is the force of the tensile reinforcement. The force C_f of the compressive reinforcement is expressed in equation 4.31 where σ_{fc} is the stress in the compressive reinforcement and A_{fc} is the amount of compressive reinforcement.

$$C_f = \sigma_{fc} A_{fc} \qquad \text{.....4. 31}$$

The concrete force is expressed in the equation 4.32.

$$C_c = 0.85 f_c b \gamma n_2 \qquad \text{.....4. 32}$$

From equation 4.29

$$n_2 = \frac{\varepsilon_{cu}}{\psi} \qquad \text{.....4. 33}$$

and substituting into equation 4.32 gives

$$C_c = 0.85 f_c b \gamma \left(\frac{\varepsilon_{cu}}{\psi} \right) \qquad \text{.....4. 34}$$

The force in the tensile reinforcement is given in equation 4.35, where σ_{ft} is the stress in the tensile reinforcement.

$$T_f = \sigma_{ft} A_{ft} \quad \ldots\ldots 4.35$$

Now as our key unknown is n_1, let us start searching for it. From equation 4.29, we can write

$$\psi = \frac{\varepsilon_{fc}}{n_1 - d_1} \quad \ldots\ldots 4.36$$

and then solve for ε_{fc}

$$\varepsilon_{fc} = \psi(n_1 - d_1) \quad \ldots\ldots 4.37$$

The stress in the compressive reinforcement is calculated using equation 4.38

$$\sigma_{fc} = \varepsilon_{fc} E_{fc} \quad \ldots\ldots 4.38$$

which can be inserted into the equation 4.31 to obtain the force in the FRP compressive reinforcement in equation 4.39.

$$C_f = \psi(n_1 - d_1) E_{fc} A_{fc} \quad \ldots\ldots 4.39$$

Now we need to look for another expression which relates n_1 with other known parameters. Therefore, from expression 4.29, we extract the relationship 4.41, and then solve for ε_{ft} in equation 4.42

$$\psi = \frac{\varepsilon_{ft}}{d - n_1} \quad \ldots\ldots 4.41$$

$$\varepsilon_{ft} = \psi(d - n_1) \quad \ldots\ldots 4.42$$

As

$$\sigma_{ft} = \varepsilon_{ft} E_{ft} \quad \ldots\ldots 4.43$$

Combining equations 4.35, 4.42 and 4.43, gives equation 4.44 for the force T_f of the tensile reinforcement.

$$T_f = \psi(d - n_1) E_{ft} A_{ft} \quad \ldots\ldots 4.44$$

Substituting equations 4.34, 4.39 and 4.44 into 4.30, gives the following equation of equilibrium

$$\psi(n_1 - d_1) E_{fc} A_{fc} + 0.85 f_c b \gamma \left(\frac{\varepsilon_{cu}}{\psi}\right) = \psi(d - n_1) E_{ft} A_{ft} \quad \ldots\ldots 4.45$$

which being rearranged and solving for n_1 to gives

$$n_1 = \frac{\left(dE_{ft}A_{ft} + d_1 E_{fc} A_{fc}\right) - 0.85 f_c b \gamma \left(\frac{\varepsilon_{cu}}{\psi^2}\right)}{\left(E_{fc}A_{fc} + E_{ft}A_{ft}\right)} \quad \ldots\ldots 4.46$$

Equation 4.46 can be broken into K_1 in equation 4.47, K_2 in equation 4.48 and K_3 in equation 4.49 for easy manipulation so that equation 4.46 becomes equation 4.50.

$$K_1 = dE_{ft}A_{ft} + d_1E_{fc}A_{fc} \quad \text{.....4.47}$$

$$K_2 = 0.85f_c b\,\gamma\,\varepsilon_{cu} \quad \text{.....4.48}$$

$$K_3 = E_{ft}A_{ft} + E_{fc}A_{fc} \quad \text{.....4.49}$$

$$n_1 = \frac{1}{K_3}\left(K_1 - \frac{K_2}{\psi^2}\right) \quad \text{.....4.50}$$

The internal moment M_{nc} provided by the compressive concrete is calculated using equation 4.51

$$M_{nc} = C_c\,z_c \quad \text{.....4.51}$$

where C_c is the concrete force and z_c is the lever arm of the force C_c about the level of the tensile force T_f. In addition, the lever arm z_c can be expressed as in equation 4.52.

$$z_c = d - n_1 + n_2\left(1 - \frac{\gamma}{2}\right) \quad \text{.....4.52}$$

Inserting C_c from equation 4.34 and z_c from equation 4.52 gives

$$M_{nc} = 0.85 f_c b \gamma \left(\frac{\varepsilon_{cu}}{\psi}\right)\left(d - n_1 + n_2\left(1 - \frac{\gamma}{2}\right)\right) \quad \ldots\ldots 4.53$$

Then substituting K_3 from equation 4.49 and n_1 from equation 4.50 in equation 4.53 gives equation 4.54.

$$M_{nc} = \frac{K_2}{\psi}\left(d - \frac{1}{K_3}\left(K_1 + \frac{K_2}{\psi^2}\right) + \frac{\varepsilon_{cu}}{\psi}\left(1 - \frac{\gamma}{2}\right)\right) \quad \ldots\ldots 4.54$$

The internal moment M_{fc} provided by the compressive reinforcement is the force C_f in equation 4.39 times the lever arm z_f in figure 4.5d where

$$z_f = d - d_1 \quad \ldots\ldots 4.55$$

Hence, the moment M_{fc} is

$$M_{fc} = \psi(n_1 - d_1)E_{fc}A_{fc}(d - d_1) \quad \ldots\ldots 4.56$$

Substituting n_1 from equation 4.50 in equation 4.56 gives equation 4.57.

$$M_{fc} = \psi\left(\frac{1}{K_3}\left(K_1 + \frac{K_2}{\psi^2}\right) - d_1\right)E_{fc}A_{fc}(d - d_1) \quad \ldots\ldots 4.57$$

The internal moment M_n of the beam is the summation of the moment M_{nc} and the moment M_{fc}.

$$M_n = M_{nc} + M_{fc} \quad \text{.....4.58}$$

Substituting M_{nc} from equation 4.54 and M_{fc} from equation 4.57 in equation 4.58 gives equation 4.59.

$$M_n = \frac{K_2}{\psi}\left(d - \frac{1}{K_3}\left(K_1 - \frac{K_2}{\psi^2}\right) + \frac{\varepsilon_{cu}}{\psi}\left(1 - \frac{\gamma}{2}\right)\right) + \psi\left(\frac{1}{K_3}\left(K_1 - \frac{K_2}{\psi^2}\right) - d_1\right)E_{fc}A_{fc}(d - d_1)$$

.....4.59

Equation 4.59 represents the general equation for the moment-curvature relationship of a doubly reinforced concrete beam with FRP reinforcing bars for curvatures ψ greater than ψ_1. The curvature ψ_1 is that at which the top fiber of concrete of the beam start crushing.

Example

Calculation of the falling branch of the moment-curvature relationship of the RC beam shown in figure 4.4. The properties of the concrete beam are as follow:

Beam properties

b = 200 mm

d = 270 mm

d_1 = 30 mm

f_c = 30 MPa

$A_{fc} = 628\ mm^2$

$A_{ft} = 942\ mm^2$

$\sigma_{fcu} = 437\ MPa$

$\sigma_{ftu} = 624\ MPa$

$E_{fc} = 37191\ MPa$

$E_{ft} = 51482\ MPa$

Analysis at $\psi = 50 \times 10^{-6}\ mm^{-1}$

Let 0.004 be the concrete ultimate strain capacity ε_{cu}, which was calculated for beam 1 in chapter 3.

The internal moment of the beam is calculated using equation 4.59 in conjunction with equations 4.47, 4.48 and 4.49.

Equation 4.47:

$$K_1 = dE_{ft}A_{ft} + d_1E_{fc}A_{fc}$$

$$K_1 = 270 \times 51482 \times 942 + 30 \times 37191 \times 628 = 13794610320$$

Equation 4.48:

$$K_2 = 0.85f_c b \gamma \varepsilon_{cu}$$

$$K_2 = 0.85 \times 30 \times 200 \times 0.836 \times 0.004 = 17$$

Equation 4.49:

$K_3 = E_{ft}A_{ft} + E_{fc}A_{fc}$

$K_3 = 51482 \times 942 + 37191 \times 628 = 71851992$

Equation 4.59:

$$M_n = \frac{K_2}{\psi}\left(d - \frac{1}{K_3}\left(K_1 - \frac{K_2}{\psi^2}\right) + \frac{\varepsilon_{cu}}{\psi}\left(1 - \frac{\gamma}{2}\right)\right) + \psi\left(\frac{1}{K_3}\left(K_1 - \frac{K_2}{\psi^2}\right) - d_1\right)E_{fc}A_{fc}(d - d_1)$$

$$M_n = \left(\begin{array}{l} \dfrac{17}{50\times10^{-6}}\left(270 - \dfrac{1}{71851992}\left(13794610320 - \dfrac{17}{(50\times10^{-6})^2}\right) + \dfrac{0.004}{50\times10^{-6}}\left(1 - \dfrac{0.836}{2}\right)\right) \\ + 50\times10^{-6}\left(\dfrac{1}{71851992}\left(13794610320 - \dfrac{17}{(50\times10^{-6})^2}\right) - 30\right)37191\times628(270-30) \end{array}\right)10^{-6}$$

$M_n = 93.6$ kNm

Summary

Results are shown in table 4.2 for four different curvatures ψ and the graph of the falling branch of the moment-curvature relationship is shown in figure 4.6.

Finally, figure 4.7 shows the two curves calculated previously, in order to compare their trend. In this figure, the reader can see clearly how the compressive reinforcement of FRP reinforcing bars, takes over from the compressive concrete when it fails, generating ductility of the beam. The curve of the singly reinforced concrete beam drops down suddenly, whereas the curve of the doubly reinforced concrete beam keeps almost horizontal which is the characteristic behaviour of ductile beams. The peak flexural

strength M_n of both beams are practically the same as can be seen in figure 4.7 although the trend of the falling branch between them is significantly different.

Table 4.2. – *Results for a doubly reinforced concrete beam.*

Curvature ψ [mm^{-1}]	Internal moment [kNm]
50×10^{-6}	93.6
60×10^{-6}	84.3
70×10^{-6}	83.5
80×10^{-6}	86.7

The comprehensive procedure for designing a ductile RC beam with FRP reinforcing bars can be summarised as follow: firstly, the beam is assumed to be a singly reinforced in order to calculate both the internal moment strength M_n of the beam and the curvature ψ at which the top fiber of concrete starts crushing. After that the beam is analysed as a doubly reinforced using equation 4.59 to calculate the whole falling branch of the moment-curvature relationship for curvatures ψ greater than the curvature ψ at which the top fiber of concrete start crushing. Care must be taken when calculating the falling branch of the moment-curvature relationship not to exceed either the ultimate strain capacity ε_{fcu} of the FRP compressive rebars or the ultimate strain capacity ε_{ftu} of the FRP tensile rebars.

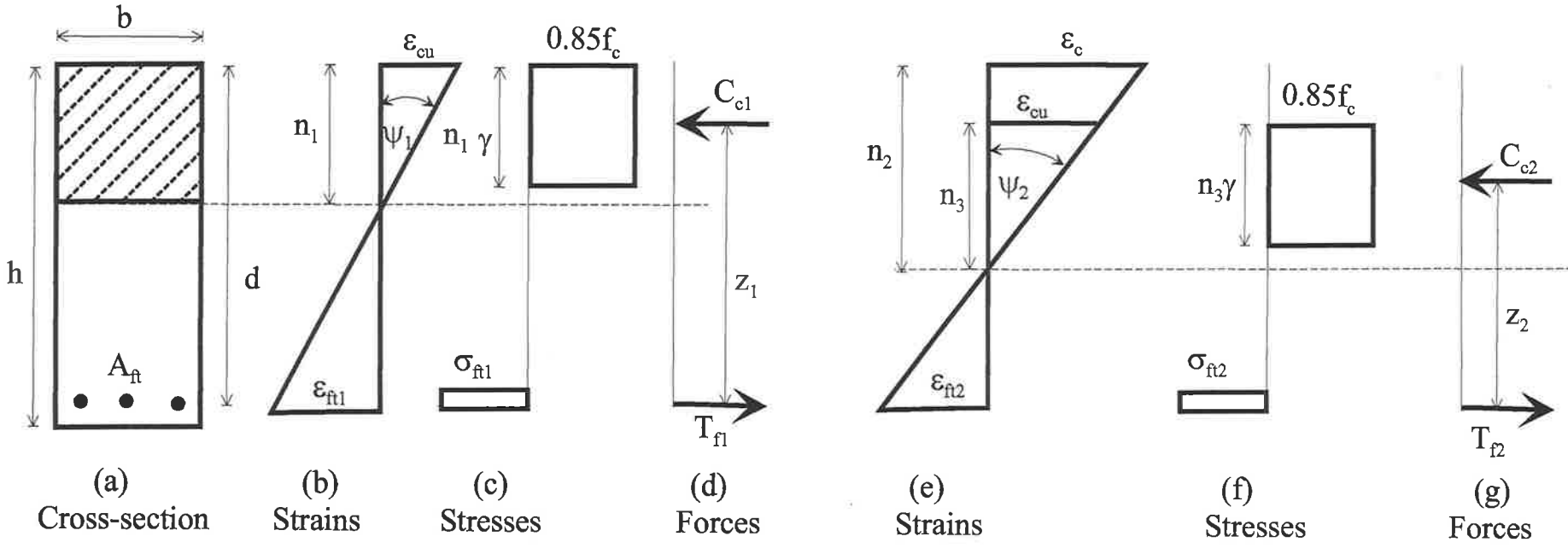

Figure 4.1.- Singly reinforced concrete beam with FRP reinforcing bars.

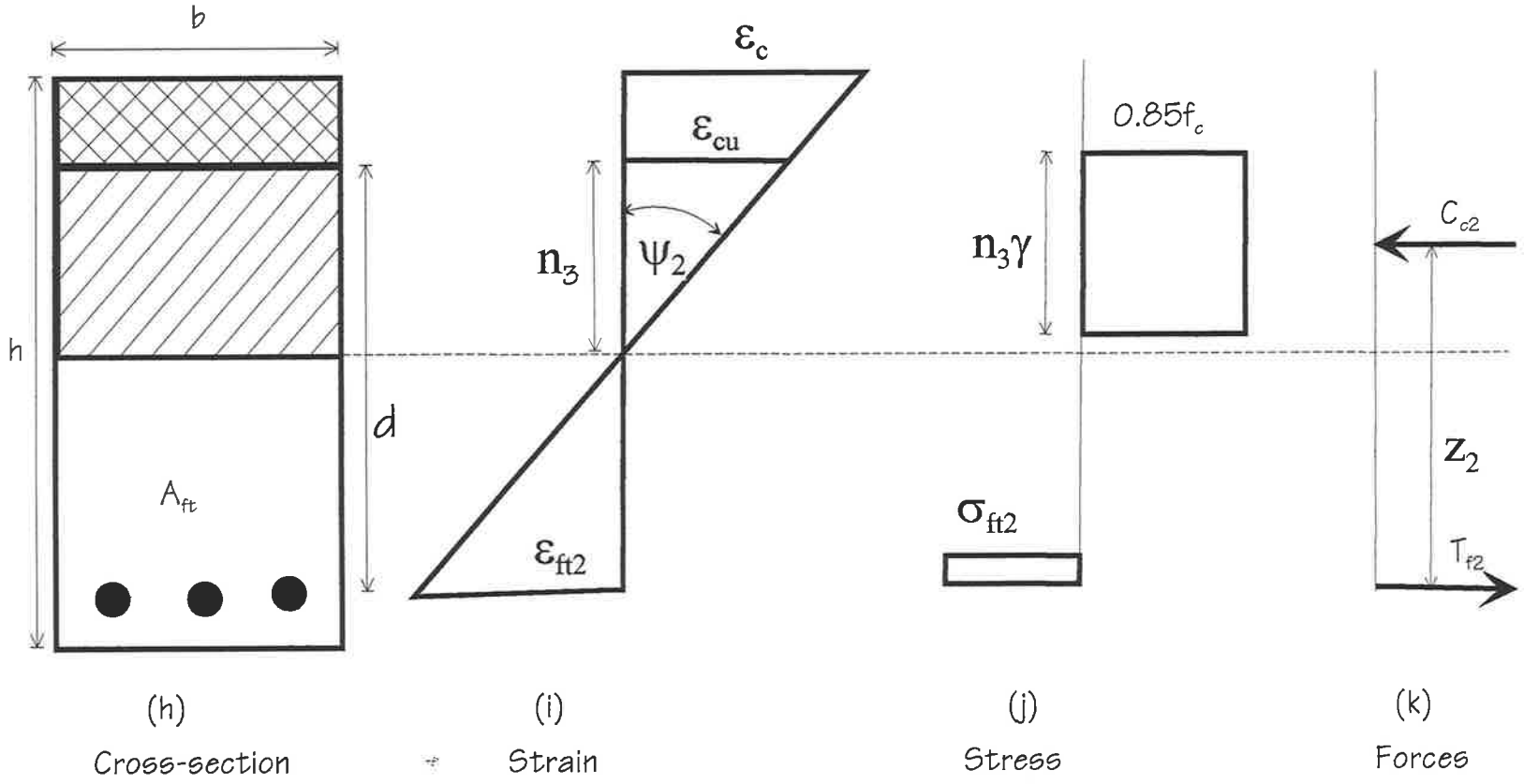

Figure 4.2. - Diagram for the alternative analysis method.

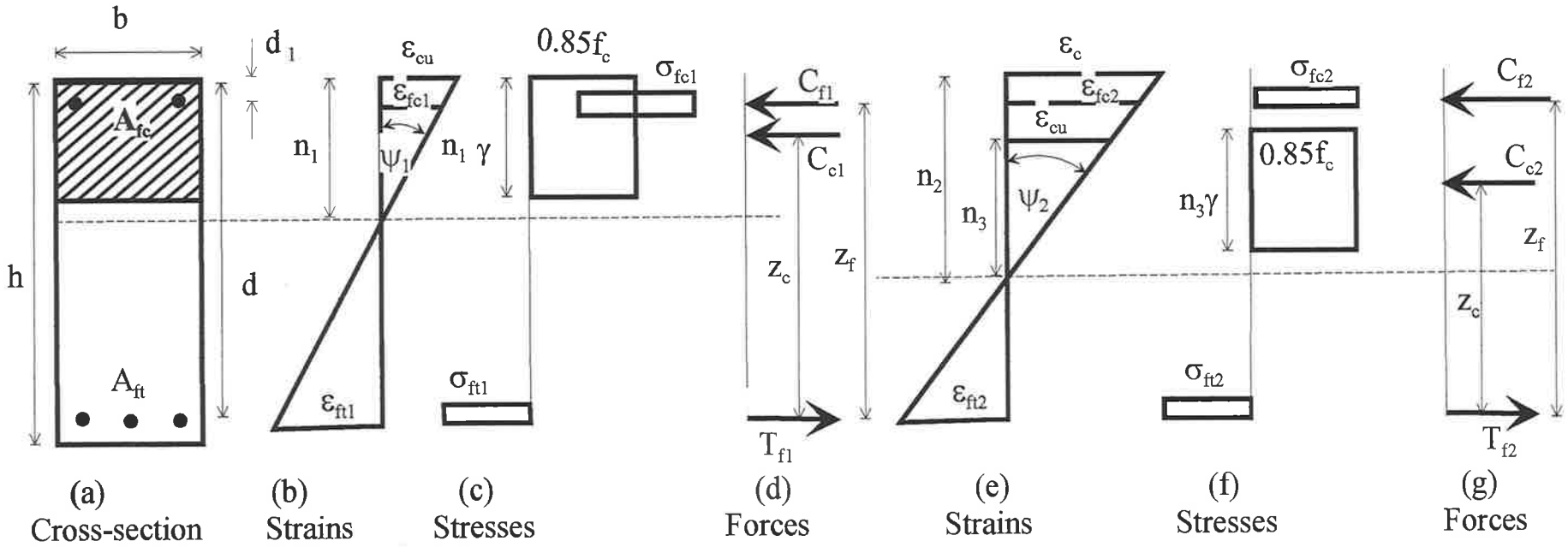

Figure 4.3.- Doubly reinforced concrete beam with FRP reinforcing bars.

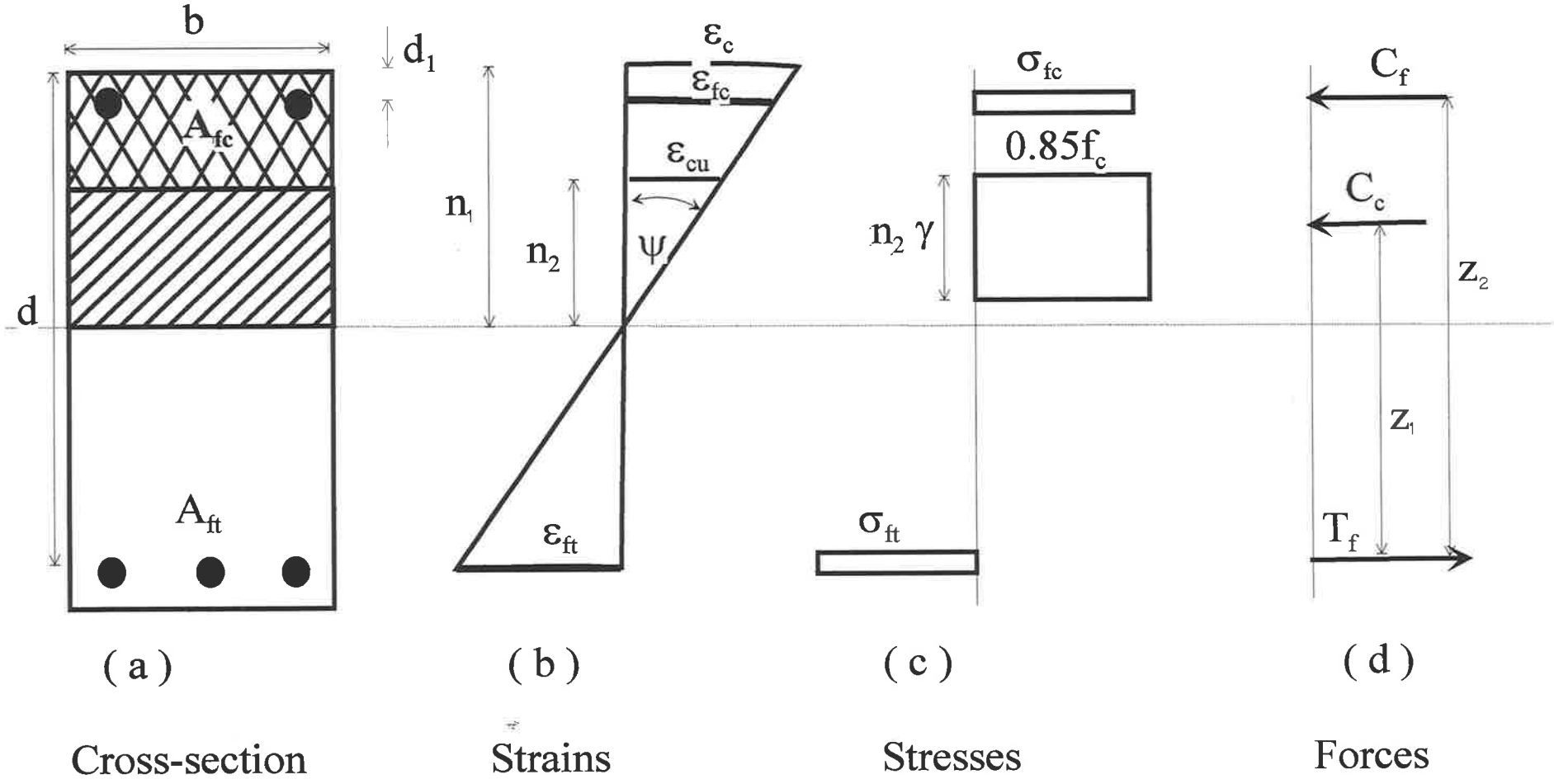

Figure 4.4.- Doubly reinforced concrete beam with FRP reinforcing bars.

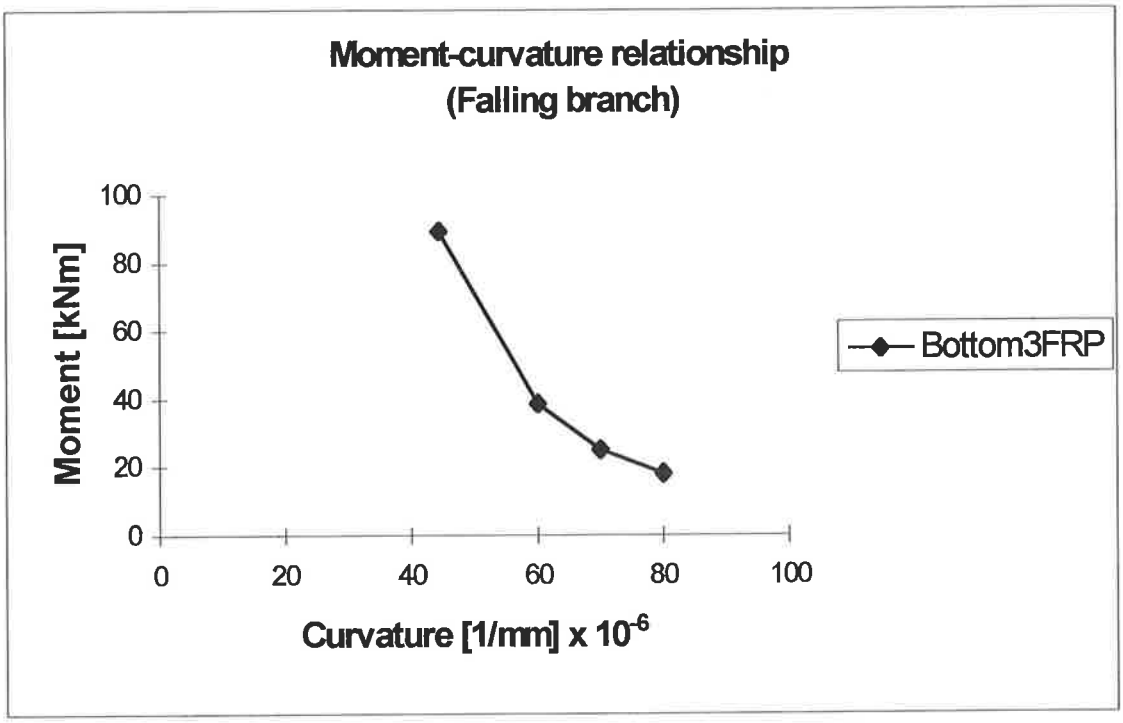

Figure 4.5. – Falling branch of the moment-curvature relationship of a singly reinforced concrete beam.

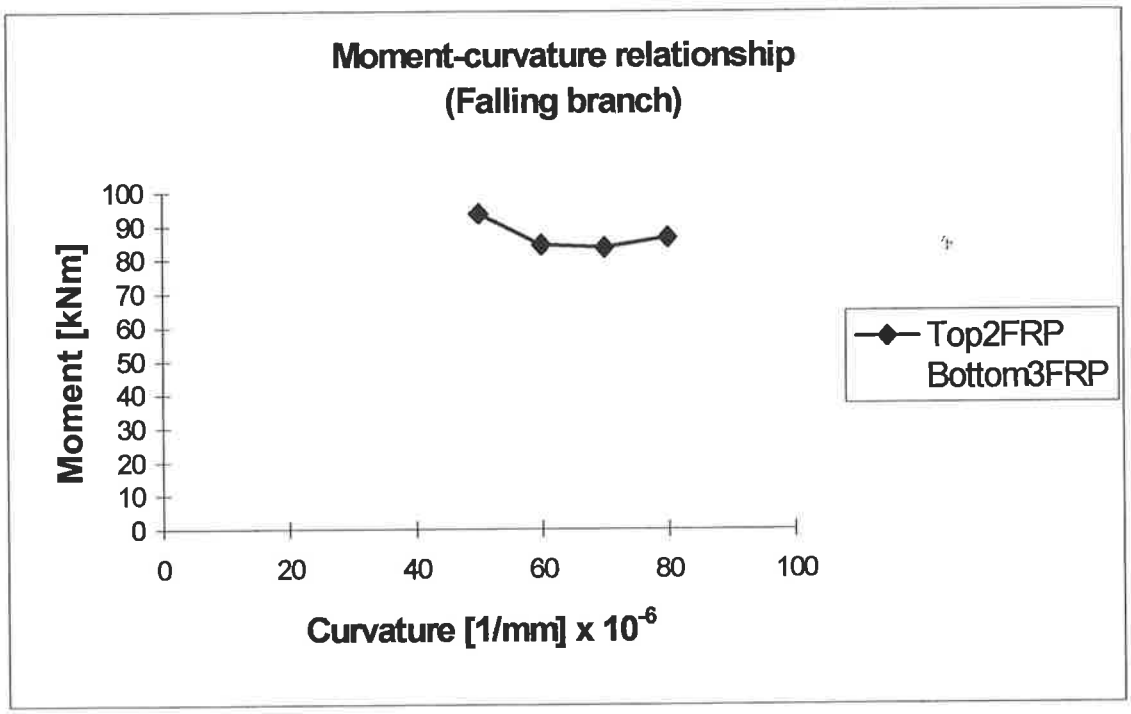

Figure 4.6. – Falling branch of the moment-curvature relationship of a doubly reinforced concrete beam.

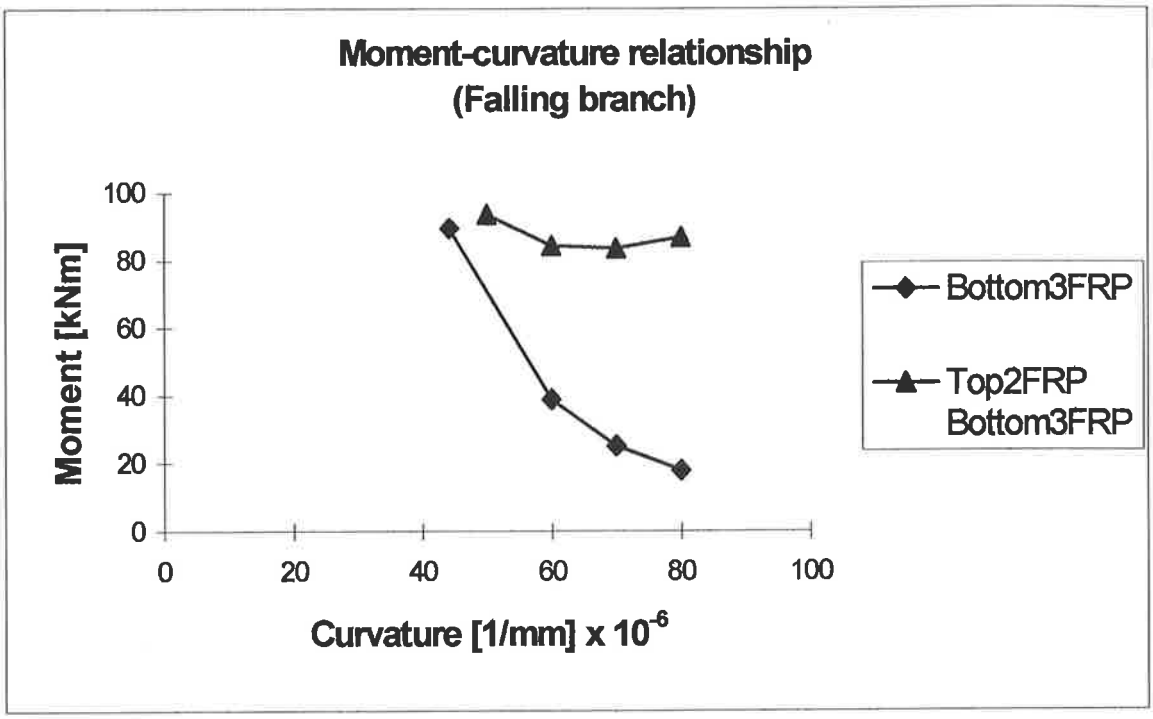

Figure 4.7. – Falling branch of the moment-curvature relationship of two different beams.

Chapter 5

Segmental analysis versus rectangular block of stresses analysis

5.1 Introduction

Two methods of analysis are discussed in this chapter. The segmental analysis method discussed in chapter 3 and the rectangular block of stresses analysis method discussed in chapter 4. The aim is to investigate the discrepancies between these two

methods, and determine the reasons for these discrepancies. To do so, first a graphic comparison is made between the moment-curvature relationships calculated using the segmental analysis method and the rectangular block of stresses analysis method. This is done for the following two main cases: a reinforced concrete beam with 3 FRP reinforcing bars at the bottom only; and a reinforced concrete beam with 2 FRP reinforcing bars at the top and 3 FRP reinforcing bars at the bottom. Later, the variations of the concrete force and its position are evaluated for specific values of curvature, to determine the causes for the discrepancies between the values of internal moment using each method. Finally, an appropriate solution is proposed to correct the falling branch of the moment-curvature relationship using the segmental analysis method to make it coincident with the falling branch of the moment-curvature relationship calculated through the rectangular block of stresses method.

5.2 Moment-curvature relationship.

In chapter 3 it was shown that the segmental analysis method can be used to determine the moment-curvature relationship from the origin up to failure. However, the rectangular block of stresses analysis, as shown in chapter 4, can only derive the falling branch of the moment-curvature relationship. Figure 5.1 shows the moment-curvature relationship of an RC beam with 3 FRP reinforcing bars of 20-mm diameter and 624 MPa strength at the bottom only, which is plotted using both the segmental analysis method and the rectangular block of stresses method. Both curves are close only at the flexural strength of the concrete beam where the internal moment is 87.1 kNm using the segmental analysis method, and 89.4 kNm using the rectangular block of stresses analysis. In the rest of the graph, the internal moment using the rectangular block of

stresses analysis is lower that the internal moment using the segmental analysis method for the same values of curvature ψ. Furthermore, the brittleness of the beam is evident in both methods of analysis, because once the top fiber of concrete fails, then the whole beam fails collapsing suddenly without warning.

Figure 5.2 shows the moment-curvature relationship of a doubly reinforced concrete beam with 2 FRP reinforcing bars of 20-mm diameter and 437 MPa strength at the top and 3 FRP reinforcing bars of 20-mm diameter and 624 MPa strength at the bottom. The internal moment using both methods is almost the same as the concrete starts crushing. The strength using the segmental analysis method is 98.0 kNm and using the rectangular block of stresses analysis it is 93.7 kNm. In the rest of the graph, the values of the internal moment using the rectangular block of stresses analysis is a bit lower than that using the segmental analysis method. In this case, the ductility of the concrete beam is evident using both methods because both curves show a horizontal trend from the maximum value of internal moment to the failure of the concrete beam. The difference in the moments at failure, between the two methods, is only 16.2 kNm.

5.3 Concrete stress distribution and position of the concrete's force

The concrete stress distribution along the cross-section of the beam is a parabolic one when using the segmental analysis method as shown in figure 5.3c. In contrast, when using the rectangular block of stresses analysis method, the stress distribution is assumed to be a rectangular one, as can be seen in figure 5.3e. The analysis is carried out for specific values of curvature ψ as it will be seen later.

First, let us describe the content in figure 5.3. The cross-section of the beam is described in figure 5.3a. Figure 5.3b describes the strain distribution. Figure 5.3c

describes the stress distribution using the segmental analysis method, meanwhile, figure 5.3d describes the forces and their positions derived through the segmental analysis method. Figure 5.3e describes the rectangular block of stresses, and figure 5.3f describes the forces and their positions derived using the rectangular block of stresses method.

Analysis at the curvature ψ of 45×10^{-6} mm^{-1}.

The position of the concrete force using the segmental analysis, is 225 mm away from the direction of the tensile force (see figure 5.3d). The position of concrete force using the rectangular block of stresses is 232 mm away from the tensile force as shown in figure 5.3f. Notice that the magnitudes of the concrete force and their positions are quite similar using both methods of analysis. The internal moment is also close using both methods being 87.1 kNm using the segmental analysis method and 89.4 kNm using the rectangular block of stresses method as shown in figure 5.1. No major difference exists between the internal moment and the positions of the concrete forces using the two method at the curvature ψ of 45×10^{-6} mm^{-1}.

The difference between the results from each method is more evident at the curvatures ψ of 60×10^{-6} mm^{-1}, 70×10^{-6} mm^{-1} and 80×10^{-6} mm^{-1} which can be seen in figures 5.1, 5.4, 5.5 and 5.6. For each curvature, the lever arm of the axial forces using the rectangular block of stresses analysis is about 50 mm smaller than the lever arm using the segmental analysis method. In addition, the concrete force using the rectangular block of stresses method is between 105 kN and 118 kN smaller than the concrete force using the segmental analysis method.

5.4 Influence of the concrete force beyond its ultimate strain in the evaluation of the internal moment of the beam.

In the discussion above, is underlined the differences of both the magnitudes of the concrete force and the position of that force with respect to the tensile force from one method of analysis to the other. What happens is that when using the rectangular block of stresses analysis, the concrete force is restricted to values of the concrete strain no greater than the concrete ultimate strain, which is rounded to 0.004. Meanwhile, when using the segmental analysis method, the force of the concrete is calculated for all the values of the concrete strain in the stress-strain relationship curve belonging to Wang's et al and shown in figure 2.32. Taken into account are the forces corresponding to concrete strains greater than 0.004 which causes the centroid of the concrete stresses distribution to move further up than the centroid of the rectangular block of stress. Consequently, the lever arm using the segmental analysis approach also becomes larger than the lever arm using the rectangular block of stresses analysis.

Let us look at what happens after restricting the segmental analysis method to the concrete ultimate strains less than or equal to 0.004. This means that no longer are taken into account the forces of the concrete with strains greater than 0.004. Figures 5.7, 5.8 and 5.9 show the effects of restricting the segmental analysis to concrete strains not greater than 0.004. The hatched areas of the stresses profile describe the concrete forces for strains greater than 0.004 and the area below describes the concrete force for strains less than or equal to 0.004. Two concrete forces are represented in the figures, one force for the hatched area and one force below. Notice that the force below the hatched area is similar to the concrete force calculated using the rectangular block of stresses analysis. Also, the size of the lever arm of the force below the hatched area becomes closer to the

lever arm of the concrete force using the rectangular block of stresses with an average difference of about 30 mm.

Figure 5.10 shows the variations of both the stress distributions and the positions of the concrete forces as the curvature ψ is changed. In figure 5.10a, the top of the stress distribution corresponds to the concrete ultimate strain ε_{cu} of 0.004, therefore, no hatched area is present. In figure 5.10c, the curvature ψ has been increased, hence, the stress at ultimate strain ε_{cu} is a bit lower than that in figure 5.10a. The concrete stress at ultimate strain is at the bottom of the hatched area of the stresses distribution in figure 5.10c. The same analysis is for figures 5.10e and for figures 5.10g.

Figure 5.11 shows the variations of both the concrete force and their position using the rectangular block of stresses analysis for the same values of curvature ψ as in figure 5.10. The horizontal dashed line for each figure represents the neutral axis of the cross-section of the beam.

By restricting the segmental analysis method to the concrete ultimate strain of 0.004, the falling branch of the moment-curvature relationship coincides with the falling branch calculated using the rectangular block of stresses method, as can be seen in figure 5.12, where the continuous line represents the curve using the segmental analysis method and the marked line represents the curve using the rectangular block of stresses method. The moment-curvature relationship in figure 5.12 corresponds to an RC beam with 3 FRP rebars of 20-mm diameter and 624 MPa strength at the bottom only. Segm004 stands for 'segmental analysis method with the concrete strain restricted to 0.004'.

On the other hand, figure 5.13 shows the moment-curvature relationship of an RC beam with 2 FRP rebars of 20-mm diameter and 437 MPa strength at the top and 3 FRP rebars of 20-mm diameter and 624 MPa strength at the bottom. The continuous line

corresponds to the moment-curvature relationship using the segmental analysis method, and the marked line corresponds to the falling branch calculated using the rectangular block of stresses analysis method. The falling branches using both methods of analysis are coincident.

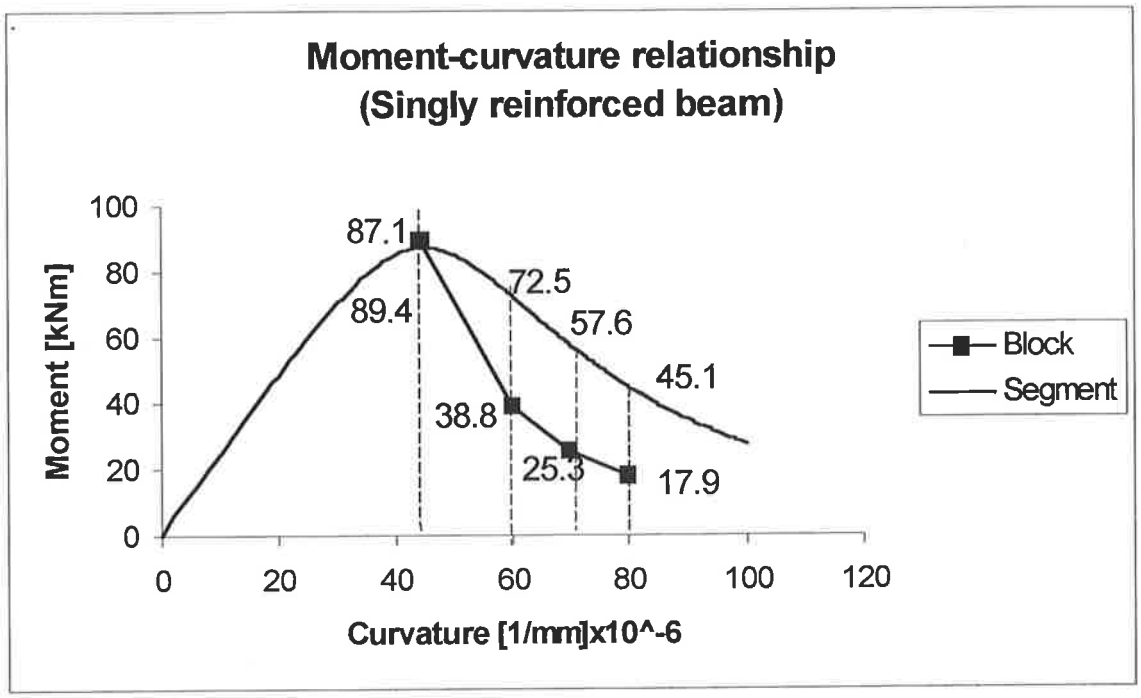

Figure 5.1. – Moment-curvature relationship of a singly reinforced concrete beam.

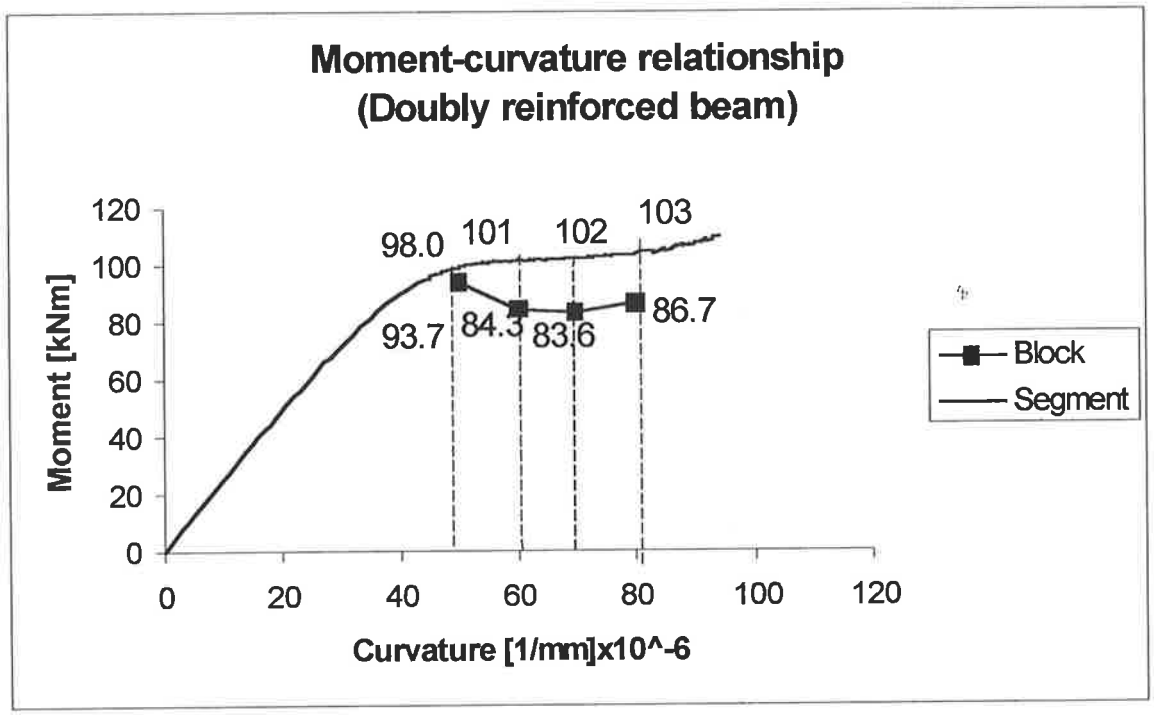

Figure 5.2. – Moment-curvature relationship of a doubly reinforced concrete beam.

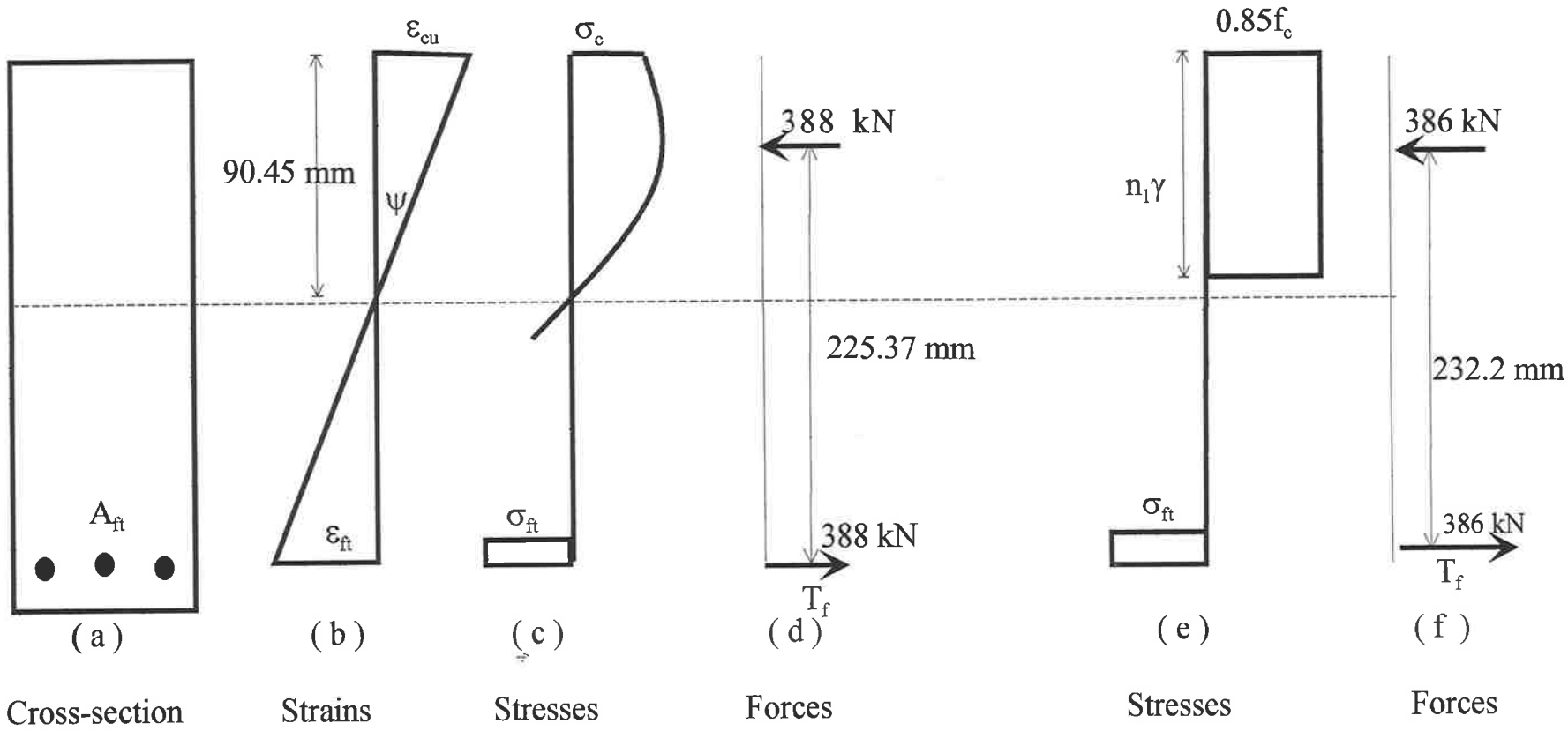

Figure 5.3.- Magnitude and position of the concrete forces.

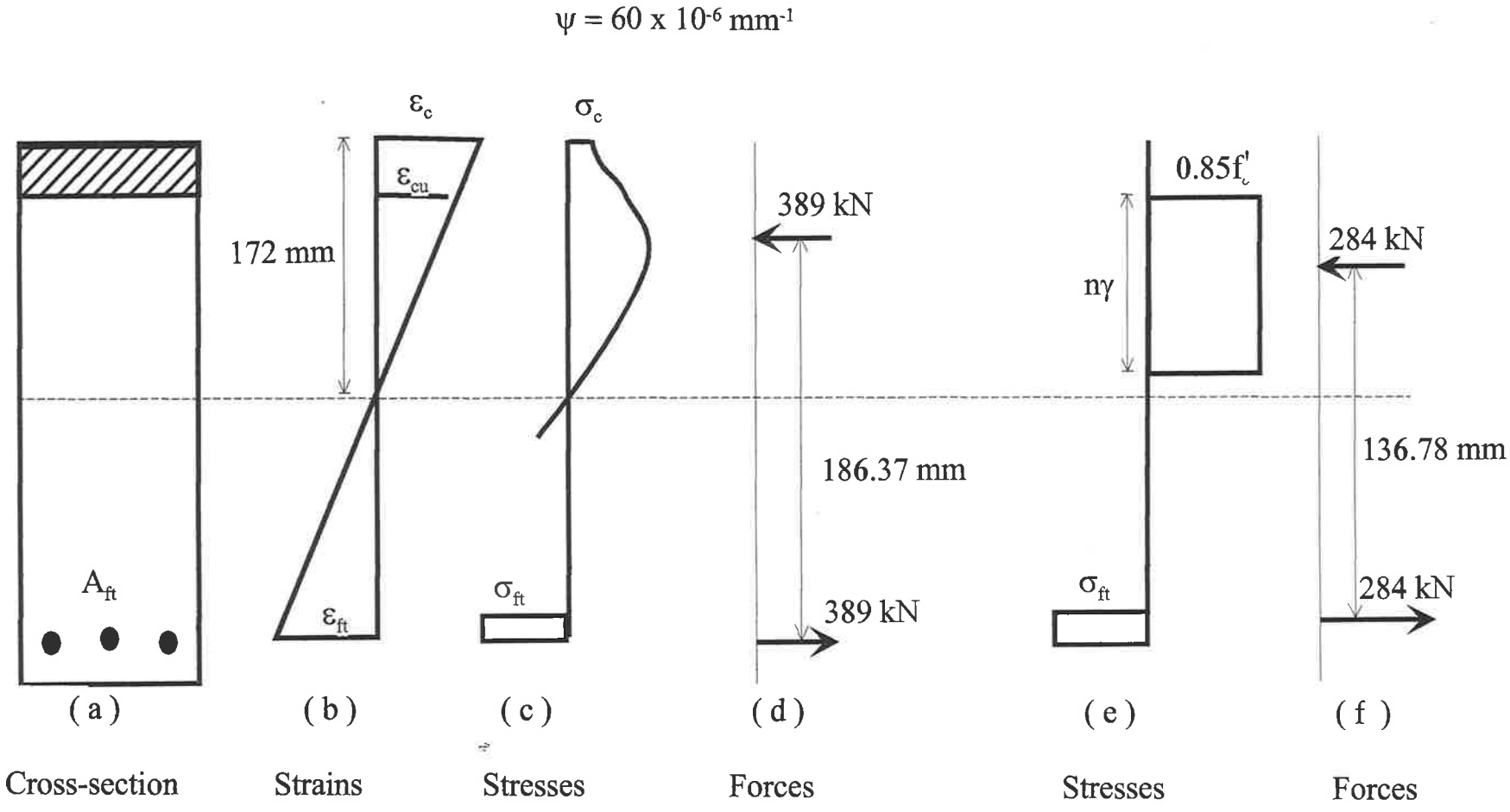

Figure 5.4.- Magnitude and posistion of the concrete forces.

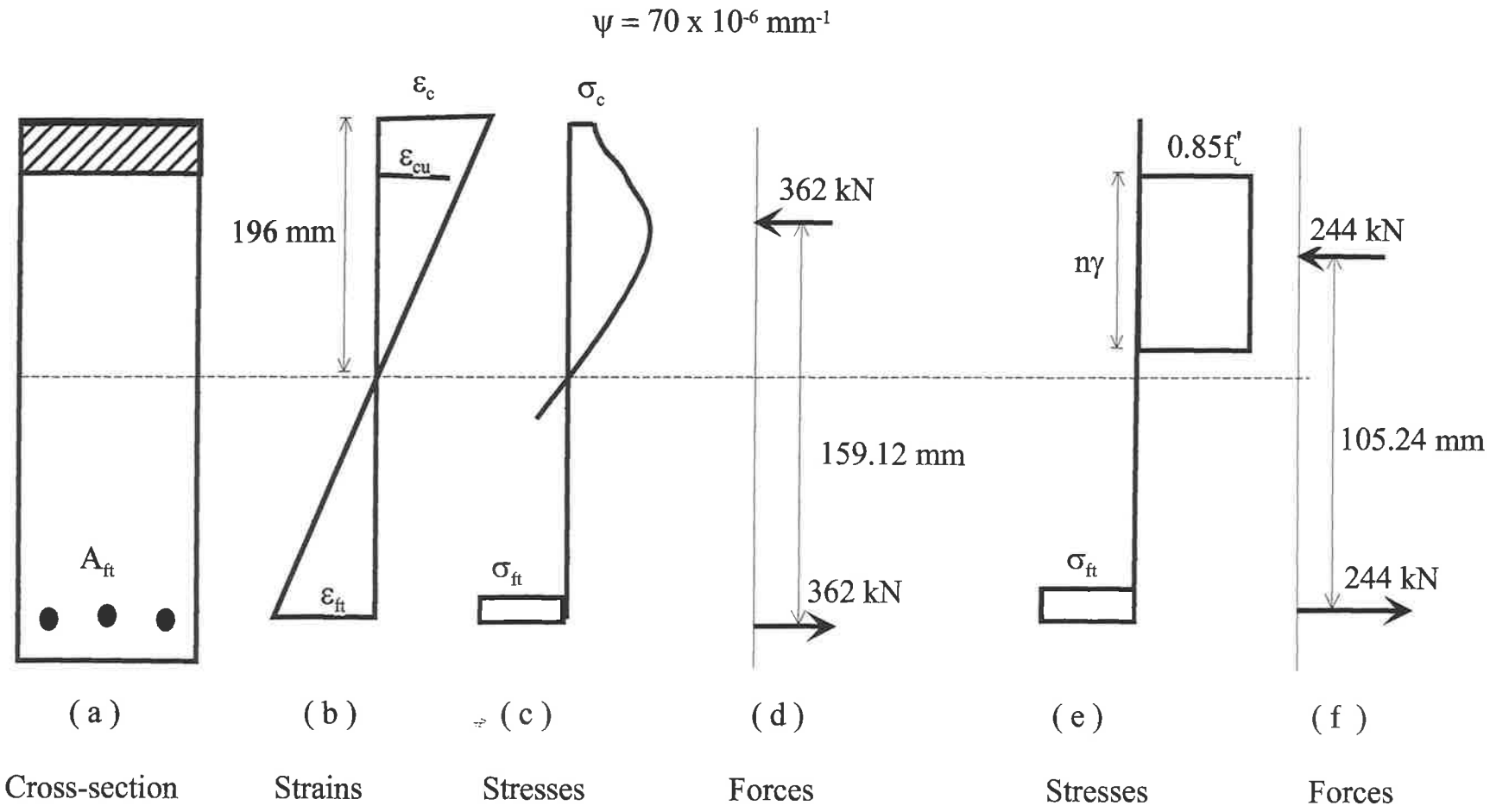

Figure 5.5.- Magnitude and position of the concrete forces.

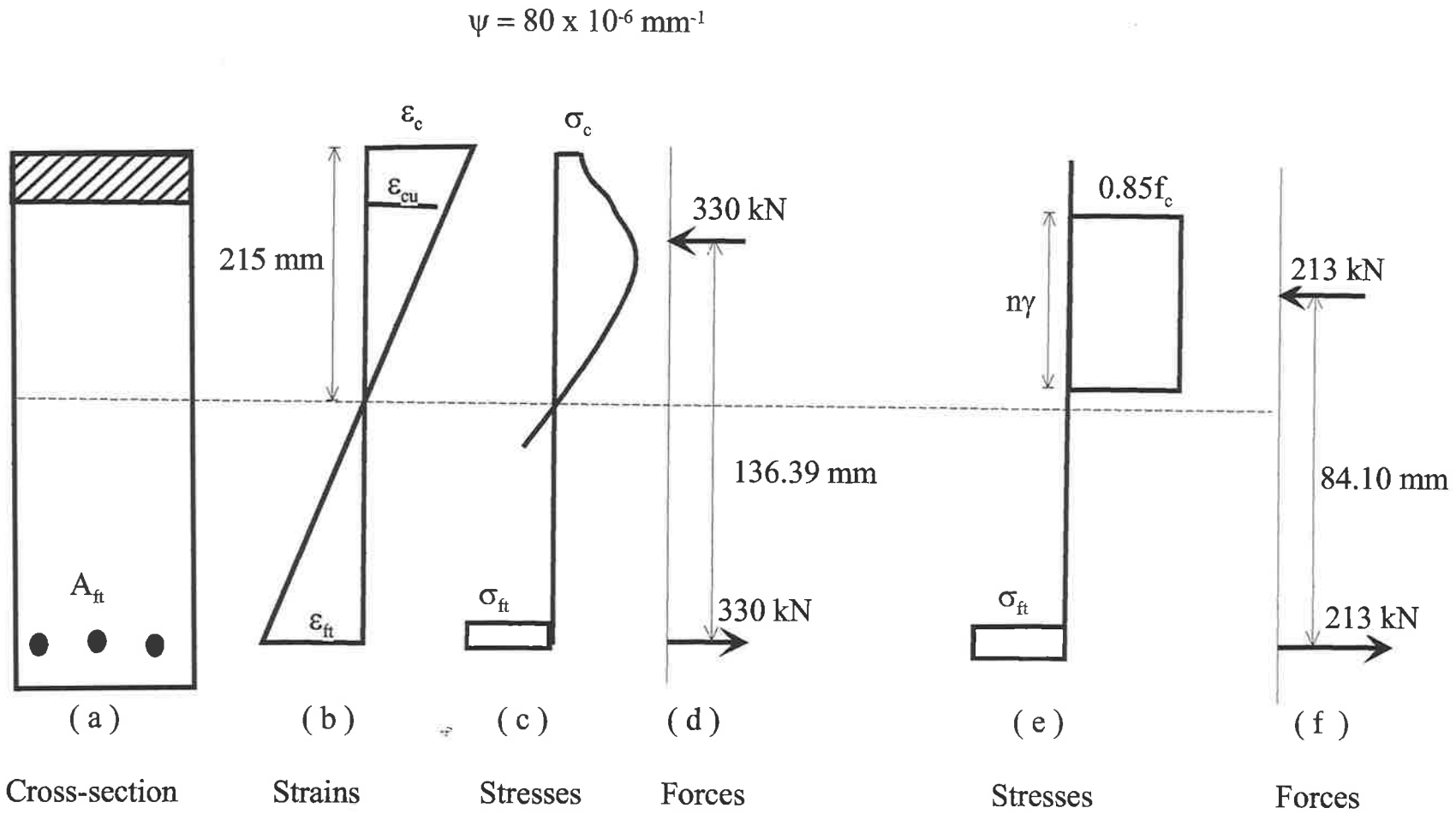

Figure 5.6.-Magnitude and position of the concrete forces.

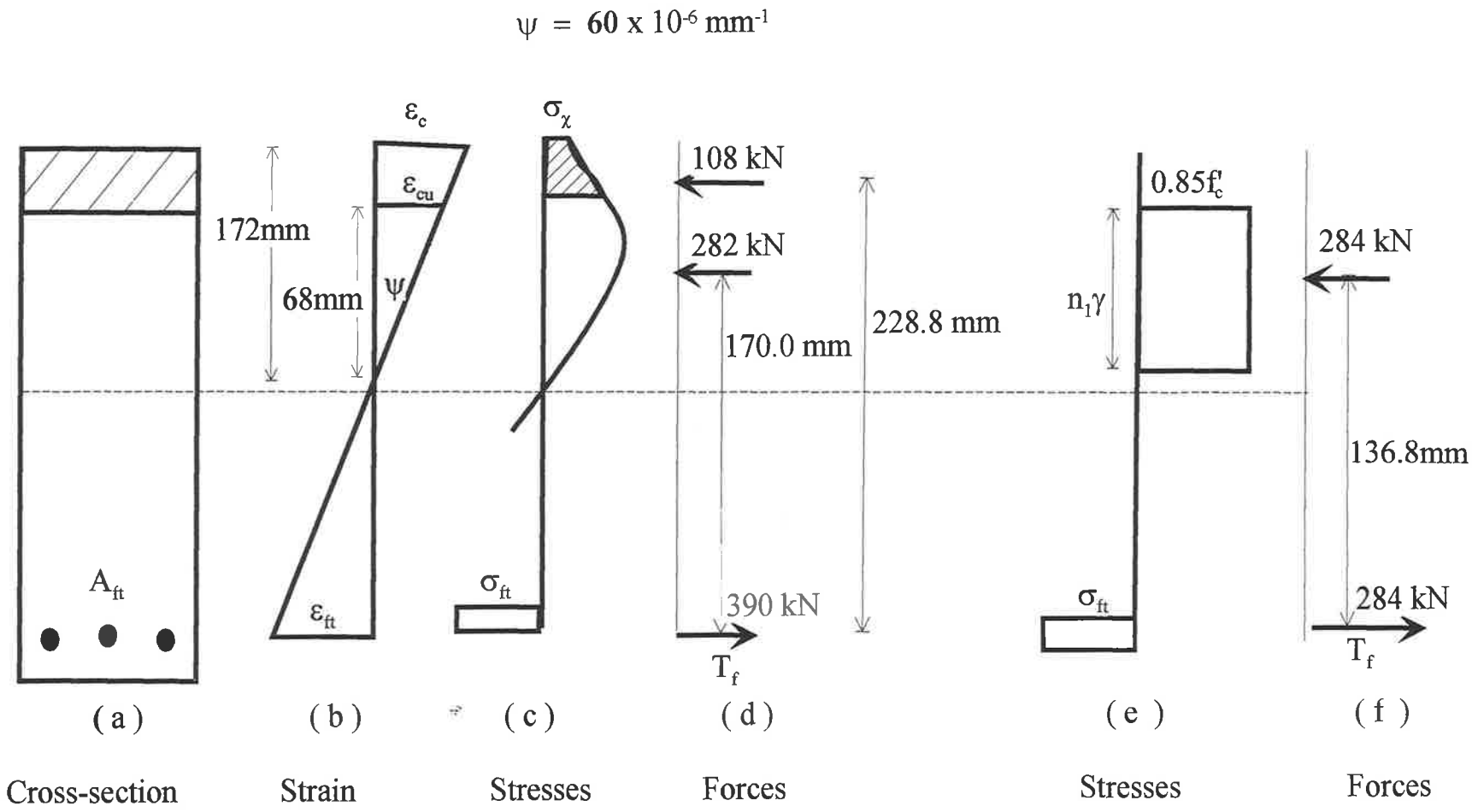

Figure 5.7.- Magnitude and position of the concrete forces.

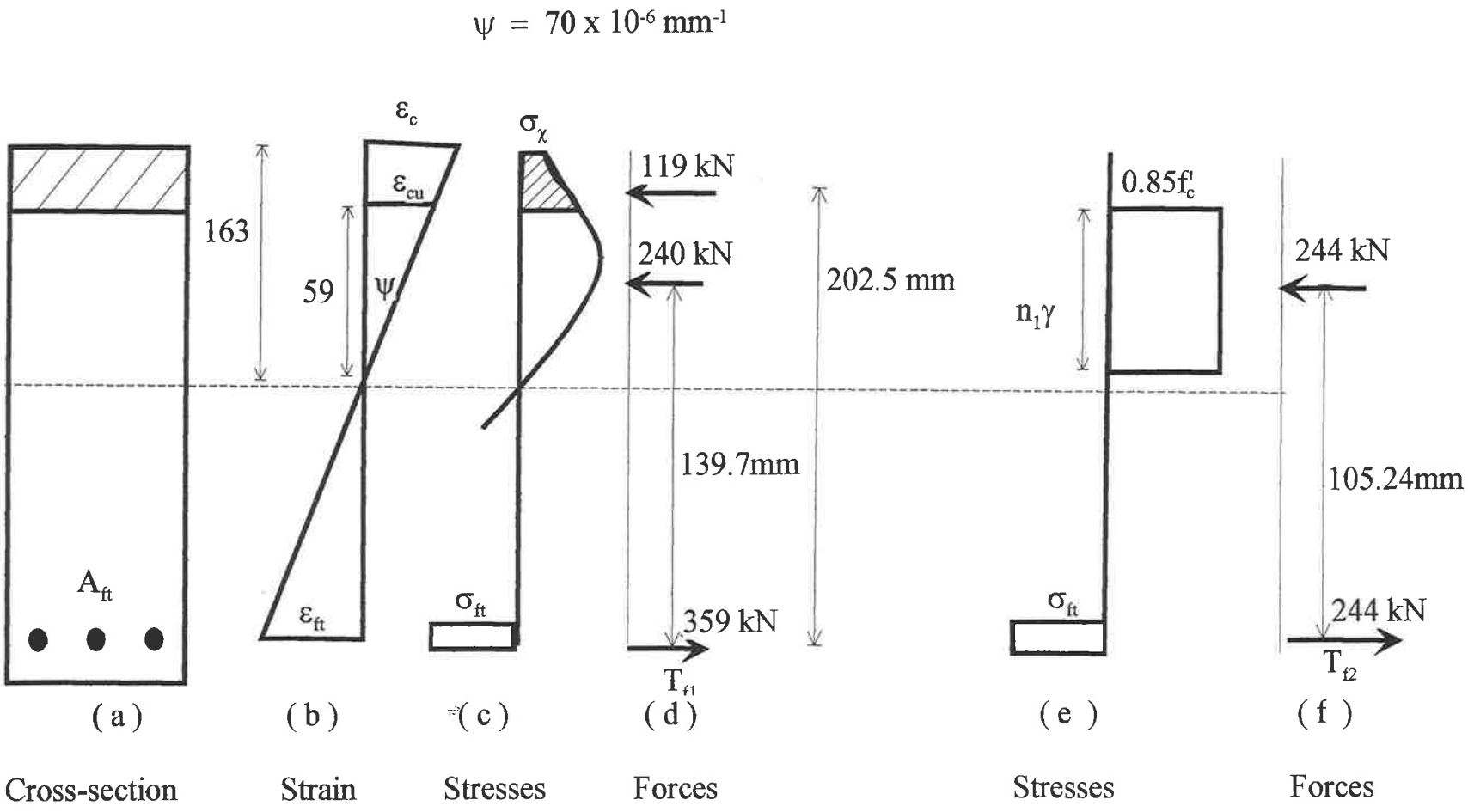

Figure 5.8.- Magnitude and position of the concrete forces.

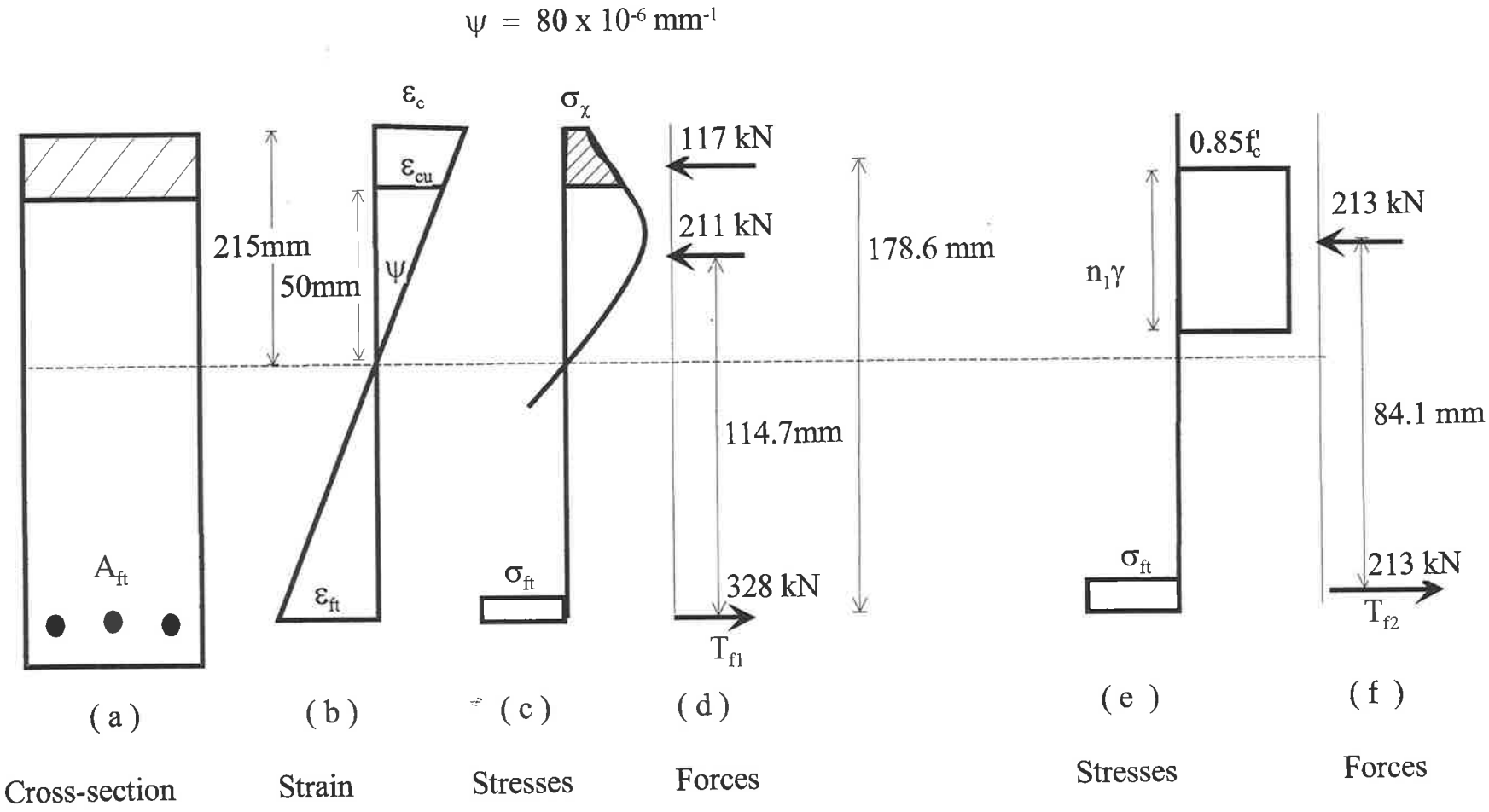

Figure 5.9.- Magnitude and position of the concrete forces.

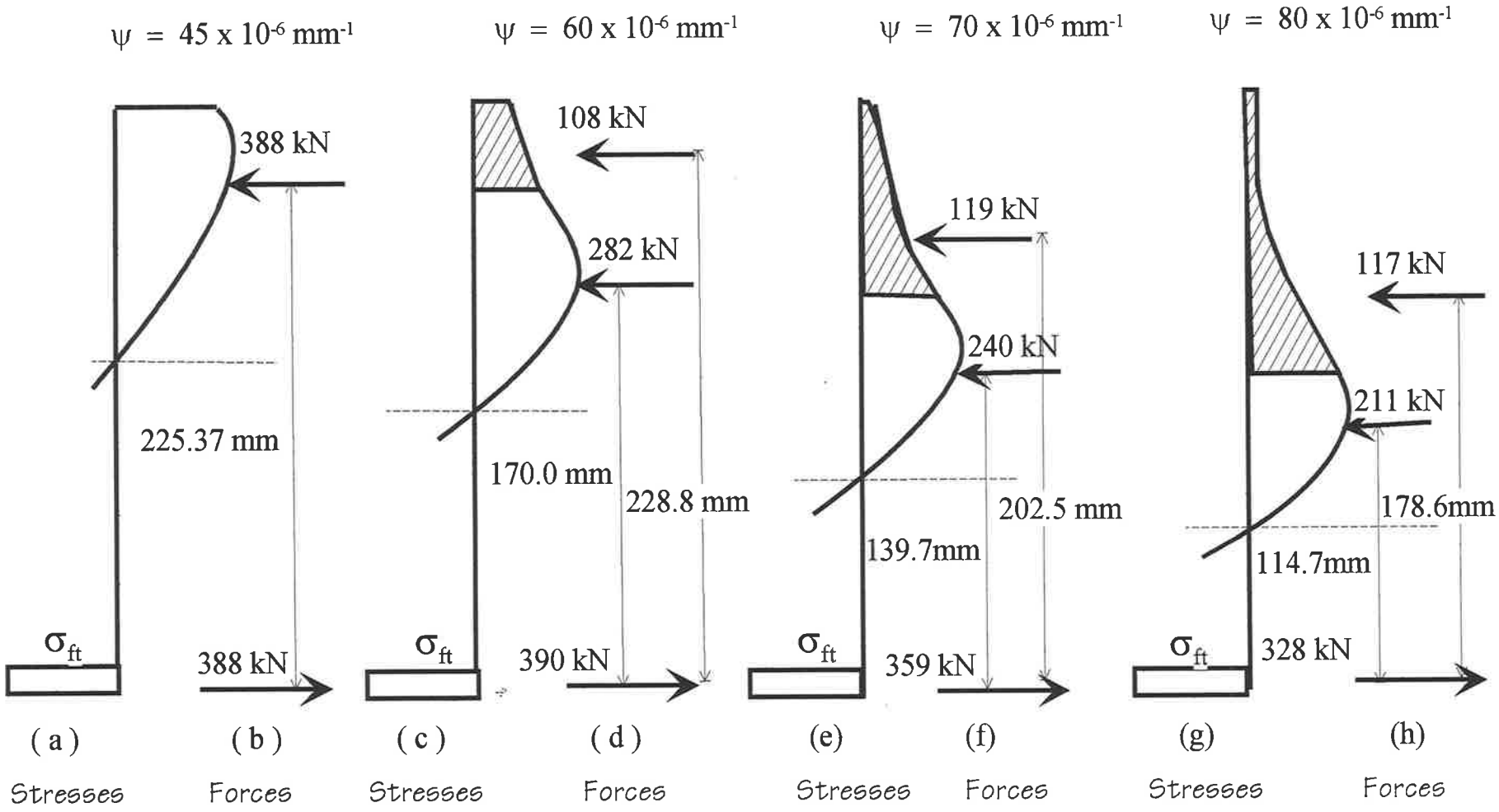

Figure 5.10.- Concrete stress distributions and forces using the segmental analysis method.

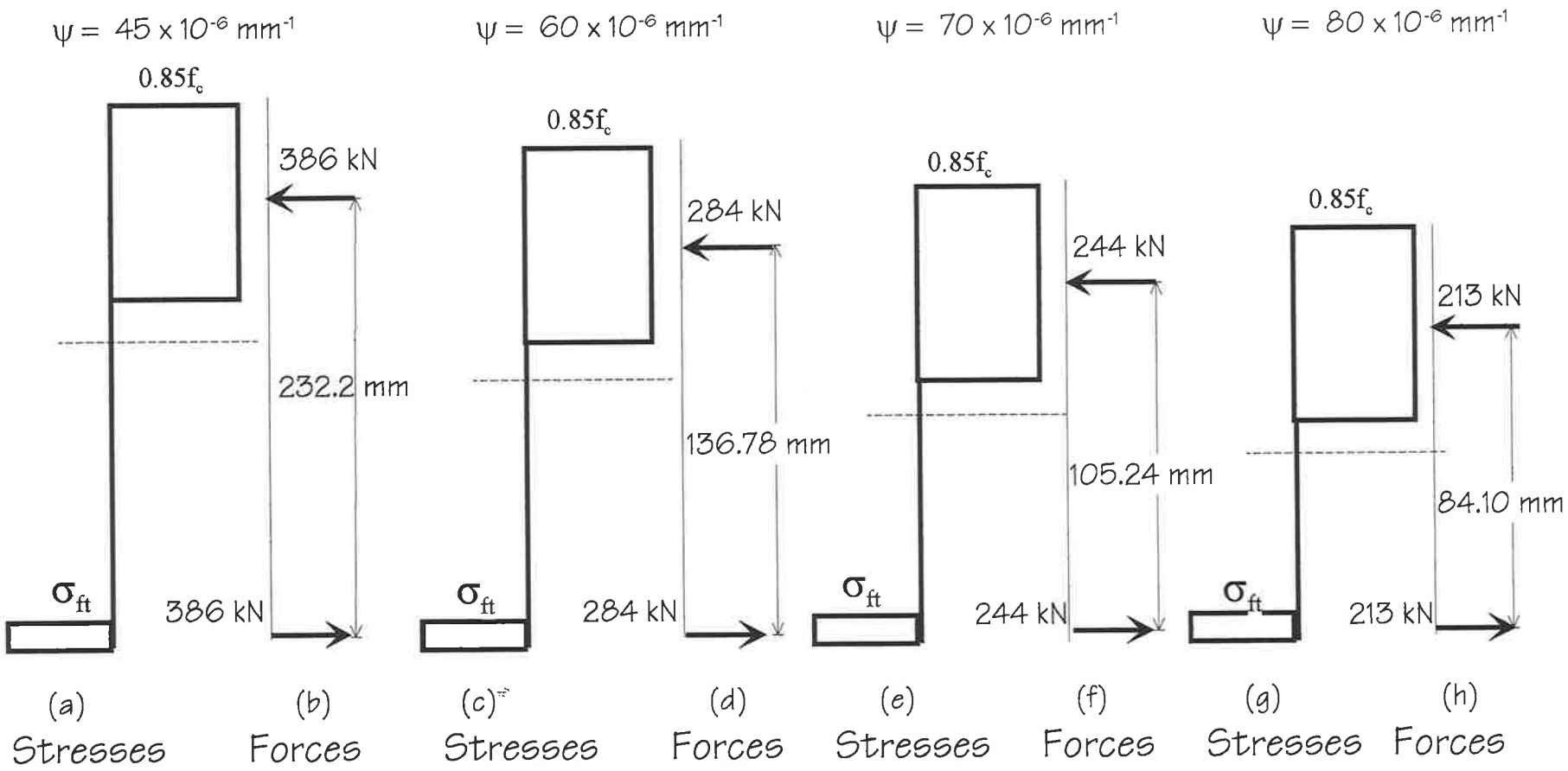

Figure 5.11.- Magnitude and position of the concrete forces using the rectangular block of stresses analysis method.

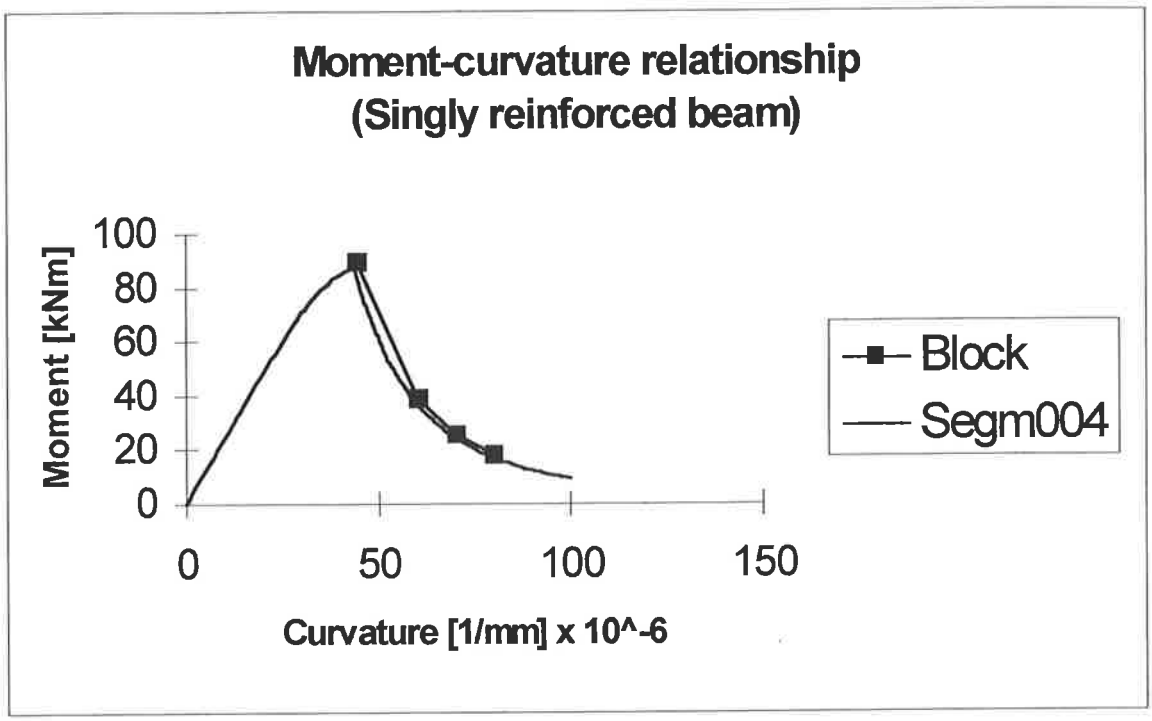

Figure 5.12. – Moment-curvature relationship of a singly reinforced concrete beam.

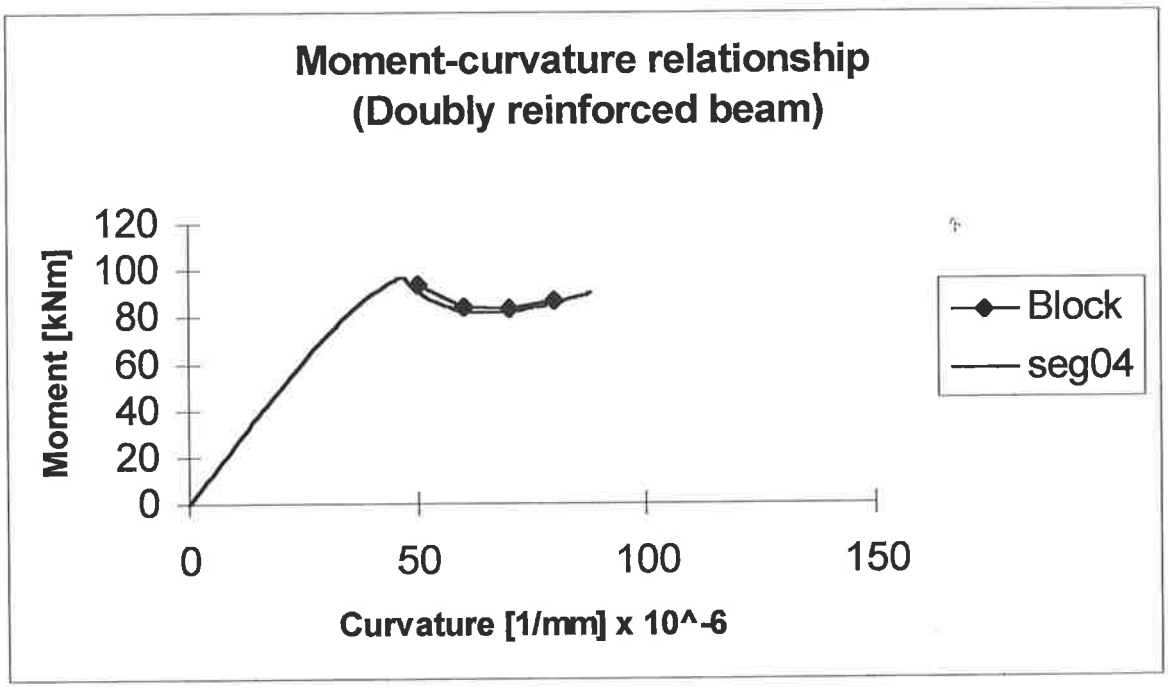

Figure 5.13. – Moment-curvature relationship of a doubly reinforced concrete beam.

Chapter 6

Parametric study

6.1 Introduction

In this chapter are studied the influence exerted by the variations of the main parameters involved in the design of reinforced concrete beams with FRP reinforcing bars. The parameters taken into account are the amount of reinforcement, the strength and Young's modulus in the reinforcing bars, the concrete strength, and the dimensions of the cross-section of the beams. In addition, there are three beams with steel rebars to compare their moment-curvature relationships with the moment-curvature relationships of beams with FRP rebars. For each group of beams there is a figure showing the moment-curvature relationship, where the reader can see easily the flexural behavior of the beams.

6.2 **Properties of the beams.**

Eleven beam specimens have been simulated to analyse the influence exerted by the variation of the main parameters involved in the structural design of the beams. Details of the specimens are in table 6.1 and their cross-sections are in figures from 6.1 to 6.4. Firstly, let us go through table 6.1 to see in detail the properties of the beams. Table 6.1 contains 13 columns, where the first eight columns correspond to the properties of the beams and the rest of the columns correspond to results.

Column 1 shows the identification of the beams from beam1 to beam 11. Column 2 shows the amount of tensile reinforcement A_t in terms of the number of rebars, type of rebars and size of rebars. The type of rebars is described as FRP for fiber reinforced plastic rebars, and Y for steel rebars. The number before the type of rebars describes the amount of rebars, and the number in front describes their size. For instance, $3FRP_{20}$ means 3 FRP rebars of 20-mm diameter which give the amount of tensile reinforcement A_t of beam 1. Column 3 shows the amount of compressive reinforcement A_c of the beams. Column 4 shows the strength σ_{ten} of the tensile reinforcement in MPa, where the subscript 'ten' stands for tensile. Column 5 shows the strength σ_{com} of the compressive reinforcement of the beams in MPa, where the subscript 'com' stands for compressive. Columns 6 and 7 show the Young's moduli E_{ten} and E_{com} of the reinforcing bars in MPa. Column 8 shows the concrete strength in MPa.

a) Description of the beams

Beam 1

Beam 1 has 3 FRP rebars of 20-mm diameter and 624 MPa strength at the bottom only (see table 6.1 and figure 6.1a). The concrete strength is 30 MPa.

Beam 2

Beam 2 has 3 FRP rebars of 20-mm diameter and 624 MPa strength at the bottom, and 1 FRP rebar of 20-mm diameter and 437 MPa strength at the top (see table 6.1 and figure 6.1b). The concrete strength is 30 MPa.

Beam 3

Beam 3 has 3 FRP rebars of 20-mm diameter and 624 MPa strength at the bottom, and 2 FRP rebars of 20-mm diameter and 437 MPa strength (see table 6.1 and figure 6.1c). The concrete strength is 30 MPa.

Beam 4

Beam 4 has 3 FRP rebars of 20-mm diameter and 624 MPa strength at the bottom, and 1 steel rebar of 20-mm diameter and 410 MPa yield strength at the top (see table 6.1 and figure 6.2a). The concrete strength is 30 MPa.

Beam 5

Beam 5 has 3 FRP rebars of 20-mm diameter and 624 MPa strength at the bottom, and 1 FRP rebar of 20-mm diameter and 624 MPa strength at the top (see table 6.1 and figure 6.2b). The concrete strength is 30 MPa.

Beam 6

Beam 6 has 2 steel rebars of 20-mm diameter and 410 yield strength at the bottom only (see table 6.1 and figure 6.2c). The concrete strength is 30 MPa.

Beam 7

Beam 7 has 3 steel rebars of 20-mm diameter and 410 MPa yield strength at the bottom only (see table 6.1 and figure 6.2d). The concrete strength is 30 MPa.

Beam 8

Beam 8 has 3 FRP rebars of 20-mm diameter and 624 MPa strength at the bottom, and 2 FRP rebars of 20-mm diameter and 437 MPa strength at the top (see table 6.1 and figure 6.3a). The concrete strength is 40 MPa.

Beam 9

Beam 9 has 3 FRP rebars of 20-mm diameter and 624 MPa strength at the bottom, and 2 FRP rebars of 20-mm diameter and 437 MPa strength at the top (see table 6.1 and figure 6.3b). The concrete strength is 50 MPa.

Beam 10

Beam 10 has 3 FRP rebars of 20-mm diameter and 624 MPa strength at the bottom, and 2 FRP rebars of 20-mm diameter and 437 MPa strength at the top (see table 6.1 and figure 6.3c). The concrete strength is 60 MPa.

Beam 11

Beam 11 has 3 FRP rebars of 20-mm diameter and 624 MPa strength at the bottom, and 2 FRP rebars of 20-mm diameter and 437 MPa strength at the top (see table 6.1 and figure 6.4). The concrete strength is 30 MPa. The particularity of beam 11 is the width of the cross-section which has been increased to 225 mm.

6.3 Parametric study

The parametric study is based in the moment-curvature relationship of the beams. The moment-curvature relationship of the beams has been calculated using the segmental analysis method described in chapter 3. Table 6.1 shows the results in the columns from 9 to 13. The results are: the moment at concrete crushing (M. c. crushing) in column 9; peak moment in column 10; final moment in column 11; ductility in column 12; and mode of failure in column 13. Abbreviations in column 13 are related to the mode of failure of the beams, for instance: 'c. crush.' means concrete crushing; 'f. c. r.' means fracture of compressive reinforcement; 'both' means that the concrete crushes simultaneously with the fracture of the tensile reinforcement; and the abbreviation 'f. t. r.' means fracture of the tensile reinforcement. In addition, in columns 9, 10 and 11, the internal moment is related to the curvature at which such a moment occurs. For instance, the internal moment of beam 2 as the concrete crushes is 91.9 kNm at the curvature ψ of 45×10^{-6} mm^{-1} (91.9/45); the peak moment of beam 2 is 93.2 kNm at the curvature ψ of 51×10^{-6} mm^{-1} (93.2/51); and the final moment of beam 2 is 80.9 kNm at the curvature ψ of 78×10^{-6} mm^{-1} (80.9/78).

6.3.1 Parametric study of beams by the amount of compressive reinforcement.

Beams 1, 2 and 3 have 3 FRP rebars of 20-mm diameter and 624 MPa strength at the bottom. The difference between them is the reinforcement in the compression zone (see table 6.1 and figure 6.1 for these 3 beams). Figure 6.5 shows the moment-curvature relationship of the three beams. These three beams show the same flexural rigidity given that the tensile reinforcement in the three beams is the same. The crushing of the concrete occurred at the curvature ψ of 45×10^{-6} mm^{-1} with an ultimate strain capacity ε_{cu} of

0.00426 (from the segmental analysis). The difference in the moment-curvature relationship is most of all in the falling branch. The falling branch of beam 1 is steeply down because of the concrete crushing; therefore, no plateau is present in beam 1, which is an indication of the brittle failure of the beam. The falling branch of beam 2 is less steep than beam 1, which is an indication that the compressive reinforcement takes over from the crushed concrete prolonging the serviceability of the beam. A short plateau is described in the curve of beam 2, from the point of concrete crushing to the fracture of the compressive reinforcement, which means that some degree of ductility is present. Beam 3 presents a better structural alternative because its plateau is longer than the plateau of beam 2. The plateau of beam 3 goes from the point where the concrete crushes to the point where the compressive reinforcement breaks. Looking at figure 6.5, it can be seen that compressive reinforcement in RC beams with FRP rebars plays a very important roll in providing ductile behaviour to the beam.

6.3.2 Parametric study of concrete beams by Type, strength and Young's modulus of compressive reinforcement

Beams 2, 4 and 5 have a similar reinforcement at the bottom; their differences are in the compressive reinforcement with regard to type, strength and Young's modulus (see table 6.1 and figures 6.1b, 6.2a and 6.2b for details). The three beams have one rebar only at the top of different types, strengths and Young's moduli. Figure 6.6 shows the moment-curvature relationship of beams 2, 4 and 5. Beam 2 has 1 FRP rebar of 20-mm diameter and 437 MPa strength with a Young's modulus of 37191 MPa. Beam 4 has 1 steel rebar of 20-mm diameter and 410 MPa yield strength with a Young's modulus of 200000 MPa.

Beam 5 has 1 FRP rebar of 20-mm diameter and 624 MPa strength with a Young's modulus of 51482 MPa.

Beams 2 and 5 seem quite similar one from each other regarding to their falling branches; however, beam 5 looks more ductile than beam 2 because in addition to the horizontality of its falling branch, the plateau of beam 5 is extended beyond the falling branch of beam 2. The compressive rebar of beam 2 broke earlier than the compressive rebar of beam 5. The failure of both beam 2 and beam 5 is due to fracture of the FRP compressive rebars.

In contrast to beam 2 and beam 5, the compressive steel rebar of beam 4 does not fracture because the steel rebar yields. Therefore, after yielding the steel rebar in the compression zone, it only increases the strength of the beam along of the falling branch following the same trend of the falling branch of beam 1 which has no compressive reinforcement (see figure 3.13).

The falling branch of the moment-curvature relationship of beam 4 shows a steep downward tendency similar to the falling branch of beam 1. The graph stops because the curvature ψ of 100×10^{-6} mm^{-1} is the last one taken into account during the calculation; otherwise, the curve would continue with the internal moment trending to zero as the curvature ψ trends to infinity. Hence, beam 4 does not show any ductile behaviour.

Influence of Young's modulus in the compressive rebars is noticeable with respect to ductility in beams 2, 4 and 5. The three beams have the same amount of reinforcement at the top; however, their mechanical behaviour is different due to the different Young's modulus of the rebars.

6.3.3 Parametric study of concrete beams by type, strength, Young's modulus and the amount of tensile reinforcement

A parametric study by type, strength, Young's modulus and amount of tensile reinforcement is carried out for beams 1, 6 and 7. These three beams have no compressive reinforcement at all. The difference between them is in the tensile reinforcement. Beam 6 has two steel rebars of 20-mm diameter and 410 MPa yield strength with a Young's modulus of 200000 MPa; meanwhile beam 7 has three rebars of 20-mm diameter and 410 MPa yield strength with a Young's modulus of 200000 MPa.

The moment-curvature relationships of beams 1, 6 and 7 are in figure 6.7. Notice that the difference is not only in the falling branch but also in the ascending branch of the moment-curvature relationship. The slope of both beam 6 and beam 7 in the ascending branch are greater than the slope of beam 1, due to the higher Young's modulus of the tensile reinforcement of these beams. As the slope of the ascending branch of the moment-curvature relationship determines the flexural stiffness of the beams, then it can be concluded that beam 6 and beam 7 are stiffer than beam 1. On the other hand, the slope of beam 7 is greater than the slope of beam 6. Both beams have tensile rebars of the same Young's modulus but in different amounts. It can be concluded that beam 7 is stiffer than beam 6 because the amount of reinforcement. Therefore, both the amount of tensile reinforcement and the Young's modulus of such reinforcement determines the flexural stiffness of RC beams.

The falling branch of the moment-curvature relationship of beams 1, 6 and 7 are also different. Beam 1 fails because the compressive concrete crushes soon after reaching its ultimate strain capacity ε_{cu} presenting a brittle failure. Beam 6 fails in a very ductile fashion with an extended plateau from the point where the tensile steel bars yield until

the concrete crushes. The plateau of beam 6 starts at the curvature ψ of 16×10^{-6} mm^{-1} ending at the curvature ψ of 80×10^{-6} mm^{1}. In contrast, beam 7 shows a very short plateau which goes from the yield point of the tensile bars until the top concrete crushes. The falling branch of the moment-curvature relationship of beams 6 and 7 is evidence that increasing the amount of tensile reinforcement improves the strength of RC beams in detriment to the ductility of the beams.

6.3.4 **Parametric study of RC beams by the concrete strength.**

Four RC beams with different concrete strengths and similar reinforcement are analysed to verify the influence of concrete strength in their flexural behaviour. The beams analysed are beams 3, 8, 9 and 10. The four beams have two FRP rebars of 20-mm diameter and 437 MPa strength with Young's modulus of 37191 MPa at the top; and 3 FRP rebars of 20-mm diameter and 624 MPa strength with Young's modulus of 51482 MPa at the bottom. The difference between them is the concrete strength. The concrete strength of beam 3 is 30 MPa; beam 8 is 40 MPa; beam 9 is 50 MPa; and beam 10 is 60 MPa. See table 6.1 and figures 6.1c, 6.3a, 6.3b and 6.3c for details of these beams.

Figure 6.8 shows the moment-curvature relationship of beams 3, 8, 9 and 10. Beam 3 in figure 6.8 shows less strength than the other ones but it shows a ductile behavior; the failure of beam 3 is due to fracture of the compressive reinforcement. Beams 8 and 9 failed in a characteristic fashion. The compressive concrete crushed at the same time that the tensile reinforcement fractured. Hence, the failure of these beams occurs in a catastrophic manner. The moment-curvature relationship of beam 10 is almost a straight line. This is because the tensile reinforcement fractures before the compressive concrete

crushes. Figure 6.8 shows that increasing the concrete strength whilst keeping a low strength tensile reinforcement, RC beams become stronger but with a lost of ductility.

6.3.5 Parametric study of RC beams by cross-sections size

A parametric study of two RC beams with different cross-section sizes is carried out to investigate the effects of varying the cross-section's size. Both beams 3 and 11 have at the top, 2 FRP rebars of 20-mm diameter and 437 MPa strength with Young's modulus of 37191 MPa; and at the bottom, 3 FRP rebars of 20-mm diameter and 624 MPa strength with Young's modulus of 51482 MPa. The concrete strength of both beams is 30 MPa. The difference between them is the width of their cross-sections. Beam 3 is 200 mm width and beam 11 is 225 mm width (see table 6.1 and figures 6.1c and 6.4 for details). Figure 6.9 shows the moment-curvature relationships of both beams. Figure 6.9 shows that increasing moderately the width of the cross-section of the beam no significant changes occur in the moment-curvature relationship of the beams. The failure of beams 3 and 11 are due to fracture of the FRP rebars at the top of the beams.

Table 6.1. – Beams properties and results.

Beam specimens (1)	A_t $[mm]^2$ (2)	A_c $[mm]^2$ (3)	σ_{ten} [MPa] (4)	σ_{com} [MPa] (5)	E_{ten} [MPa] (6)	E_{com} [MPa] (7)	f_c [MPa] (8)	M. c. crushing [kNm] (9)	Peak moment [kNm] (10)	Final moment [kNm] (11)	Ductility (12)	Failure mode (13)
Beam 1	$3FRP_{20}$	–	624	–	51482	–	30	87.4/45	87.4/45	—	no	c. crush.
Beam 2	$3FRP_{20}$	$1FRP_{20}$	624	437	51482	37191	30	91.9/45	93.2/51	80.9/78	no	f. c. r.
Beam 3	$3FRP_{20}$	$2FRP_{20}$	624	437	51482	37191	30	96.6/45	110/94	110/94	yes	f. c. r.
Beam 4	$3FRP_{20}$	$1Y_{20}$	624	410*	51482	200000	30	104/45	109/53	—	no	c. crush.
Beam 5	$3FRP_{20}$	$1FRP_{20}$	624	624	51482	51482	30	93.4/45	96.1/52	90.7/92	yes	f. c. r.
Beam 6	$2Y_{20}$	–	410*	–	200000	–	30	59.6/12	62.7/40	48.8/100	yes	c. crush.
Beam 7	$3Y_{20}$	–	410*	–	200000	–	30	86.6/13	89.8/27	33.6/71	no	c. crush.
Beam 8	$3FRP_{20}$	$2FRP_{20}$	624	437	51482	37191	40	131/69	131/69	131/69	no	both
Beam 9	$3FRP_{20}$	$2FRP_{20}$	624	437	51482	37191	50	130/68	130/69	130/69	no	both
Beam 10	$3FRP_{20}$	$2FRP_{20}$	624	437	51482	37191	60	—	141/60	141/60	no	f. t. r.
Beam 11	$3FRP_{20}$	$2FRP_{20}$	624	437	51482	37191	30	100/45	114/98	114/98	yes	f. c. r.

* **Yield strength of the steel rebars.**

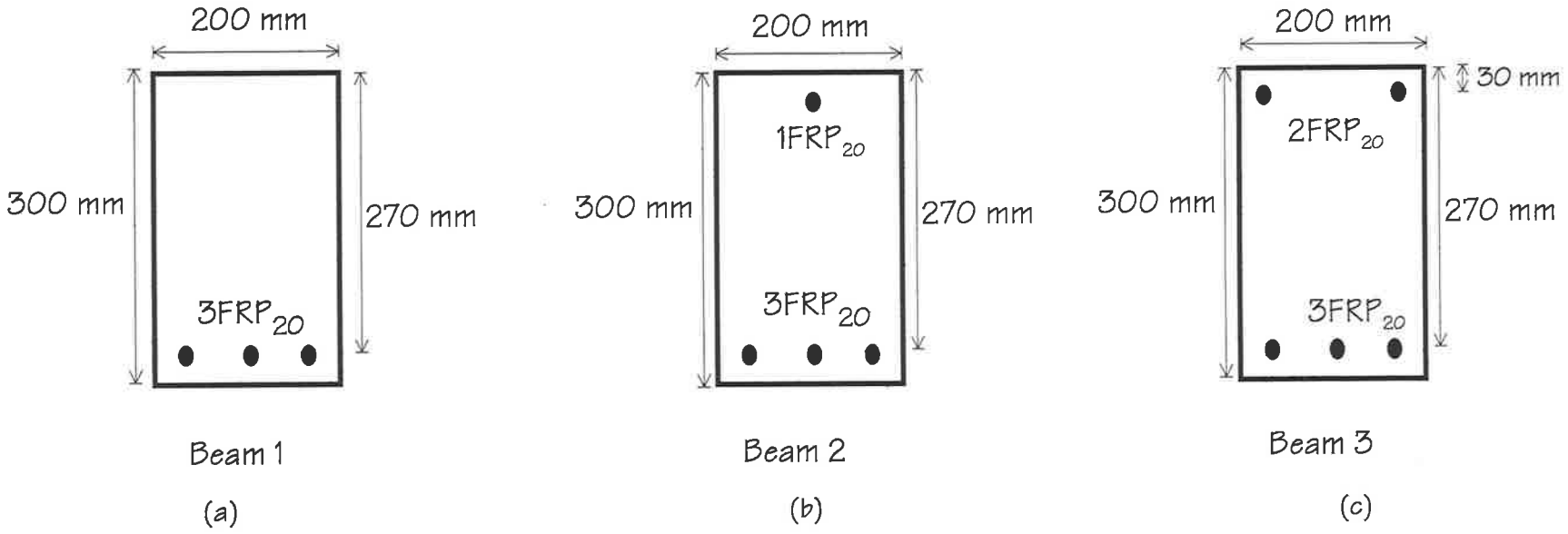

Figure 6.1.- Cross-sections of beams

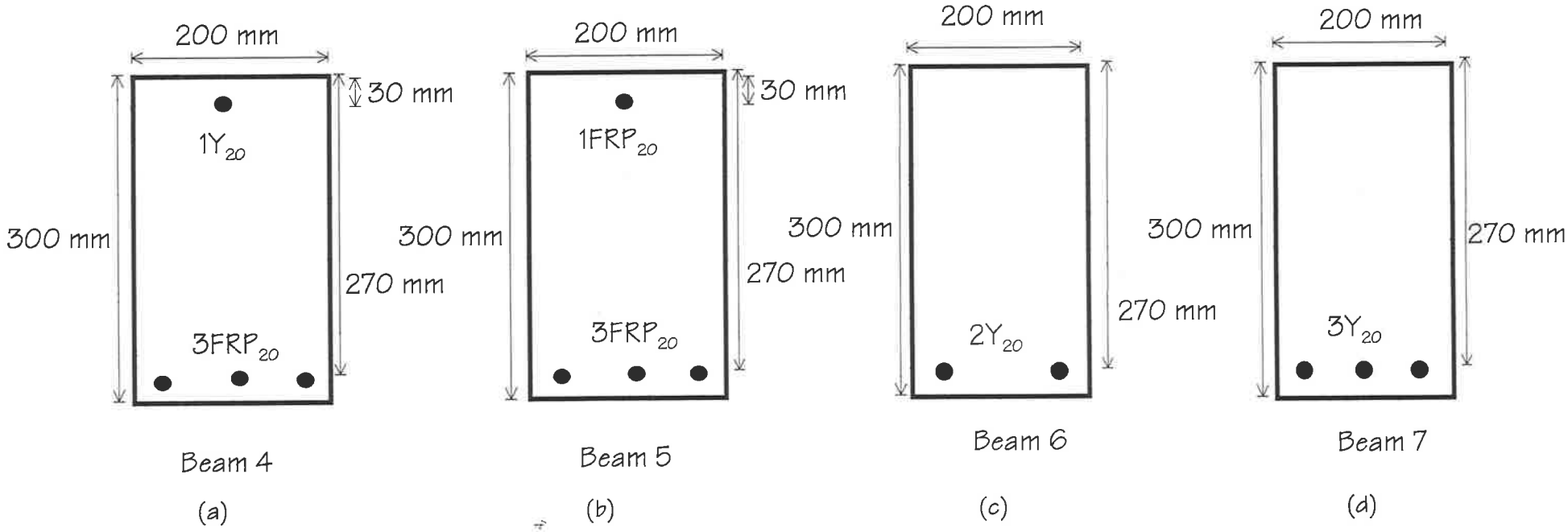

Figure 6.2.- Cross-sections of beams.

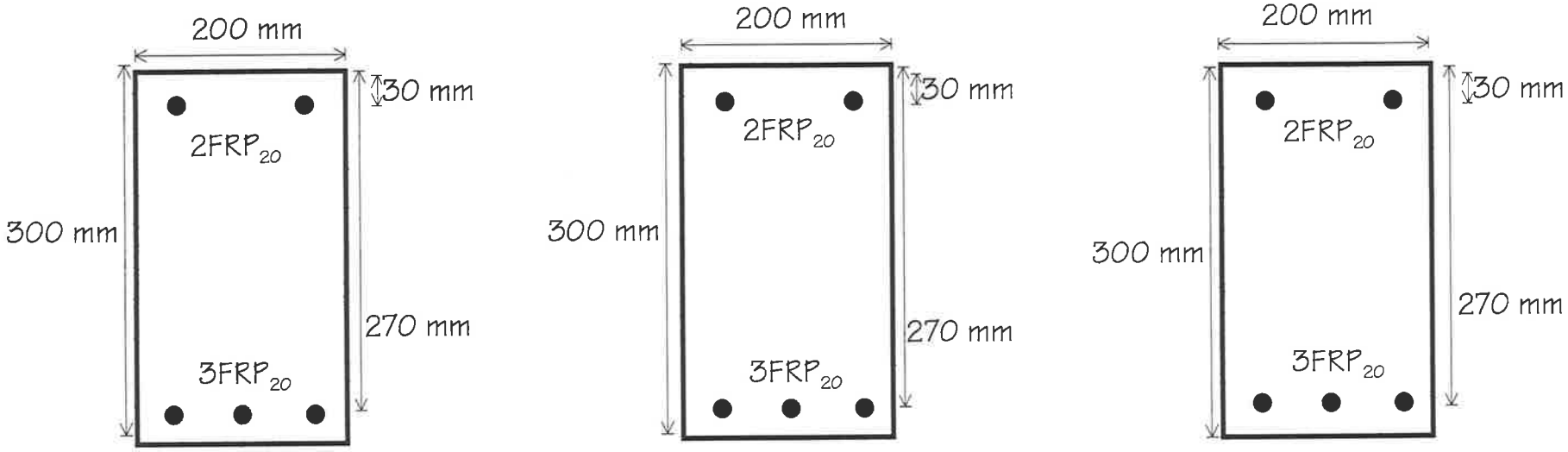

Figure 6.3. - Cross-sections of beams.

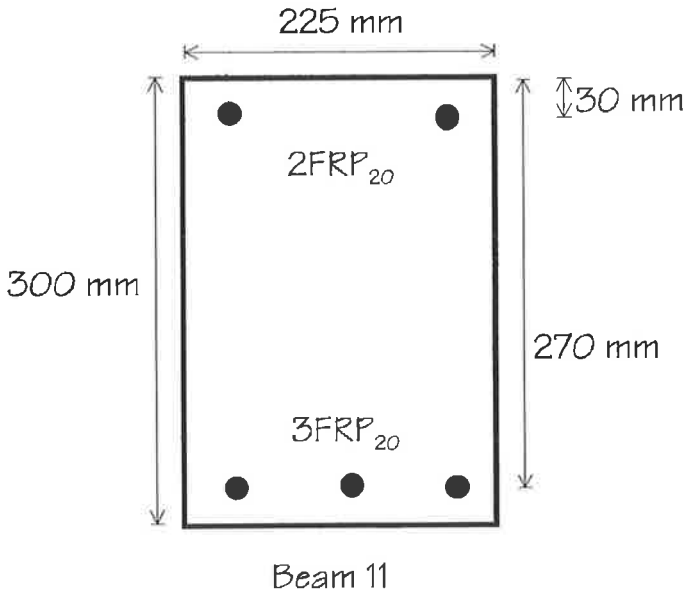

Figure 6.4. – Cross-section of beam 11.

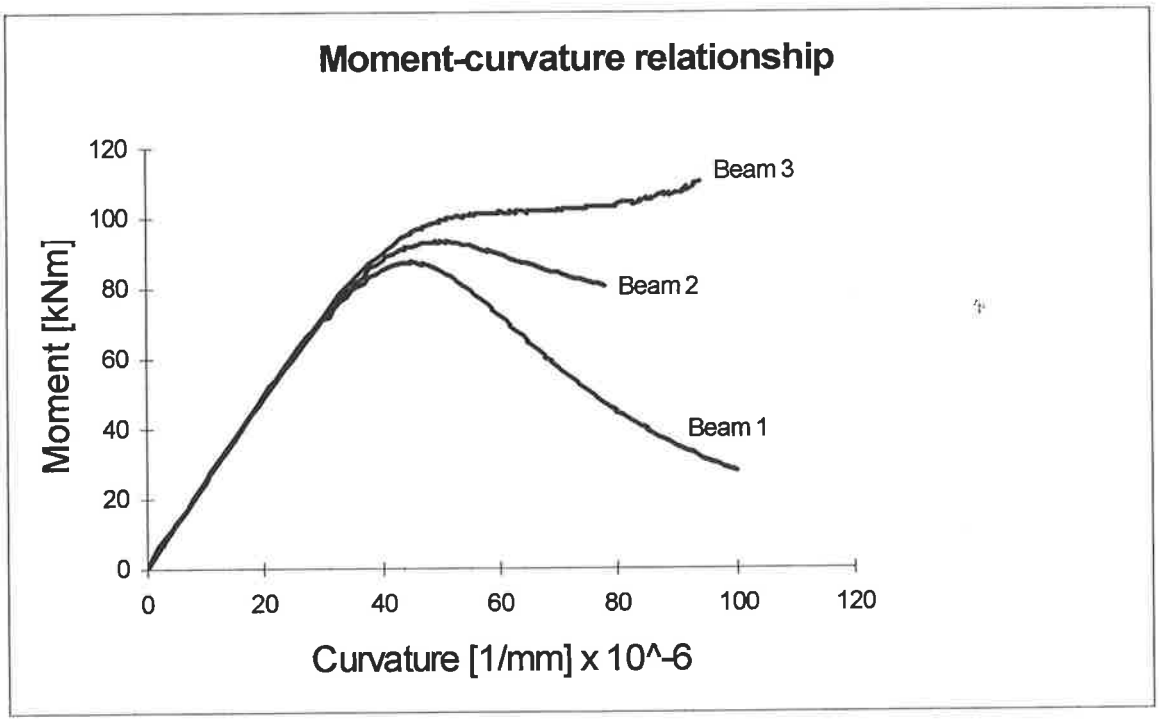

Figure 6.5. – Moment-curvature relationship of beams 1, 2 and 3.

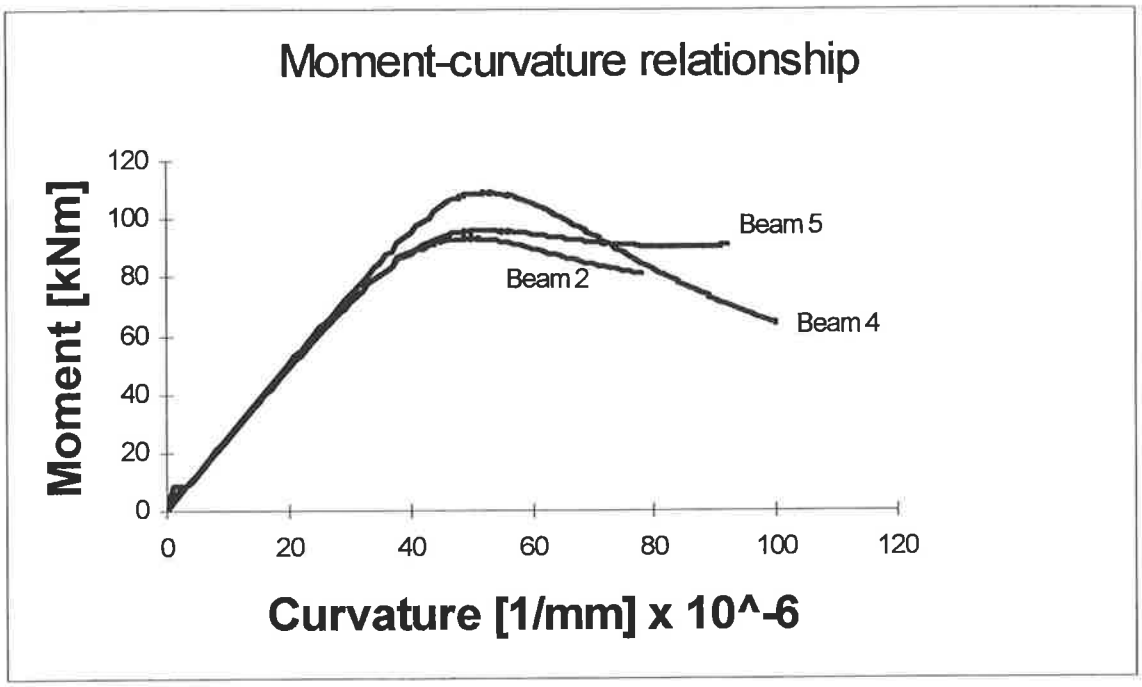

Figure 6.6. – Moment-curvature relationship of beams 2, 4 and 5.

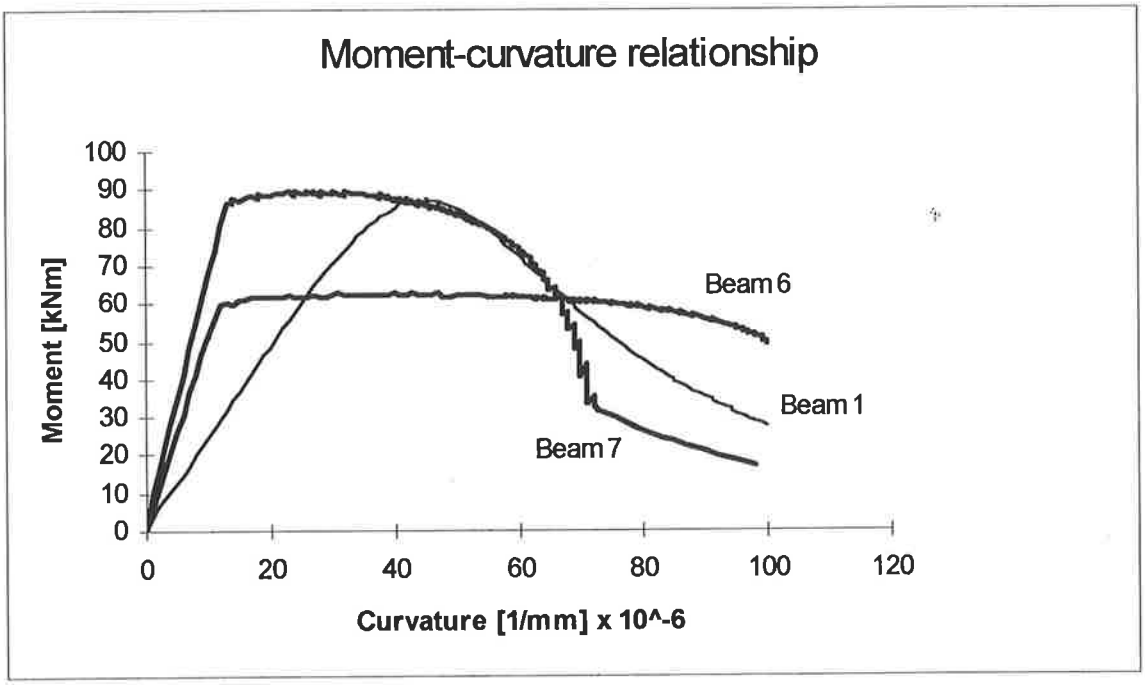

Figure 6.7. – Moment-curvature relationship of beams 1, 6 and 7.

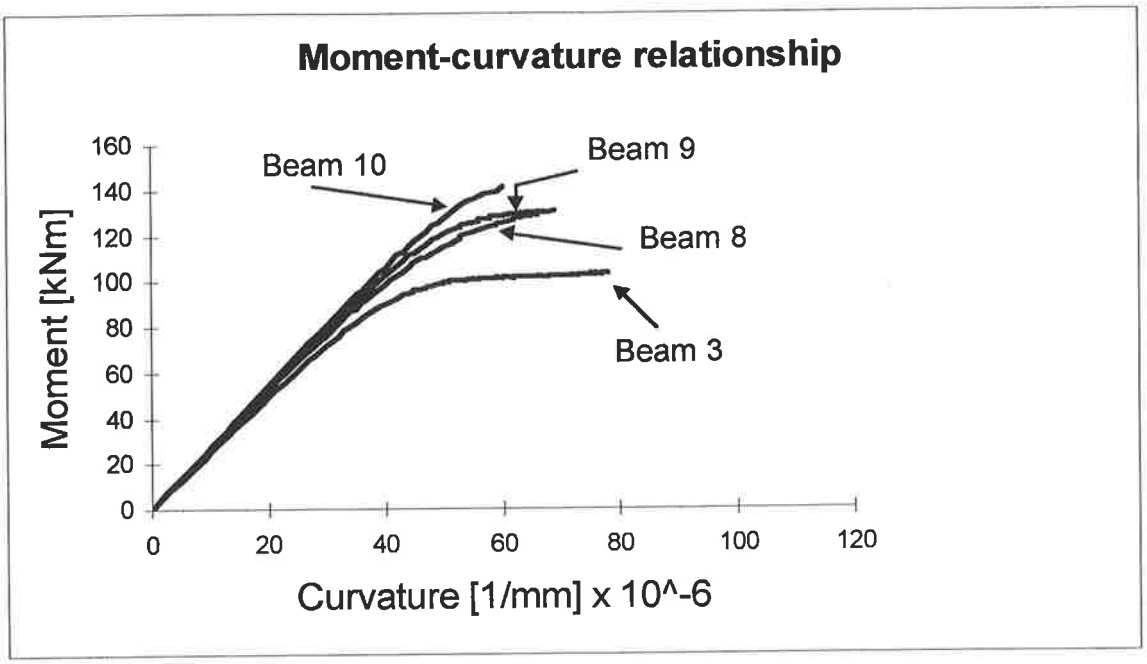

Figure 6.8. – Moment-curvature relationship of beams with different concrete strength.

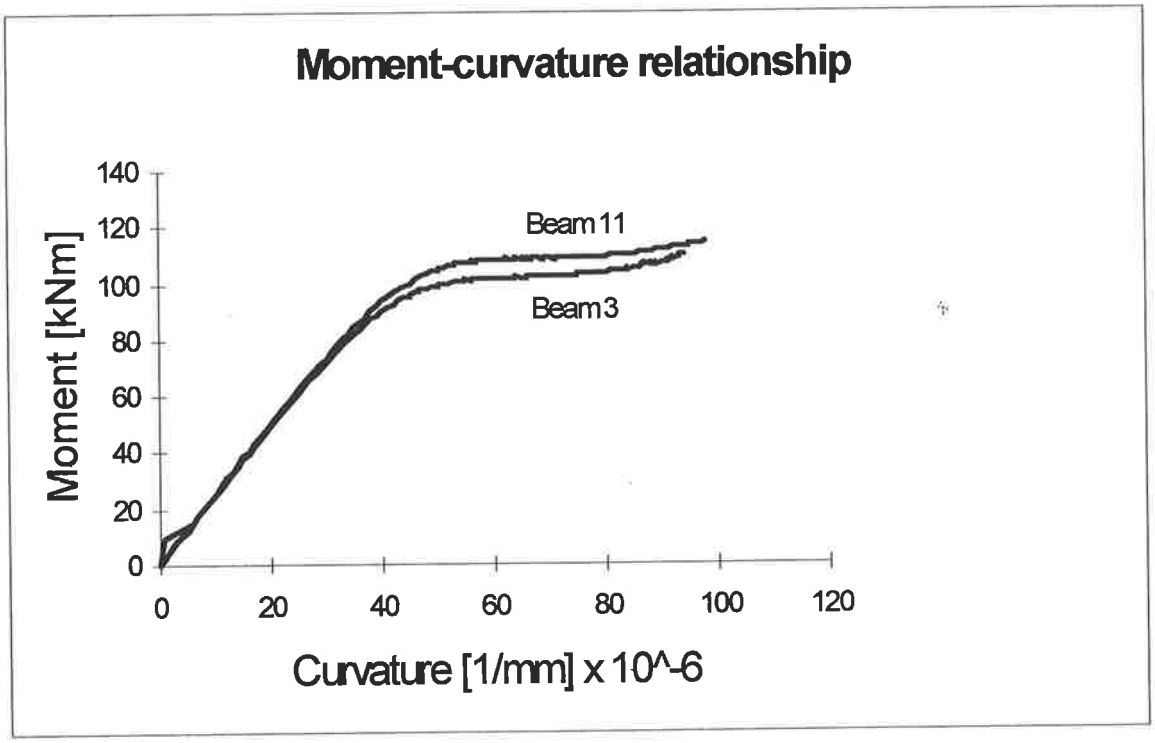

Figure 6.9. – Moment-curvature relationship of beams with different cross-sections.

Chapter 7

Design and manufacture of the beam specimens

7.1 Introduction

The discussion in this chapter is about the design and manufacture of the beam specimens. In doing so, a comprehensive description of the materials properties used in the design and manufacture of the beams is given. Five beams of 5000 mm long have been designed using different combinations of reinforcement. The combination is in regard to type, strength and elasticity modulus of the reinforcing bars, as well as the amount of reinforcement. The dimensions of the cross-sections of the specimens are shown in figure 7.1

and the distribution of shear reinforcement is described in figure 7.2. The aim is to compare the results obtained through the computer simulations using the segmental analysis method, the results obtained using the rectangular block of stresses analysis, and the results obtained through these laboratory tests.

7.2 **Materials properties**

The beam specimens were designed and manufactured using concrete strength of 30 MPa and reinforced with FRP rebars. One beam was designed and manufactured with one steel rebar at the top and 3 FRP rebars at the bottom. The steel rebars are assumed to be 410 MPa yield strength and a Young's modulus of 200000 MPa. The FRP rebars are assumed to be of two kinds; one of them is 624 MPa strength and a Young's modulus of 51482 MPa; and the another one is 437 MPa strength and a Young's modulus of 37191 MPa. The reinforcing bars, either steel or FRP, are all ribbed bars of 20-mm diameter.

7.3 Design of the beam specimens

The beam specimens were designed using the segmental analysis method described in chapter 3. Meanwhile, the cross-sections of the beams were chosen from chapter 3 and chapter 6. The parameters taken into account in the design of the beam specimens were, most importantly, those parameters that affected the ductile behavior of the beams. For instance, the amount of compressive reinforcement, the amount of tensile reinforcement, and the strength and Young's modulus in the reinforcing bars. Beams 1, 2 and 3 represent a good set of beams to determine the effects on the ductility of the beams of varying the amount of

FRP compressive reinforcement (see figure 6.5). Beam 2 and beam 4 were chosen to determine the effects on the ductility of either steel or FRP rebars in the compression zone (see figure 6.6). Beam 2 and beam 5 were chosen to determine the effects on the ductility of changing the amount of tensile reinforcement (see figure 3.14). In summary, beams 1, 2, 3, 4 and 5 are representative of the more significant combinations of reinforcement to be considered in the design of the beam specimens.

Table 7.1 shows the properties of the specimens. Column 1 in table 7.1 describes the identification of the specimens. Column 2 in table 7.1 describes the amount A_c of compressive reinforcement, where FRP and Y indicate the type of reinforcement; FRP stands for 'fiber reinforced plastic' and Y stands for steel. The number behind of the type of reinforcement describes the number of rebars and the number in front describes the size of the rebar. For instance, $2FRP_{20}$ means 2 FRP reinforcing bars of 20-mm diameter. Column 3 in table 7.1 describes the amount of reinforcement at the bottom of the beam. Column 4 describes the strength of the compressive reinforcement where the subscript 'com' means compression. Column 5 describes the strength of the tensile reinforcement, where the subscript 'ten' means tension. Columns 6 and 7 describe the Young's moduli of both the compressive reinforcement and the tensile one. Column 8 describes the concrete strength f_c.

Figure 7.1 shows the cross-sections of the beam specimens. The sections are 200-mm wide and 300-mm high. The covering concrete is 20 mm around the section, therefore, the centroid of the reinforcing bars at the top of the beams is 30 mm down from the top edge of the beams. The effective depth of beams 1 to 4 is 270 mm, and the effective depth of beam 5 is 262 mm. The identification of the reinforcement in the beams is the same as in table 7.1.

Table 7.1. –Properties of the beam specimens.

Beam (1)	A_c (2)	A_t (3)	σ_{com} [MPa] (4)	σ_{ten} [MPa] (5)	E_{com} [MPa] (6)	E_{ten} [MPa] (7)	f_c [MPa] (8)
B1	0	$3FRP_{20}$	–	624	–	51482	30
B2	$1FRP_{20}$	$3FRP_{20}$	437	624	37191	51482	30
B3	$2FRP_{20}$	$3FRP_{20}$	437	624	37191	51482	30
B4	$1Y_{20}$	$3FRP_{20}$	410*	624	200000	51482	30
B5	$1FRP_{20}$	$5FRP_{20}$	624	624	51482	51482	30

* **Yield strength of the steel rebar.**

7.4 Manufacture of the specimens

The manufacture of the beam specimens was carried out in two main steps, which consist of the preparation of the reinforcing cages and then the casting of the concrete.

A concrete strength of 30 MPa was requested for the manufacture of the beam specimens.

Beam 1

Beam 1 is shown in figure 7.3a and has 3 FRP reinforcing bars of 20-mm diameter and 624 MPa strength with a Young's modulus of 51482 MPa at the bottom. In addition, it has two undeformed steel rebars of 10-mm diameter at the top for the purpose of only holding the stirrups in position. The smooth surface of the undeformed bars does not allow bond stress between the bars and the concrete. The reader can see some plastic supports between

the stirrups and the mould, which gives a constant covering of concrete around the reinforcement. Furthermore, the moulds are reinforced with strong pieces of timber to guarantee the prismatic shape of the beams.

Beam 2

Beam 2 is shown in figure 7.3b, and has 3 FRP rebar of 20-mm diameter and 624 MPa strength with a Young's modulus of 51482 MPa at the bottom. In addition, it has one FRP rebar of 20-mm diameter and 437 MPa strength with a Young's modulus of 37191 MPa at the top.

Beam 3

Figure 7.3c shows beam 3, which has 3 FRP reinforcing bars of 20-mm diameter and 624 MPa strength with a Young's modulus of 51482 MPa at the bottom. In addition, it has two FRP rebars of 20-mm diameter and 437 MPa strength with a Young's modulus of 37191 MPa at the top.

Beam 4

Beam 4 is shown in figure 7.4a and has 3 FRP rebars of 20-mm diameter and 624 MPa strength with a Young's modulus of 51482 MPa at the bottom. It has 1 deformed steel rebar of 20-mm diameter and 410 MPa yield strength with a Young's modulus of 200000 MPa at the top.

Beam 5

Beam 5 is shown in the figure 7.4b, and has 5 FRP rebars of 20-mm diameter and 624 MPa strength with a Young's modulus of 51482 MPa at the bottom. At the top, it has one FRP rebar of 20-mm diameter and 624 MPa strength with a Young's modulus of 51482 MPa. The mechanical properties of the FRP reinforcing bars at the top and at the bottom of the beam are the same.

Figure 7.5 shows an aerial view of beam 2 to illustrate the layout of the reinforcing bars and the uniform distribution of the stirrups along the beams. The cage reinforcement of the set of beam specimens can be seen in figure 7.6. The beams were cast with a requested concrete strength of 30 MPa. Cylinders and unreinforced concrete beams were also made to determine strength, elasticity modulus and flexural tensile strength of the concrete.

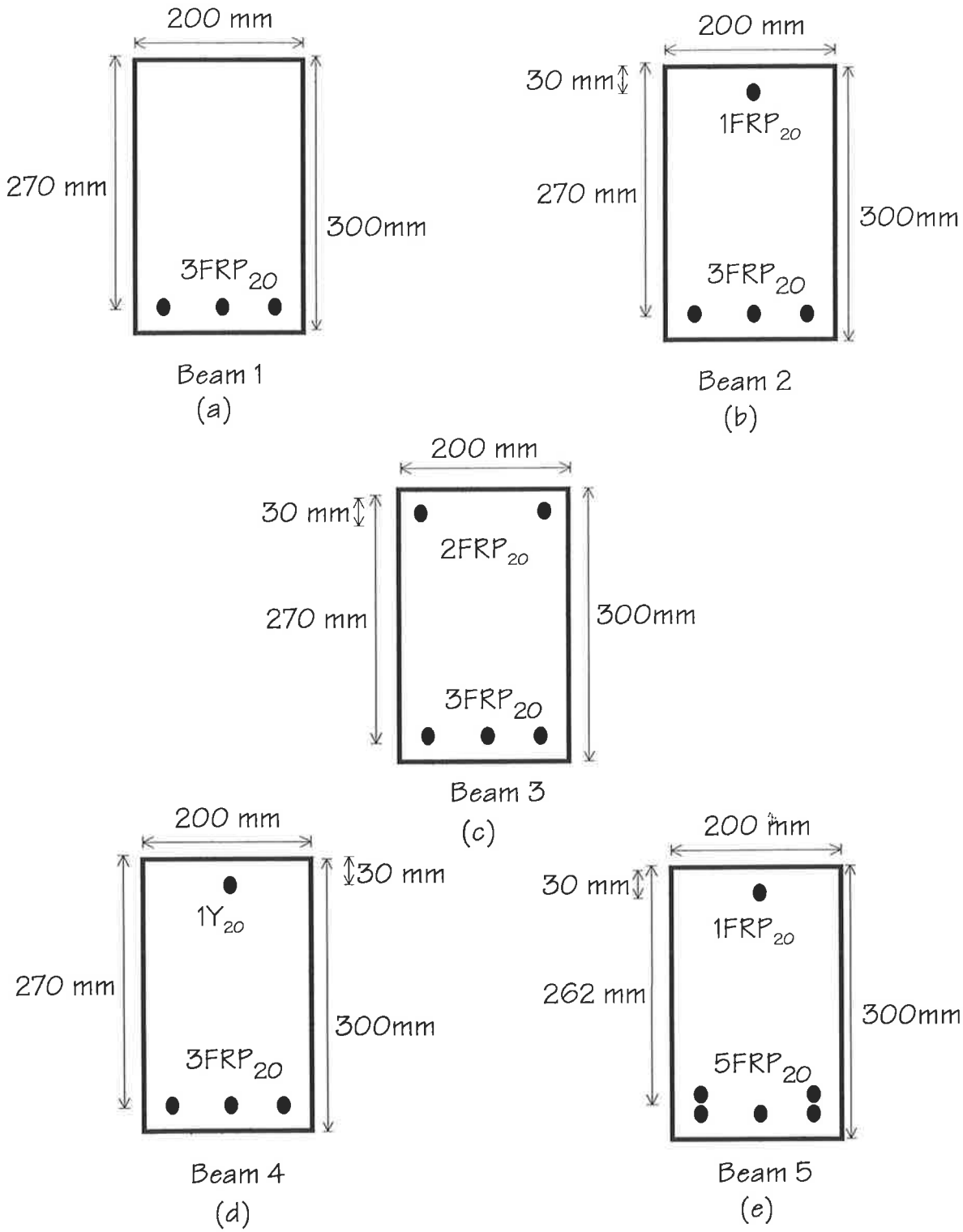

Figure 7.1.- Cross-sections of the beam specimens.

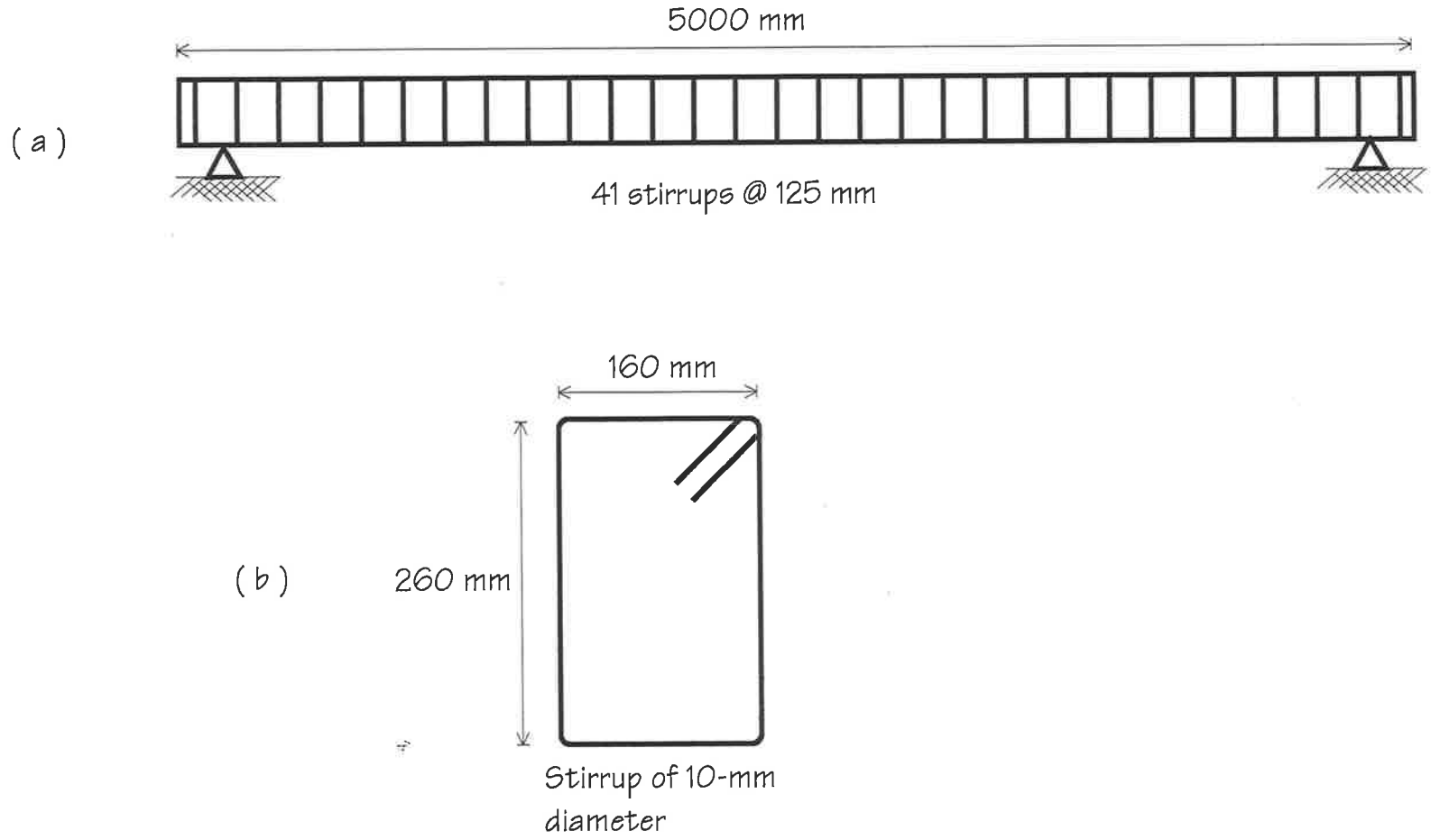

Figure 7.2.- Shear reinforcement.

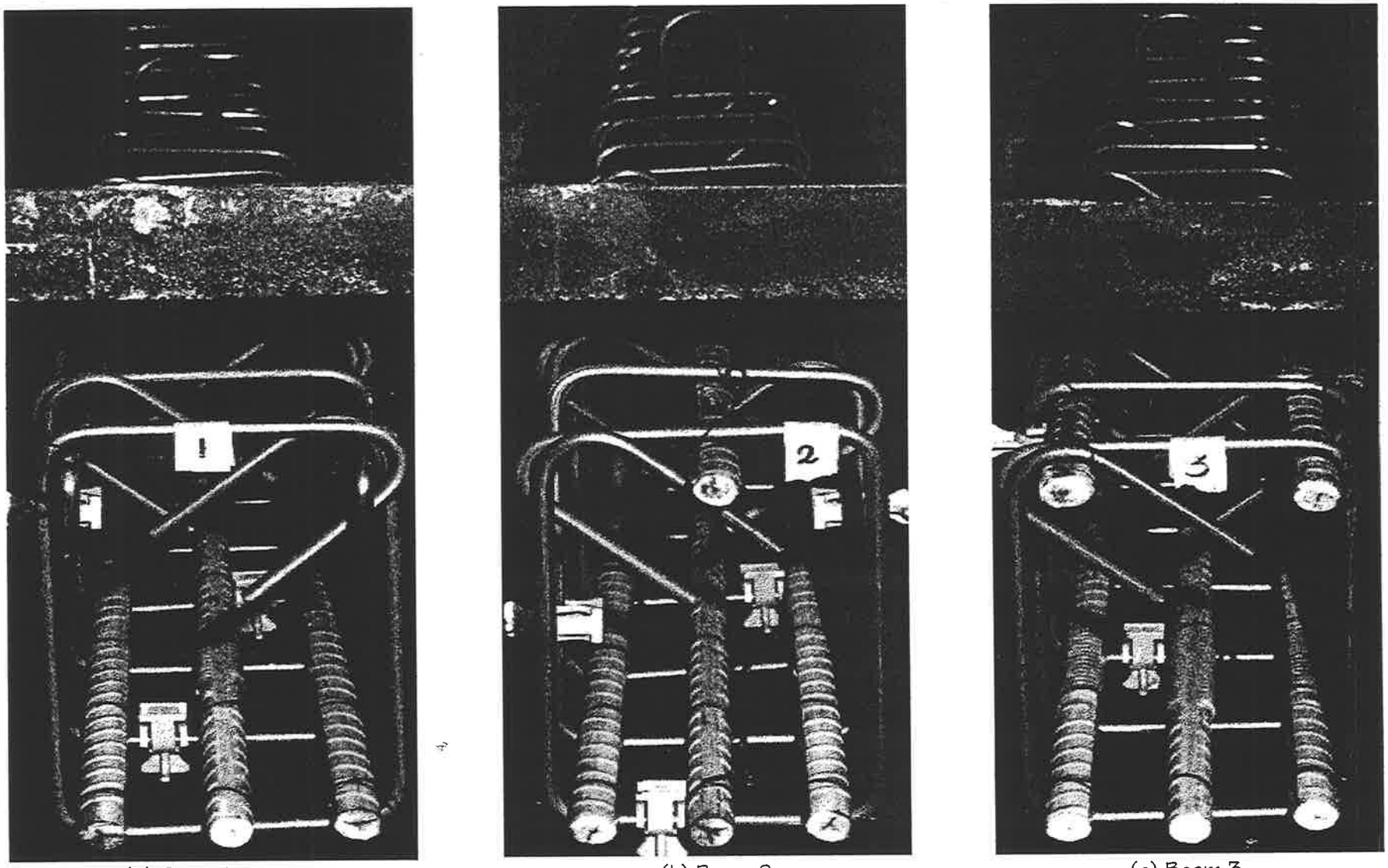

(a) Beam 1 (b) Beam 2 (c) Beam 3

Figure 7.3. – Reinforcement cages of beam specimens.

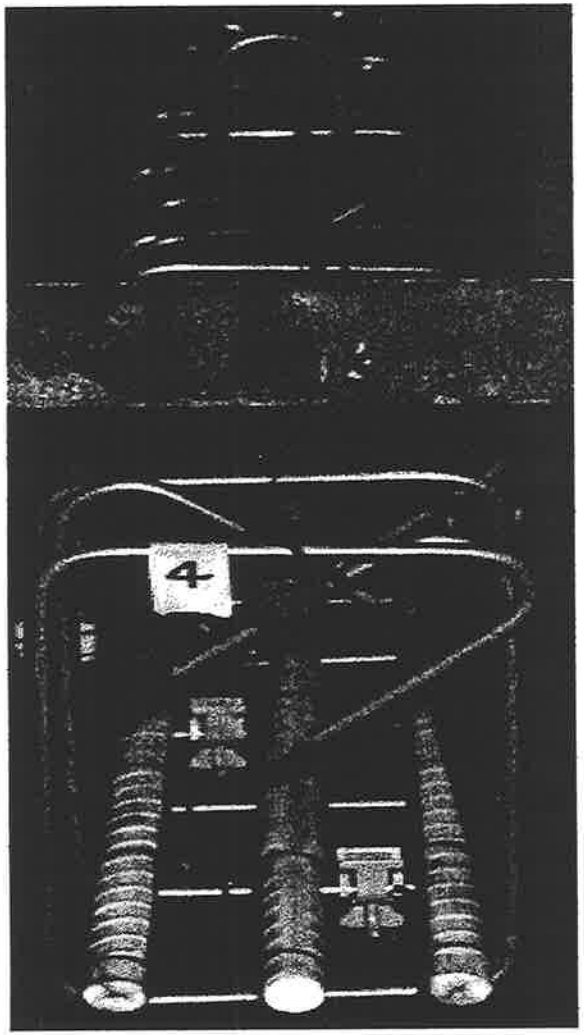

(a) Beam 4

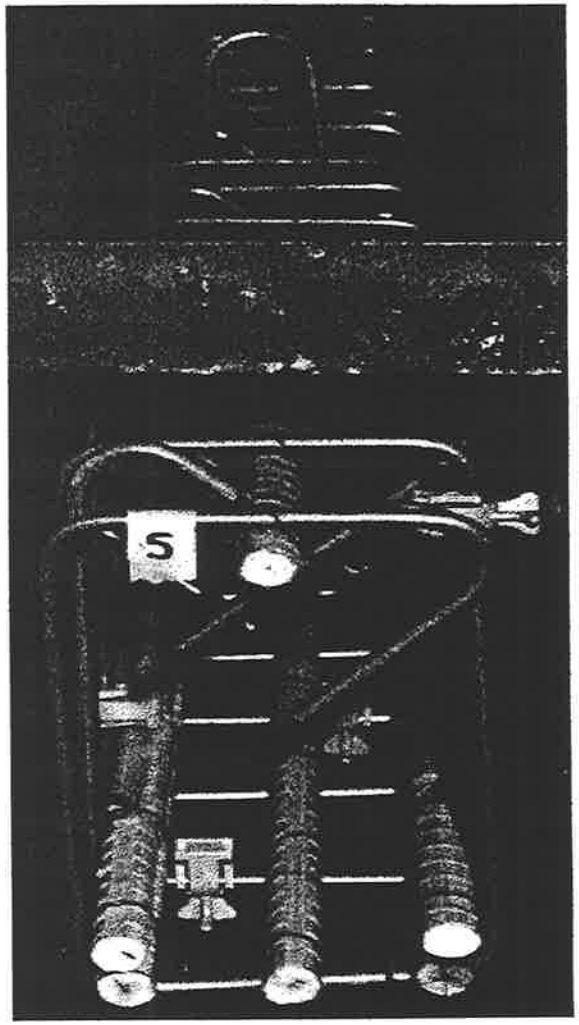

(b) Beam 5

Figure 7.4. – Reinforcement cage of beam specimens.

Figure 7.5. – Aerial view of the reinforcement cage of beam 2.

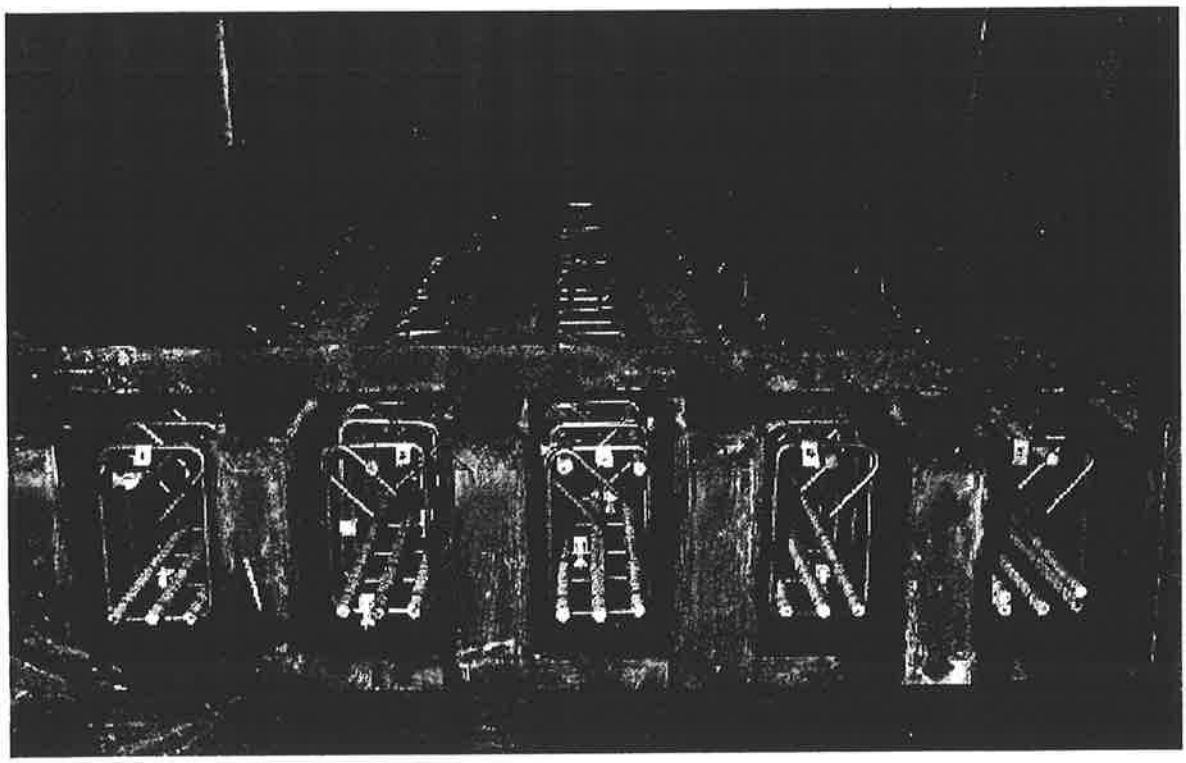

Figure 7.6. – Reinforcement cage of the 5 beam specimens.

Chapter 8

Test rig, instrumentation, test results and processed data

8.1 Introduction.

The first step in this chapter is to describe the equipment and instrumentation used for the testing of the beams as well as the schematic representation of the procedure of the test program. Photographs and drawings are used to illustrate the test rig and instrumentation. For each beam, the test procedure is described in a step by step basis and illustrated with photographs. Through photographs, it is easy to follow the progressive cracking of the beams, as the load is incremented. In addition, the mode of failure of not

only the concrete but also the reinforcing bars is seen clearly through photographs. The processed data for each beam is presented in tables and graphs. Finally, is given the test program for the materials involved in the manufacture of the beam specimens such as the concrete, the FRP bars and the steel bars.

8.2 Equipment and instrumentation.

The beams were tested using a rigid steel double frame as shown in figure 8.1, where beam 1 has been set up. A hydraulic jack is attached to the topside of the steel frame, which is used to apply the load over the beam specimens (hereafter the beams). A bearing steel beam (hereafter the bearing beam) is between the hydraulic jack and the specimen.

A manual-operating piston that is connected to the jack, shown on the floor in figure 8.1, is used to gradually apply a displacement on the beam. The loading signal is transmitted to the computer by means of the cable from the lower end of the hydraulic jack. The supports of the beam and the supports of the bearing beam are all on roller bearings. Figure 8.2 shows the way the load has to be applied. Beneath the beam in figure 8.1 is a dial gauge to read and measure the vertical displacement of the midspan of the beam. Also, there is an electronic transducer to automatically record the vertical displacement at the midspan. Figures 8.3 shows the dial gauge and the transducer beneath of the beam.

Figure 8.4 shows the measurement equipment used during the tests of the beams. On the desk at the left, there are several demec measurement gauges in their cases. The measurement gauges are used for the measurement of the displacement between the demecs. Figure 8.5 shows the layout of the demecs at both sides of the beams. The rows of demecs are marked with letters from A to G and the columns of demecs are marked

with numbers from 1 to 7. Figure 8.6 shows the distance between the rows and columns of demecs before loading the beam. The demec measurement gauges have one fixed end and a mobile end with a dial, with division of one 10000^{th} of an inch. In the measurement of the displacements, demec gauges of 8-inch length and 4-inch length are used. The demec gauges of 4-inch length are for the measurement of the displacement of the demecs in rows A and C from column 1 to column 7. Whereas, the gauges of 8-inch length are for the measurement of the displacements between all the demecs in columns 3 and 5. In addition, a digital screen to monitor the jack loading is on the desk in figure 8.4 where can be seen the cable coming from the jack. Behind the digital screen, there is a power source supply. On the desk at the right are the UCAM (Universal Computer Aid Measurement) machine and an IBM computer set.

The UCAM machine processes both the measurement of loading and the vertical displacement through the transducer at the midspan of the beam. The UCAM machine receives the signal of loading from the hydraulic jack and the vertical displacement of the midspan of the beam from the transducer beneath of the beam. The signals are then converted into text and collected into a text file in the computer.

The faces A and B of the beams are painted an off-white colour for monitoring the crack pattern. Demecs are glued to both sides of the beam in a matrix array between the two loading points to measure the horizontal displacement between them when loading the beam and, therefore, to calculate the corresponding strains. Figure 8.6 shows the layout of the demecs on one face of the beam. The columns of demecs are numbered from left to right and the rows are labelled from top to bottom on side A. However, the columns of demecs are numbered from right to left and the rows are labelled from top to bottom on side B. The reason for numbering the columns of demecs in such a way is to

denote them with the same number for both sides of the beam. For instance, column 3 at side A is also column 3 at side B of the beam.

8.3 Test procedure and processed data.

At the beginning of a test, the beam is tested under load control and demec readings are taken after each increment of load as in figure 8.121 where the author is taking demec measurements. However, as the beam reaches the maximum strength foreseen in design, then the beam is tested under displacement control. That is the load is applied up to a particular value of deflection in small amounts.

Furthermore, the test is carried out in two parts. The first part is just loading the beam progressively and then unloading. The first vertical cracks are called primary cracks herein, which appeared when the loading starts, and the cracks coming from the primary cracks are called secondary cracks. Consequently, the cracks coming from the secondary cracks are called tertiary cracks just to facilitate their identification. The second part of the test is reloading the beam from zero again up to the ultimate failure. The first demec reading is taken before loading the beam, which is used as a benchmark for the next measurements.

8.3.1 Beam 1.

Beam 1, which is shown in figures 7.1a and 7.3a and described in sections 7.3 and 7.4 of chapter 7, does not have deformed rebars in the zone of compression but three FRP rebars in the zone of tension only.

8.3.1.1.1 Test procedure.

The test procedure started with the measurement of the initial distance within the demecs at both sides of the beam, which were used as a benchmark to define the displacement of the demecs during loading the beam.

The loading of beam 1 started with 10 kN as can be seen in figure 8.7. Six vertical flexural cracks (primary cracks) appeared within the constant moment region. Figure 8.8 shows side B of the beam with a similar crack pattern for the same load of 10 kN. Figure 8.9 shows the beam at the load of 20 kN, where it can be seen that the cracks propagated to the ends of the beam. The number of cracks within the constant moment region increased from 6 to 8 with the load of 20 kN. At the load of 30 kN, the number of cracks in the constant moment region remained constant increasing only the size of the cracks as can be seen in figure 8.10. Figure 8.11 shows a close-up of the beam under 30 kN of load in which can be seen clearly the verticality of the cracks. Practically, the amount and size of the cracks remained invariable up to the application of 85 kN of load (see figure 8.12). Thereafter, the beam was displaced in increments of 5 mm.

The cracks became larger propagating towards the top of the beam, especially outside the constant moment region. In addition, small non-vertical cracks (secondary cracks) appeared at the lower end of vertical cracks as can be seen in figure 8.12. Notwithstanding, the trend of the primary cracks is still in the vertical direction. The shape of the cracks changed substantially when the beam was loaded with 95 kN, because the upper end of the cracks inclined towards the midspan of the beam, which can be seen in figure 8.13. The inclination of the upper end of the vertical cracks and the appearance of the small non-vertical cracks at the bottom of the beam could be due to the bond between the FRP rebars and the surrounding concrete. Figure 8.14 shows the beam under

103 kN of load. In this figure, it can be seen that the cracks become larger crossing the row D of demecs in the constant moment region.

The beam was loaded up to 117.0 kN during the first part of the test and then it was unloaded (see figure 8.15). Tertiary cracks appeared which can be seen at the right hand side of figure 8.15. No changes were noted of the cracks between column 3 and column 5 of demecs. However, the cracks outside of the loading zone underwent a substantial change becoming inclined towards the midspan of the beam. When the beam was unloaded, cracks marked U appeared at the topside of the beam. Some of the cracks marked U converged with the primary cracks.

The beam was then reloaded from 0 kN at the rate of 10 kN at a time up to 122.1 kN where the beam failed. Figures 8.16, to 8.18 show views of the failure of the beam at 122.1 kN of load. In these figures can be seen the crushing of the concrete at the top of the beam. The failure of the beam was noisy due to debonding of the smooth rebars at the top of the beam. The strength of the beam decreased gradually from 122.1 kN up to failure and the sequence of the ultimate failure can be seen through figures 8.19 to 8.21.

Figure 8.22 shows the debonding effects of the smooth reinforcing bars at the top of the beam. The wedge of concrete at the end of the beam was pushed 60 mm away from the beam. These bars did not undergo any noticeable deformation at the midspan of the beam as can be seen in figures 8.23, 8.26 and 8.28. Therefore, the beam behaved as a singly reinforced beam with no reinforcement at the top, as was foreseen in the original design. Conversely, the FRP rebars at the bottom of the beam underwent deformation such as splitting off the glass fiber of the rebars. Figures 8.23, 8.24, 8.25, 8.27 and 8.28 show several views of the FRP reinforcing bars at the ultimate failure of the beam.

8.3.1.2 Processed data.

In the following section is shown the moment-deflection relationship of beam 1. Also the moment-curvature relationship of the beam and the variation of the crack sizes.

8.3.1.2.1 Moment-deflection relationship.

The moment-deflection relationship has been plotted using the data obtained from the electronic transducer placed beneath of the beam (see figures 8.3). Figure 8.29 shows the moment-deflection relationship of beam 1 in which can be seen three important points marked A, B and C. Point A indicates both the end of the elastic range when the concrete crushes and the peak moment of the beam. Soon after the beam reached its peak moment the strength dropped down suddenly to point B describing a brittle failure. After crushing the concrete the beam did not regained strength collapsing finally at point C of the curve.

8.3.1.2.2 Moment-curvature relationship.

The internal moment M_n of the beam for a particular load P is one half of the load (P/2) times the distance (1.9 m) between the loading point and the support at the end of the beam (see equation 8.1 where the units are kNm). In addition, the internal moment of the beam is constant between the two loading points.

$$M_n = 1.9\ (P/2) \qquad \ldots\ldots 8.1$$

The segment between columns 3 and 5 of the demecs in figures 8.5 and 8.6 is inside the loading points; therefore, the internal moment in such a segment is that within the loading points. The same procedure was used to calculate the internal moment and the

corresponding curvature of the beam for every load. Consequently, we can get the moment-curvature relationship that is in figure 8.30. The moment-curvature relationship is shown up to failure of the concrete.

8.3.1.2.3 Crack sizes.

Figures 8.7 to 8.15 show two vertical cracks only within the columns of demecs 3 and 5. Therefore, to calculate the cracks' size it is only a matter of calculating the displacement between the lower row of demecs for every load. The average size of the cracks is one half of the displacement between such demecs. Figure 8.31 shows the variation of the cracks' size in terms of the applied load over the beam. In figure 8.31, it can be seen that the moment dropped down to zero when the beam was unloaded however, the crack's size did not reduce to zero. This happened due to the bond effect between the FRP rebars and the surrounding concrete.

8.3.2 Beam 2.

Beam 2, which is shown in figures 7.1b and 7.3b and described in sections 7.3 and 7.4 of chapter 7, has 1 FRP rebar at the top and 3 FRP rebars at the bottom.

8.3.2.1 Test procedure.

The test procedure started with the measurement of the initial distance within the demecs at both sides of the beam, which were used as a benchmark to define the displacement of demecs during loading the beam (see figure 8.32). Demec B5 was missing in the side A of the beam.

The loading started with the application of 10 kN on the beam. Figure 8.33 shows the appearance of the first 9 cracks along the beam. Nevertheless, 6 cracks appeared within the loading zone and 2 cracks between the rows 3 and 5 of demecs. One of the cracks between rows 3 and 5 of demecs reached row E of demecs.

The number of cracks in the loading zone increased to 8 with the application of 19.5 kN as in figure 8.34. Also the depth of the cracks increased. There was no significant change in the cracking pattern until the load was increased to 60 kN (see figure 8.35). The cracks reached the ends of the beam and the larger cracks are near to the loading points. The two cracks between the columns 3 and 5 crossed the row D; therefore, the measurement is only for the rows A and C of demecs given that demec B5 is missing.

The beam was unloaded after 60 kN and the concrete cracked at the top edge of the beam (see figure 8.36). The beam recovered its shape almost up to the original position, which in turn means that the beam, with 60 kN of load, was still in the elastic range. The beam was reloaded from 0 kN at the rate of 20 kN at a time and no significant changes were shown until the load of 90 kN. With this load, appeared three sorts of cracks such as primary cracks, secondary cracks and topside cracks in the beam (see figure 8.37).

The topside cracks are vertical, meanwhile, the secondary cracks are non-vertical. In addition, the upper ends of the primary cracks become inclined towards the midspan of the beam which is caused by bond effect between the FRP rebars and the surrounding concrete. No major changes are shown in figure 8.38 at the load of 105 kN. However, at the load of 118.8 kN the concrete at the top of the beam split off (see figure 8.39) and the cracks near the loading points became larger. The number of cracks in the constant moment region remained constant. Demecs measurements could not be continued because of the concrete split off and consequently the demecs in columns 3 where no

longer available. The displacement was applied in increments of 3 mm up to failure of the beam. Figures 8.39 to 8.41 show the progressive failure of the beam up to collapse.

Loose concrete was removed from the beam to investigate the state of the reinforcing bars at failure of the beam, not only at the top but also at the bottom of the beam (see figures 8.41 to 8.45). Looking at figures 8.42 to 8.47, the FRP rebar at the top did not show any damage. This was because the failure of the FRP rebars at top of the beam was due to compressive crushing plus a shear effect caused by the steel stirrups. Figures 8.48 to 8.50 show the damaged FRP rebars after unloading the beam. The treads of the stirrups can be seen on the surface of the FRP rebars after failure in figures 8.48 to 8.50.

The FRP rebars at the bottom of the beam failed in different way from the FRP rebar at the top. The rebars at the bottom of the beam failed due to the splitting off the glass-fibres between them due to the absence of the confining deformations or ribs of the bars. The deformations or ribs of the FRP rebars were made of resin only, which meant that they could not confine the fibers of the bars. Figures 8.51 to 8.53 show the FRP rebars at the bottom of beam after failure. Figure 8.52 shows the FRP rebars at the bottom of the beam where can be seen the failure of all three rebars. Whereas, figure 8.53 shows one FRP rebar at the other side of the beam. Notice in figures 8.52 and 8.53 that no shear effect underwent the rebars at the bottom of the beam despite being in contact with steel stirrups.

8.3.2.2 Processed data.

In the following section is shown the moment-deflection relationship of the beam. Also the moment-curvature relationship of the beam and the variation of the crack sizes.

8.3.2.2.1 Moment-deflection relationship.

Data recorded from the electronic transducer was used to plot the moment-deflection relationship. Figure 8.54 shows the moment-deflection relationship of beam 2. In this figure are defined 5 interesting points A, B, C, D and E. The straight line between the origin and point A, where the concrete crushes, defines the elastic range of the beam. After crushing of the concrete, the flexural strength of the beam declined to the point B and then recovered up to the point C where the beam failed falling suddenly to point D. The collapse of the beam was delayed between D and E. The collapse of the beam came at point E of the moment-deflection relationship. The beauty in this figure is the plateau between A and C with a slight indentation in B. The internal moment of the beam kept almost constant which is an indication that the failure of the beam was ductile.

8.3.2.2.2 Moment-curvature relationship.

The internal moment of the beam for each applied load has been calculated using equation 8.1. The moment-curvature relationship is shown in figure 8.55. In figure 8.55 can be seen the moment-curvature relationship for the elastic range only. The reason is that the demecs came off when the concrete crushed and, consequently, demec measurement were no longer taken.

8.3.2.2.3 Crack sizes.

Looking at figure 8.40, two cracks can be seen between the rows of demecs 3 and 5 only. Hence, the crack size is the average of these two cracks. The calculation is carried out using the same procedure as for beam 1. Figure 8.56 shows the variation of the cracks' sizes in terms of the variation of the internal moment of the beam. Notice in

figure 8.56 that the deflection did return to zero when the beam was unloaded due to the bond effects between the FRP rebars and the concrete.

8.3.3 Beam three.

Beam 3, which is shown in figure 7.1c and 7.3c of chapter 7 and described in sections 7.3 and 7.4 of chapter 7, has two FRP rebars at the top and three FRP rebars at the bottom.

8.3.3.1 Test procedure.

Loading of beam 3 started with 10 kN (see figure 8.57) which generated the first 4 cracks in the constant moment region. One crack appeared between columns 3 and 5 of demecs. No substantial changes in the beam were shown with the application of 20 kN and 30 kN. However with the application of 40 kN, increased to 8 the number of cracks in the constant moment region (see figures 8.58 and 8.59). All cracks are not only vertical but also uniformly distributed which in turn means that there is a good bond stress between the FRP rebars and the concrete. The cracking extended to the ends of the beam and in addition, the deflection of the beam became very noticeable. No substantial changes happened at the load of 50 kN regarding the cracks between the columns 3 and 5 of demecs (see the figure 8.60). However at 90 kN (see the figure 8.61), the crack pattern changed significantly; the size of some cracks increased in a non-vertical direction such as the crack near the label of the beam at the right hand side of figure 8.61.

Of interest is the fact that the two cracks between columns 3 and 5 of the demecs remained almost invariable even at 90 kN which means that the neutral axis depth kept steady (see figure 8.62). In addition, in figure 8.62 can be seen 4 secondary cracks. One

secondary crack is at the bottom of a vertical crack below the loading point at the left-hand side in figure 8.62. Another secondary crack is at the bottom of the vertical crack below the right-hand side loading point. The other two secondary cracks can be seen at the right end of figure 8.62. From here, the loading of the beam was governed by displacements at the rate of 3 mm at a time. The concrete at the top of the beam started coming off at the load of 104.4 kN (see figures 8.63). In addition, the trends of the upper ends of the cracks near the loading points were towards the midspan of the beam.

Demec measurements were taken until the demecs in columns 3 and 5 came off completely at the load of 107.9 kN (see figure 8.64). However, the collapse of the beam did not happen yet because the compressive reinforcement took over from the crushed concrete keeping the beam still in place. Figures 8.65 to 8.67 show the sequence of failure of the beam. Loosening of the concrete at the top and the bottom of the beam occurred at the load of 114.2 kN (see the figure 8.67).

The loose concrete was removed after unloading the beam to inspect the state of the FRP reinforcement, not only the tensile one but also the compressive one (see the figure 8.68). Figures 8.69 to 8.71 show the failure of the FRP rebars at the top of the beam where can be seen treads of the steel stirrups over the rebars. The failure of the compressive rebars was due to compressive crushing plus the shear effect by the steel stirrups. In contrast, the failure of the FRP rebars at the bottom of the beam occurred by splitting off the glass fibers from the resin binding matrix as can be seen in figure 8.72.

8.3.3.2 Processed data.

In the following section is shown the moment-deflection relationship of the beam. Also the moment-curvature relationship of the beam and the variation of the crack sizes.

8.3.3.2.1 Moment-deflection relationship.

The moment-deflection relationship has been plotted using the data obtained from the electronic transducer placed beneath of the beam (see figure 8.3). Figure 8.73 shows the moment-deflection relationship of beam 3 where can be seen 5 interesting points marked from A to E. Point A denotes the concrete crushing and then an indentation in point B. After crushing the concrete, the strength of the beam is extended up to the point C where the peak moment takes place and then the beam collapses. It can be inferred by looking at the section between A and C in figure 8.73 that the extension of the curve is provided by the compressive FRP rebars.

Another point of interest is the fact that the line between A and B is non vertical. Furthermore, the plateau between A and C is larger than the plateau of beam 2 and, also, the internal moment of C is greater than the internal moment of A. This is an indication that the compressive FRP rebars gave ductility to the beam.

8.3.3.2.2 Moment-curvature relationship.

The internal moment M_n of the beam, for each load applied to the beam is calculated using equation 8.1. Figure 8.74 shows the moment-curvature relationship calculated up to the concrete crushing.

8.3.3.2.3 Crack sizes.

From figures 8.58 to 8.67 can be seen the presence of only two cracks between the rows of demecs 3 and 5. Hence, the size of one crack is the average of the displacement between the demecs G3 and G5. Figure 8.75 shows the variation of crack's sizes in terms of the variation of the internal moment of beam 3.

8.3.4 Beam 4.

Beam 4, which is shown in figures 7.1d and 7.4a of chapter 7 and described in sections 7.3 and 7.4 of chapter 7, has one steel deformed bar at the top and three FRP rebars at the bottom.

8.3.4.1 Test procedure.

The test procedure of beam 4 started with the initial demec measurement before loading the beam. The loading started with the application of 10 kN and the first 5 cracks appeared in the constant moment region (see figure 8.76). Between columns 3 and 5 of the demecs, only one crack crossed row E of the demecs. The cracks are all vertical ones. As the load was incremented to 20 kN, the amount of cracks increased from 5 to 8 including a second crack between columns 3 and 5 of the demecs (see figure 8.77). As the load was incremented to 30 kN, the number of cracks remained the same but not their lengths which were larger, crossing row D of demecs between columns 3 and 5 (see figure 8.78).

Apart from the increment of the deflection of the beam, no major changes in the crack pattern were observed with the load of 40 kN (see figure 8.79). The cracks are all vertical and uniformly distributed. The deflection of the beam is very noticeable at this stage due to the low Young's modulus of the tensile FRP rebars. The load was incremented up to 60 kN and then the beam was unloaded at the rate of 20 kN at a time until 0 kN (see figure 8.80). As the beam was unloaded, cracks appeared from the top of the beam. The beam then was reloaded at the rate of 10 kN at a time up to 90 kN (see figure 8.81).

Looking at figure 8.81, we can see one crack at the top of the beam, just at the left-hand side of the figure. This crack was because of unloading the beam. If we look carefully at the bottom of figure 8.81 just at the right-hand side, we can see the appearance of secondary cracks as well. Figure 8.82 shows the rising of the cracks in an inclined trend towards the midspan of the beam at the load of 110 kN. The size of the cracks between columns 3 and 5 of the demecs remain the same. Dramatic changes are seen in figure 8.83 as the load was incremented to 119.7 kN, where vertical cracks were connected together through secondary cracks. In figure 8.84, can be seen the beginning of the concrete spalling at the top of the beam as the load was incremented at 122.1 kN.

Most of the vertical cracks have been connected to each other through secondary cracks. In addition it can be seen that the cracks coming from the bottom of the beam are about to join with the cracks coming from the top of the beam. The crack propagation is more evident in figure 8.85, nevertheless, the beam was stable at the load of 122.1 kN. Figures 8.86 to 8.89 show the sequential failure of the beam until collapsing. The beam was finally unloaded as can be seen in figure 8.90 and then the loose concrete was removed to investigate the state of the reinforcing bars not only at the top but also at the bottom. Figures 8.90 to 8.92 show that the steel rebar at the top of the beam failed by buckling. Figures 8.93 and 8.94 show the mode of failure of the FRP rebars at the bottom of the beam. The failure of the FRP rebars was by splitting off the glass fibers.

8.3.4.2 Processed data.

In the following section is shown the moment-deflection relationship of the beam. Also the moment-curvature relationship of the beam and the variation of the crack sizes.

8.3.4.2.1 Moment-deflection relationship.

The moment-deflection relationship has been plotted using the data obtained from the electronic transducer placed beneath of the beam (see figure 8.3). Figure 8.95 shows the moment-deflection relationship of beam 4 in which can be seen 4 important points marked from A to D. Point A denotes the point in the curve where the concrete at the top of the beam crushed, falling down to B. After that, the beam showed some recovery up to C, regaining strength and then falling to the ultimate failure in D.

8.3.4.2.2 Moment-curvature relationship.

The internal moment of the beam is calculated using equation 8.1 for each load applied to the beam. Figure 8.96 shows the moment-curvature relationship of the beam up to concrete crushing which coincides with point A in figure 8.95.

8.3.4.2.3 Crack sizes.

Figures from 8.77 to 8.83 show two cracks only between the rows of demecs 3 and 5, hence, the crack's size is taken as the average of the size of these two cracks. Figure 8.97 shows the variation of crack sizes in terms of the variation of the internal moment of the beam.

8.3.5 Beam five.

Beam 5, which is shown in figures 7.1e and 7.4b and described in sections 7.3 and 7.4 of chapter 7, has 1 FRP rebar at the top and 5 FRP rebars at the bottom.

8.3.5.1 Test procedure.

The loading of the beam started with 10 kN as can be seen in figures 8.98 and 8.99. Five vertical cracks in the constant moment region appeared with the first load which included the two cracks between the columns of demecs 3 and 5. The number of cracks in the constant moment region increased to 8 as the load was incremented to 20 kN as can be seen in figure 8.100. In this figure can be seen the uniformity of the crack distribution along the beam. Figure 8.101 shows the constant moment region at side A of the beam and figure 8.102 shows the same region at side B of the beam.

Notice that the cracks crossed normal to the axis of the beam from side A to side B of the beam. As the load was incremented to 30 kN, the lengths of the cracks increased but the number of cracks remained the same as can be seen in figure 8.103. Figures 8.104 and 8.105 show the beam after incrementing the load to 40 kN and then to 60 kN with no significant changes. However, as the load was incremented to 100 kN then appeared secondary cracks from the bottom of the vertical cracks outside of the constant moment region. Figure 8.106 shows side A of the beam and figure 8.107 shows side B of the beam in which can be seen the appearance of secondary cracks outside of the constant moment region.

The beam was displaced at the rate of 3 mm at a time up to the load of 119.5 kN when the concrete at the top of the beam started crushing and the beam collapsed with a catastrophic brittle failure. Figures 8.108 to 8.112 show the progressive failure of the beam and figures 8.113 and 8.14 show the spalling of the concrete at failure of the beam.

The loose concrete was removed to inspect the state of the reinforcing bars not only at the top of the beam but also at the bottom as in figures 8.115 and 8.116. Figures 8.117 and 8.118 are aerial views of the FRP rebar at top of the beam after failure. In these

figures it can be seen that FRP rebar failed by the shear effect caused by not only the compressive force but also by the abrasion of the steel stirrup. In contrast, the FRP rebars at the bottom of the beam did not fail at all as can be seen in figures 8.119 and 8.120. Figure 8.121 shows the author taking demec measurements during the test of beam 5.

8.3.5.2 Processed data.

In the following section is shown the moment-deflection relationship of the beam. Also the moment-curvature relationship of the beam and the variation of the crack sizes.

5.3.5.2.1 Moment-deflection relationship.

The moment-deflection relationship of beam 5 has been derived in the same manner as for the previous beams. Figure 8.122 shows the moment-deflection relationship of beam 5 where can be seen two points marked A and B. Point A denotes the point in the curve where the concrete crushed and point B describes the collapse of the beam.

8.3.5.2.2 Moment-curvature relationship.

Figure 8.123 shows the moment-curvature relationship of beam 5 in which can be seen that the moment has been calculate from the origin up to the concrete crushing.

8.3.5.2.3 Crack sizes.

The crack's sizes in beam 5 have been calculated in the same way as for the previous beams. Figure 8.124 shows the variation of the crack's size in terms of the variation of the internal moment of the beam. The up and down of the curve denotes unloading and reloading of the beam during the test.

8.3.6 Materials.

A comprehensive test of the materials involved in the manufacturing of the RC beams with FRP and steel reinforcing bars are covered in this part of chapter 8. The testing program began with the investigation of the mechanical properties of the concrete mix such as compressive strength and Young's modulus, tensile strength and modulus of rupture. Tables and graphs help the reader to get through the results. Next were tested FRP rebars and steel rebars.

8.3.6.1 Concrete.

The main properties of the concrete to be investigated are the compressive strength and Young's modulus [41], the tensile strength [42], and the modulus of rupture (flexural strength) [43]. Before testing the concrete specimens for compression, concrete cubes were crushed to determine the ultimate load at which the concrete fails.

a) Young's modulus.

Concrete cubes were crushed to determine the ultimate load at which the concrete crushes before testing the concrete cylinder specimens. The design of the cylinder specimens is shown in figure 8.125 with a 100-mm diameter and 200-mm height.

Rigid caps were placed at both ends of the cylinder to uniformly distribute the axial load P applied with a hydraulic machine. Figure 8.126 shows schematically the set up of the cylinder before testing.

The reader can see two clamps around the cylinder for holding firmly the measuring gauge. The bridging bolt at the left-hand side is free of friction to allow only vertical displacements of the clamps. In addition, at the right-hand side is the measuring dial gauge for the measurement of the axial deformation of the concrete cylinder. Once the

specimen is set up then it is placed into the compression machine for the application of a gradual axial load.

The axial load was applied by means of a hydraulic machine at the ratio of 260 ± 40 kN per minute, up to 45% of the ultimate load that was previously determined through the crushing of the concrete cubes. The stress in the concrete is calculated by dividing the load P by the sectional area of the cylinder for each increment of load as in equation 8.2.

$$\sigma_c = \frac{4P}{\pi D^2} \qquad \ldots\ldots 8.2$$

were σ_c is the concrete stress, P is the axial load and D is the cylinder diameter.

Seven cylinders were tested and the stress-strain relationships of the 7 test series are shown in figure 8.127. Apparently, in figure 8.127 there are only 6 curves. What happens is that two of the curves are coincident.

The slope of the stress-strain curve gives the concrete's Young's modulus. Notice that the stress-strain curves do not have a constant slope but a varying slope from the origin of the co-ordinates to about 5 MPa. Therefore, to obtain the concrete's Young's modulus for the elastic range of the stress-strain relationship, the curves have to be corrected using the linear regression method. The correction is for stresses greater than 5 MPa. The slope of the corrected curve gives the elasticity modulus of the concrete at compression.

Table 8.1 shows the identification and dimensions of the cylinders as well as the results of the tests. Column 1 of the table shows the identification number of the cylinders tested for Young's modulus. Columns 2, 3 and 4 described both the dimensions and the weights of the cylinders. Column 5 shows the age of the specimens. Column 6 shows the

individual Young's modulus of each cylinder. Column 7 shows the average Young's modulus not only at the age of 63 days but also at the age of 90 days. Column 8 shows the standard deviation of the Young's modulus at both 63 and 90 days of age.

Cyl # (1)	Diam. [mm] (2)	Height [mm] (3)	Weight [grams] (4)	Age (5)	E_c (6)	Average E_c (7)	STDEV (8)
1	101	200.0	3720.9	63	32484		
2	101	200.0	3758.8	63	35466		
5	101	200.0	3738.2	63	32441	33464	1734
10	100	200.0	3717.2	90	37057		
20	100	202.0	3734.0	90	35790		
21	100	201.5	3722.4	90	34958		
24	100.5	199.5	3707.2	90	33911	35429	1330

Table 8.1. – Derivation of the concrete Young's modulus.

b) Concrete compressive strength.

The load P was applied at the rate of 260 ± 40 kN per minute up to rupture for the test of the concrete strength. The compressive strength of the concrete cylinder was calculated using equation 8.3.

$$f_c = \frac{4P_u}{\pi D^2} \qquad \text{.....8.3}$$

where f_c is the concrete strength, P_u is the ultimate load, and D is the concrete cylinder diameter.

Table 8.2 shows the identification number and the properties of the concrete cylinders from column (1) to column (4). Column (5) holds the age of the cylinders and column (6) the ultimate load at which the cylinder was broken. Column (7) shows the sectional area of the cylinder and column (8) the strength of the cylinders at failure.

Column (9) shows the average strength of 50.2 MPa for the cylinders tested at the age of 63 days and 51.2 MPa for the cylinder tested at the age of 90 days. Column (10) shows the standard deviation of the concrete strengths for the cylinders tested at 63 days and 90 days of age.

Cyl. # (1)	Diam. [mm] (2)	Height [mm] (3)	Weight [grams] (4)	Age [days] (5)	U. load [kN] (6)	Area [mm2] (7)	Strength [MPa] (8)	Aver. [MPa] (9)	STDEV [MPa] (10)
1	101	200.0	3720.9	63	403.0	8011.8	50.3		
2	101	200.0	3758.8	63	404.0	8011.8	50.4		
5	101	200.0	3738.2	63	399.5	8011.8	49.9	50.2	0.295
10	100	200.0	3717.2	90	396.0	7854.0	50.4		
20	100	202.0	3734.0	90	408.5	7854.0	52.0		
21	100	201.5	3722.4	90	409.0	7854.0	52.1		
24	100.5	199.5	3707.2	90	399.5	7932.7	50.4	51.2	0.955

Table 8. 2. – Derivation of the concrete compressive cylinder strength.

c) ***Tensile strength of the concrete.***

The tensile strength of the concrete is calculated using the indirect method of the Brazil or splitting test. This method consists of placing horizontally a concrete cylinder and loading it with a uniformly distributed load along its length up to failure (see figure 8.128). To ensure immobility of the cylinder during test, an appropriate jig must be set up. The tensile strength is calculated using the following equation

$$f_t = \frac{2000P_u}{\pi LD} \qquad \text{.....8.4}$$

Where f_t is the tensile strength of the concrete in MPa; P_u is the ultimate load in kN; L is the length of the concrete cylinder in mm; and D is the diameter in mm. Table 8.3 shows

the dimensions of the concrete cylinders in columns (2) and (3). Column (4) shows the weights of the cylinders. The time since the cast and curing is in column (5). The breaking load or ultimate load is in column (6). The tensile strength f_t is in column (7). In column (8) are the average strength not only at 63 day of age buy also 90 days of age. Finally, in column (9) is the standard deviation of the tensile strength at 63 days and 90 days of age.

Cyl. # (1)	Diam. [mm] (2)	Length [mm] (3)	Weight [grams] (4)	Age [days] (5)	Ult. load [kN] (6)	Strength [MPa] (7)	Aver. [MPa] (8)	STDEV [MPa] (9)
11	100.8	202.0	3760.6	63	138.4	4.36		
14	100.2	201.0	3730.9	63	144.0	4.56		
19	101.0	201.0	3768.8	63	116.8	3.66		
22	100.6	201.0	3749.1	63	117.0	3.68	4.07	0.46
6	100.5	201.0	3756.0	90	134.0	4.22		
8	100.5	201.0	3754.8	90	150.0	4.73		
17	100.0	200.5	3765.0	90	145.6	4.62	4.52	0.27

Table 8. 3.– Derivation of the concrete indirect tensile strength.

d) Flexural strength or modulus of rupture.

The flexural strength test is carried out by placing a non reinforced concrete beam over two roller supports and then applying a two points centred load (see figure 8.129). Table 8.4 shows the dimensions, weight and age of the beam specimens. The modulus of rupture of each beam is in column (7) of table 8.4 and the average strength at 63 days and 90 days of age are in column (8). The standard deviations at both ages are in column (9). The flexural strength is calculated using the following equation:

$$f_{ct} = \frac{PL(1000)}{BD^2} \qquad \text{.....8.5}$$

where f_{ct} is the modulus of rupture or flexural strength in MPa; P is the ultimate load in kN; L is the span length in mm; B is the width of the specimen at the section of failure in mm; D is the depth of specimen at the section of failure in mm.

Beam	B	D	L	Weight	Age	Ult. load	Modulus of Rupt.	Average MR	STDEV
#	[mm			[grams]	[days]	[kN]	[MPa]	[MPa]	[MPa]
(1)	(2)			(4)	(5)	(6)	(7)	(8)	(9)
2	100	101	500	11997.3	63	15.3	7.51		
1	100	102	500	11979.8	63	15.3	7.39		
3	100	102	500	12008.4	63	14.5	6.97	7.29	0.28
4	101	101	500	12033.7	90	17.4	8.43		
5	101	101	500	12097.5	90	18.9	9.15		
6	101	101	500	12107.5	90	16.9	8.20	8.59	0.49

Table 8. 4. – Derivation of the modulus of rupture of the concrete.

8.3.6.2 Reinforcing bars.

FRP bars and steel bars were tested through the pulling machine to determine their mechanical properties. Firstly, were tested FRP bars to calculate the tensile strength and the corresponding Young's modulus and then were tested steel bars to determine yield strength and ultimate strength. Strain gauges were placed at the middle of the FRP bars to determine displacement and, therefore, to measure strains. The test results are explained through tables and graphs.

a) FRP bars.

Two sorts of FRP reinforcing bars were tested, one of them was of 15 Tonnes nominal strength and the another of 30 Tonnes nominal strength according to the manufacturer. Although the two specimens look similar (see figure 8.130) they have different strength and Young's moduli. The reinforcing glass-fiber is of the E-glass type and the binding matrix is a resin type. The density of the cured resin is 1.12 gram/cm^3 and the Young's modulus of the resin is 3.4 GPa.

Figure 8.131 shows the set up of the specimens before testing. The reader can see that some of them have been machined in the middle. The aim of machining some of the specimens is to ensure failure where the dimensions are known. At the ends of the specimens, there are aluminium sleeves glued to the specimens to provide a reliable grip. Figure 8.133a shows schematically the set up of non machined specimens. Meanwhile, figure 8.133b shows schematically the set up of machined specimens. Strain gauges were placed in the middle of the specimens to record the deformation of the bar during the test.

The mode of failure of the FRP reinforcing bars is shown in figure 8.132. Table 8.5 shows the properties of the bar specimens as well as the test results. Let us have a look at table 8.5. Column (1) indicates the bar type where the first digits represent the load in Tonnes at which the bar breaks according to the manufacturer. FRP stands for Fiber Reinforced Plastic and the last digit indicates the identification number of the bar specimen. Column (2) indicates the percentage of glass-fiber per volume of bar. Column (3) indicates the percentage of glass-fiber per weight of the bar. Column (4) indicates whether or not the coupons have been machined. Column (5) indicates the diameter at the middle of the specimen. Column (6) indicates the actual load at which the specimens failed during the experimental test. Column (7) represents the strength of the specimens in

MPa. Column (8) indicates the average strength of the bars. Column (9) indicates standard deviation of the tensile strength of the bars. Column (10) indicates the individual Young's modulus of the bars. Column (11) indicates the average Young's modulus of the bars. Column (12) indicates the standard deviation of the Young's modulus of the bars. Finally, column (13) tells us the mode of failure of the specimens where 'good failure' means that the specimen broke at the middle, whereas, 'shear sleeve' means that the specimen failed prematurely at the sleeve.

The asterisks in columns (10) and (13) indicate that specimen 30T-FRP1 was not set up properly and that the strain gauges came off prematurely. Consequently, the Young's modulus was not derived. Figure 8.134 shows the stress-strain relationship of the two types of FRP bars used in this experimental work. The thick curve is for the 30 Tones type bars and the thin curve is for the 15 Tones type bars.

b) Steel bars.

Two types of steel bars were tested through the pulling machine, one of them was a deformed 20-mm diameter bar identified as Y_{20} and the another one was without deformations and of 10-mm diameter and is identified as R_{10}. The pulling test was only to investigate yield strength and ultimate strength. Table 8.6 shows the identification of the bars as well as the dimension of them. In addition in the table, are the test results along with the corresponding averages and standard deviations.

Let us have a look at table 8.6, which in column (1) shows the bars type Y_{20} and R_{10}. The subscripts 20 and 10 indicate the nominal diameter of the bars. Column (2) represents the length of the bar coupon. The distance between grips is in column (3) and is referred to as the free length. In addition, the diameter of the bars is column (4). The individual

Bar type (1)	V_f [%] (2)	W_f [%] (3)	Mach. (4)	Diam. [mm] (5)	P_u [kN] (6)	σ_{ft} [MPa] (7)	Ave. σ_{ft} [MPa] (8)	STDEV [MPa] (9)	E_{ft} [MPa] (10)	Ave. E_{ft} [MPa] (11)	STDEV [MPa] (12)	Failure (13)
30T-FRP1	73.2	86.2	Yes	12.4	103.6	855			****			****
30T-FRP2	73.2	86.2	Yes	12.3	110	843			46076			Good
30T-FRP3	73.2	86.2	Yes	12.6	107.7	628			48105			Good
30T-FRP4	73.2	86.2	No	20	201.4	627			51561			Good
30T-FRP5	73.2	86.2	No	20	220.5	701			51411			Shear sleeve
30T-FRP6	73.2	86.2	No	20	208.2	544	700	126	50144	49459	2344	Good
15T-FRP1	35	38	Yes	12.4	45.1	375			22012			Shear sleeve
15T-FRP2	35	38	Yes	12.6	63.5	435			27751			Good
15T-FRP3	35	38	Yes	12.5	57.9	466			23941			Good
15T-FRP4	35	38	No	20	127.2	404			27301			Good
15T-FRP5	35	38	No	20	121.5	385			27164			Shear sleeve
15T-FRP6	35	38	No	20	138.9	440	420	38	26543	25785	2292	Good

Table 8.5. – Strength and Young's modulus of FRP rebars.

yield strength is in column (5) and the average and standard deviation are in the columns (6) and column (7) respectively. The ultimate strength, the average ultimate strength and the standard deviation of the ultimate strength are in the columns (8), (9) and (10) respectively.

Bar type (1)	L [mm] (2)	Free length [mm] (3)	D [mm] (4)	Yield str. [MPa] (5)	Av. [MPa] (6)	STDEV [MPa] (7)	Ult. str. [MPa] (8)	Aver. [MPa] (9)	STDEV [MPa] (10)
Y20-a	500	300	20	466			566		
Y20-b	500	300	20	466			570		
Y20-c	500	300	20	465	465.7	0.58	568	568.0	2.0
R10-a	450	250	9.9	502			560		
R10-b	450	250	9.9	500			559.7		
R10-c	450	250	9.9	511	504.3	5.86	564	561.23	2.4

Table 8.6. – Test results of the steel bars.

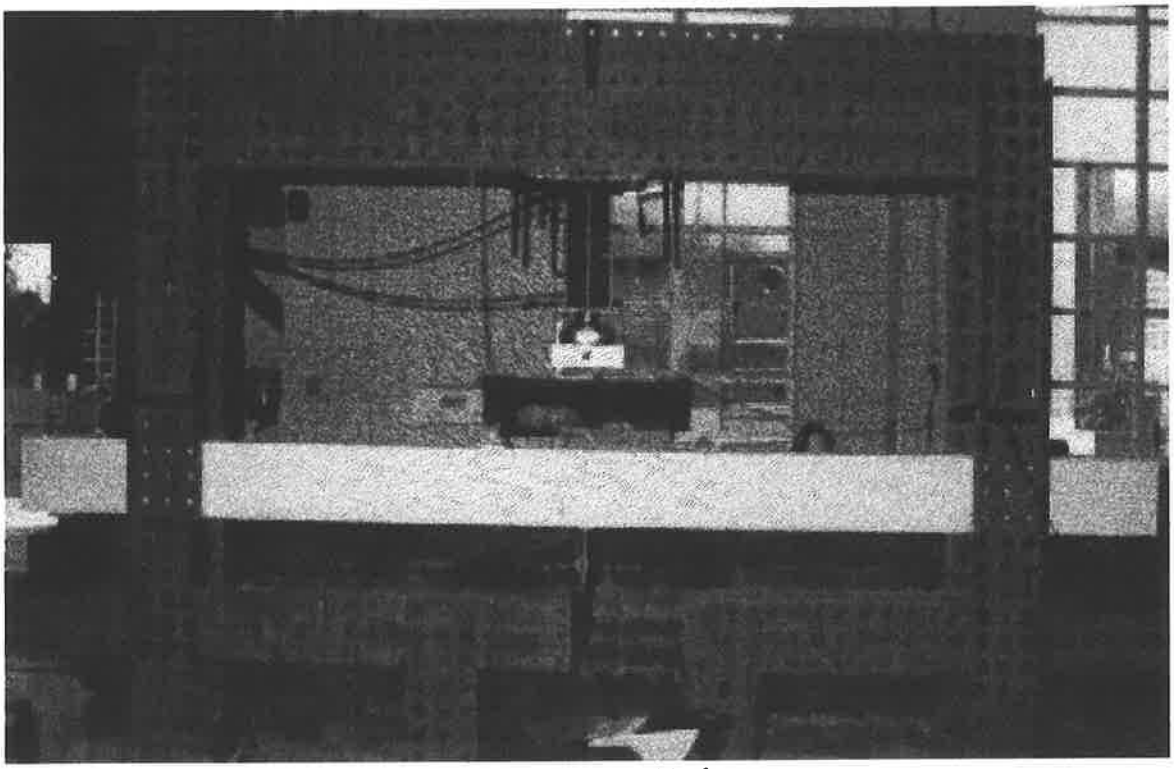

Figure 8.1. – Set up of beam 1 in the rigid steel double frame.

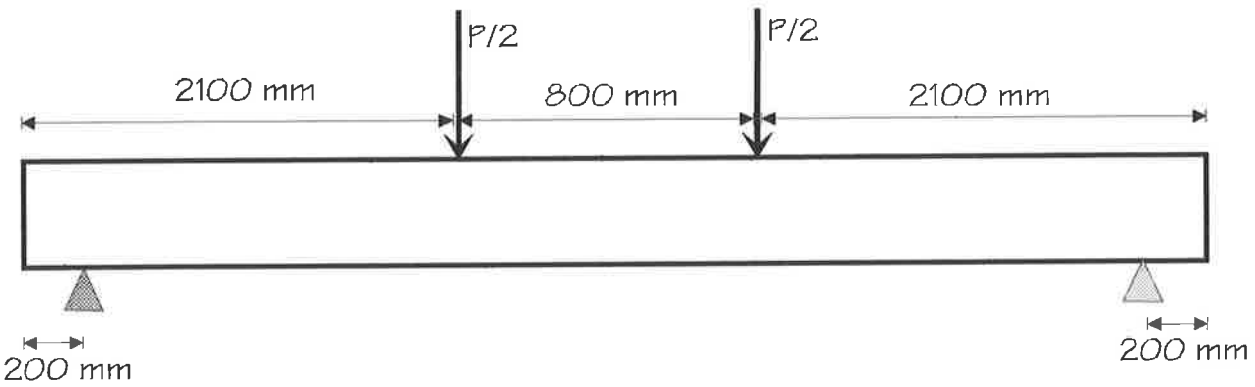

Figure 8.2. – Schematic loading of the beams.

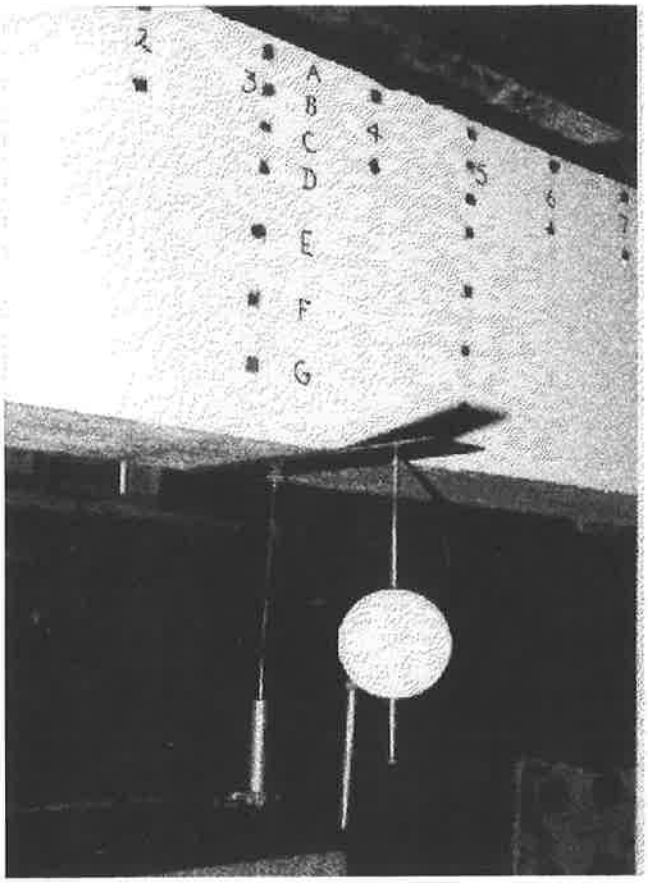

Figure 8.3. – Dial gauge and electronic transducer.

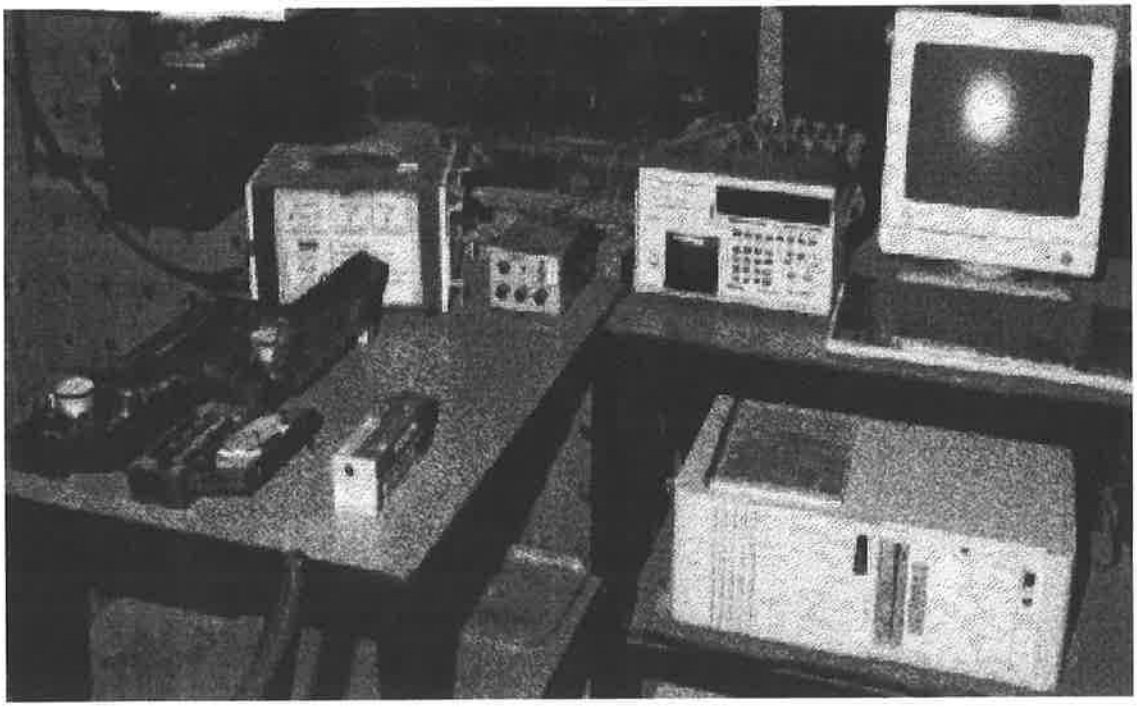

Figure 8.4. – Measurement equipment.

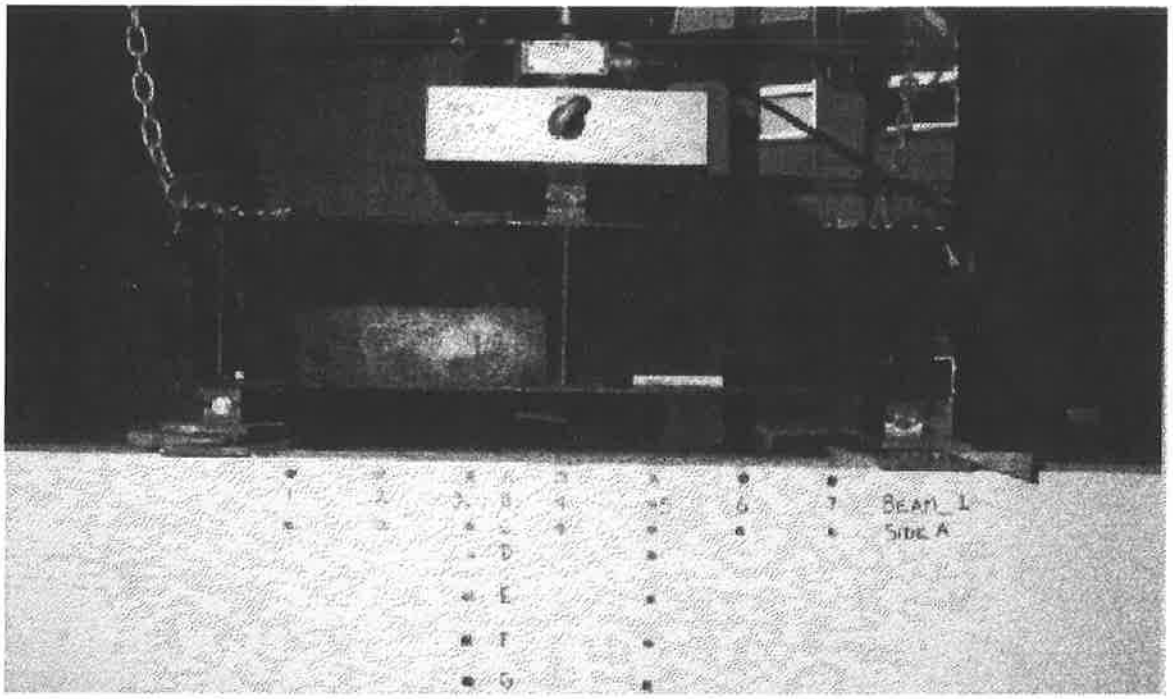

Figure 8.5. – Demec distributions.

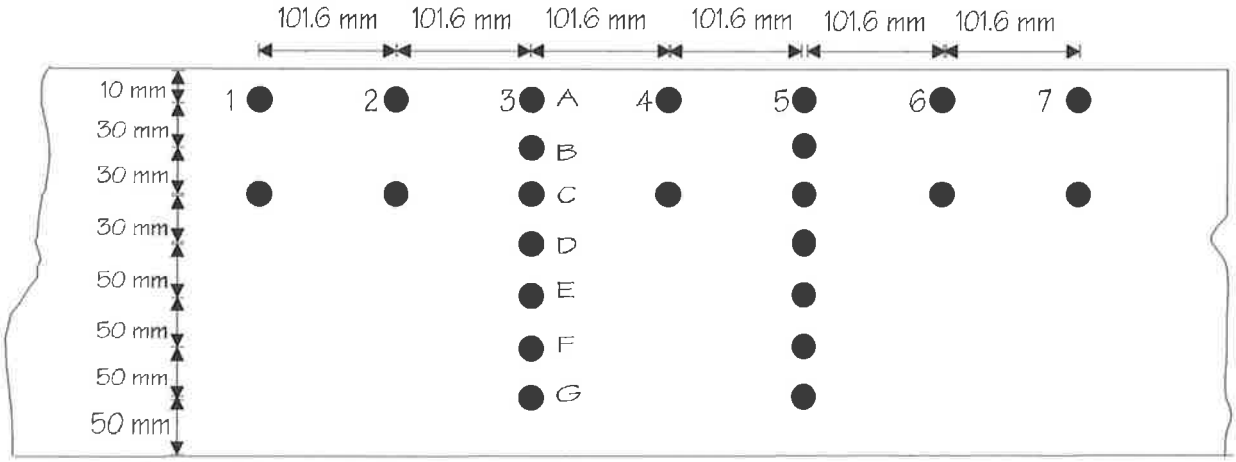

Figure 8. 6 – Schematic distribution of demecs.

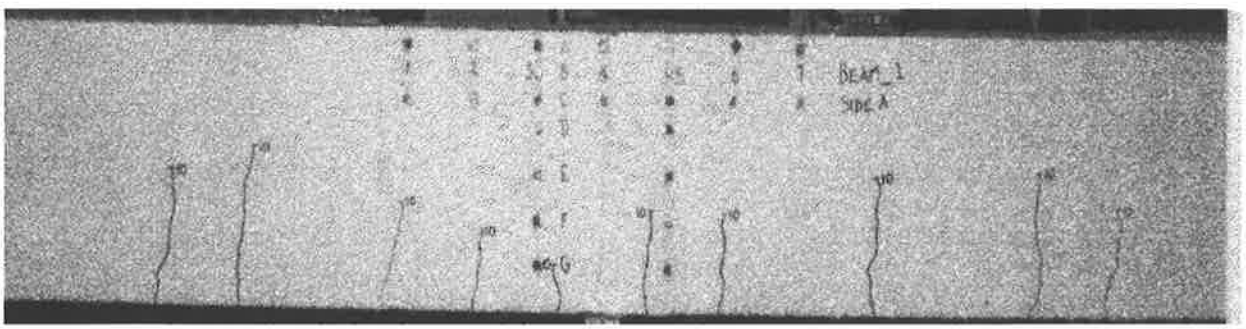

Figure 8.7. – Beam 1 side A at 10 kN.

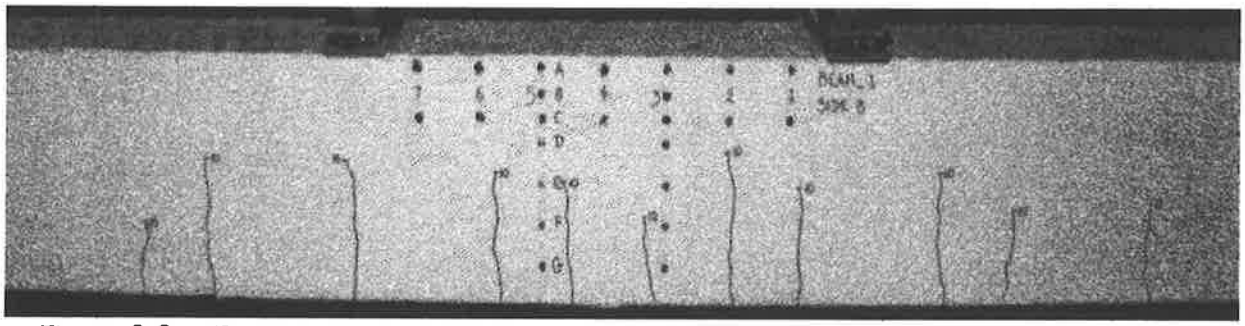

Figure 8.8. – Beam 1 side B at 10 kN.

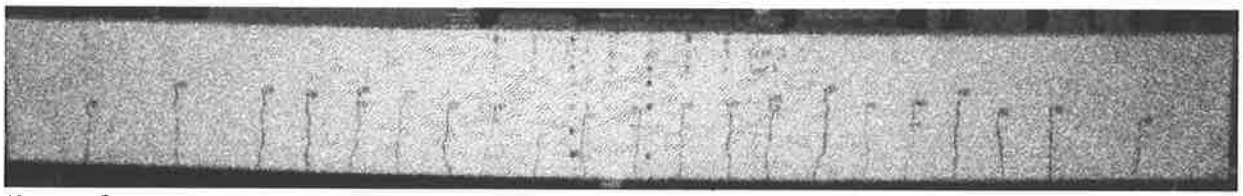

Figure 8.9 – Beam 1 at 20 kN.

Figure 8.10 – Beam 1 at 30 kN.

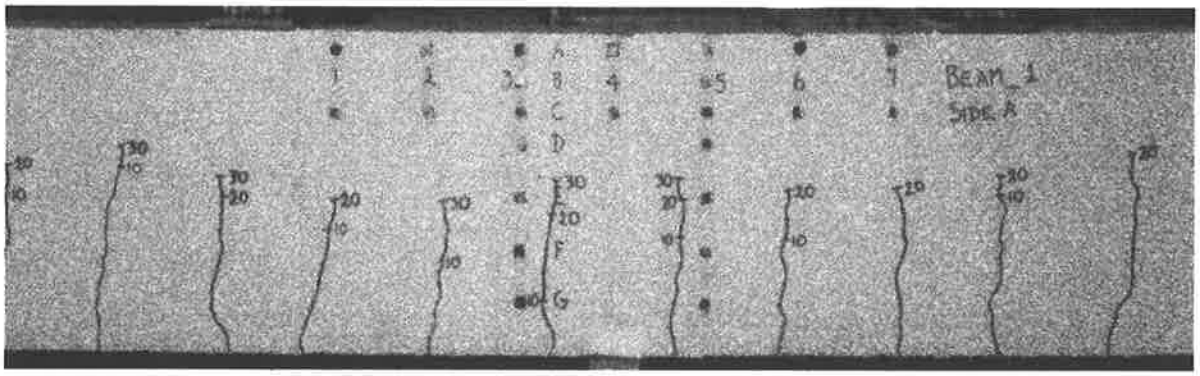

Figure 8.11. – Beam 1 at 30 kN

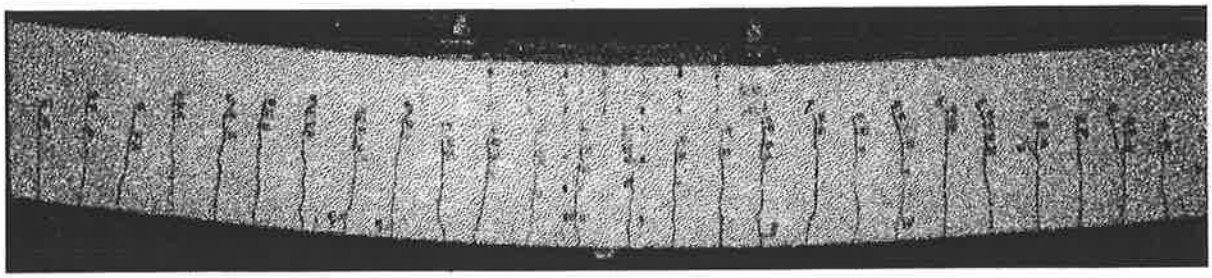

Figure 8.12. – Beam 1 at 85 kN.

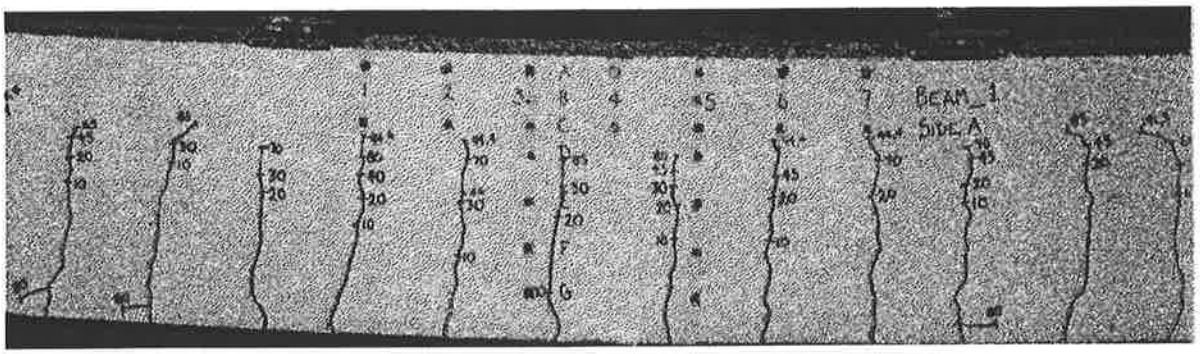

Figure 8.13. – Beam 1 at 95 kN.

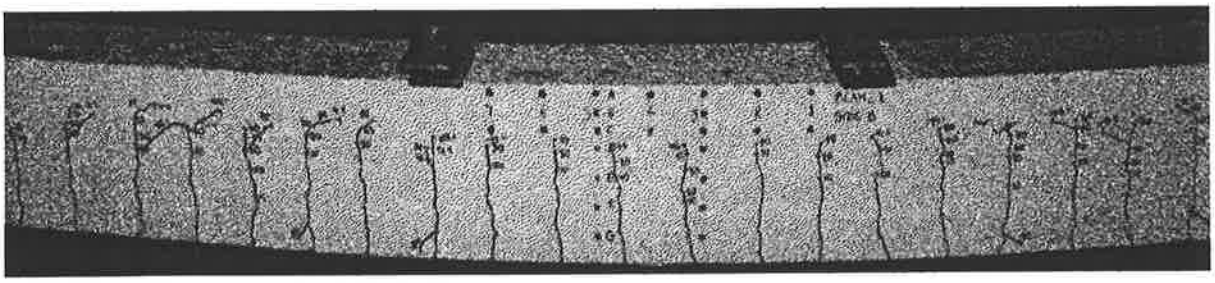

Figure 8.14. – Beam 1 at 103 kN.

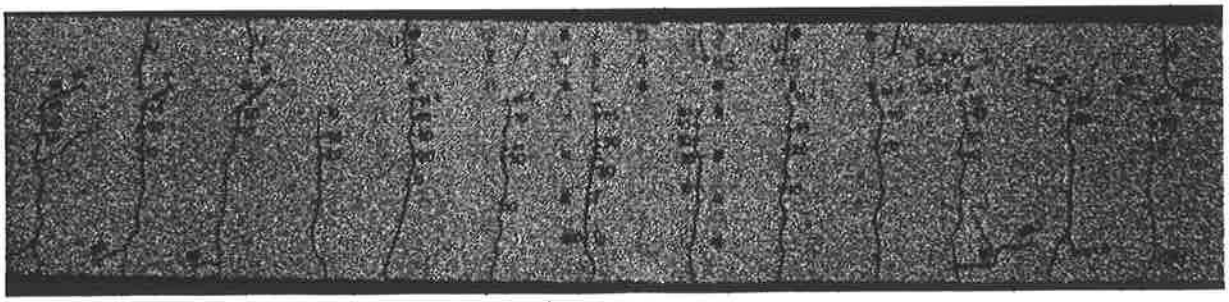

Figure 8.15. – Beam 1 unloaded after 117.0 kN.

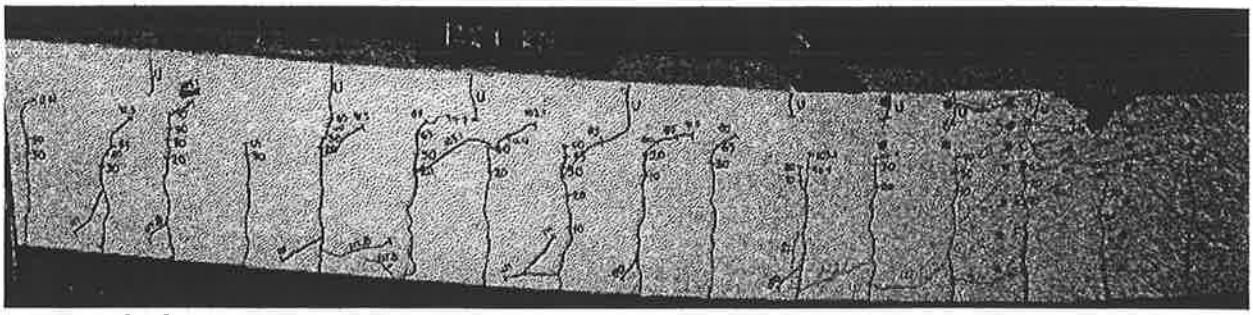

Figure 8.16. – Beam 1 at 122.1 kN.

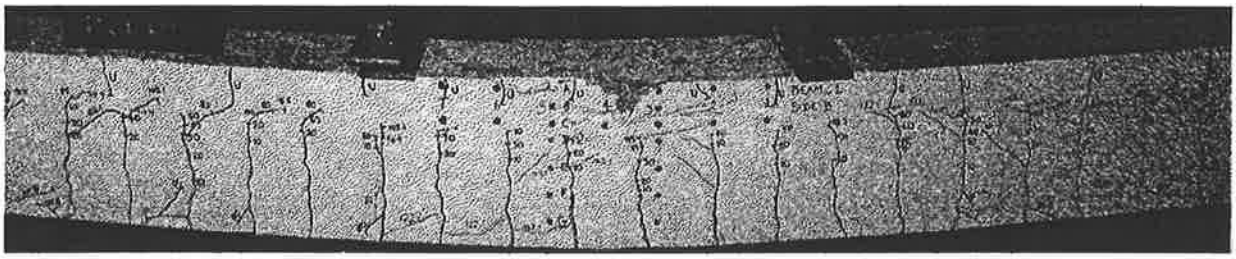

Figure 8.17. – Beam 1 at 122.1 kN.

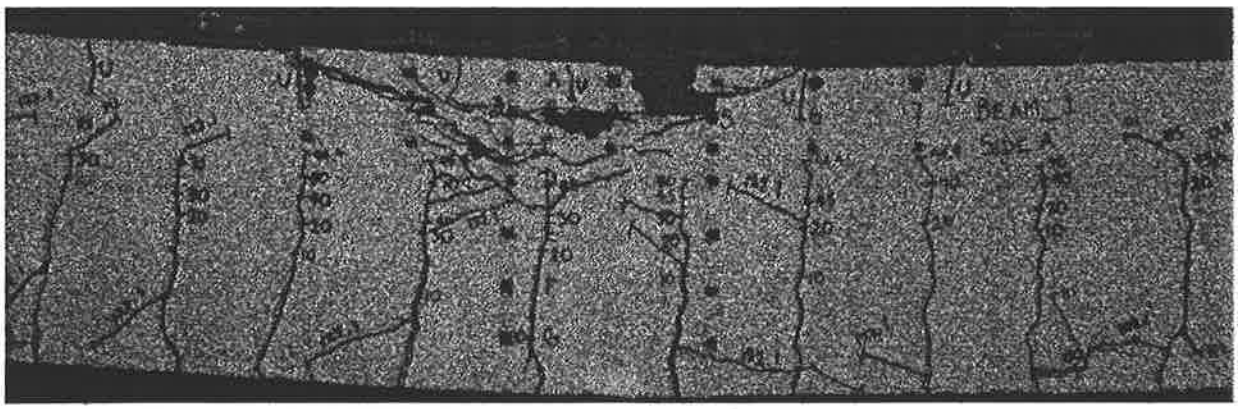

Figure 8.18. – Beam 1 at 122.1 kN.

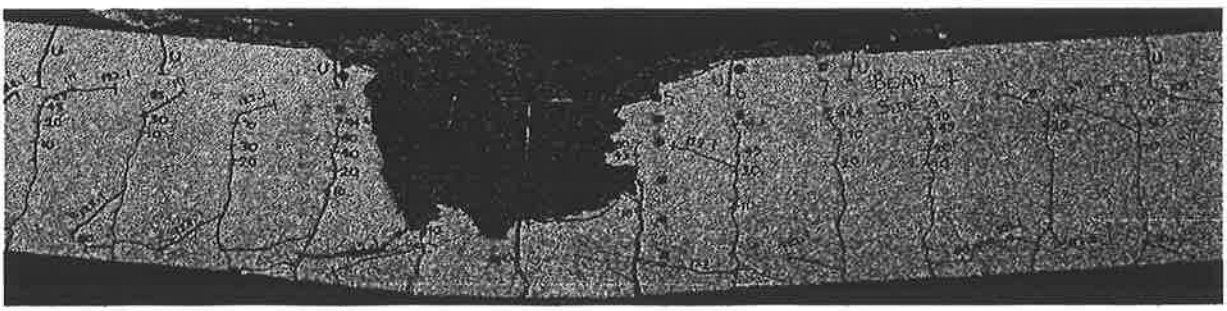

Figure 8.19. – Beam 1 at 23.3 kN.

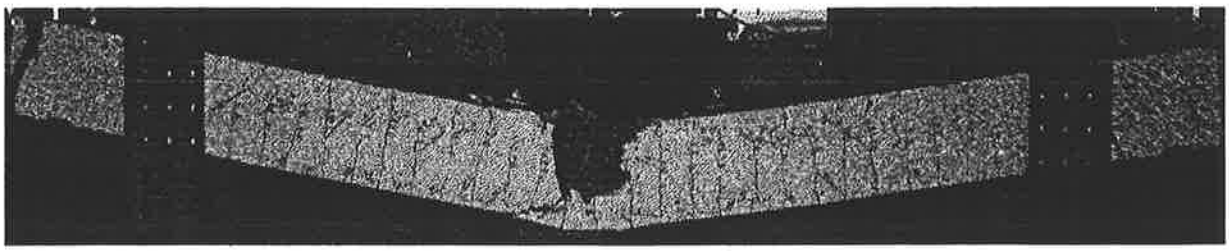

Figure 8.20. – Beam 1 at 12.9 kN.

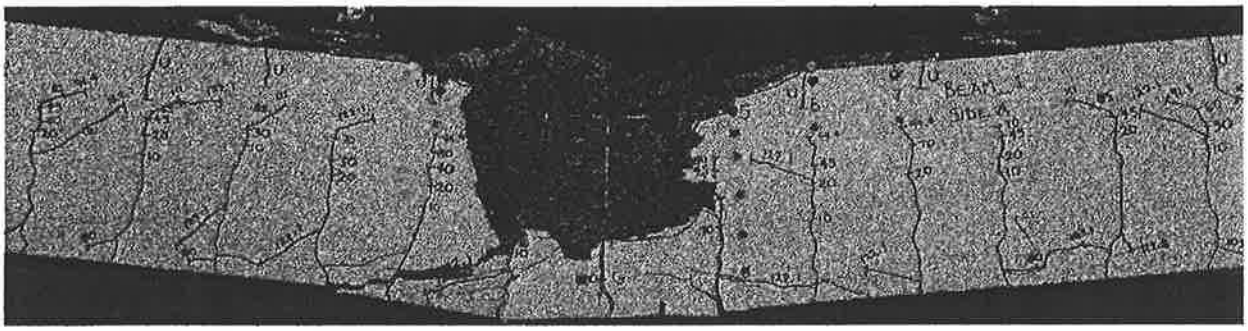

Figure 8.21. – Beam at failure.

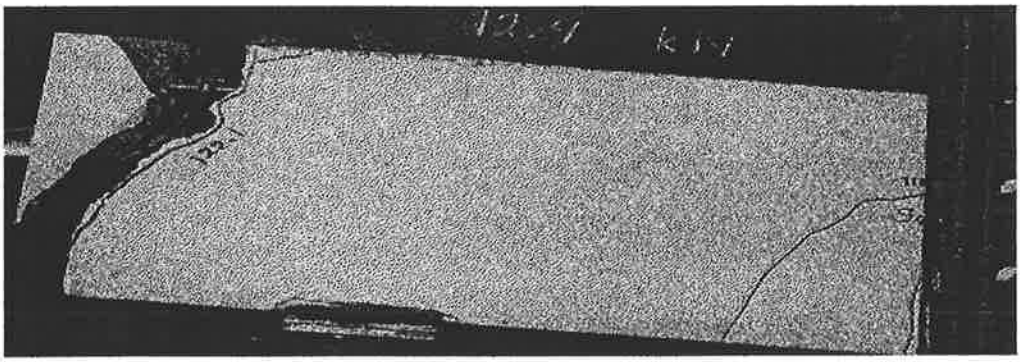

Figure 8.22. – Crack due to debonding of rebars at the top.

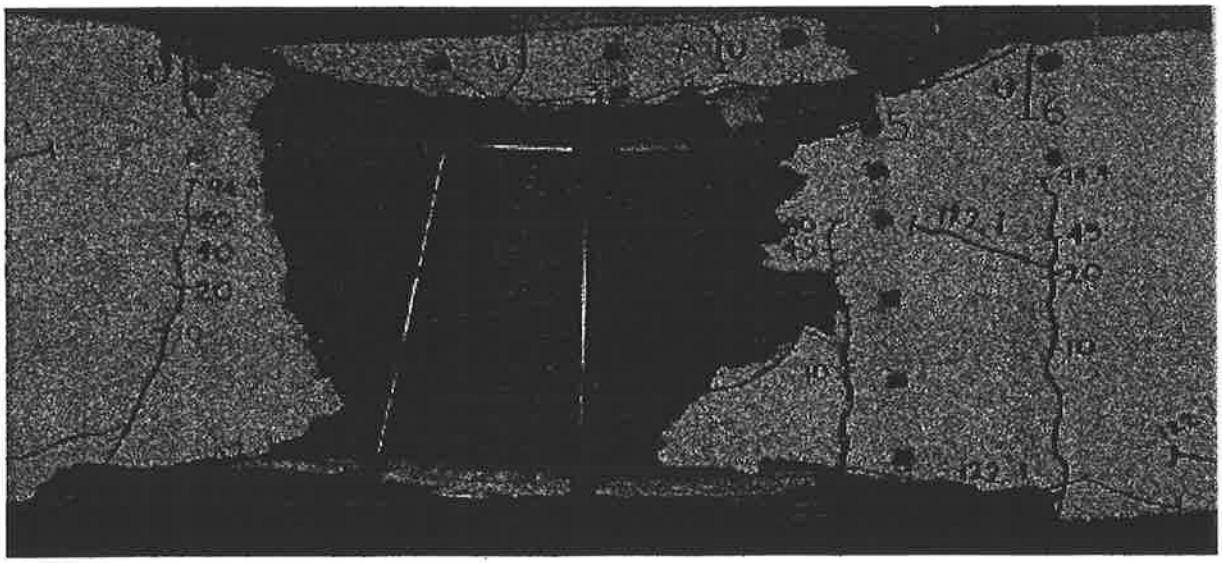

Figure 8.23. – Beam 1 after failure.

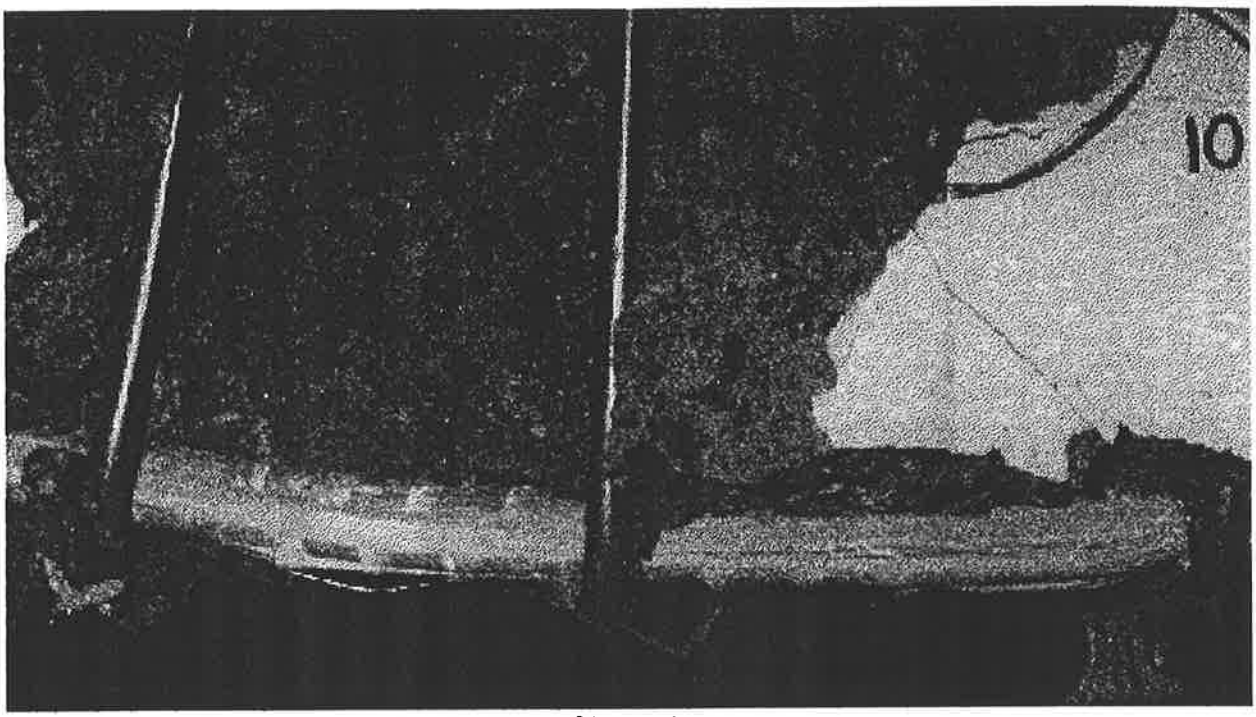

Figure 8.24. – FRP rebars at the bottom of beam 1.

Figure 8.25. – FRP rebars at the bottom of beam 1.

Figure 8.26. – Undeformed steel bars at the top of beam 1.

Figure 8.27. – FRP rebars at the bottom of beam 1.

Figure 8.28 – View of the reinforcing bars after failure of beam 1.

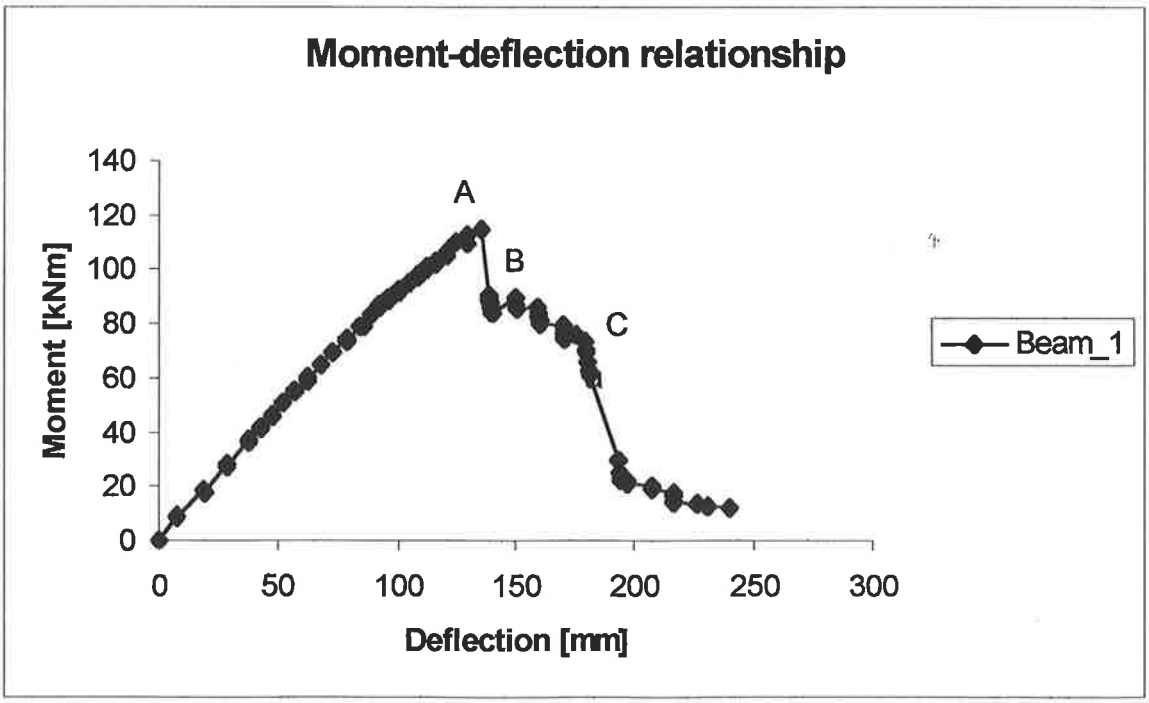

Figure 8.29. – Moment-deflection relationship of beam 1.

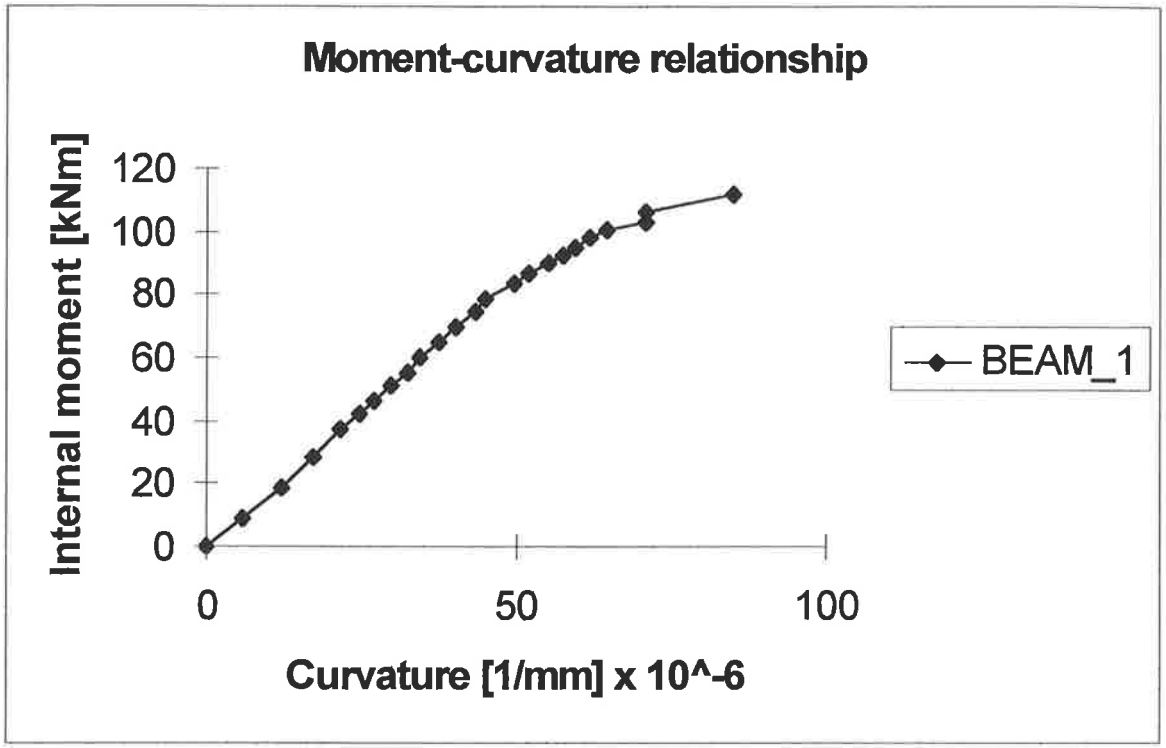

Figure 8.30. – Moment-curvature relationship of beam 1.

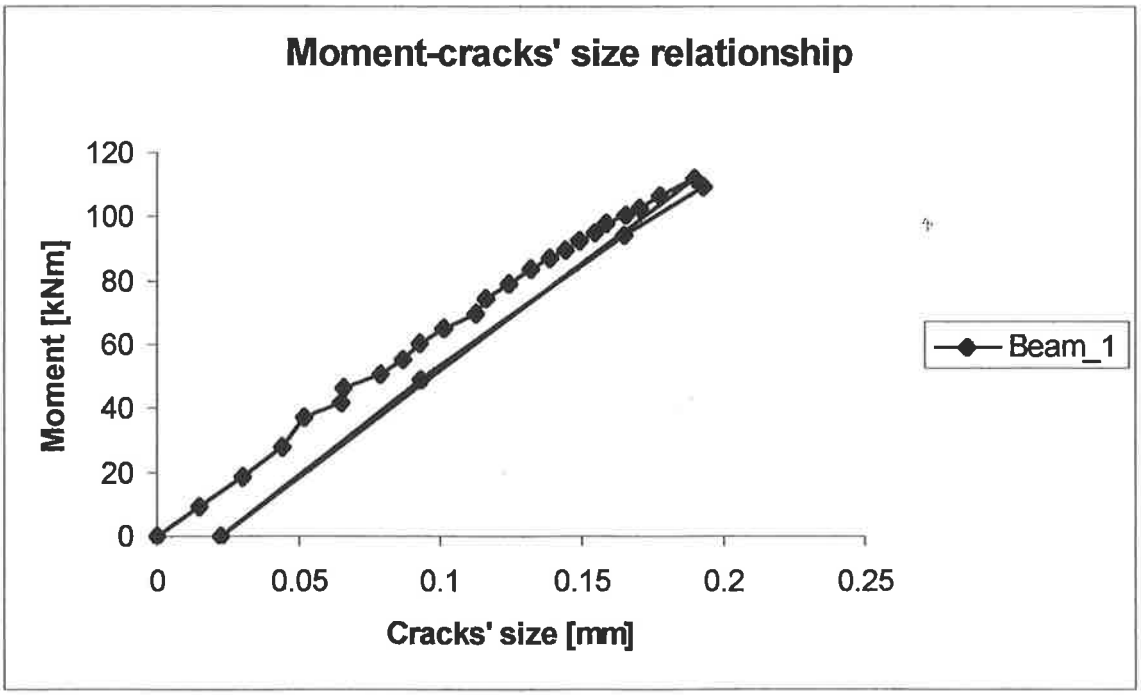

Figure 8.31. – Moment-cracks' size relationship of beam 1.

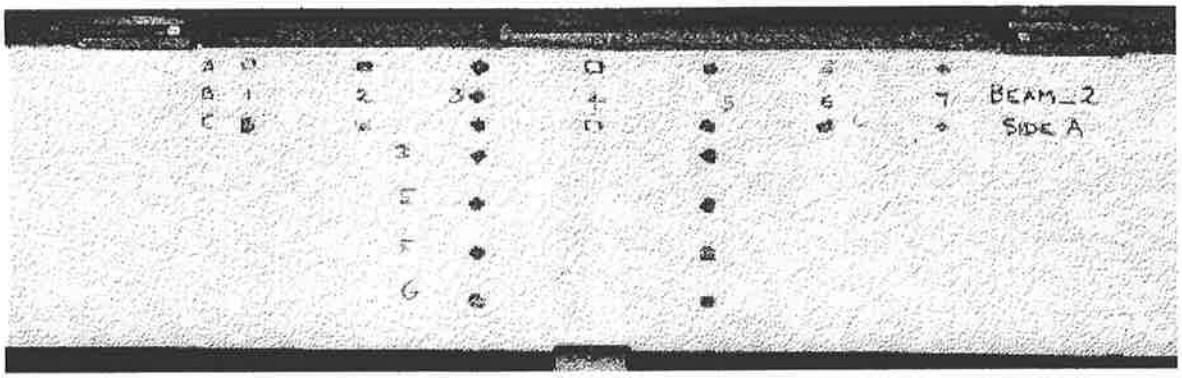

Figure 8.32. – Beam 2 before loading.

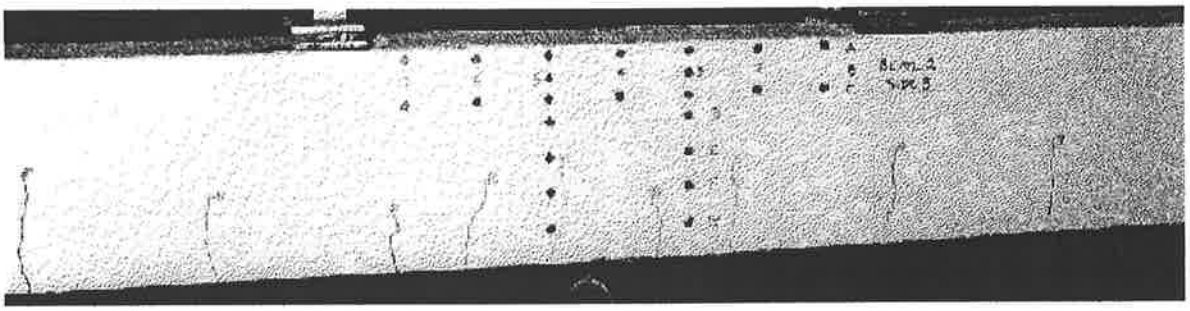

Figure 8.33. – Beam 2 at 10 kN.

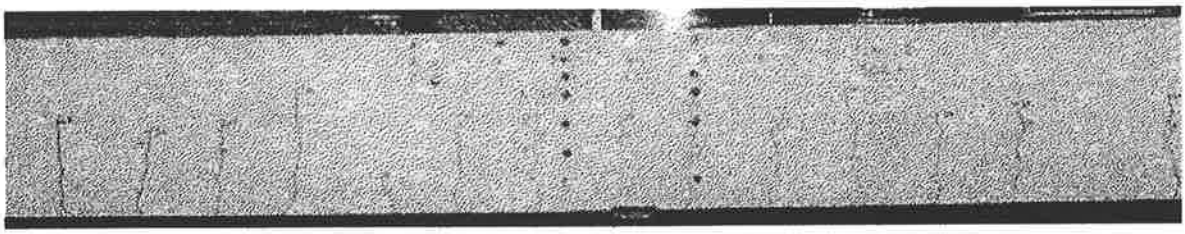

Figure 8.34. – Beam 2 at 19.5 kN.

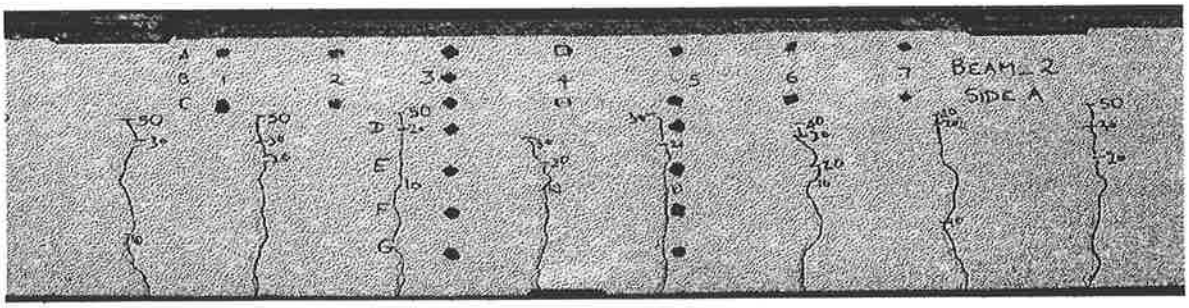

Figure 8.35. – Beam 2 at 60 kN.

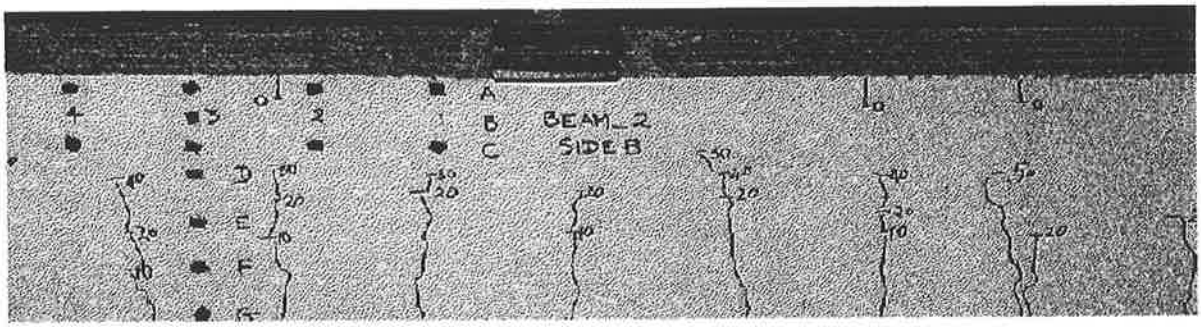

Figure 8.36. – Beam 2 unloaded.

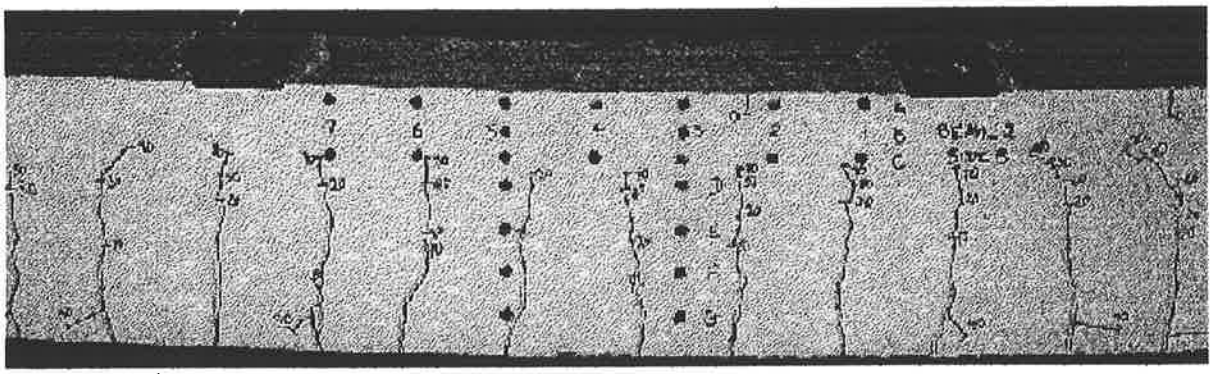

Figure 8.37. – Reloaded at 90 kN.

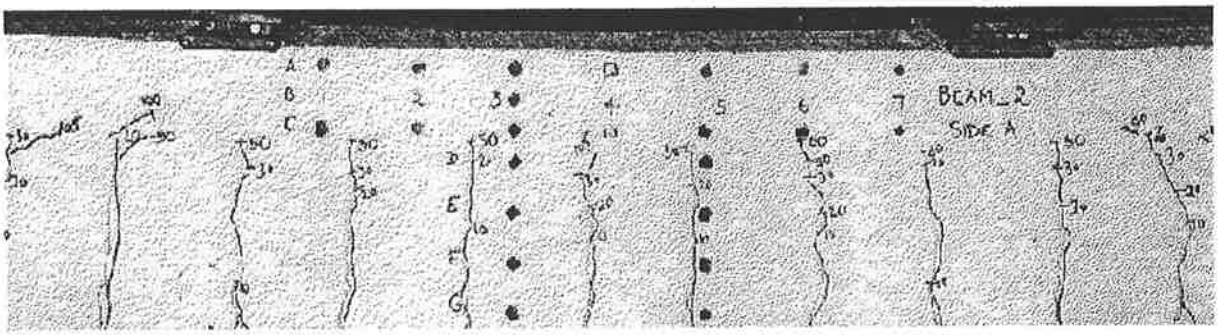

Figure 8.38. – Beam 2 reloaded at 105 kN.

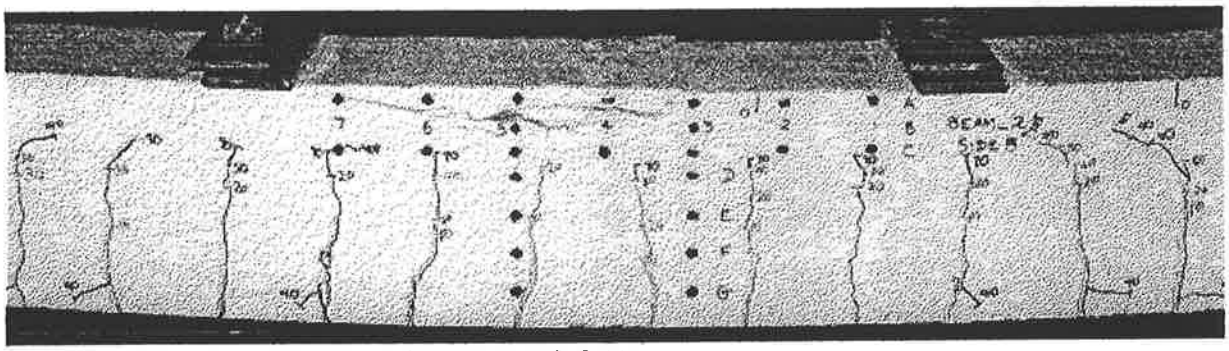

Figure 8.39. – Beam 2 starts failing at 118.8 kN.

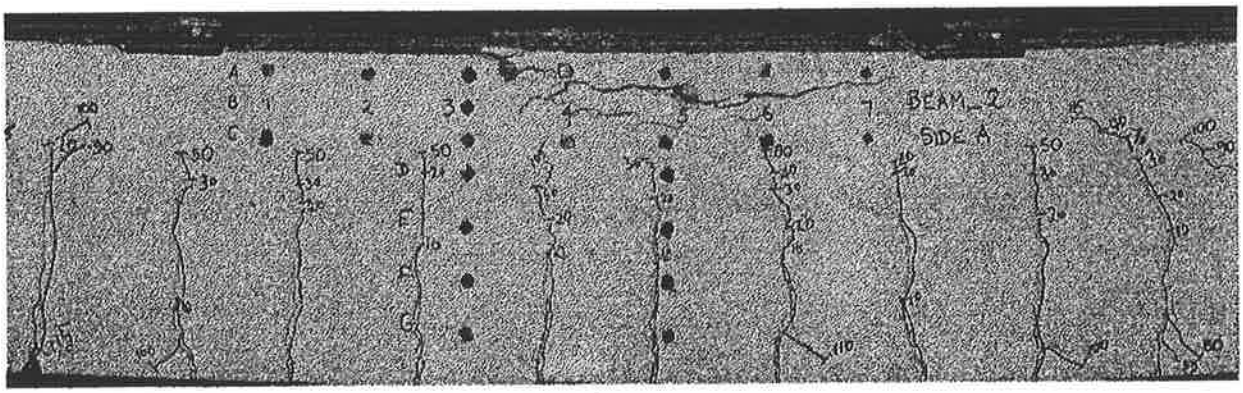

Figure 8.40. – Beam 2 starts failing at 118.8kN.

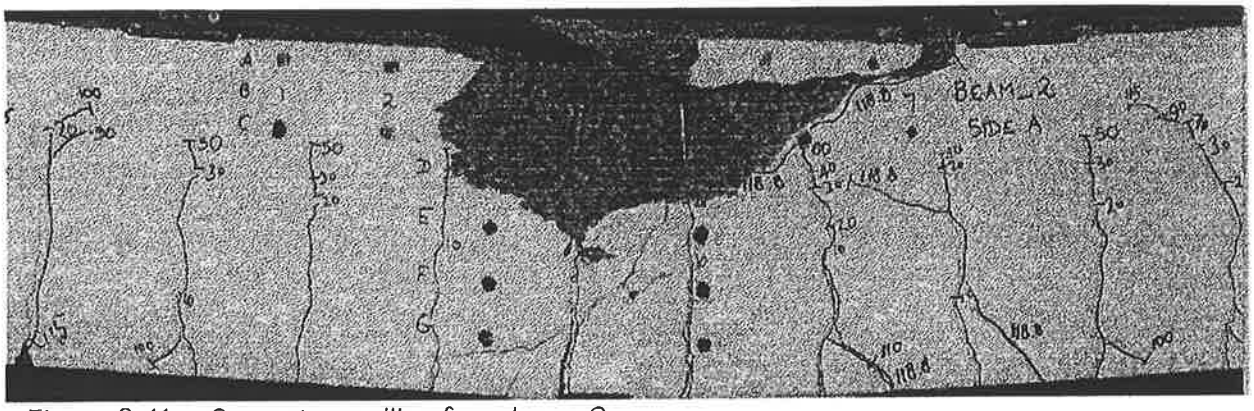

Figure 8.41. – Concrete spalling from beam 2.

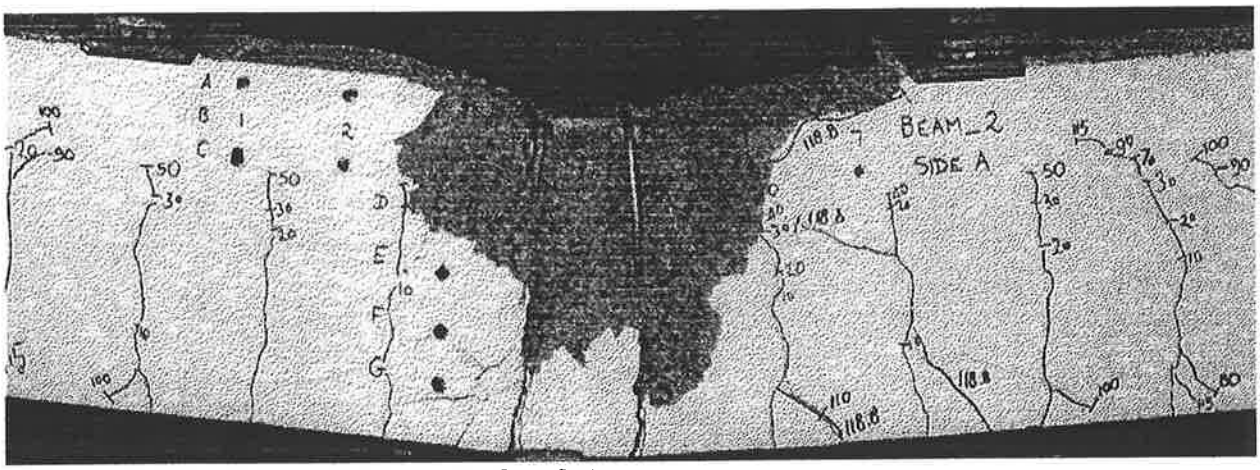

Figure 8.42. – Far view of beam 2 after failure.

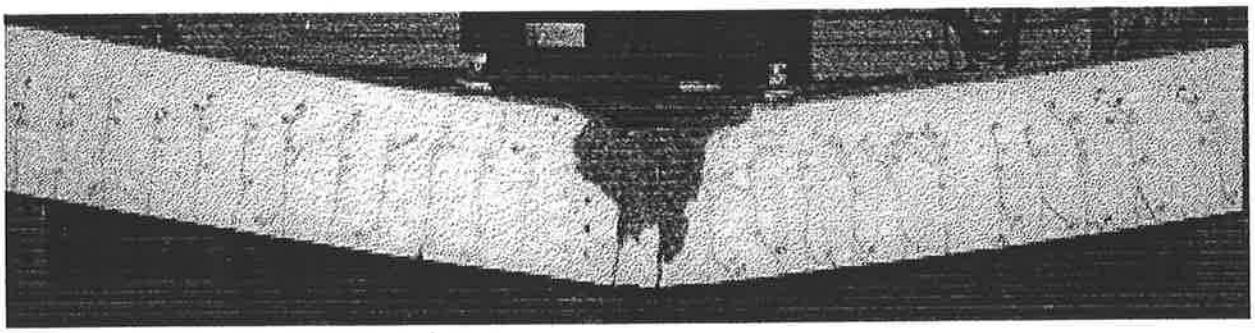

Figure 8.43. – Beam 2 after failure.

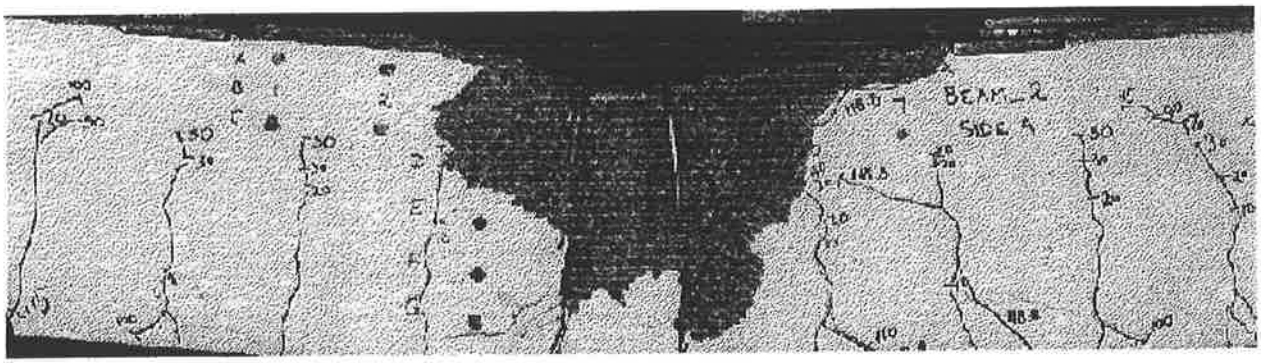

Figure 8.44. – Beam 2 after failure.

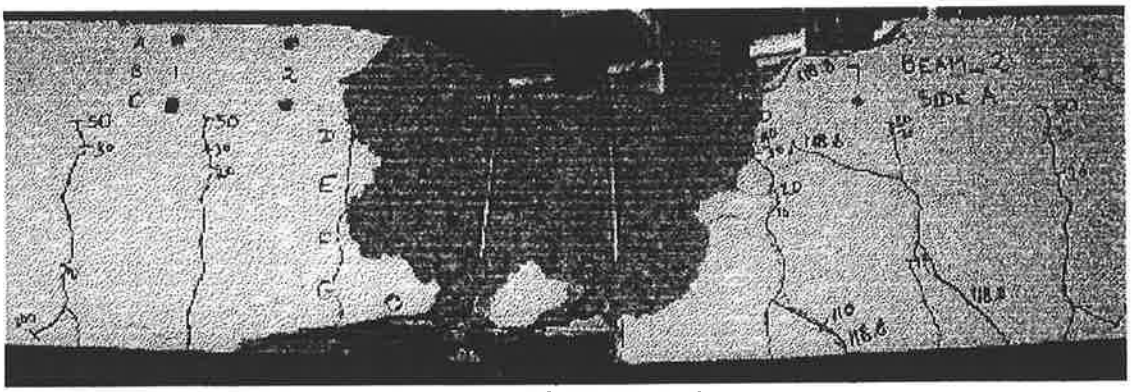

Figure 8.45. – Spalled concrete removed from beam 2.

Figure 8.46. – Failure of the FRP rebar at the top of beam 2.

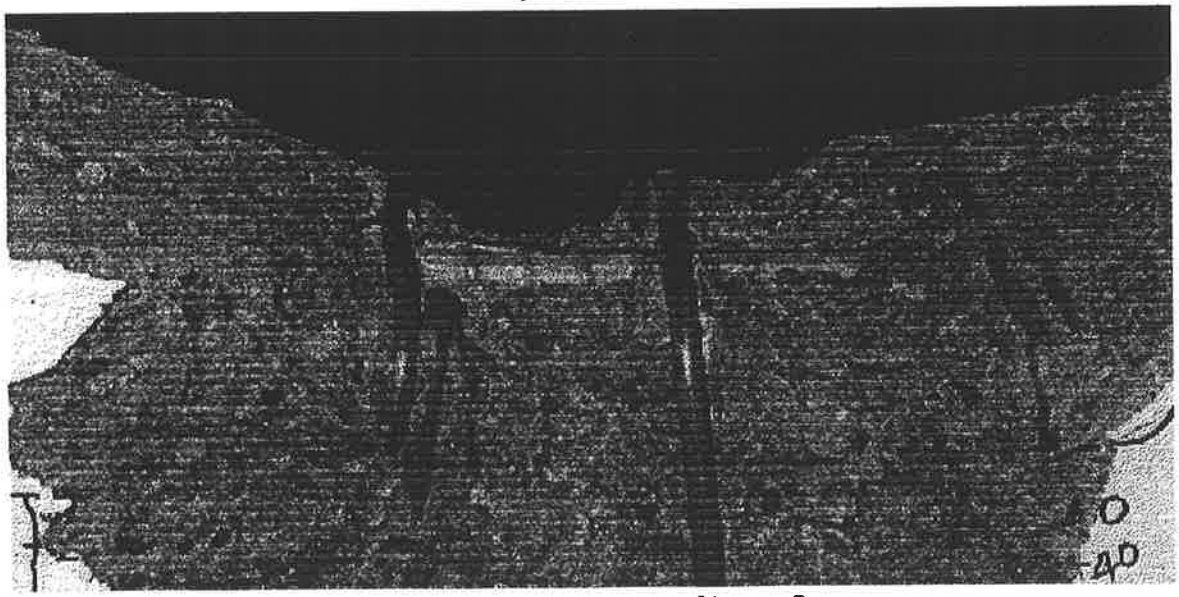

Figure 8.47. – Failure of the FRP rebar at the top of beam 2.

Figure 8.48. – FRP rebar at the top of beam 2 after failure.

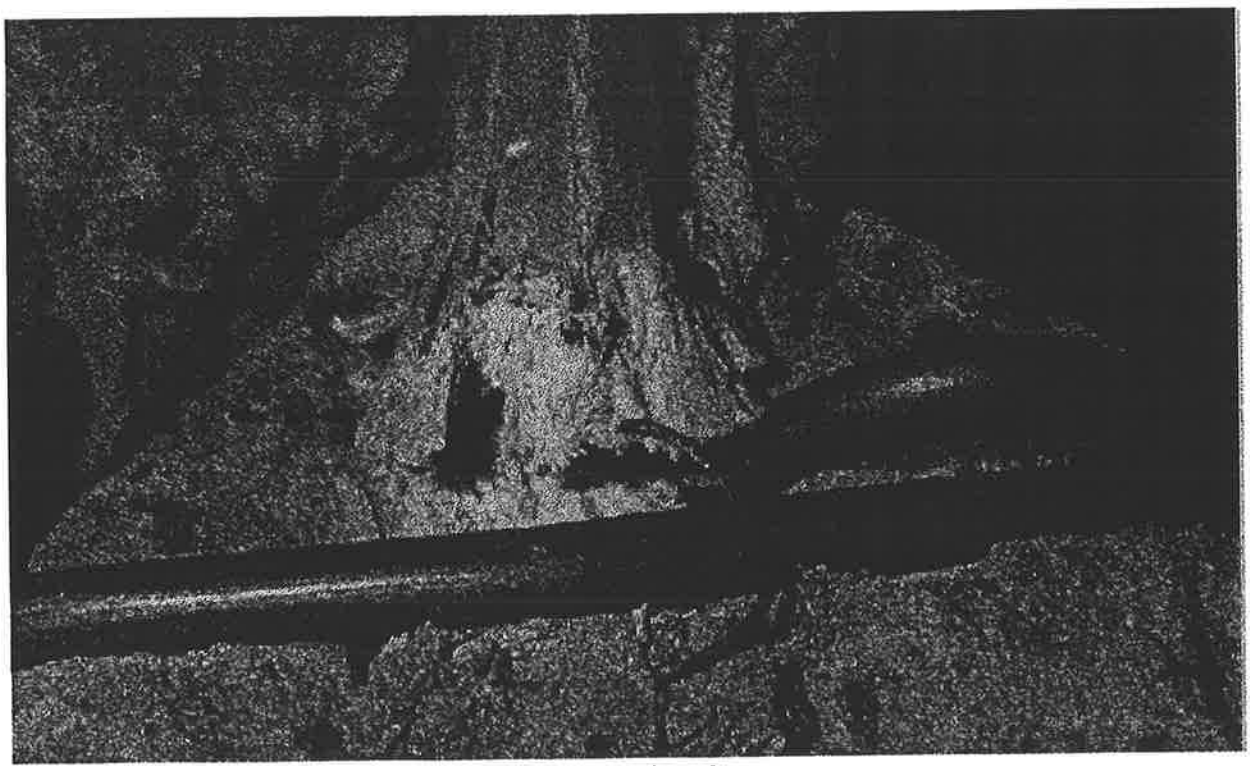

Figure 8.49. – FRP rebar at the top of beam 2 after failure.

Figure 8.50. – FRP rebar at the top of beam 2 after failure.

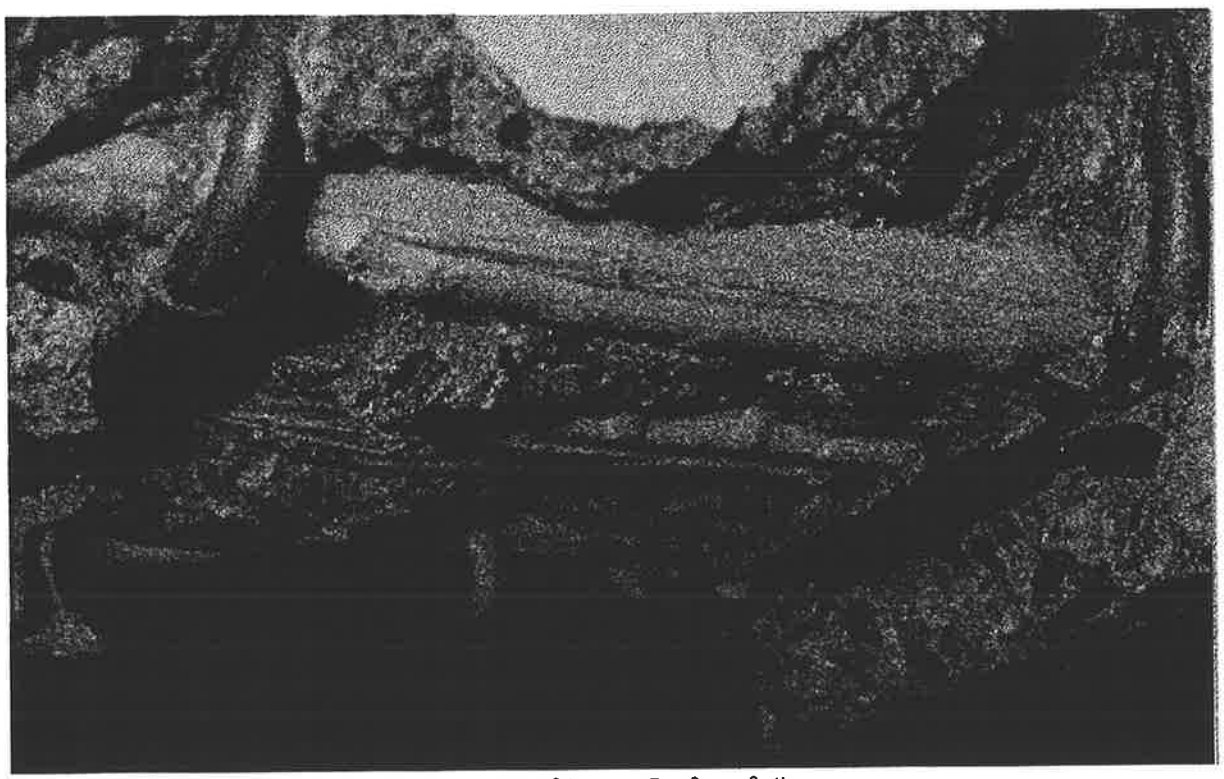

Figure 8.51. – FRP rebars at the bottom of beam 2 after failure.

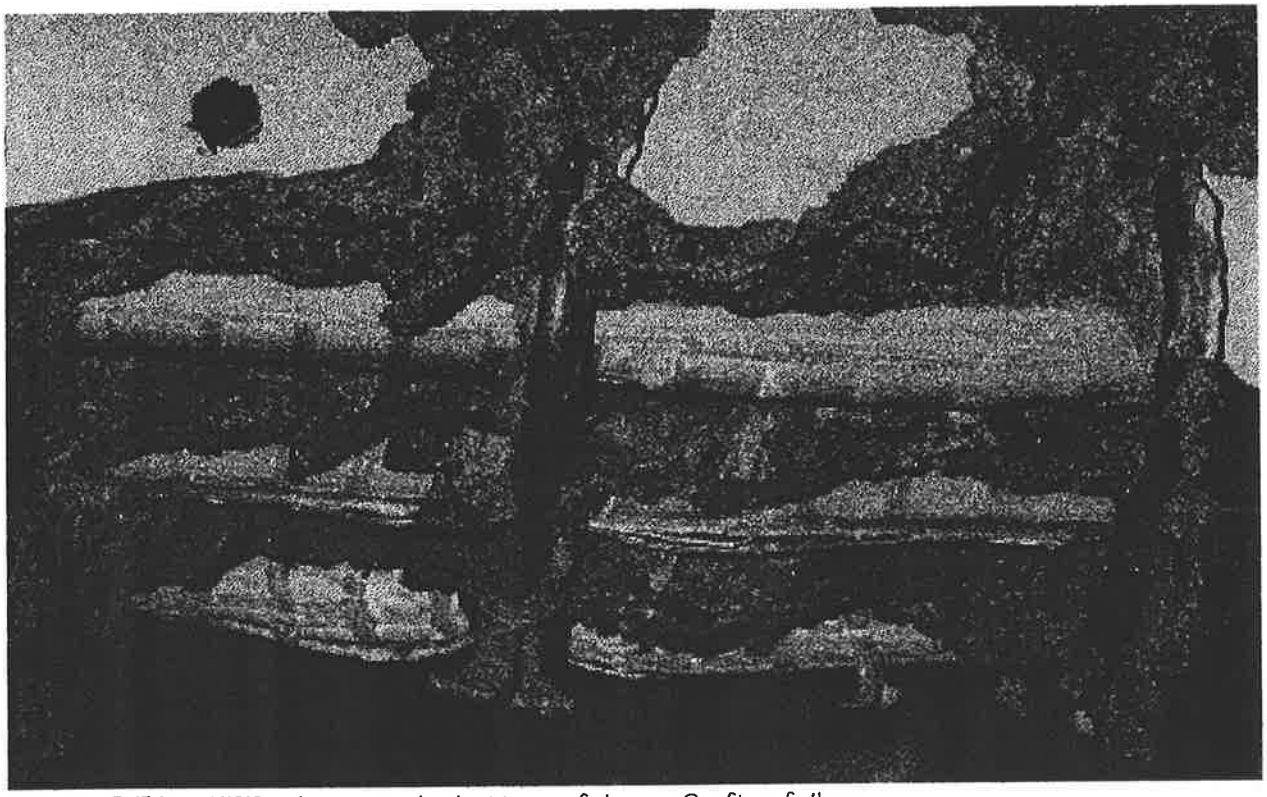

Figure 8.52. – FRP rebars at the bottom of beam 2 after failure.

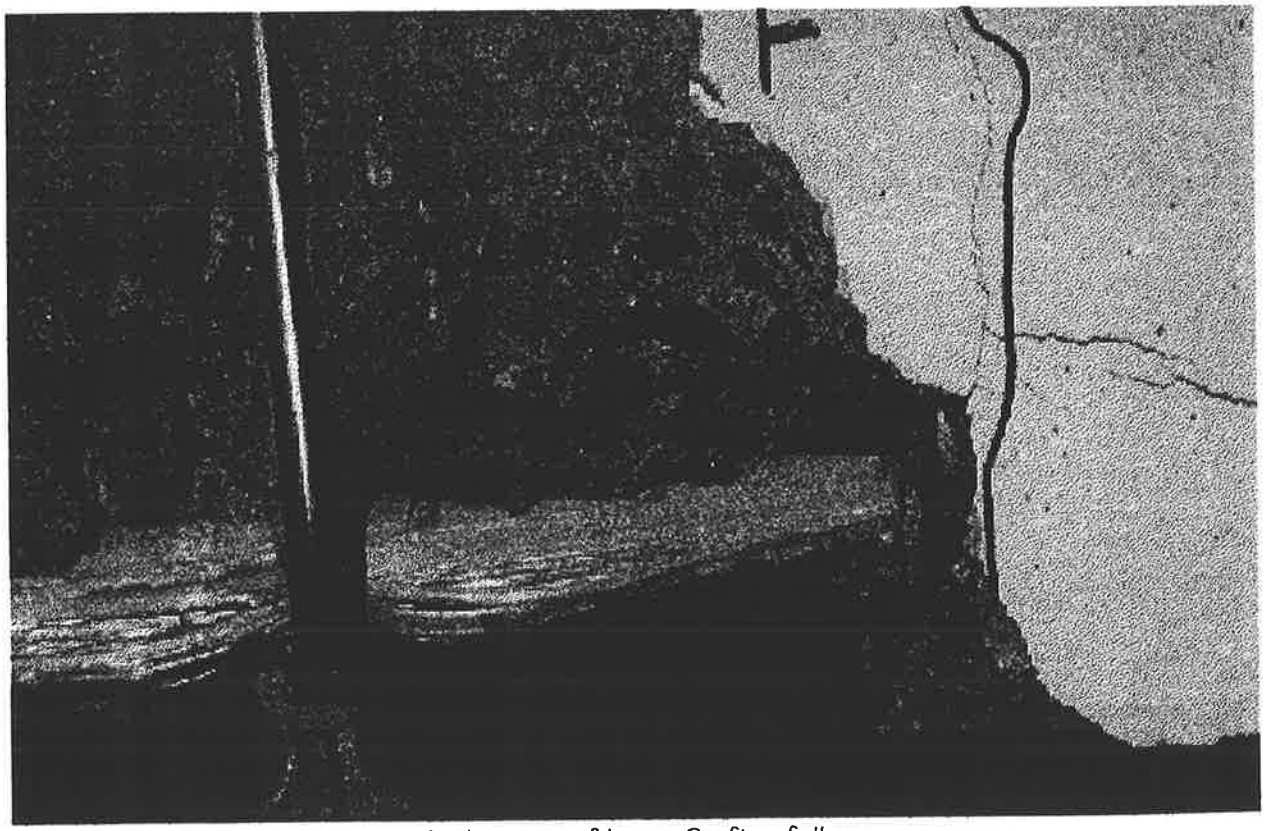

Figure 8.53. – FRP rebars at the bottom of beam 2 after failure.

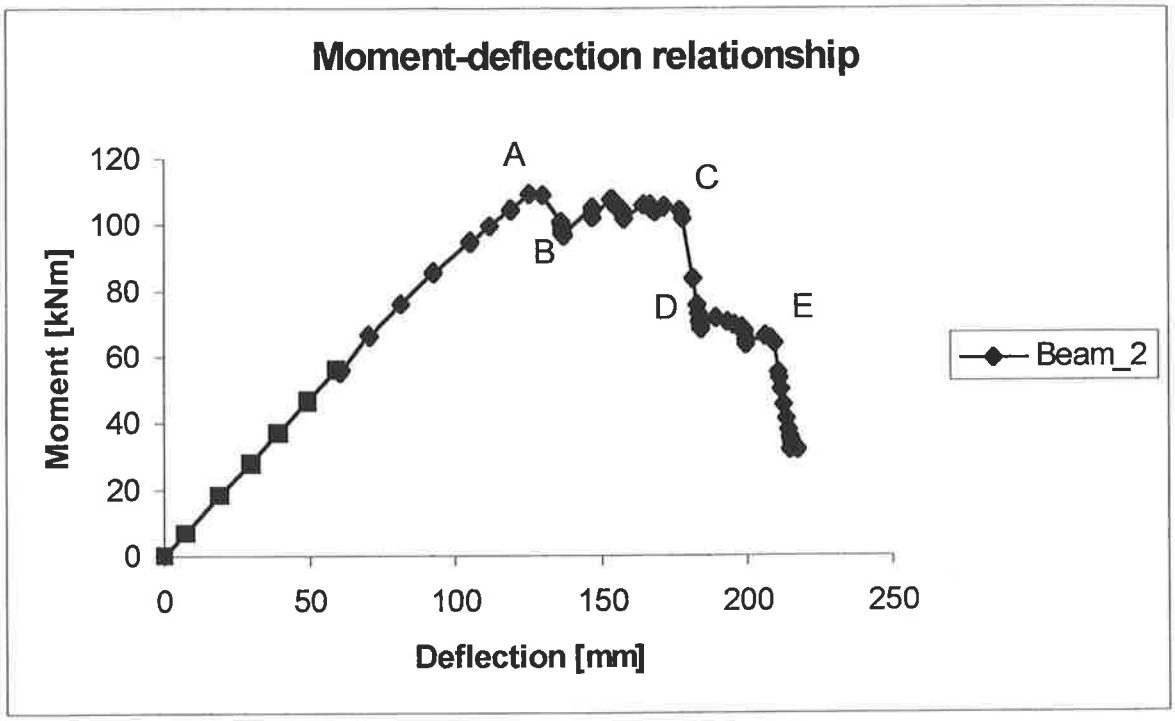

Figure 8.54. – Moment-deflection relationship of beam 2.

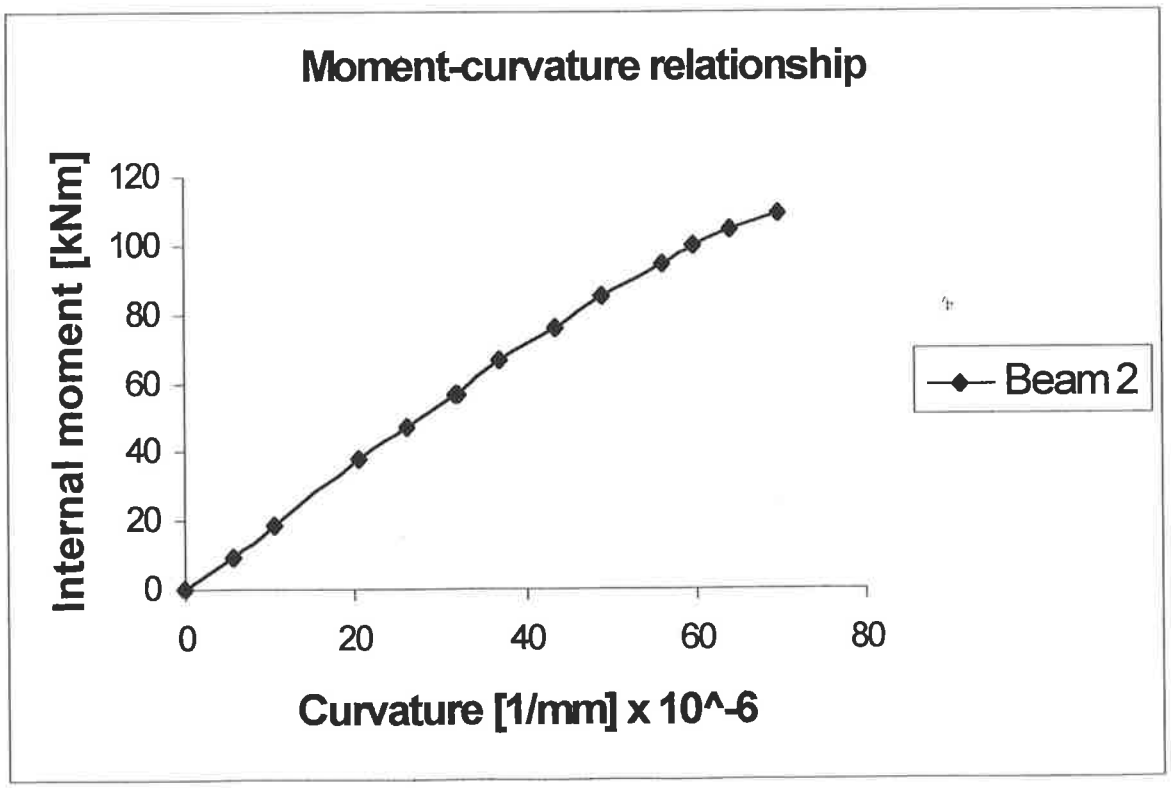

Figure 8.55. – Moment-curvature relationship of beam 2.

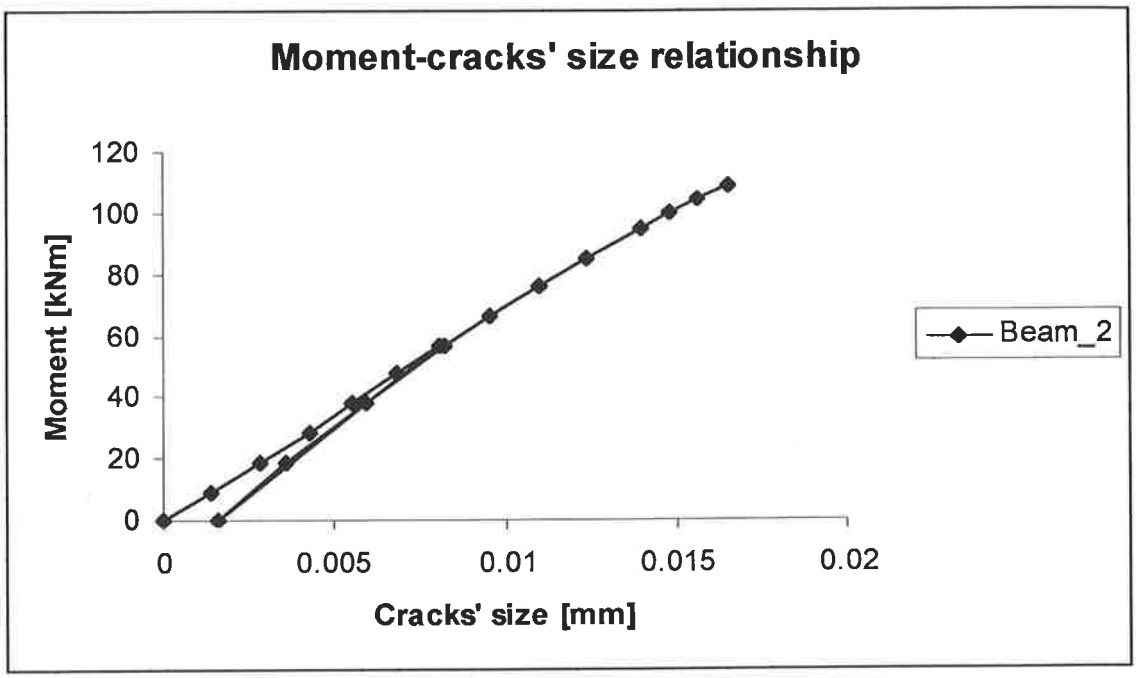

Figure 8.56. – Cracks' size of beam 2 up to crushing the top concrete.

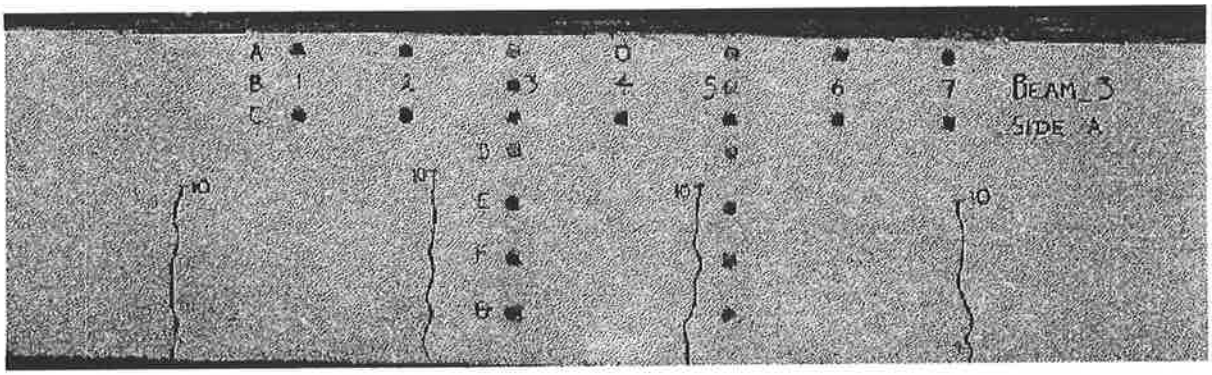

Figure 8.57. – Beam 3 at 10 kN.

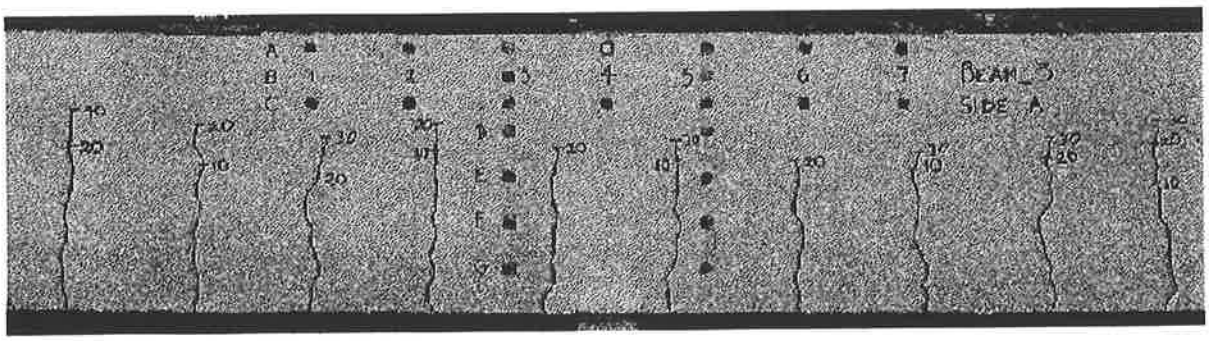

Figure 8.58. – Beam 3 at 40 kN.

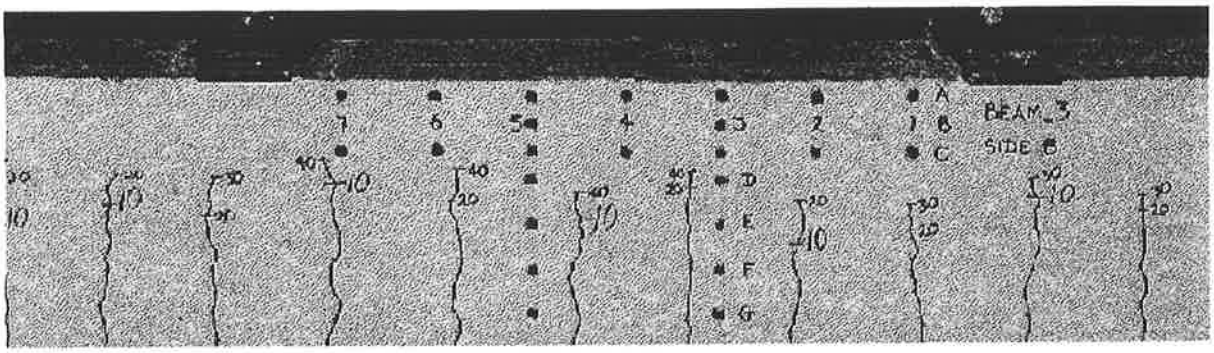

Figure 8.59. – Beam 3 at 40 kN.

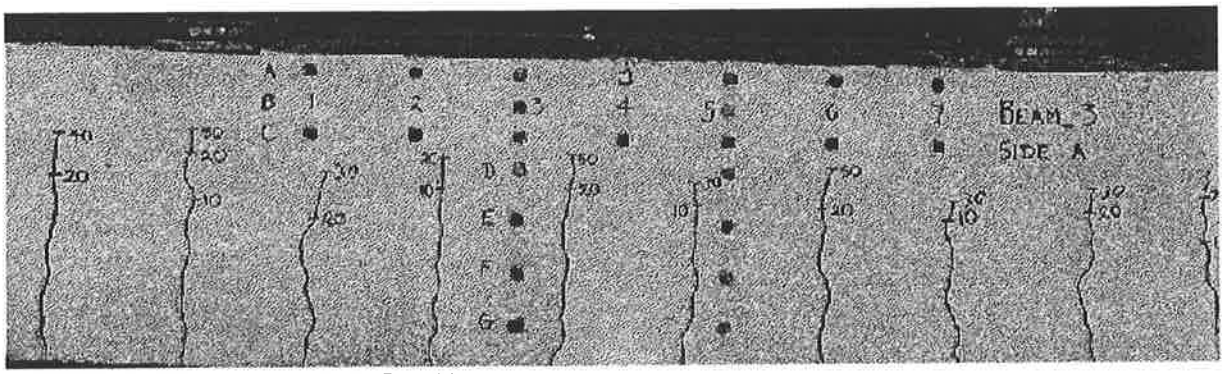

Figure 8.60. – Beam 3 at 50 kN.

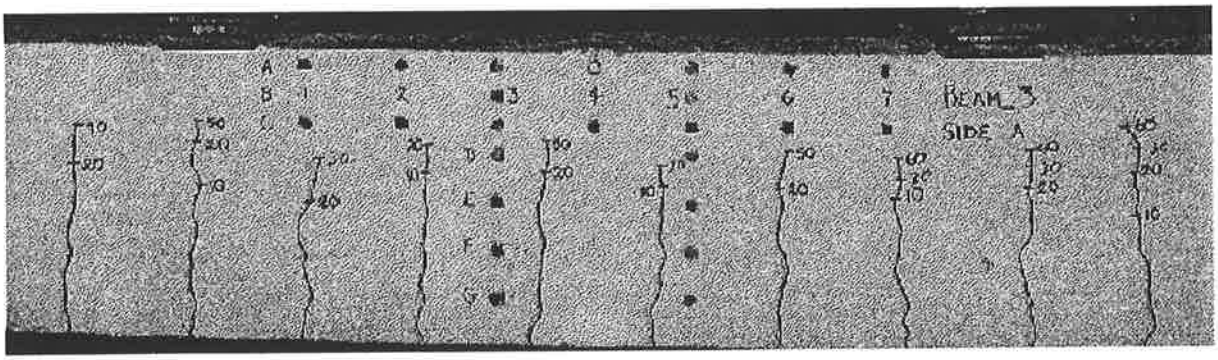

Figure 8.61. – Beam 3 at 90 kN.

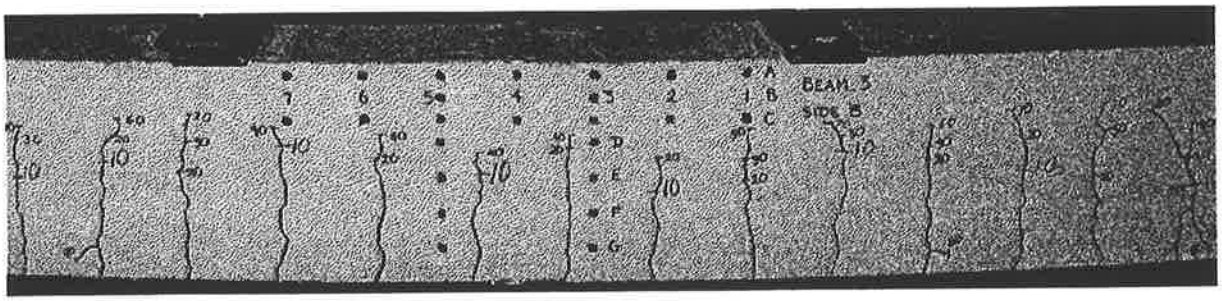

Figure 8.62. – Beam 3 at 90 kN.

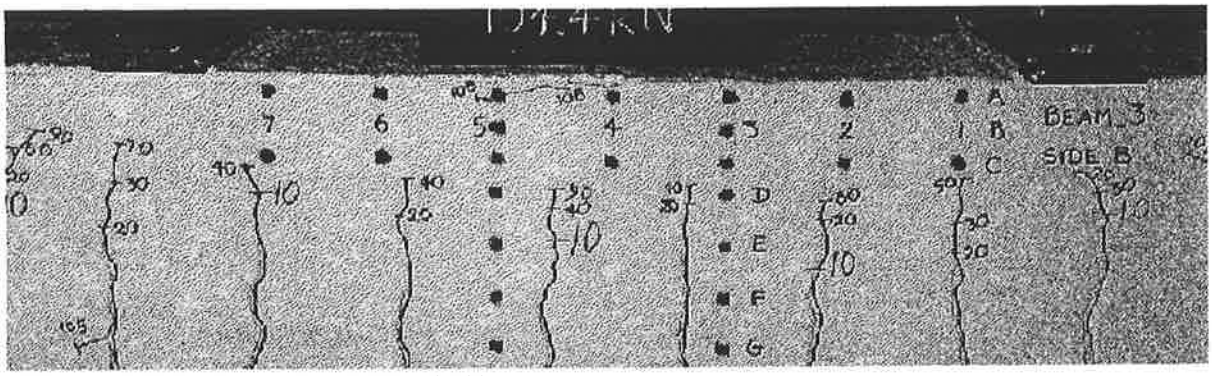

Figure 8.63. – Beam 3 at 104.4 kN.

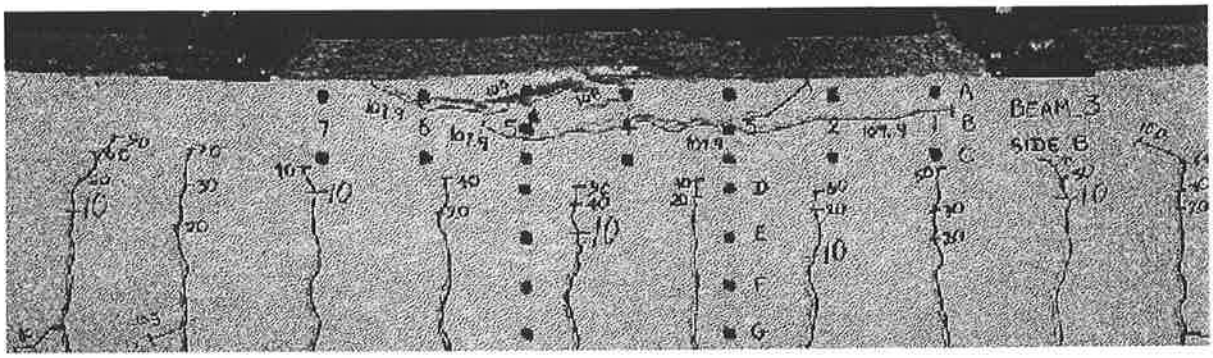

Figure 8.64. – Beam 3 at 107.9 kN.

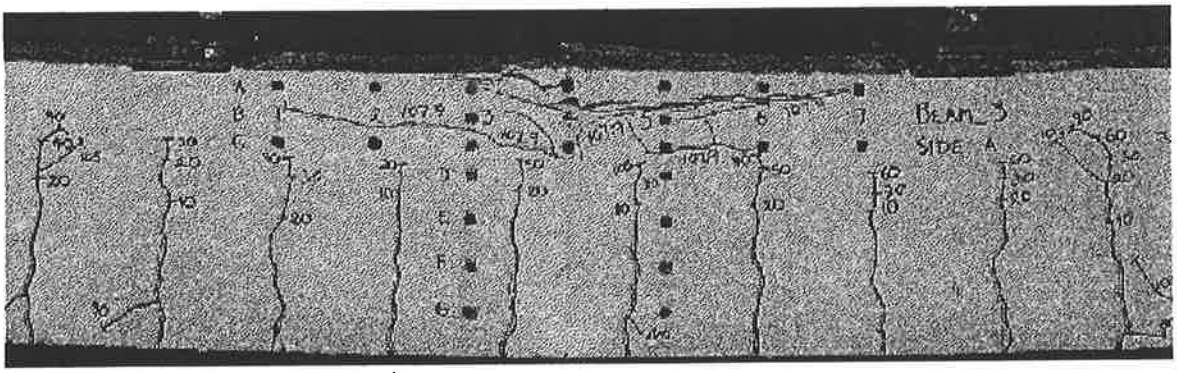

Figure 8.65. – Beam 3 at 107.9 kN.

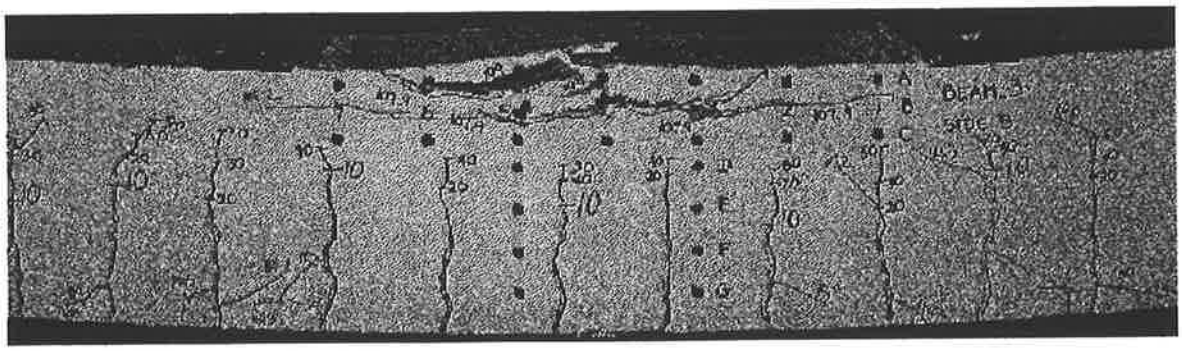

Figure 8.66. – Beam 3 at 114.2 kN.

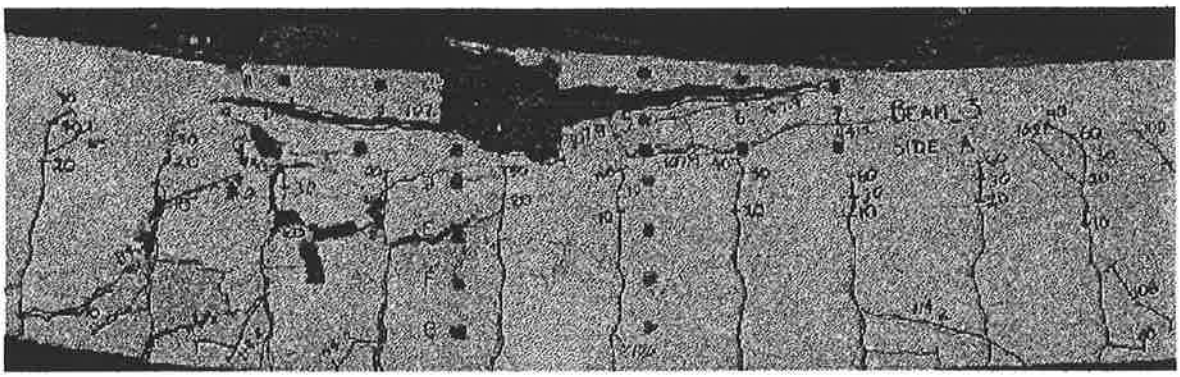

Figure 8.67. – Beam 3 at failure.

Figure 8.68. – Loose concrete removed from beam 3.

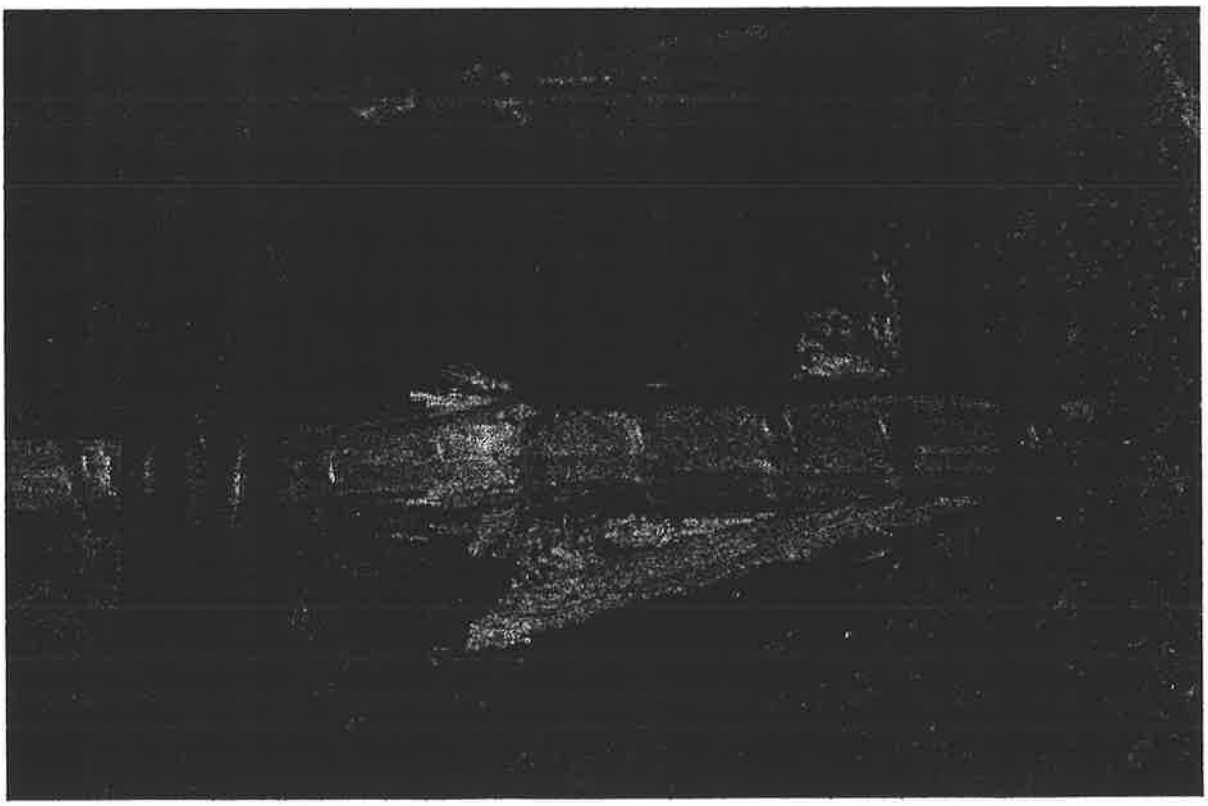

Figure 8.69. – FRP rebars at the top of beam 3 after failure.

Figure 8.70. – FRP rebars at the top of beam 3 after failure.

Figure 8.71. – FRP rebars at the top of beam 3 after failure.

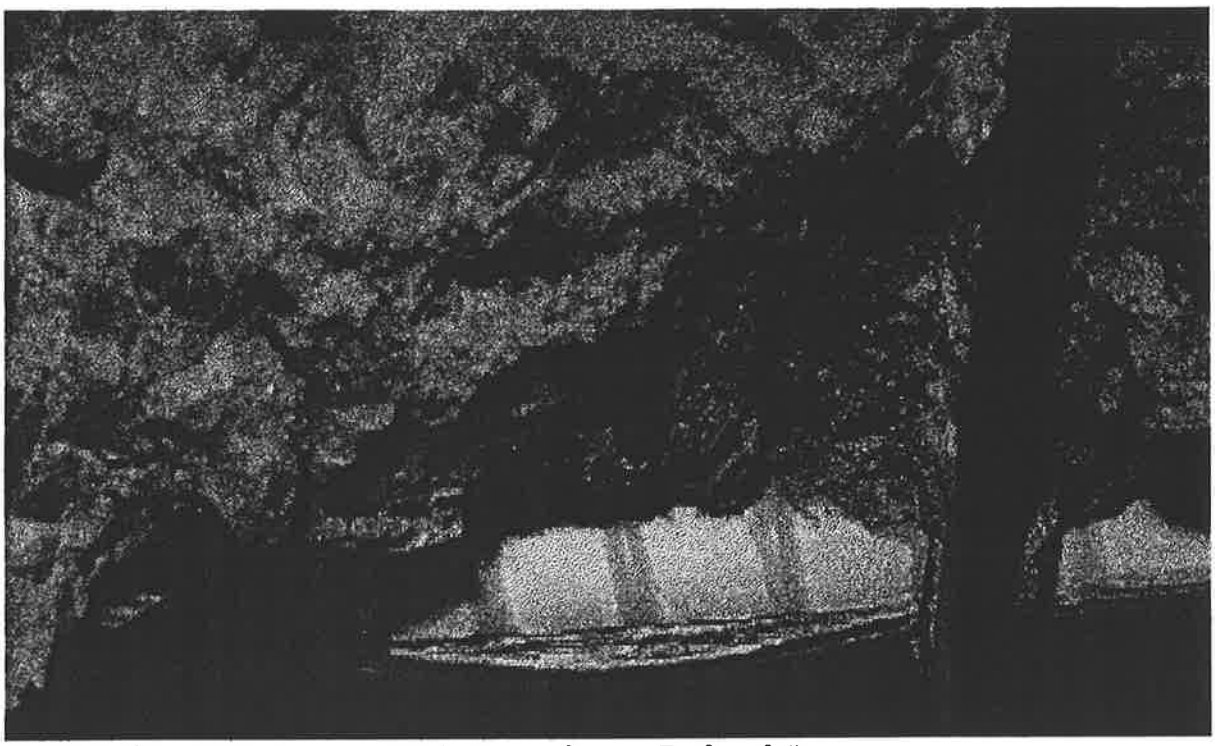

Figure 8.72. – FRP rebars at the bottom of beam 3 after failure.

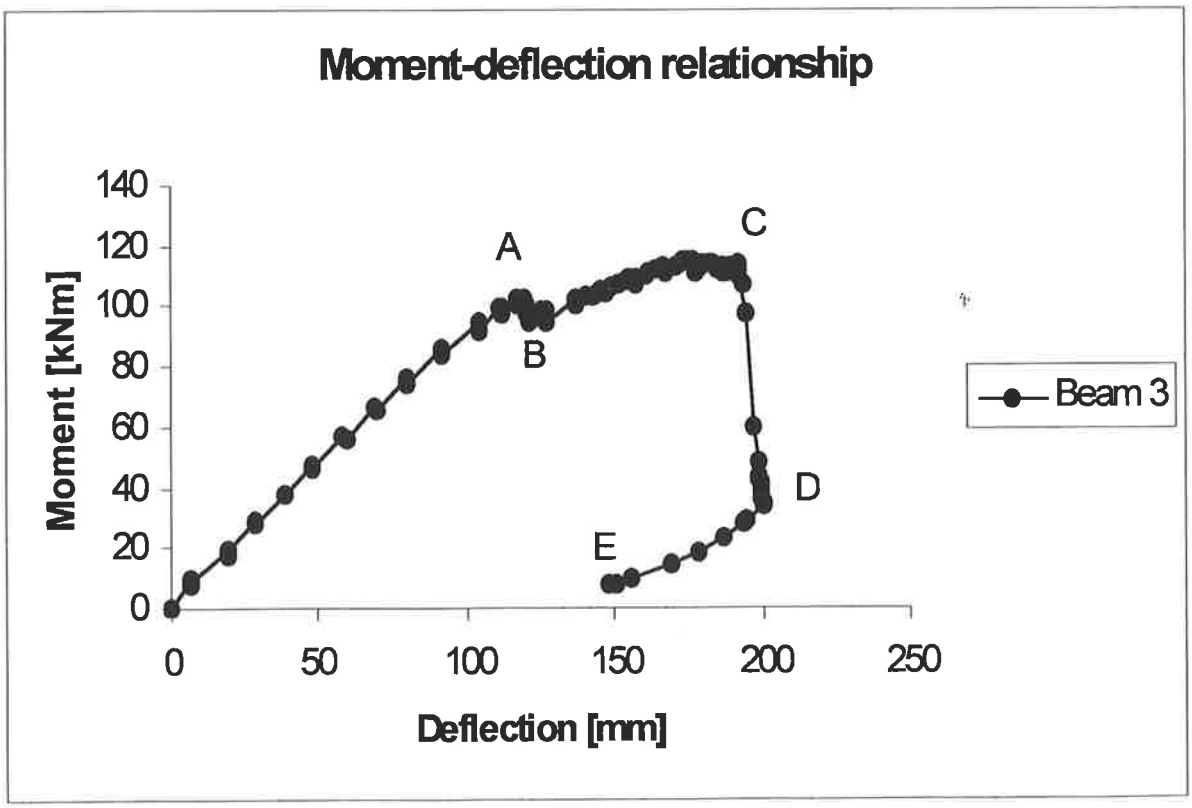

Figure 8.73. – Moment-deflection relationship of beam 3.

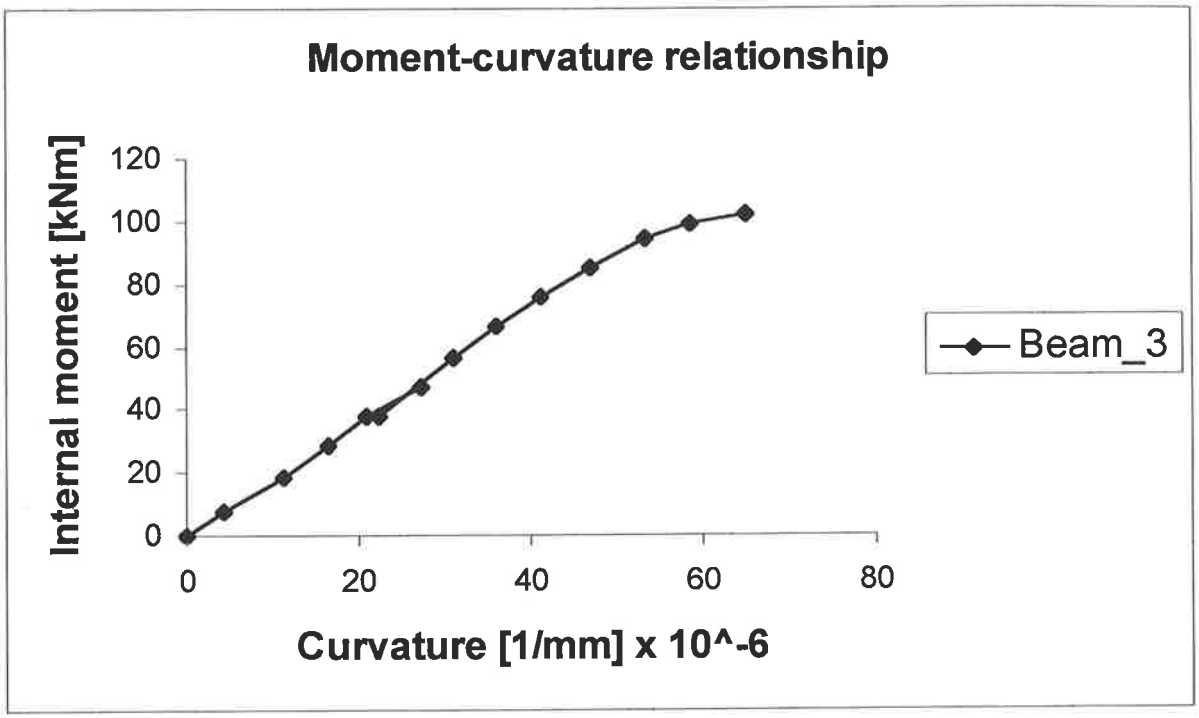

Figure 8.74. – Moment-curvature relationship of beam 3.

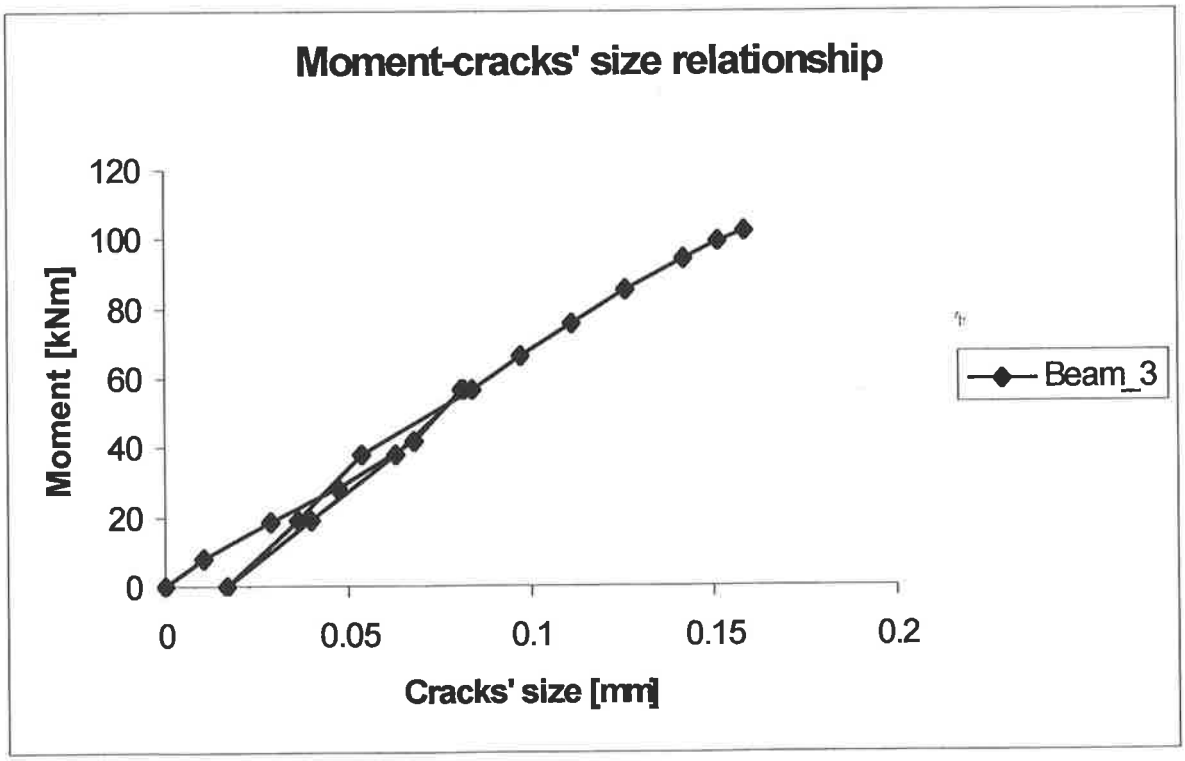

Figure 8.75. – Crack sizes in beam 3.

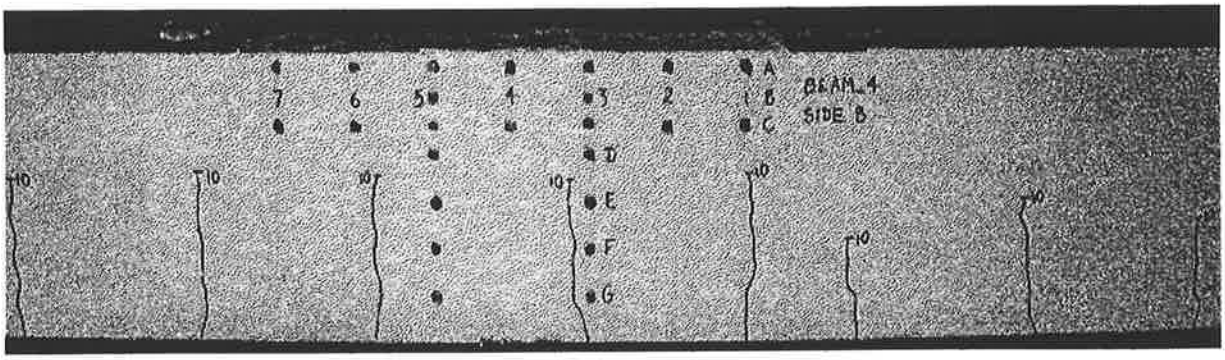

Figure 8.76. – Beam 4 at 10 kN.

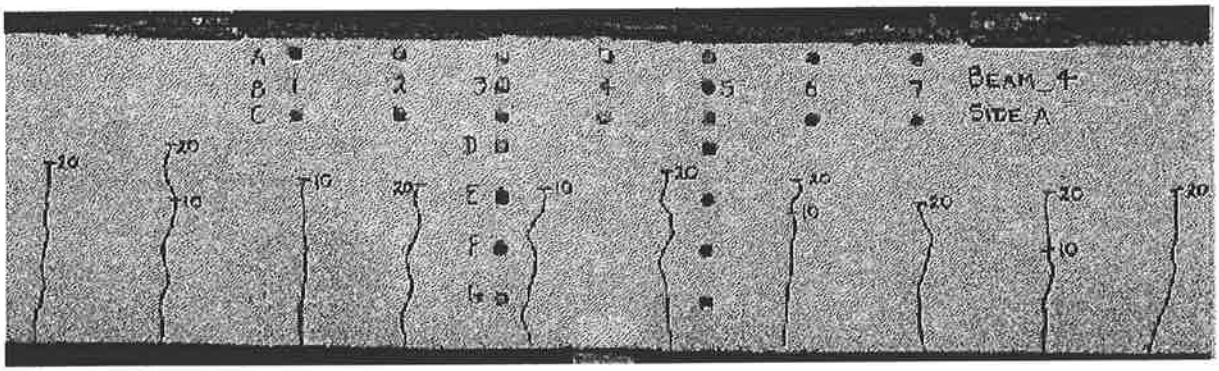

Figure 8.77. – Beam 4 at 20 kN.

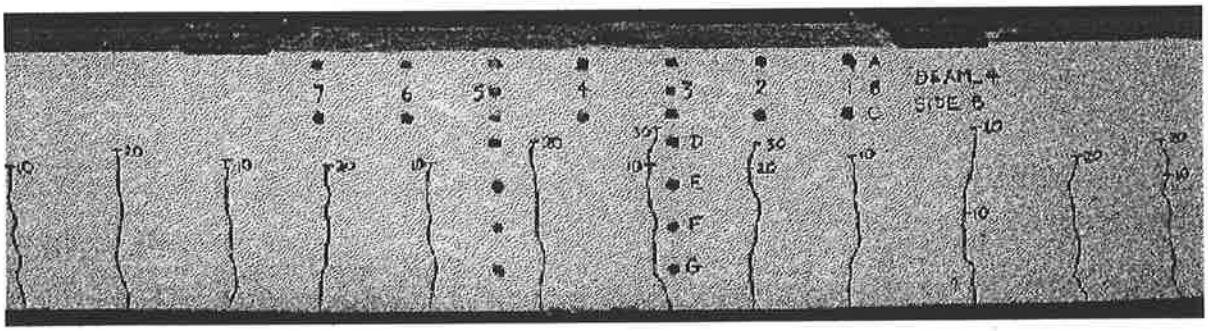

Figure 8.78. – Beam 4 at 30kN.

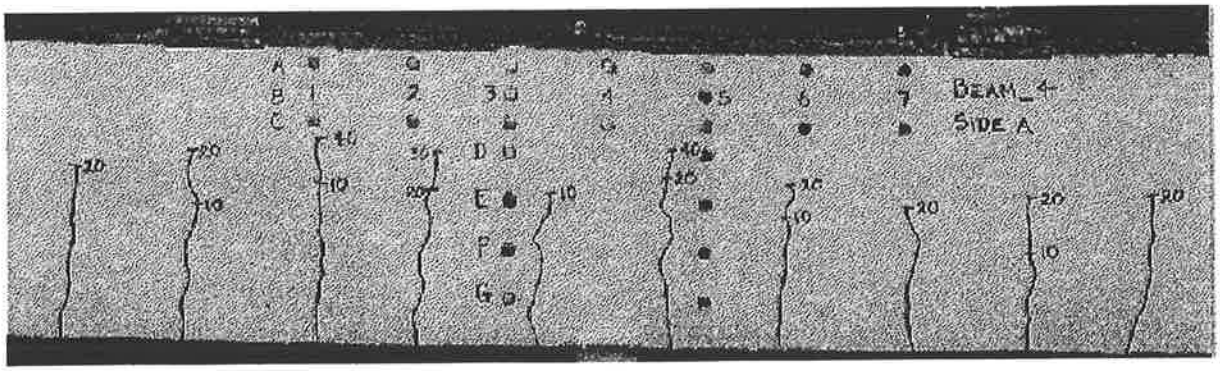

Figure 8.79. – Beam 4 at 40 kN.

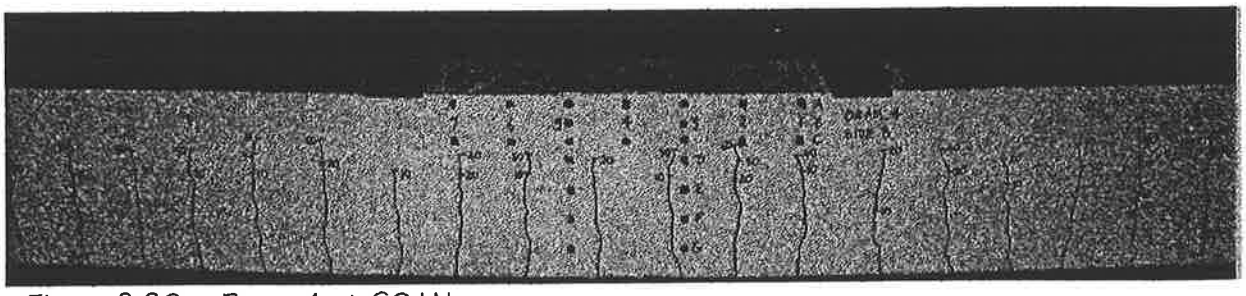

Figure 8.80. – Beam 4 at 60 kN.

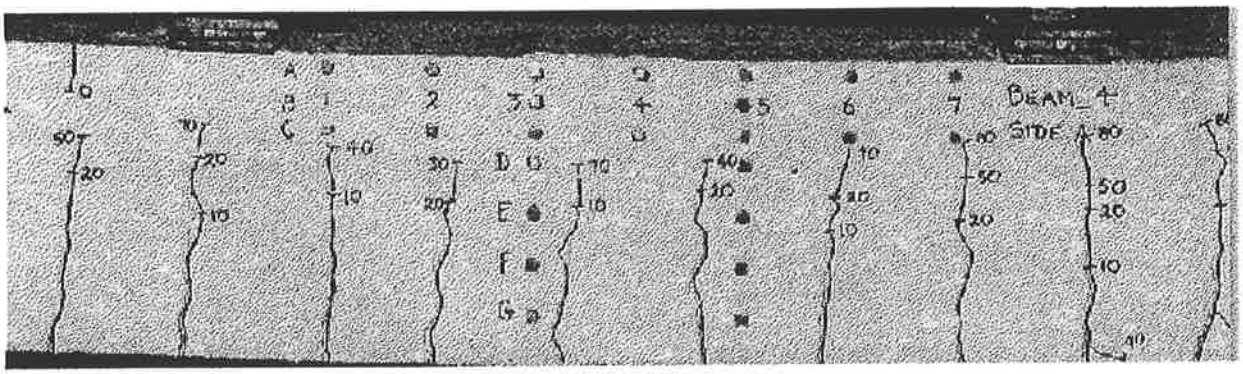

Figure 8.81. – Beam 4 at 90 kN.

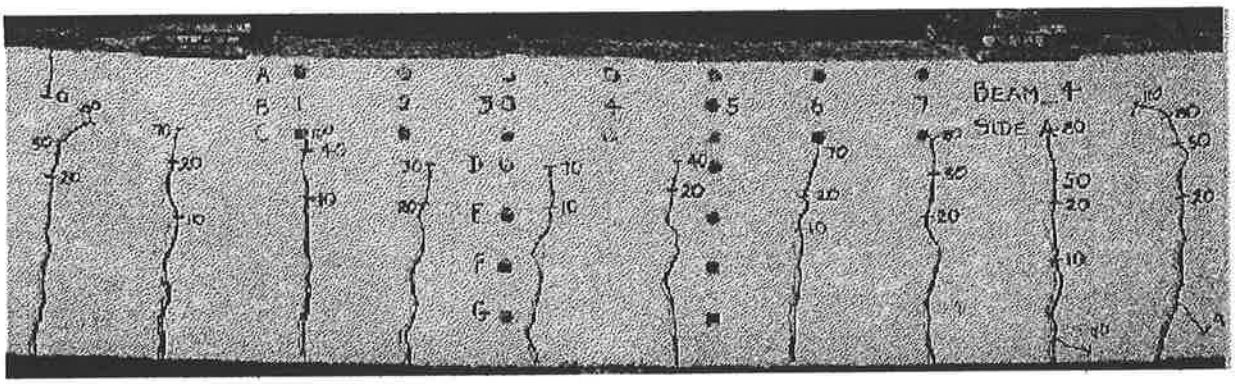

Figure 8.82. – Beam 4 at 110 kN.

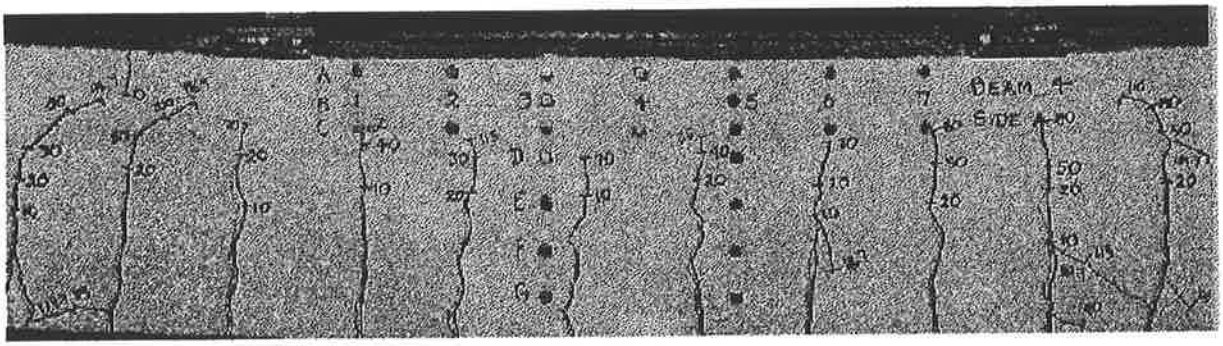

Figure 8.83. – Beam 4 at 119.7 kN.

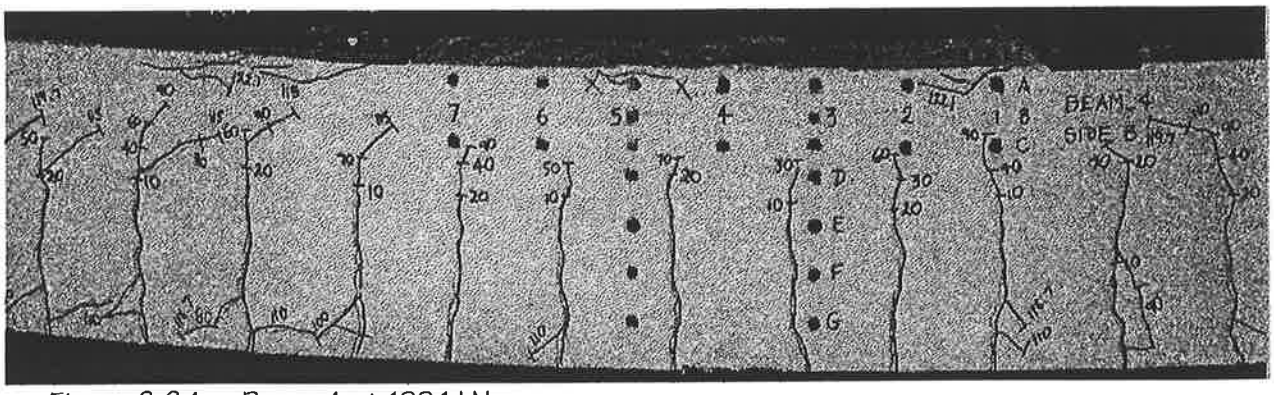

Figure 8.84. – Beam 4 at 122.1 kN.

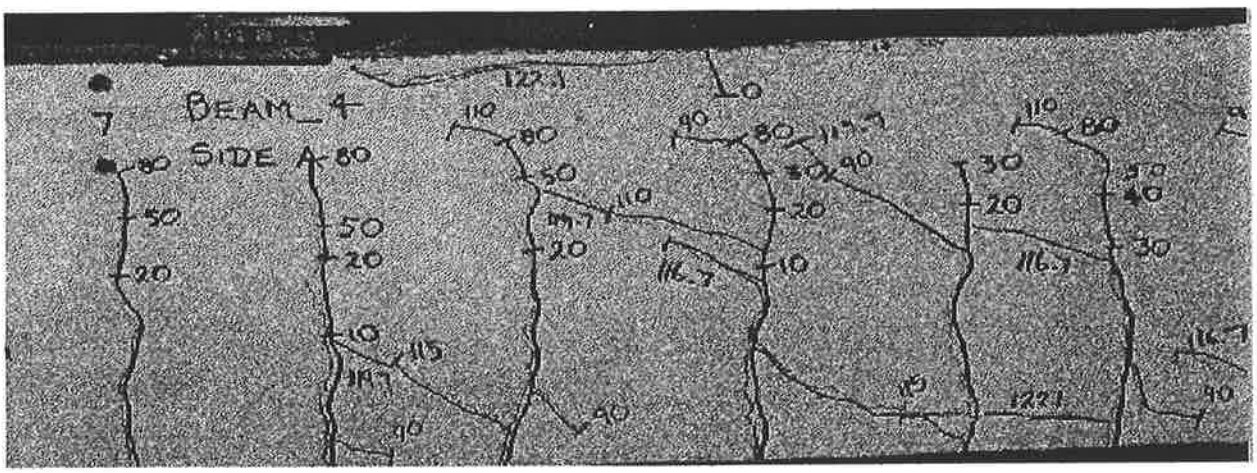

Figure 8.85. – Beam 4 at 122.1 kN.

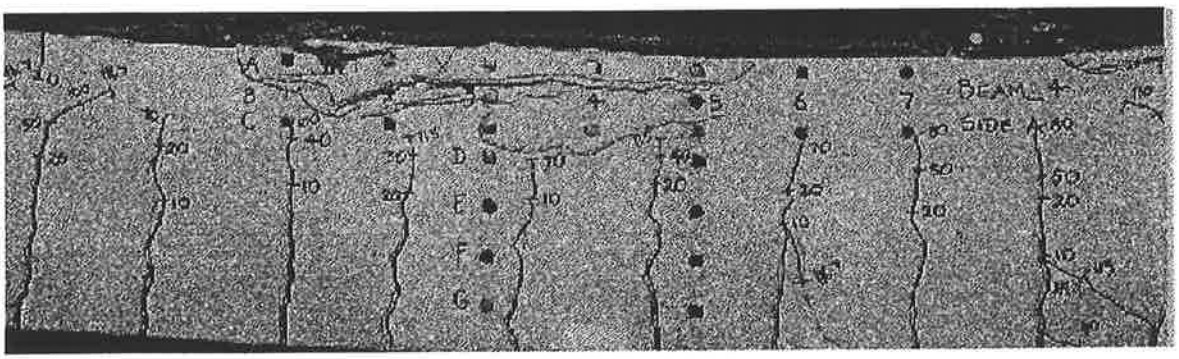

Figure 8.86. – Beam 4 at 123.9 kN.

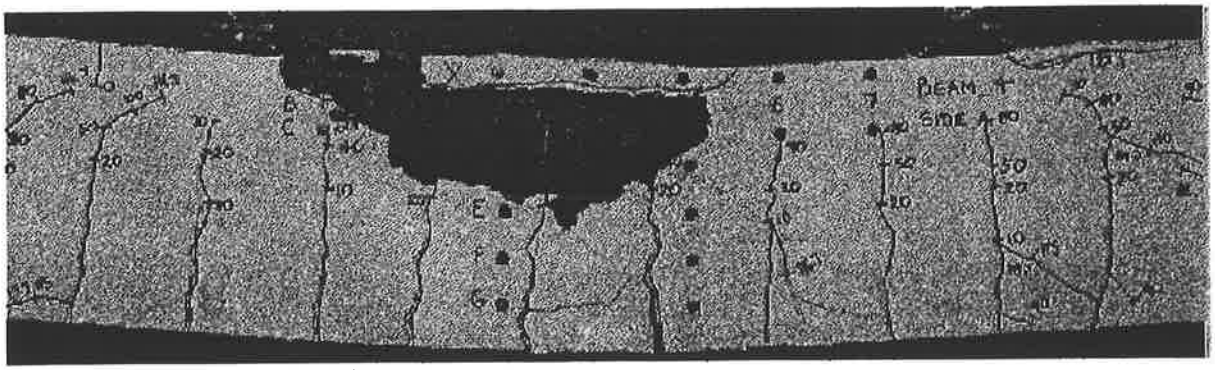

Figure 8.87. – Beam 4 at failure.

Figure 8.88. – Beam 4 at failure.

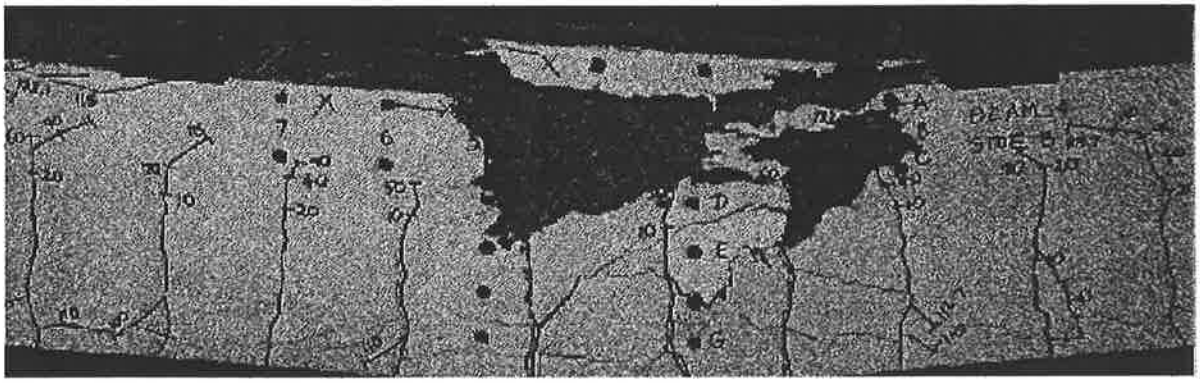

Figure 8.89. – Beam 4 at failure.

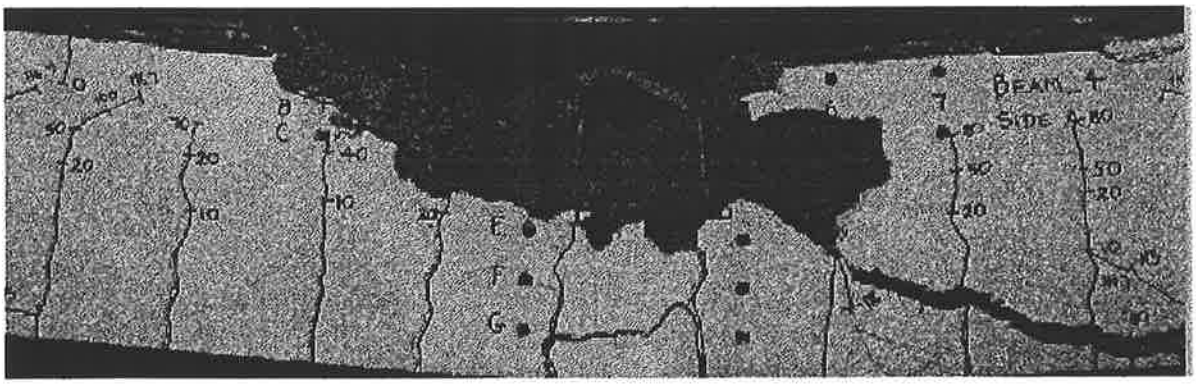

Figure 8.90. – Discovering of the steel rebar at the top of beam 4.

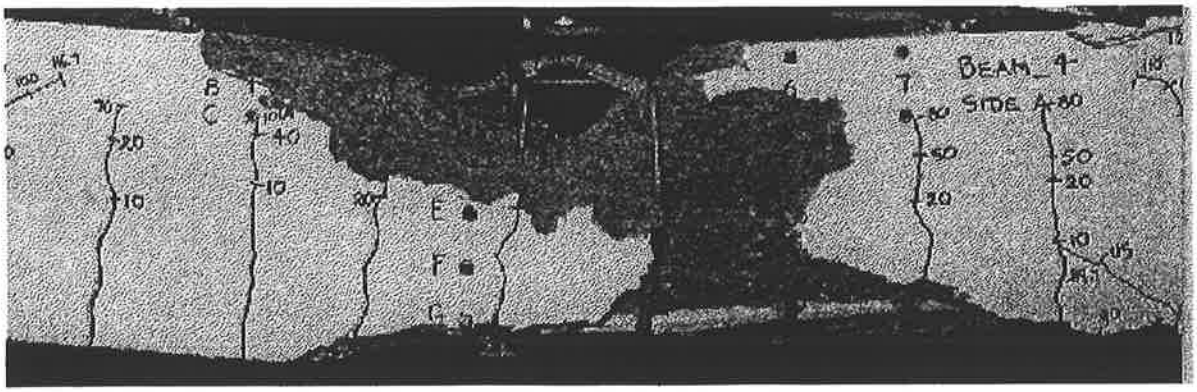

Figure 8.91. – Discovering of the FRP rebars at the bottom of beam 4.

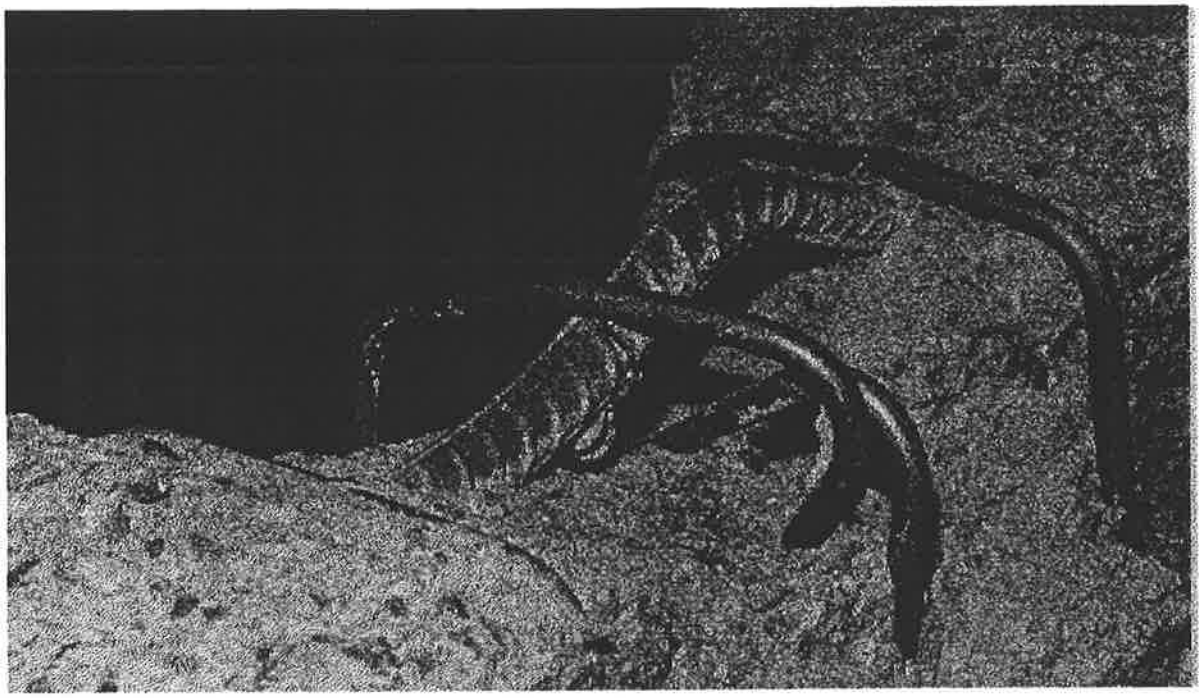

Figure 8.92. – Steel rebar at the top of beam 4.

Figure 8.93. – FRP rebars at the bottom of beam 4.

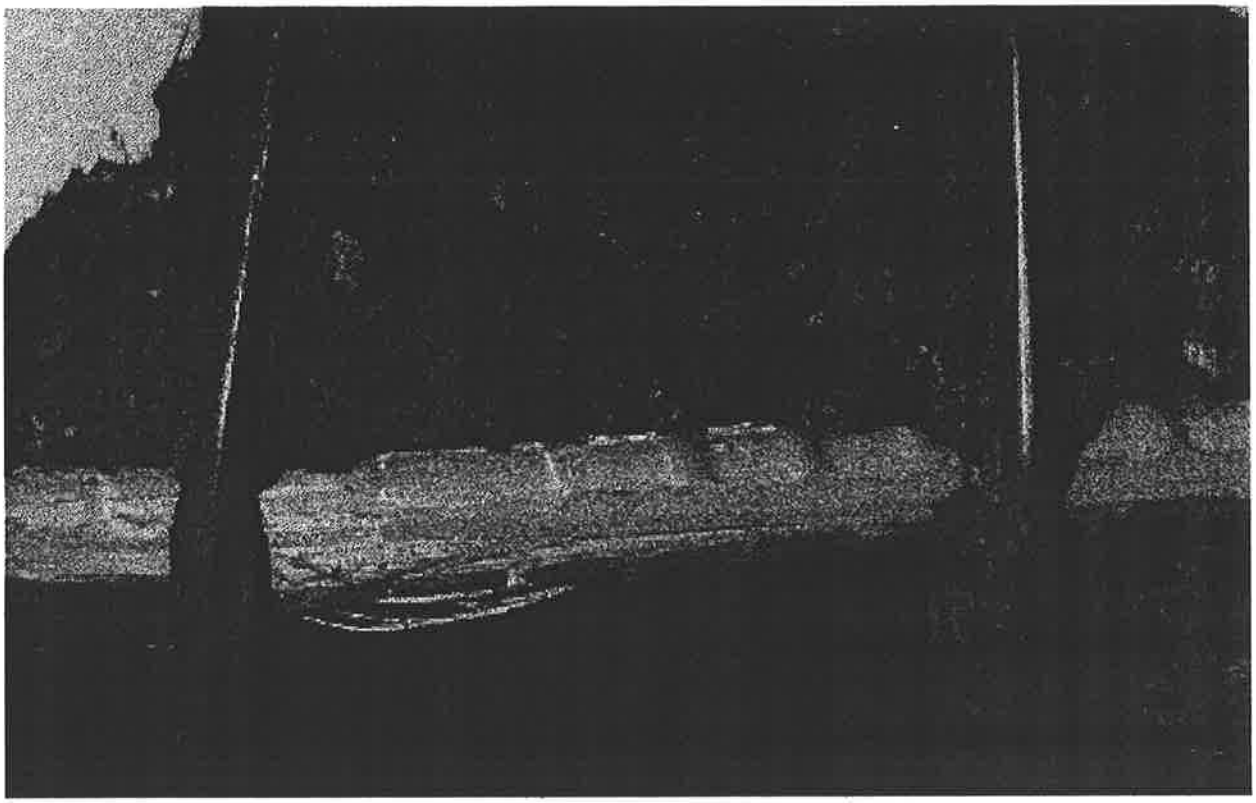

Figure 8.94. – FRP rebars at the bottom of beam 4.

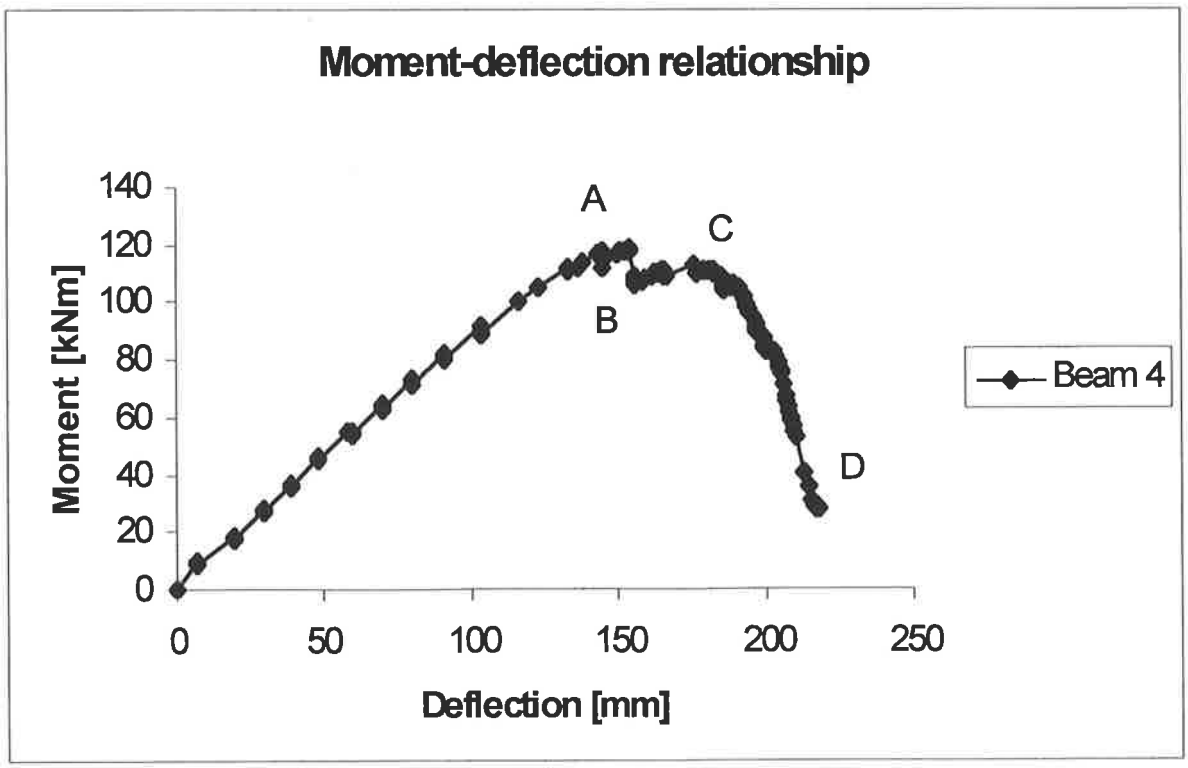

Figure 8.95. – Moment-deflection relationship of beam 4.

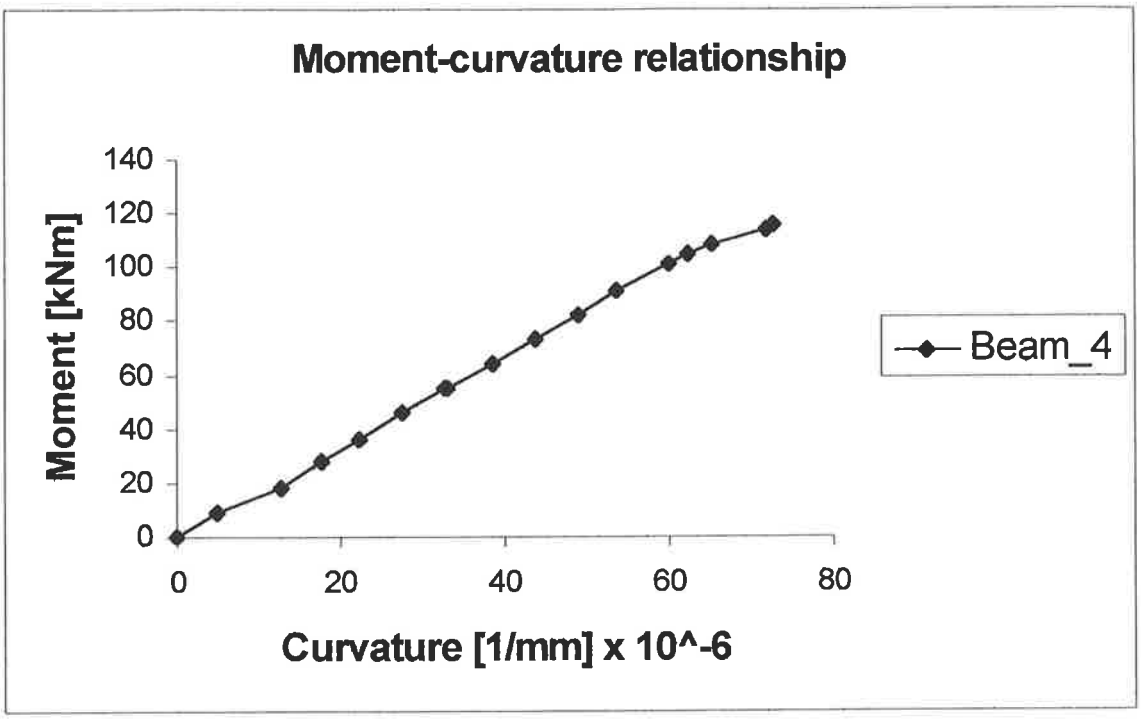

Figure 8.96. – Moment-curvature relationship of beam 4.

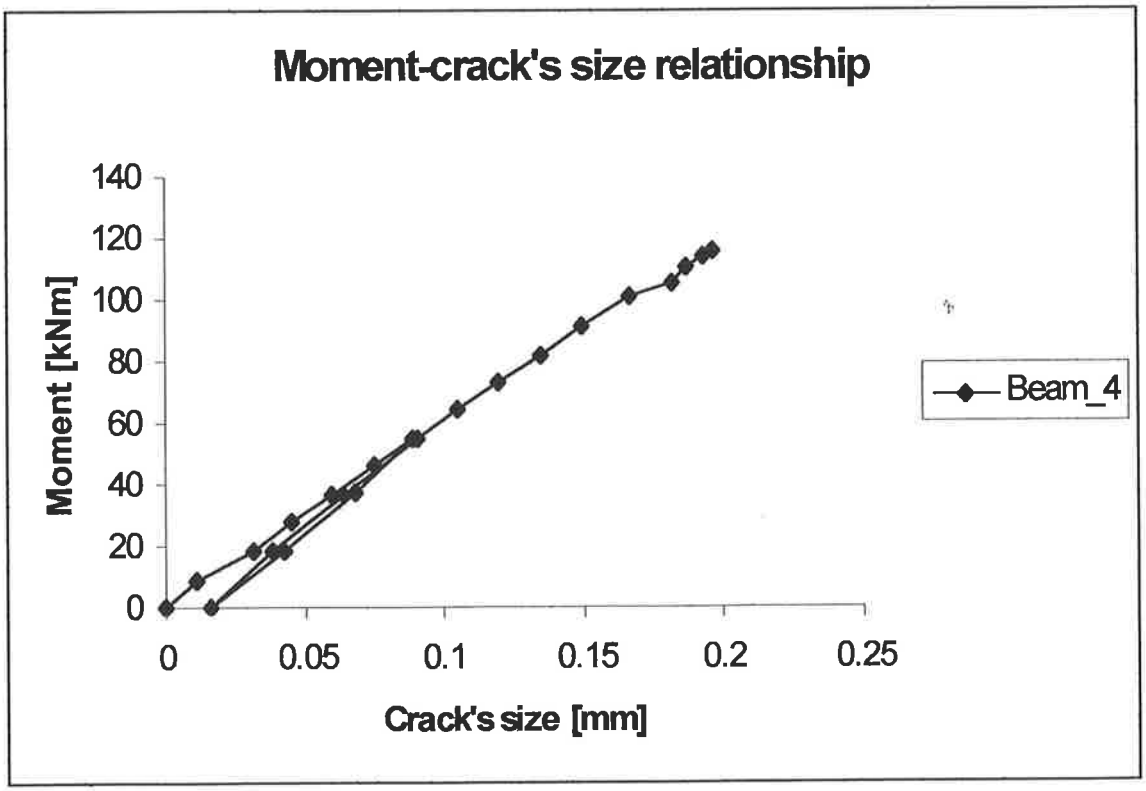

Figure 8.97. – Cracks' sizes of beam 4.

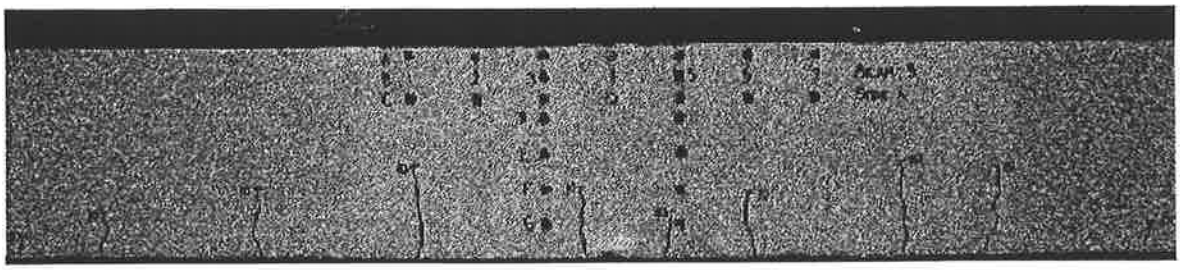

Figure 8.98. – Beam 5 at 10 kN.

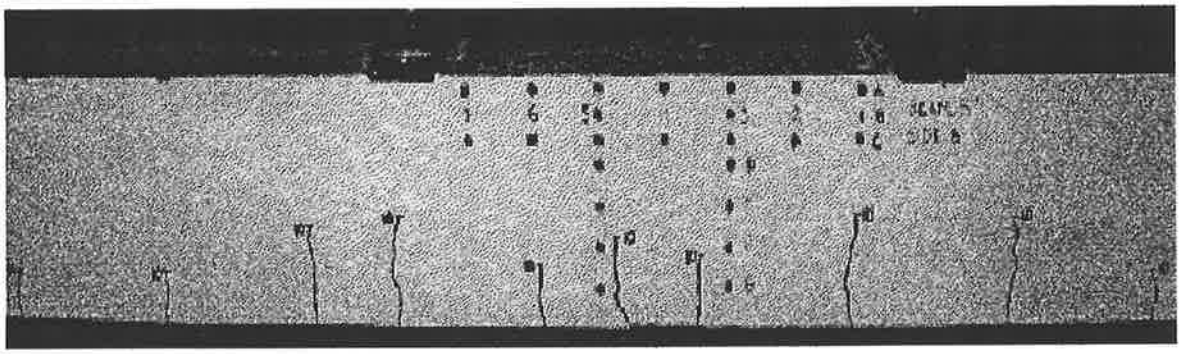

Figure 8.99. – Beam 5 at 10 kN.

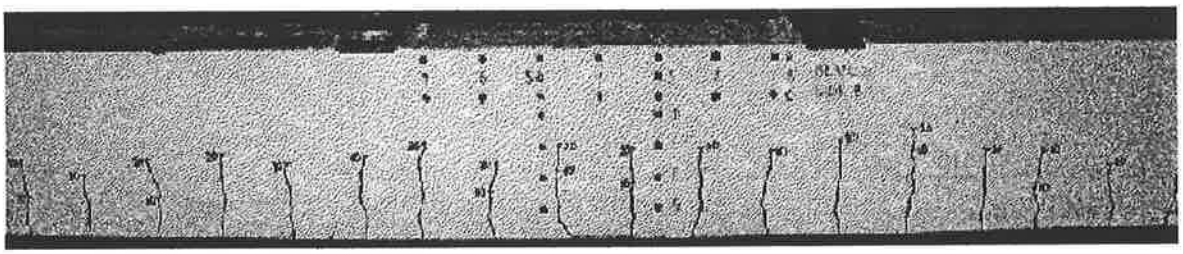

Figure 8.100. – Beam 5 at 20 kN.

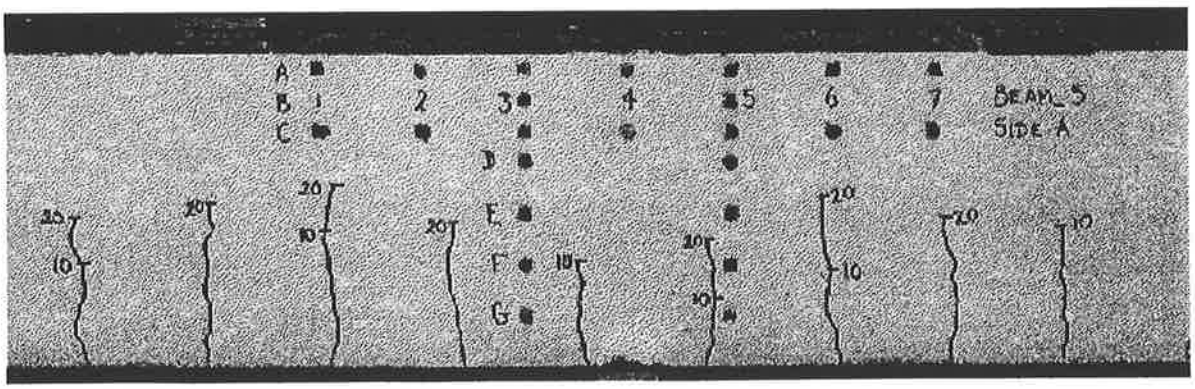

Figure 8.101. – Beam 5 at 20 kN.

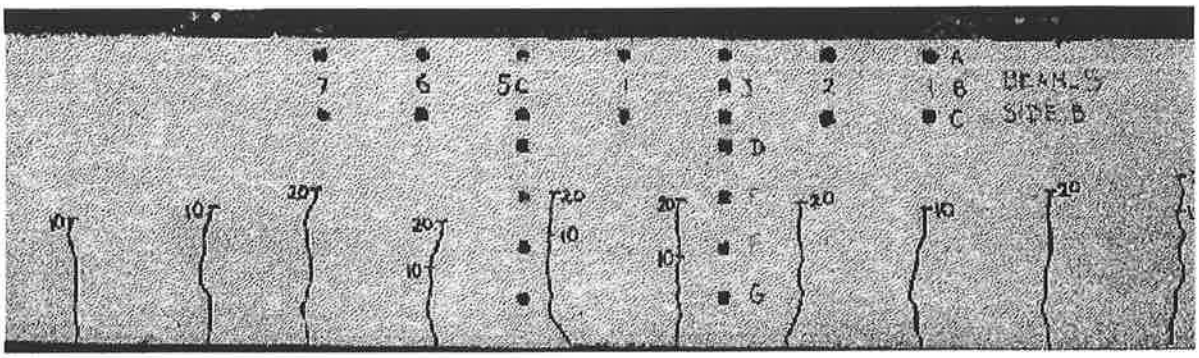

Figure 8.102. – Beam 5 at 20 kN.

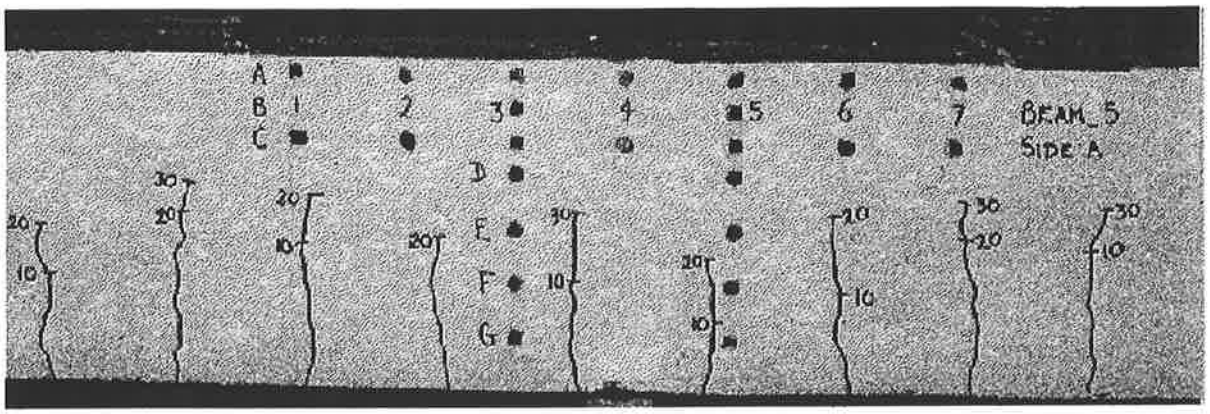

Figure 8.103. – Beam 5 at 30 kN.

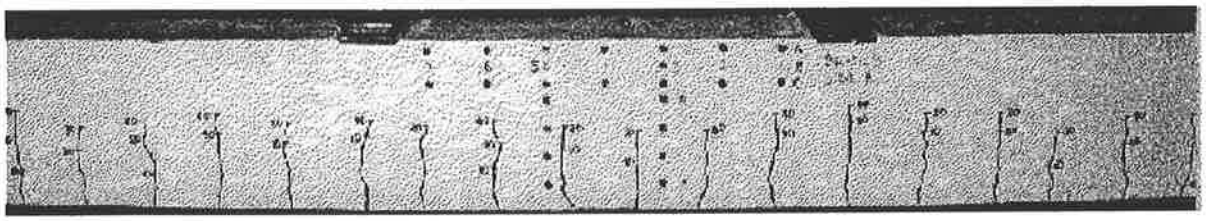

Figure 8.104. – Beam 5 at 40 kN.

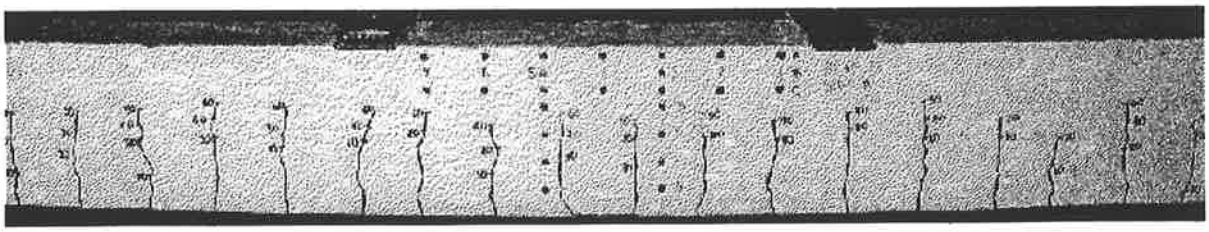

Figure 8.105. – Beam 5 at 60 kN.

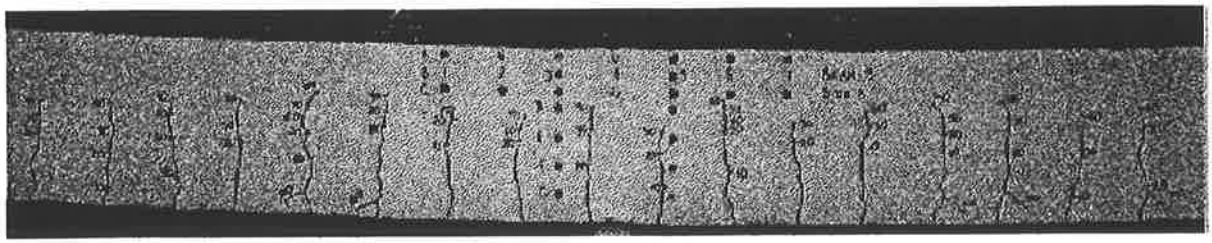

Figure 8.106. – Beam 5 at 100 kN.

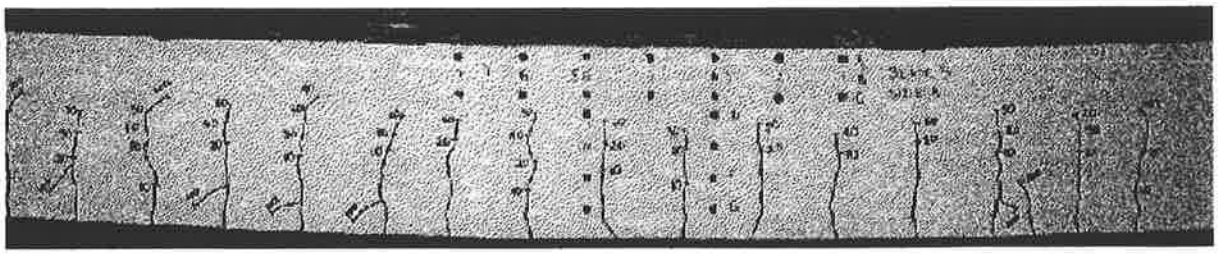

Figure 8.107. – Beam 5 at 100 kN.

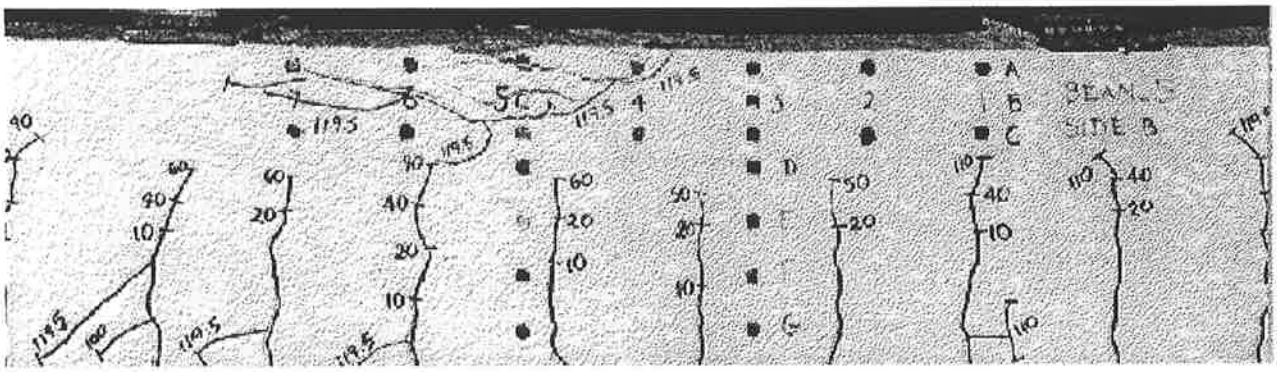

Figure 8.108. – Beam 5 at 119.5.

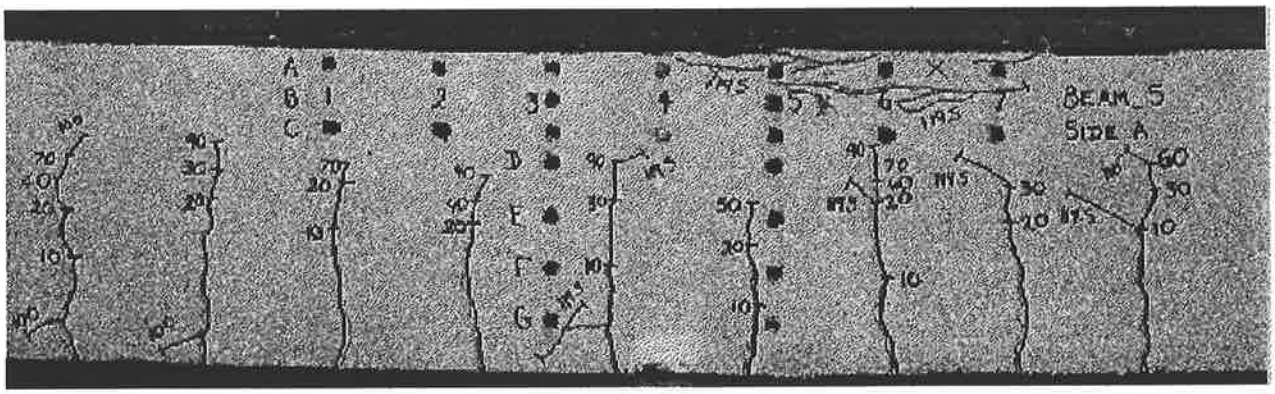

Figure 8.109. – Beam 5 at 119.5.

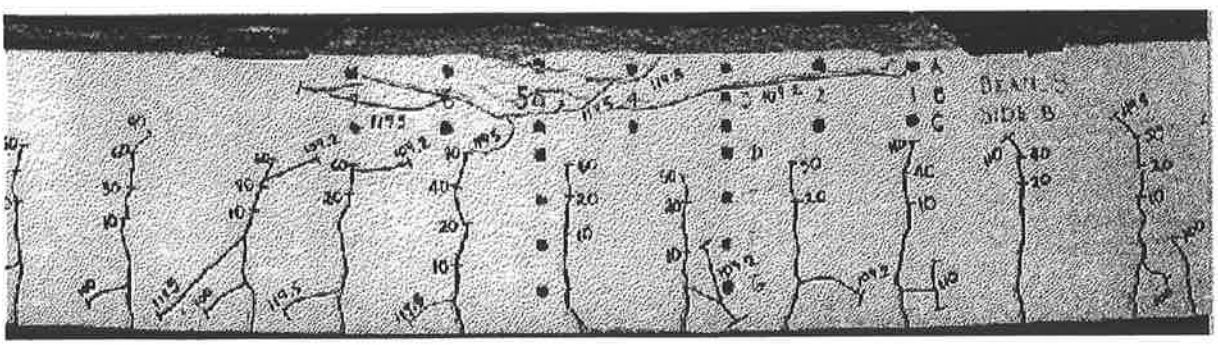

Figure 8.110. – Beam 5 at 119.5 kN.

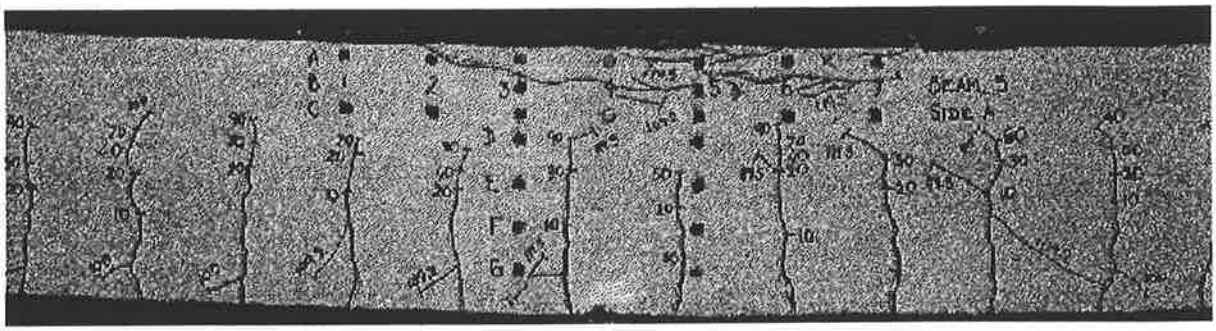

Figure 8.111. – Beam 5 at 119.5 kN.

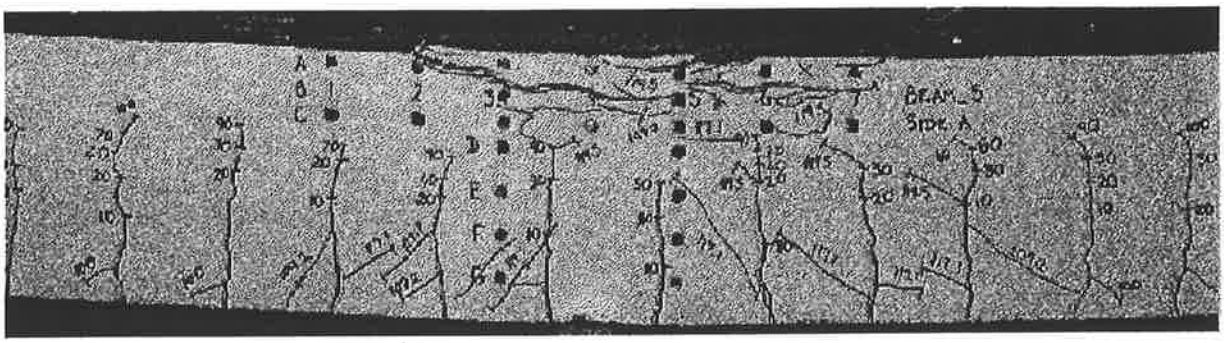

Figure 8.112. – Beam 5 at 119.5 kN.

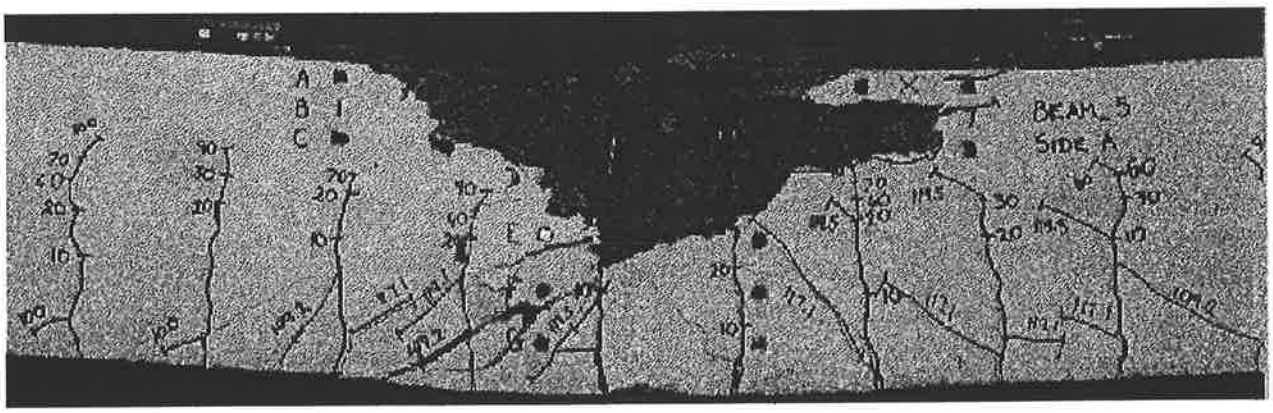

Figure 8.113. – Beam 5 at failure.

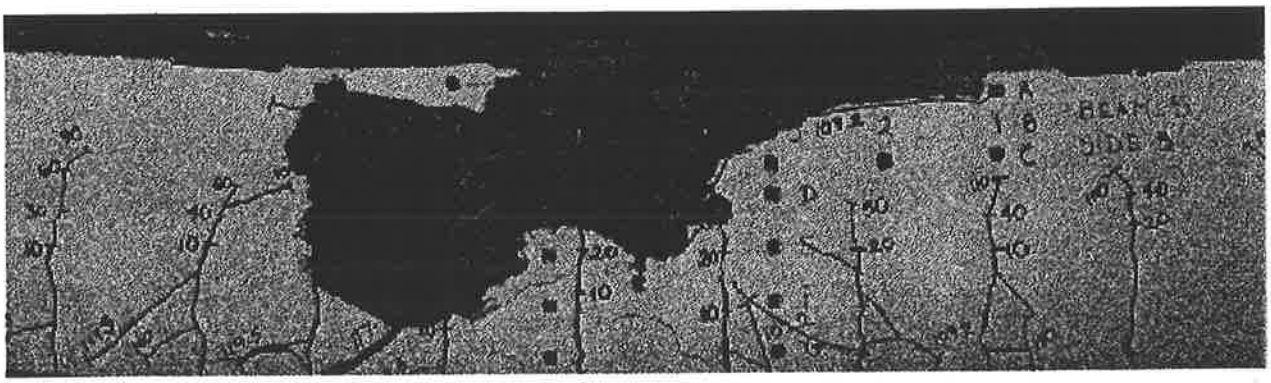

Figure 8.114. – Beam 5 at failure.

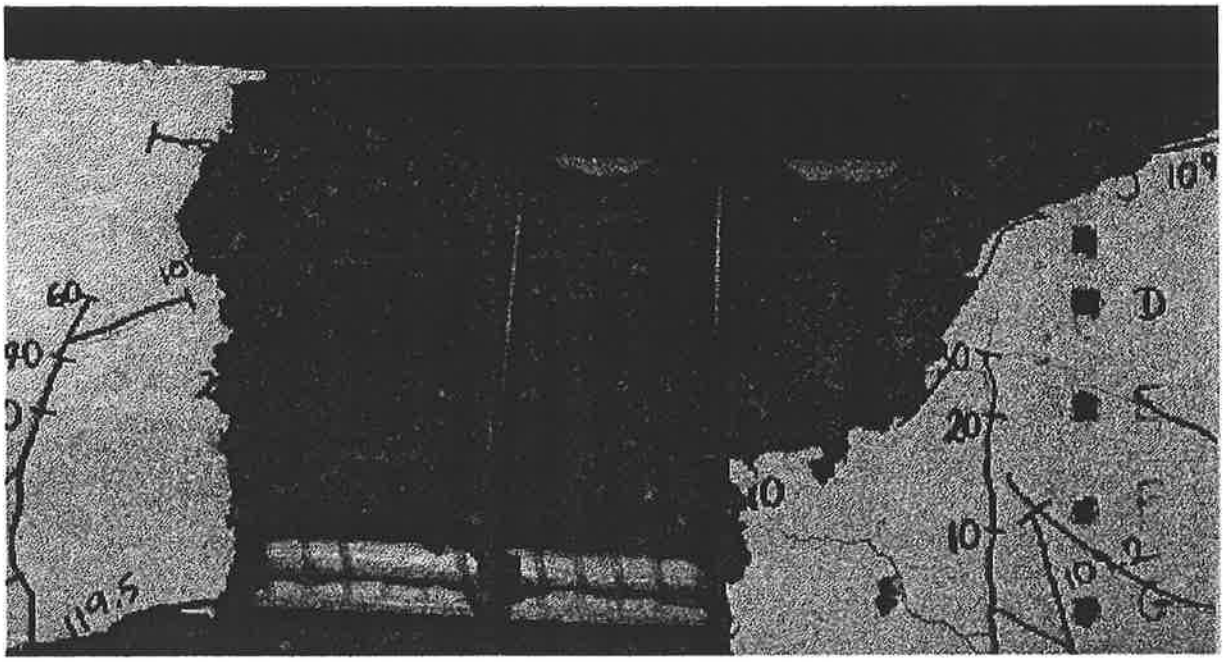

Figure 8.115. – Loose concrete removed from beam 5 after failure.

Figure 8.116. – Loose concrete removed from beam 5 after failure.

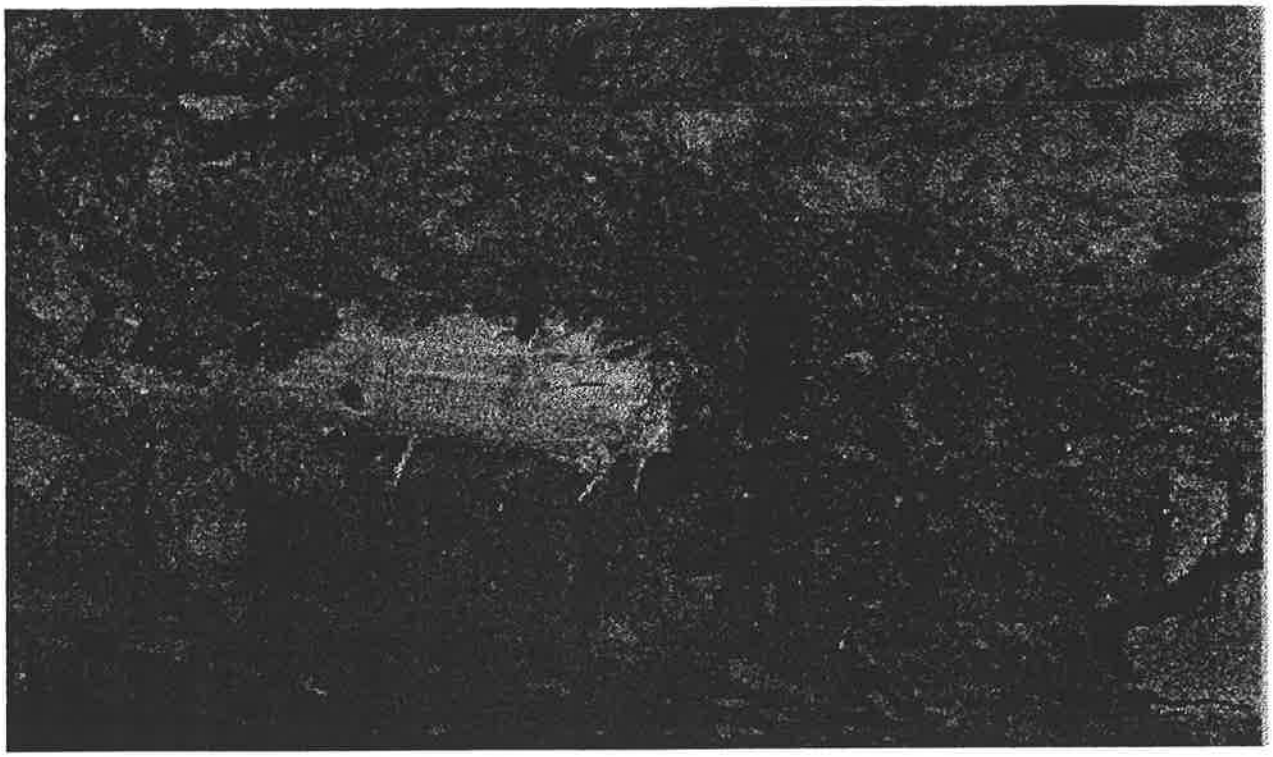

Figure 8.117. – FRP rebar at the top of beam 5.

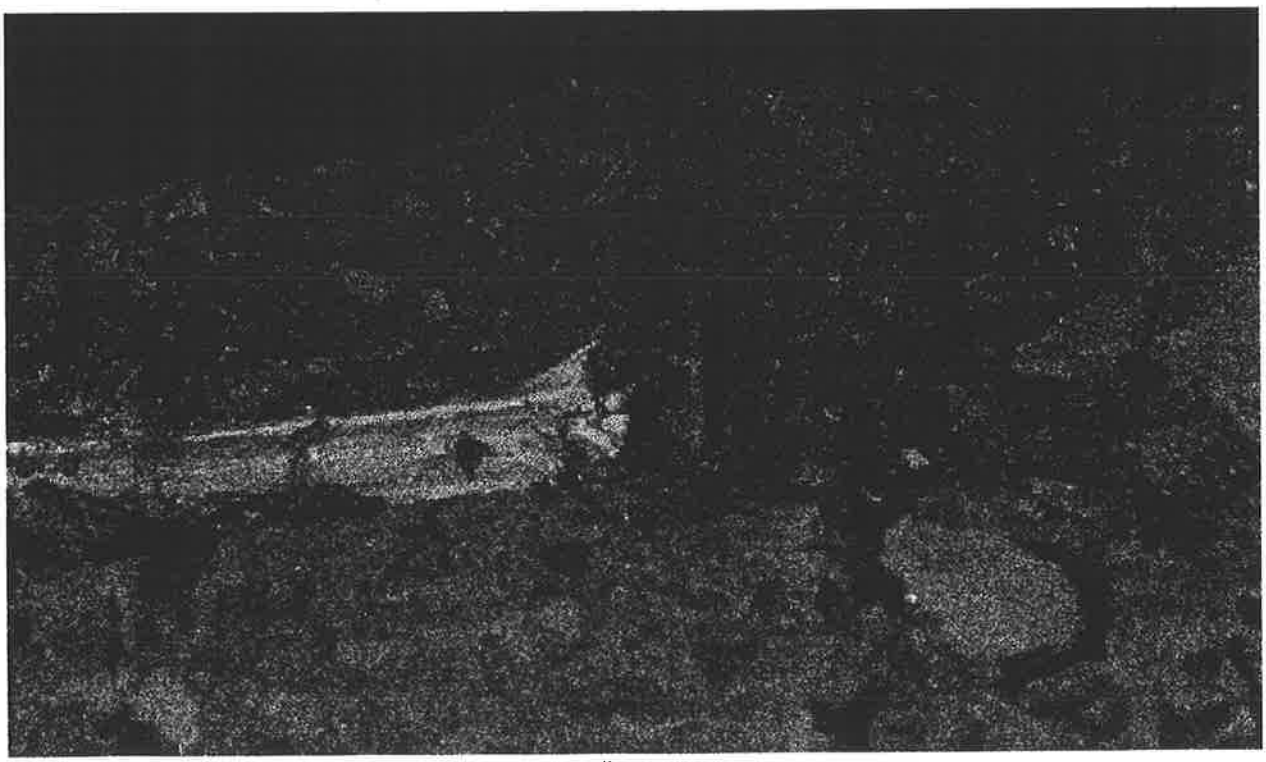

Figure 8.118. – FRP rebar at the top of beam 5.

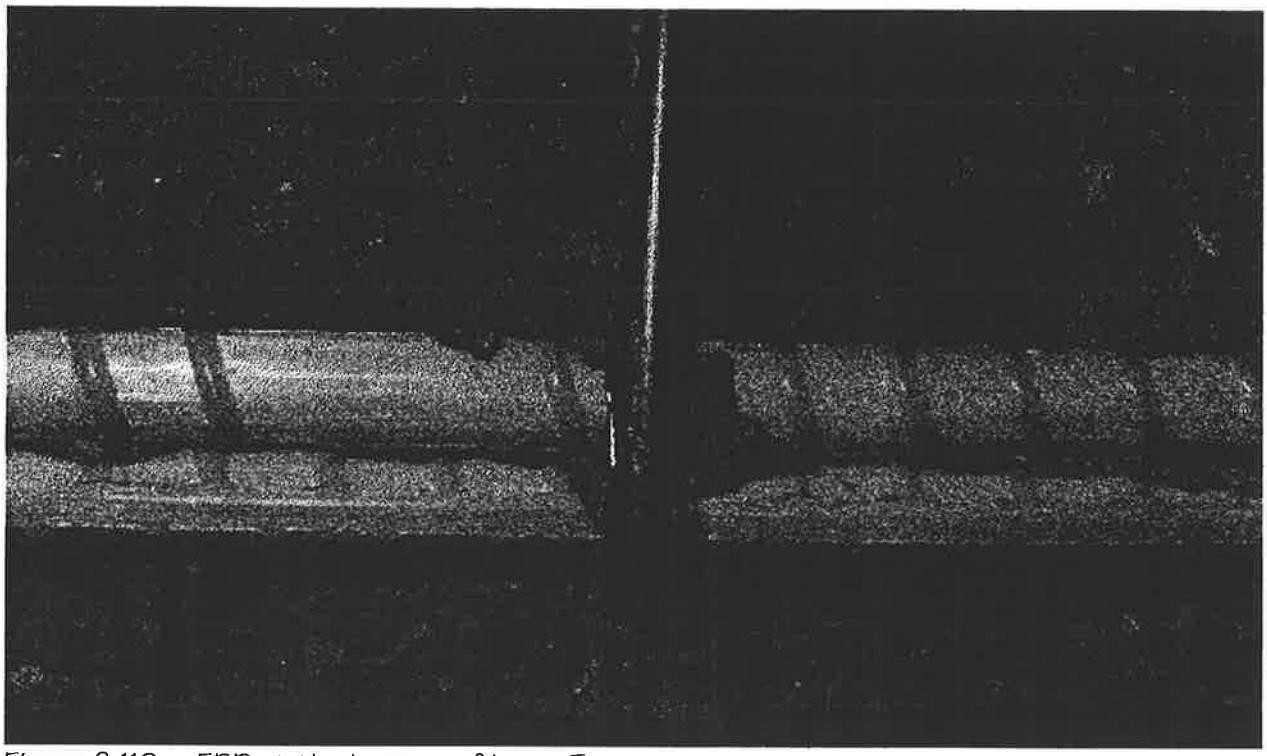

Figure 8.119. – FRP at the bottom of beam 5.

Figure 8.120. – FRP rebars at the bottom of beam 5.

Figure 8.121. – Demec measurement on beam 5.

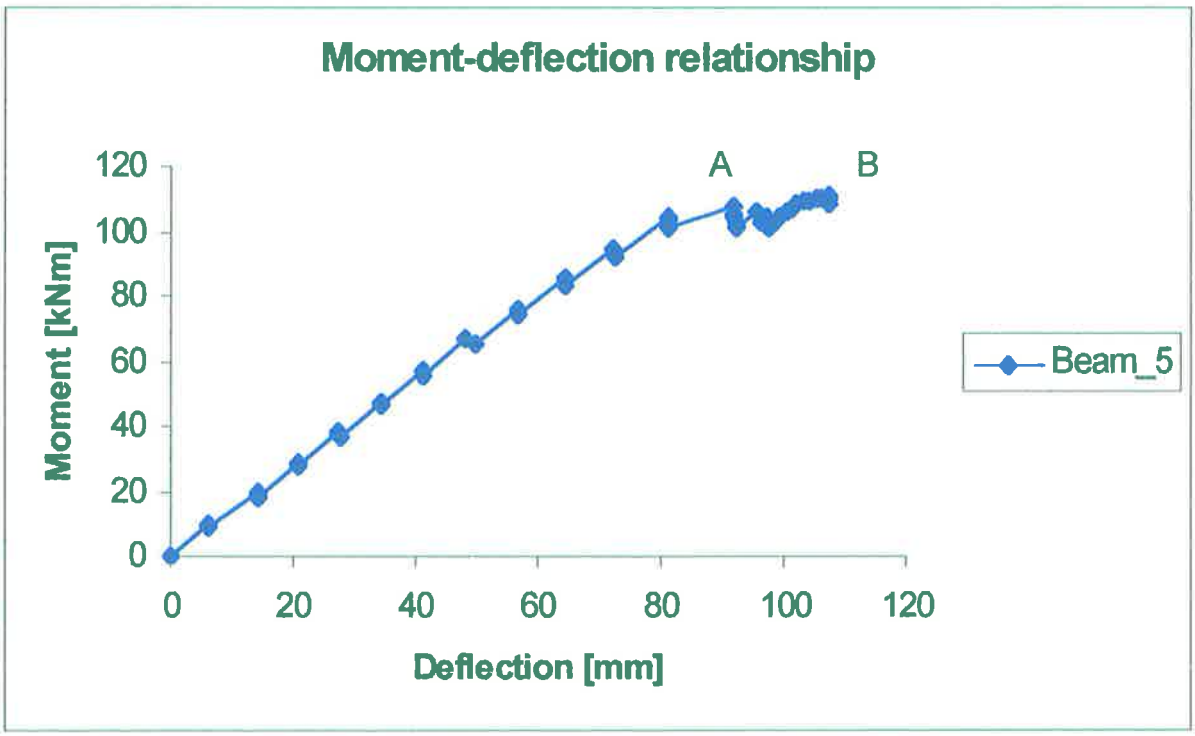

Figure 8.122. – Moment-deflection of beam 5.

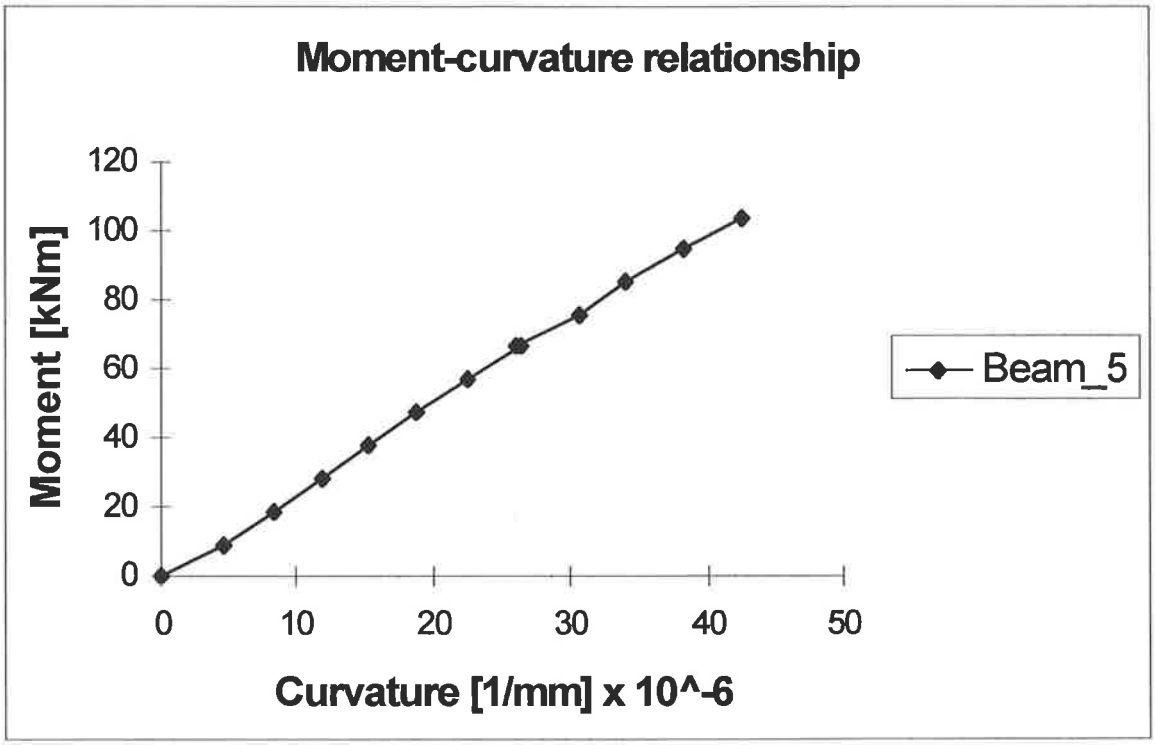

Figure 8.123. – Moment-curvature relationship of beam 5.

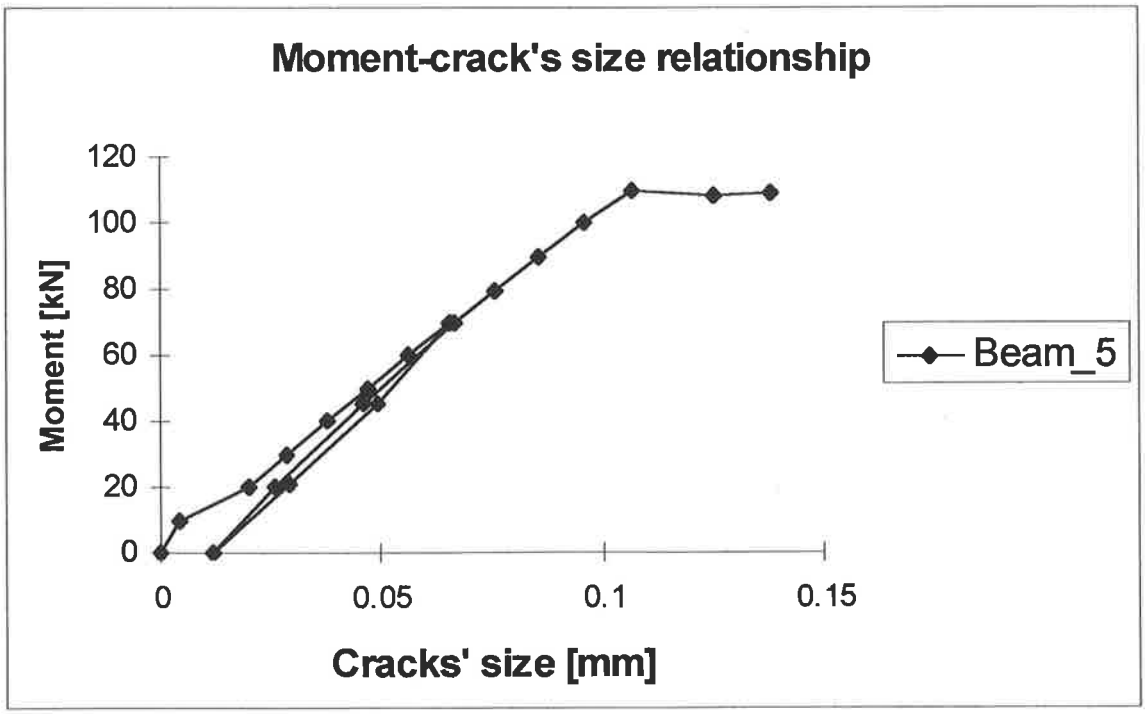

Figure 8.124. – Cracks' sizes in beam 5.

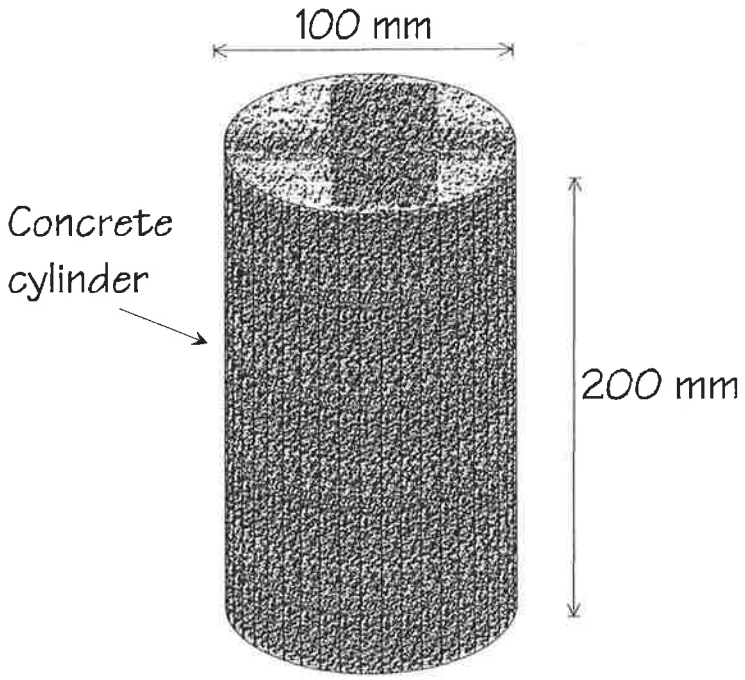

Figure 8.125. – Concrete cylinders to be tested.

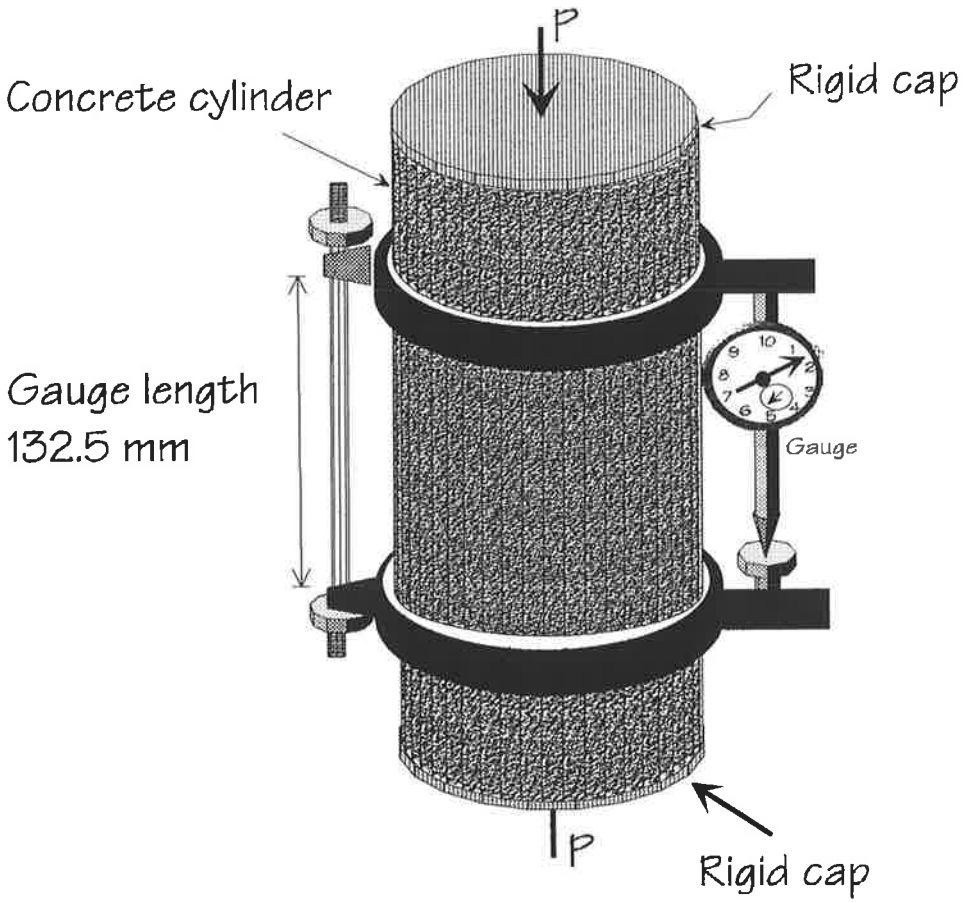

Figure 8.126. – Set up of the specimens for Young's modulus testing.

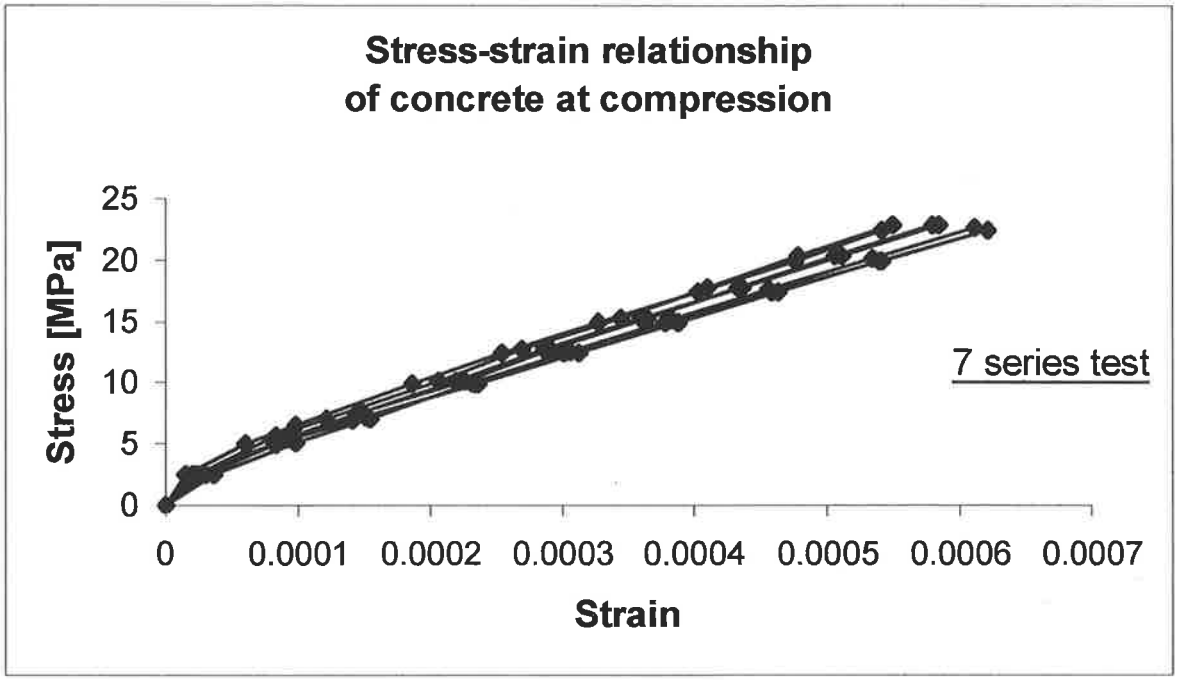

Figure 8.127. – Stress-strain relationship of concrete up to $0.45f_c$,

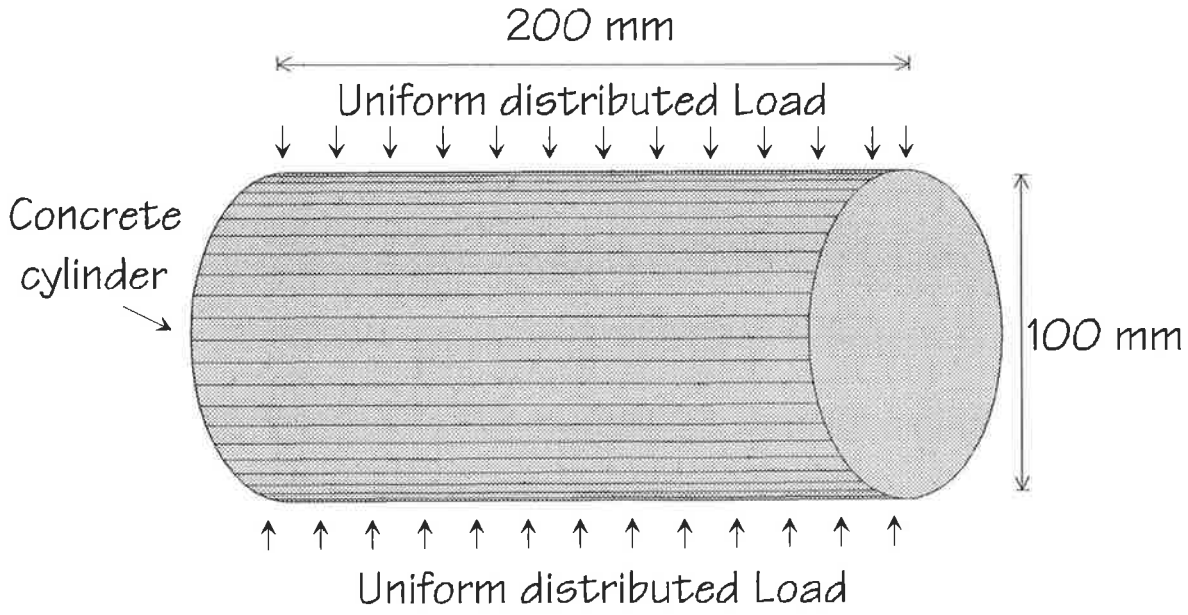

Figure 8.128. – Schematic setting of the concrete cylinder for Brazil testing.

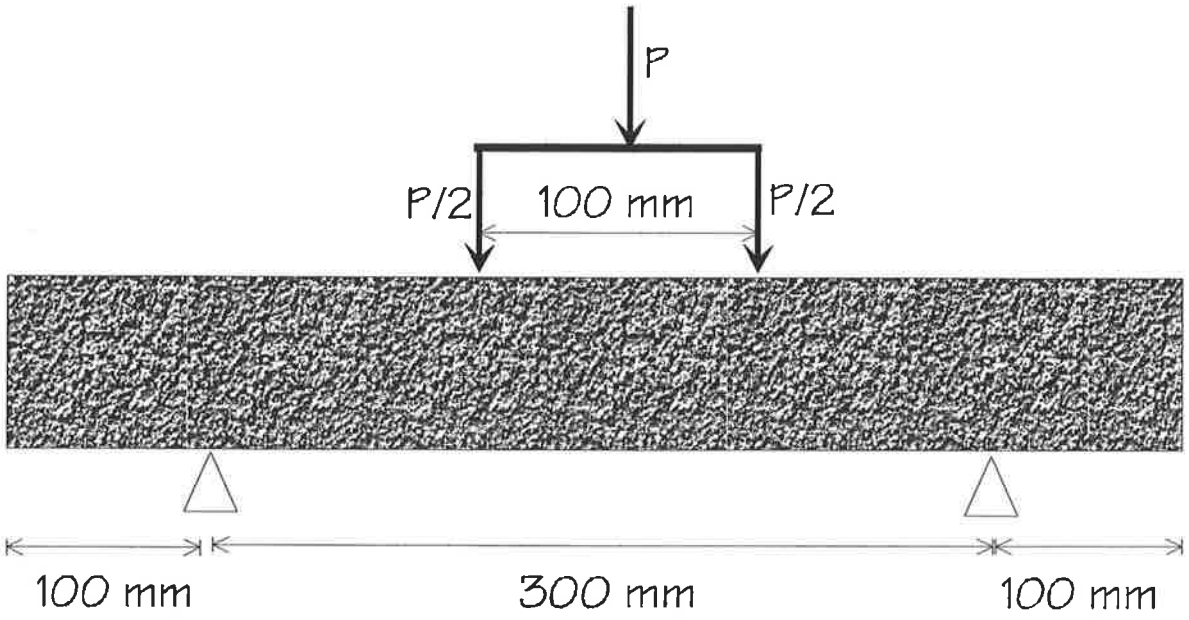

(a) Side view

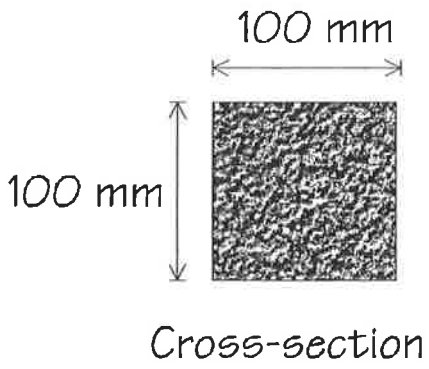

(b) Cross-section

Figure 8.129. – Schematic set up for the test of flexural strength of concrete.

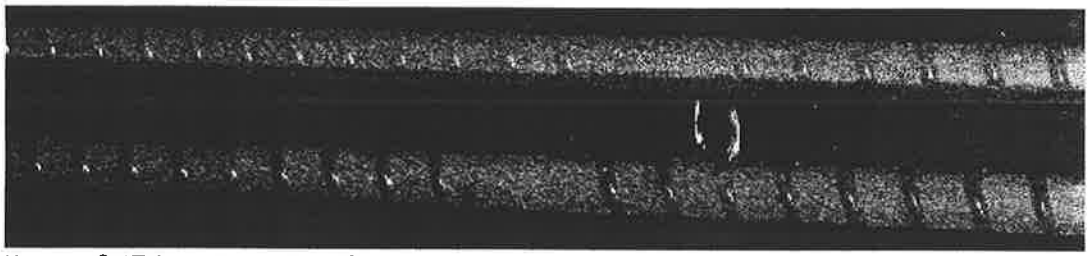

Figure 8.130. – Samples of FRP rebars.

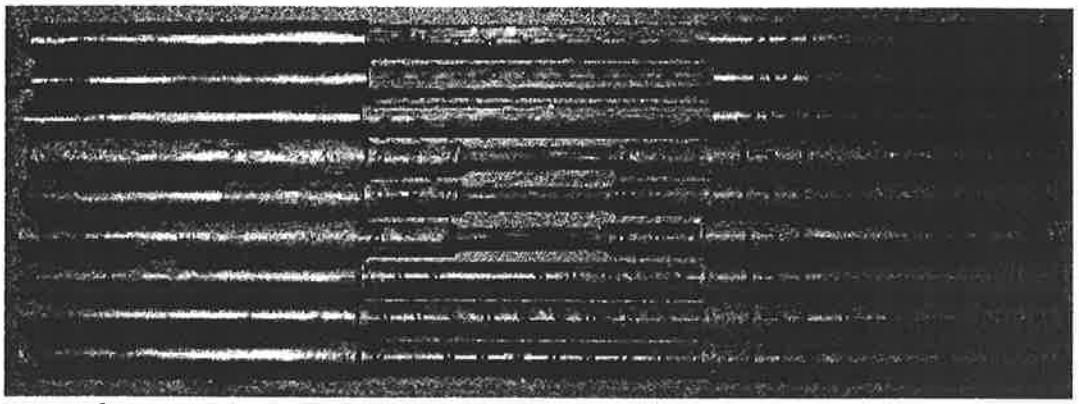

Figure 8.131. – FRP coupons before testing.

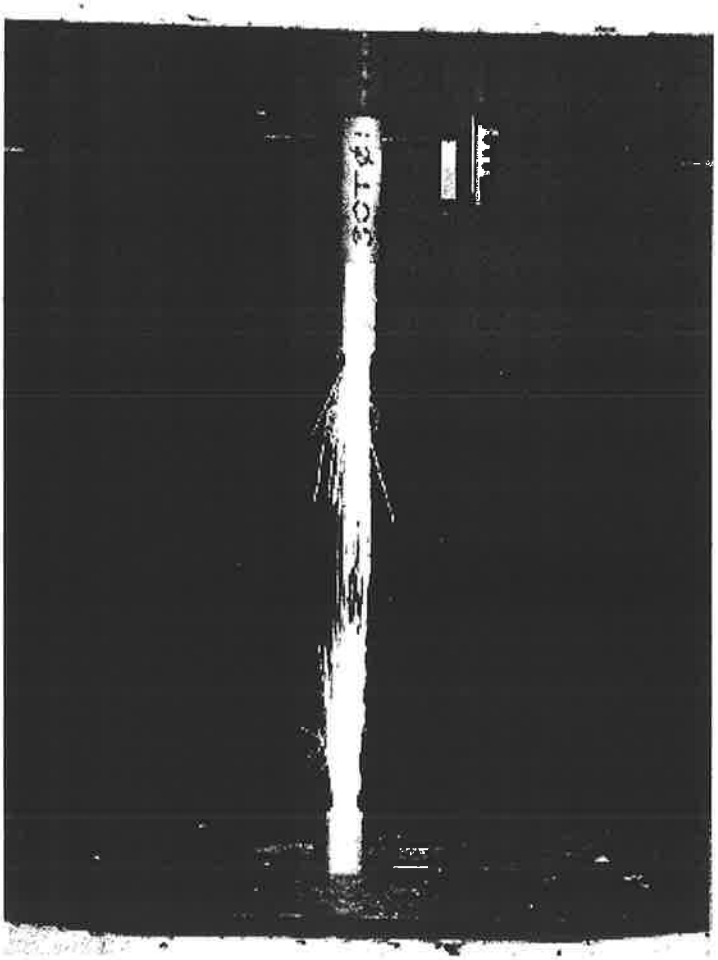

Figure 8.132. – Typical failure of FRP rebars.

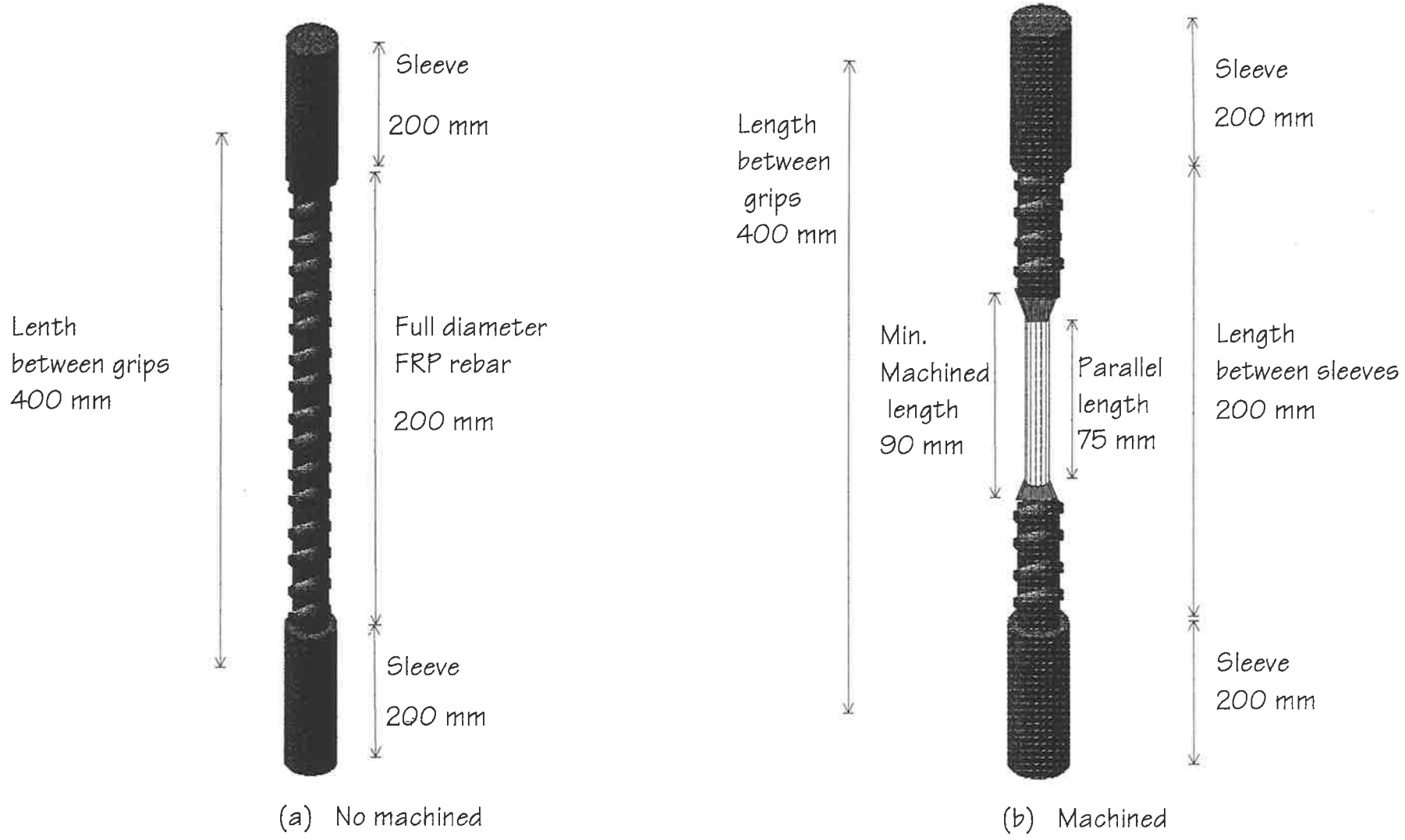

Figure 8.133. - Schematic representation of FRP coupons.

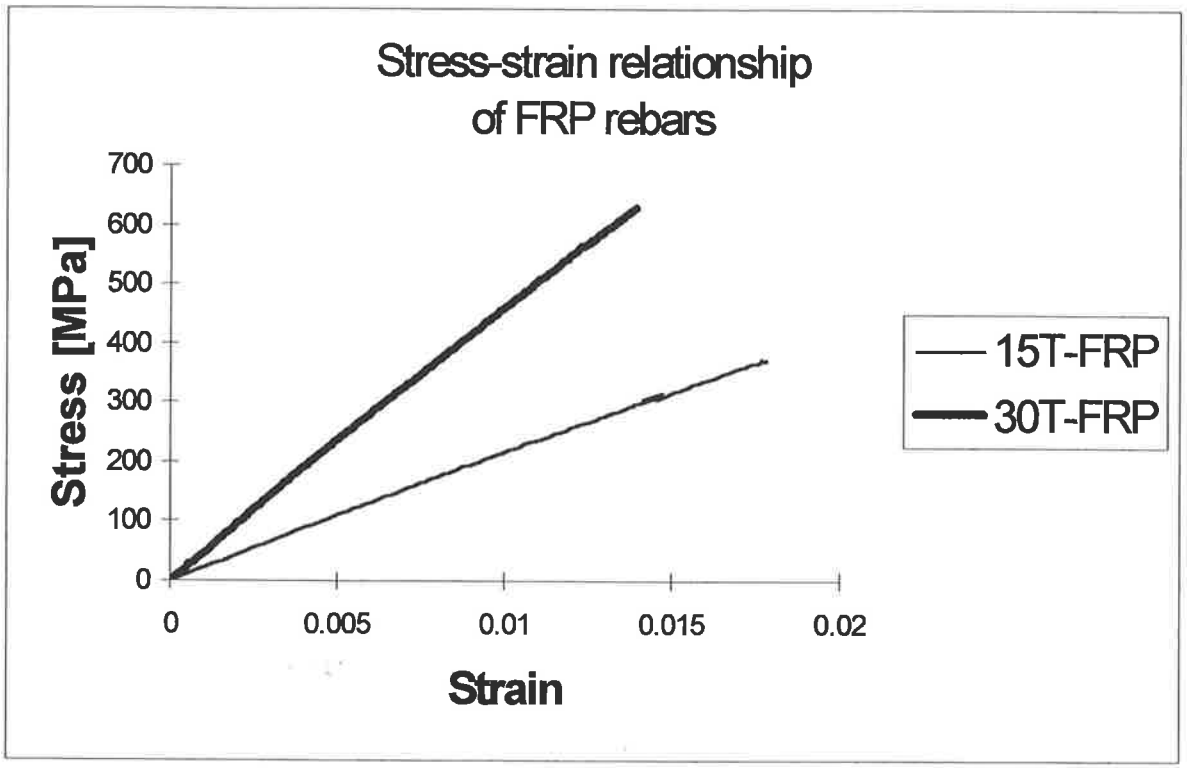

Figure 8.134. – Stress-strain relationship of two different types of FRP rebars.

Chapter 9

Analysis of results

9.1 Introduction

The aim of chapter 9 is to present a comprehensive analysis of the test results and then compare them with the two theoretical analysis methods used in the design of the beam specimens. The two analysis methods are described in detail in chapters 3 and 4.

The analysis of the results is based in not only on the moment-deflection relationship but also on the moment-curvature relationship. Firstly, is analyzed the moment-deflection relationship of the beams with different combinations of both the amount and type of reinforcement. Later, are analyzed the beams with regard to the moment-curvature relationship using the segmental analysis method. Finally, are analyzed the effects of the

amount and type of reinforcement at the top of the beams regarding the moment at concrete crushing and ultimate failure of the beams.

The plateau length of each beam is thoroughly studied as well as the changes of moment along the plateaux in the moment-deflection relationship of the beams. The calculations of the flexural rigidities of the beams are also included in this chapter.

9.2 Moment-deflection relationship

The experimental moment-deflection relationships of the beams can be visualized through figures 9.1 to 9.5. Table 9.1 summarizes the amount and strength of the reinforcing bars as well as the values of the internal moments of the beams and their deflections at critical points. Firstly, let us describe the contents of table 9.1. Column 1 identifies the beam specimens. Column 2 describes the amount of compressive reinforcement in the beams. The quantity in parenthesis below the amount of reinforcement describes the strength of the reinforcing bars. For instance in beam 2, $1FRP_{20}$/(420) means 1 FRP rebar of 20-mm diameter and 420 MPa strength. Column 3 describes the amount of tensile reinforcement. In addition, the quantity in parenthesis below the amount of reinforcement describes the strength of the reinforcing bars. For instance in beam 2, $3FRP_{20}$/(700) means 3 FRP rebars of 20-mm diameter and 700 MPa strength. Columns 4, 5 and 6 describe the internal moments of the beams and their corresponding deflections at points A, B and C in figures 9.1 to 9.5.

The values in columns 4, 5 and 6 which are given in the form x/y are the internal moments x of the beams and the corresponding deflections y at the midspan of the beams. Column 7 describes the plateau length in the moment-deflection relationship of the beams. For instance, the plateau length in beam 1 is the deflection at point C (179 mm)

minus the deflection at point A (135 mm) which gives 44-mm length. Column 8 describes the change of moment in the plateau between points A and C in the beams. For instance, the moment at point C (74 kNm) minus the moment at point A (114 kNm) in beam 1 gives –40 kNm.

9.2.1 Individual analysis

a) Beam 1

Beam 1 is shown in figures 7.1a and 7.3a and described in sections 7.3 and 7.4. The materials' properties are described in sections 8.3.6.1 and 8.3.6.2. The moment-deflection relationship of beam 1 is shown in figure 9.1, in which it can be seen that there are three important points that are marked A, B and C. Point A in figure 9.1 defines both the internal moment of the beam and the deflection at the onset of the concrete crushing.

The results are listed in column 4 of table 9.1 as 114/135, that is at point A, the internal moment of beam 1 is 114 kNm and the deflection is 135 mm. After the concrete crushes, the flexural strength of the beam falls down to point B in figure 9.1 where the internal moment is 84 kNm and the deflection is 140 mm as shown in column 5 of table 9.1. Between points B and C there is a plateau with a soft downward slope where the internal moment falls from 84 kNm at point B to 74 kNm in point C where the deflection is 179 mm. Notice that the fall off between points A and B can be described as an almost vertical path that means a sudden lost of flexural strength of the beam.

The peak moment (144 kNm) of beam 1 coincides with the moment at the concrete crushing in A in figure 9.1. The moment of the beam at ultimate failure is 74 kNm at C. Notice that the moment of the beam at ultimate failure is 40 kNm less than the peak moment (see column 8 in table 9.1). The length of the plateau is the deflection 179-mm at

ultimate failure of the beam minus the deflection 135-mm at the concrete crushing. Column 7 in table 9.1 shows the length of the plateau as 44 mm.

b) Beam 2

Beam 2 is shown in figures 7.1b and 7.3b and described in sections 7.3 and 7.4. The materials' properties are described in sections 8.3.6.1 and 8.3.6.2. Point A in figure 9.2 describes the concrete crushing with a flexural strength of 109 kNm and the deflection of 126 mm which is shown in column 4 of table 9.1 as 109/126. The strength of the beam falls from A to B in figure 9.2 with a non-vertical path (this is very important to take into account). The internal moment in point B is 97 kNm and the deflection is 137 mm which is shown as 97/137 in column 5 of table 9.1. The beam regains strength after falling off in B, describing a flat plateau between B and C; the internal moment at C is 104 kNm and the deflection is 177 mm.

The peak moment (109 kNm) occurs at the concrete crushing at A meanwhile, the moment at ultimate failure at C is 104 kNm (see figure 9.2). Notice that the moment at ultimate failure in C is almost the same as the peak moment at A. The change of moment between A and C is 5 kNm. The plateau length is the deflection of 177 mm at ultimate failure minus the deflection of 126 mm at the concrete crushing. Column 7 in table 9.1 shows the length of the plateau as 51 mm long. The presence of the plateau between A and C with a small change in moment denotes that the beam behaved in a ductile fashion.

c) Beam 3

Beam 3 is shown in figures 7.1c and 7.3c and described in sections 7.3 and 7.4. The materials' properties of beam 3 are described in sections 8.3.6.1 and 8.3.6.2. The concrete

crushed at the internal moment of 103 kNm and at a deflection of 117 mm as shown in A in figure 9.3. Column 4 in table 9.1 shows both the internal moment and the deflection at A as 103/117. The flexural strength of beam 3 at A drops down to B with a soft slope where the internal moment is 94 kNm and the deflection is 127 mm (see column 5 in table 9.1). The beam regained stress at C (see figure 9.3) where the internal moment is 112 kNm and the deflection is 192 mm (see column 6 in table 9.1).

The peak moment (112 kNm) is the same internal moment at failure of the beam at C. The plateau change is the moment 122 kNm at ultimate failure minus the moment 103 kNm at the concrete crushing. Column 8 in table 9.1 shows the plateau change as 9 kNm. The positive sign of the plateau change in column 8 of table 9.1 means that the beam gained flexural strength after the concrete crushed. On the other hand, the length of the plateau is 75 mm long. The plateau of beam 3 is 24 mm longer than the plateau of beam 2. Accordingly, beam 3 behaved in a very ductile fashion. The deflection reduced after the beam was unloaded as can be seen in figure 9.3

d) Beam 4

Beam 4 is shown in figures 7.1d and 7.4a and described in sections 7.3 and 7.4. The materials' properties of beam 4 are described in sections 8.3.6.1 and 8.3.6.2. Point A in figure 9.4 describes the point in the curve at which the concrete crushed. The internal moment of beam 4 at A is 118 kNm and the deflection is 154 mm shown as 118/154 in column 4 in table 9.1. As the concrete crushed, the internal moment of the beam dropped down to B where the internal moment is 107 kNm and the deflection is 158 mm. A very short plateau is described between B and C, which could be considered as an indentation only. The internal moment at C is 111 kNm and the deflection is 181 mm. Beam 4 does not show ductile behavior in the moment-deflection relationship.

e) Beam 5

Beam 5 is shown in figures 7.1e and 7.4b and described in sections 7.3 and 7.4. The materials' properties are described in sections 8.3.6.1 and 8.3.6.2. Figure 9.5 shows the moment-deflection relationship of beam 5 where can be seen the concrete crushing at A. The falling of the internal moment at B and the ultimate failure of the beam all occur in a small section of the curve. The failure of the beam occurred without warning in a catastrophic fashion. The values of internal moments and deflections are all in columns 4, 5 and 6 of table 9.1.

Beam (1)	A_{com} (2)	A_{ten} (3)	Moment/deflection [kNm]/[mm]				
			A (4)	B (5)	C (6)	Plateau length [mm] (7)	Plateau change [kNm] (8)
B1	—	$3FRP_{20}$ (700)	114/135	84/140	74/179	44	-40
B2	$1FRP_{20}$ (420)	$3FRP_{20}$ (700)	109/126	97/137	104/177	51	-5
B3	$2FRP_{20}$ (420)	$3FRP_{20}$ (700)	103/117	94/127	112/192	75	9
B4	$1Y_{20}$ (466)	$3FRP_{20}$ (700)	118/154	106/156	111/181	27	-7
B5	$1FRP_{20}$ (700)	$5FRP_{20}$ (700)	107/92	101/92	110/107	15	3

Table 9.1. – Moment-deflection test results.

9.2.2 Beams with the same FRP reinforcement at the bottom and different amounts of FRP reinforcement at the top.

Figure 9.6 shows the moment-deflection relationship of beams 1, 2 and 3 which have a similar ascending branch up to concrete crushing. The concrete crushing in the three beams occurs practically around the same values of moment (see column 4 in table 9.1).

The plateau of the graph of beam 3 in figure 9.6 ends in a higher position than that of beams 1 and 2. Furthermore, the plateau of beam 3 starts earlier than that of beam 1 and beam 2 and extends to a larger deflection beyond the ultimate failure deflection of beams 1 and 2 (see table 9.1). This means that the plateau of beam 3 is much longer than the plateaux of beam 1 and beam 2 (75 mm long as is shown in column 7 in table 9.1). Therefore, beam 3 shows a much more ductile behavior than beams 1 and 2.

9.2.3 Beams with different type of reinforcement at the top.

Figure 9.7 shows the moment-deflection relationships of beams 1, 2 and 4 (see also figures 9.1, 9.2 and 9.4). Beam 1 has no reinforcement at the top, beam 2 has 1 FRP rebar at the top and beam 4 has 1 Y_{20} rebar at the top. The 3 beams have 3 FRP bars at the bottom that have the same properties (see table 9.1).

The ascending branches of the 3 graphs are similar up to the concrete crushing. After the concrete crushing, the graphs are different. For instance, the falling branch of beam 1 drops down deeply and vertically soon after crushing of the concrete, from the moment of 114 kNm to the moment of 84.0 kNm, without recovering strength. The falling branch of beam 2 changes from 109 kNm as the concrete crushes to 97.0 kNm and then recovers flexural strength to 104 kNm. Finally, the falling branch of beam 4 changes from 118

kNm as the concrete crushes to 107 kNm and then it has a little recovery up to 111 kNm. The disadvantage in beam 4 is that the length of its plateau is extremely short (27 mm).

9.2.4 Beams with different amounts of FRP reinforcing bars at the bottom.

Until now, it has been seen that beams with the same amount of FRP reinforcement at the bottom have a similar ascending branch in the moment-deflection relationship. Let us see figure 9.8 where is shown the moment deflection-relationship of beams 1, 2, 3 and 5. Notice in this figure that the ascending branch of the curve of beam 5 is steeper than the ascending branch of the curves of beams 1, 2 and 3. Beams 1, 2 and 3 have 3 FRP rebars at the bottom, whereas, beam 5 has 5 FRP at the bottom. Consequently, increasing the amount of FRP rebars at the bottom of the beam, also increases the slope of the ascending branch of the moment-deflection relationship of the beam.

9.3 Moment-curvature relationship

The moment-curvature relationships of the beams were calculated for the ascending branch only because the demecs came off as the concrete crushed during the test procedure.

Figure 9.9 shows the moment-curvature relationship of beams 1 to 5. In beams 1 to 4, the concrete crushed almost at the same curvature ψ. Meanwhile, in beam 5 the concrete crushed at an earlier curvature ψ. Beams 1 to 4 had 3 FRP rebars at the bottom, whereas, beam 5 has 5 FRP rebars at the bottom. Notice that the slope of the ascending branch of the curve in beam 5 is larger than the slope of the ascending branch of the curves in beams 1 to 4. Therefore, the amount of FRP rebars at the bottom of the beams influence significantly the slope of the ascending branch of the moment-curvature relationship of

RC beams with FRP reinforcing bars in the same way than in the moment-deflection relationship.

9.4 Study of the flexural strength of the beams using the experimental results and theoretical analyses.

The first point to note is the fact that in the analysis of the results from the experimental work, there are three points well defined in the moment-deflection relationship. These points are A, B and C. Whereas, using the two theoretical analysis methods discussed in chapters 3 and 4, there are two points only such as A and C (see table 9.2). Point A defines the concrete crushing and point C defines the fracture of the compressive reinforcement. Point B in the moment-deflection relationship is available through the experimental results only.

9.4.1 Test results

Table 9.2 and figure 9.10 help us to understand the analysis of the flexural strength of beams 1, 2 and 3 which have 3 FRP rebars at the bottom. Firstly, let us look at table 9.2. Column 1 shows the number of FRP rebars at the top the beams and the type of analysis. Column 2 shows the moment at which the concrete crushes. Column 3 shows the moment of the beams soon after the concrete crushes that is available through the experimental results only. Column 4 shows the moment of the beams at failure. Now, let us look at figure 9.10. The letter T in the legend stands for 'Test'. The line AT defines the moment at concrete crushing; the line BT defines the moment soon after the concrete crushes; and the line CT defines the moment at failure of the beams.

a) Beam 1

Beam 1 does not have rebars at the top therefore, the analysis is for 0 rebars in both table 9.2 and figure 9.10. The intersection of line AT with the vertical axis in figure 9.10 defines the moment of beam 1 at concrete crushing. The moment drops down to line BT and the failure of the beam is down at the line CT. In other words, once the concrete crushes the beam does not recover flexural strength (see also figure 9.1).

b) Beam 2.

Beam 2 has 1 FRP rebar at the top therefore, the analysis is for 1 FRP rebar in figure 9.10. The moment at concrete crushing is defined by the upper most mark (diamond mark). After the concrete crushes the moment of beam 2 falls down to the square mark and then goes up to the triangle mark which defines the fracture of the compressive rebars. In other words, the moment at concrete crushing, the reduction soon after the concrete crushes and the moment at fracture of the compressive rebars, all occur almost at the same level of moment as shown in figure 9.10. In figure 9.2 can be seen the plateau defined by the moment at A, B and C.

c) Beam 3.

Beam 3 has 2 FRP rebars at the top therefore, the analysis is for 2 rebars in figure 9.10. It can be seen that for beam 3 the moment at the concrete crushing is not the upper most mark. Soon after the concrete crushes the moment reduces and then the beam not only recovers flexural strength but also gains more flexural strength. For beam 3, the upper most mark defines the fracture of the compressive reinforcement.

9.4.2 Segmental analysis.

Figure 9.11 shows the variation of moments for beams 1, 2 and 3 using the segmental analysis method. In figure 9.11, can be seen that curves A and C are only defined. Curve A defines the concrete crushing and curve C defines the ultimate failure of the beams. The concrete crushing at point A is defined for the 3 beams and is practically at the same level. However, failure at point C is defined for beams carrying compressive rebars only. Looking at figure 6.5 it can be seen that the failure of beam 1 occurs in a gradual fashion, in contrast to the mode of failure of beams 2 and 3 which happens at fracture of the compressive rebars.

9.4.3 Rectangular block of stresses analysis.

Figure 9.12 shows the change of moments for beams 1, 2 and 3 using the rectangular block of stresses analysis. As in the segmental analysis method, this analysis can only define the concrete crushing for the 3 beams and the ultimate failure for beams 2 and 3.

9.4.4 Comparison of the segmental analysis and the rectangular block of stresses analysis.

Figure 9.13 compares the changes of moment for beams 1, 2 and 3 using the segmental analysis method and the rectangular block of stresses analysis method. Notice in figure 9.13 that the moment at the concrete crushing is quite similar using both methods, however, there is a large difference for the failure of the beams. Using the rectangular block of stresses analysis, the failure of the beams occurs at a lower level than using the segmental analysis method. The character S stands for 'Segmental' and the character B stands for 'Block'.

9.4.5 Comparison of theoretical results and experimental results.

Figure 9.14 shows the changes of moment in beams 1, 2 and 3 using the experimental results and the theoretical methods. The continuous lines pertain to the experimental results. The dashed lines correspond to rectangular block of stresses analysis and the dotted lines correspond to the segmental analysis method.

9.4.6 Experimental deflections.

Figure 9.15 sows the variation of the deflection of beams 1, 2 and 3 using the experimental results. Curve A defines the deflection of the beams at the concrete crushing. Curve B defines the deflection of the beams soon after the concrete crushes. Curve C defines the deflection of the beams at ultimate failure. Finally, curve C-A defines the plateau length, which means the deflection at failure minus the deflection at the concrete crushing. Table 9.1 summarizes the plateau length in column 8.

9.4.7 Moment at concrete crushing.

The moment of the beams at concrete crushing is not the same in beams carrying different amounts or types of reinforcement at the top. Looking at column 4 in table 9.1 it can be seen that the moment at the concrete crushing is 114 kNm in beam 1. The moment is less in beam 2 (109 kNm) and even smaller in beam 3 (103 kNm). However, the moment at the concrete crushing in beam 4 is higher (118 kNm).

Figures 9.6 and 9.7 show graphically the difference of moments at the concrete crushing. The larger elastic section is for beam 1 and the shorter elastic section is for beam 3. In figure 9.7, the larger elastic section is for beam 4 and the shorter elastic section is for beam 2. In figure 9.14, curve AT defines the moment at the concrete

crushing for the 3 beams. Notice that curve AT is higher at zero FRP rebars and then diminishes at 1 FRP rebar. Curve AT goes further down at 2 FRP rebars.

Rebars at the top (1)	Internal moment of RC beams with 3 FRP rebars at the bottom. [kNm]		
	A (2)	B (3)	C (4)
Test			
0	114	84	74
1	109	97	104
2	103	94	112
Segmental			
0	116		——
1	119		90
2	123		115
Block			
0	120		——
1	123		62
2	125		88

Table 9.2. – Test results and theoretical results of beams with the same amount of rebars at the bottom and different amount of rebars at the top.

Figure 9.16 helps us to understand the reason for the decline in the moment at concrete crushing in beams with different amounts of compressive FRP rebars, as well as the reason of the rise of moment in beam 4 with the steel rebar at the top.

Let us look at figure 9.16 in conjunction with curve AT in figure 9.14 and figures 9.6 and 9.7. Let us take beam 1 as a reference to analyze the moment at concrete crushing (see figure 9.16a). In addition, let us see the Young's modulus of the concrete in table 8.1 and the Young's modulus of the compressive FRP rebars in table 8.5. The Young's modulus of the steel bars is usually taken as 200000 MPa, the Young's modulus of the concrete is 35429 MPa and the Young's modulus of the compressive FRP rebars is 25785 MPa.

The moment of beam 1 at concrete crushing is 114 kNm. The compressive force is carried only by the concrete.

Beam 2 has 1 FRP rebar of a Young's modulus 25785 MPa which is less than the Young's modulus of the concrete. Therefore, if the Young's modulus of the compressive rebar is less than the Young's modulus of the concrete, then when the concrete crushes practically the area occupied by the rebar is just a void area (see figure 9.16b). This means that the area of concrete available is less in beam 2 than in beam 1 to carry the compressive force, and, hence, the strength at crushing is reduced.

The moment at concrete crushing in beam 3 is even smaller because there are two FRP rebars in the compressive area of the concrete. The concrete area is diminished by two voids equivalent to the area occupied by the two FRP rebars (see figure 9.16c).

In contrast, the moment at concrete crushing of beam 4 is greater than the equivalent moment of beams 1, 2 and 3. This is because the Young's modulus of the steel bar at the top of the beam is greater than the Young's modulus of the concrete (see figure 9.16d). The steel rebar is capable of carrying more compressive force than the concrete delaying, therefore, the crushing of the concrete.

9.5 Flexural rigidity of RC beams with FRP rebars.

The flexural rigidity of RC beams is defined as the slope in the elastic range of the ascending branch of the moment-curvature relationship. Looking at figure 9.9, it can be inferred that beams 1 to 4 have the same flexural rigidity, whereas, beam 5 is stiffer than the former beams. Let us have a look at table 9.3 for the flexural rigidity of the beams. Column 1 in table 9.3 identifies the beam specimens. Column 2 in table 9.3 describes individually the flexural rigidity of each beam. Column 3 in table 9.2 shows the average flexural rigidity of beams 1, 2, 3 and 4. Column 4 shows the standard deviation of the flexural rigidity of the four beams. Finally, the flexural rigidity of beam 5 is given in column 2 of table 9.3. The flexural rigidity of beam 5 is greater than the flexural rigidity of beams 1, 2, 3 and 4 which is due to beam 5 having two more FRP rebars at the bottom.

Beam (1)	Flexural rigidity [kNm^2] (2)	Average [kNm^2] (3)	STDEV [kNm^2] (4)
B1	2356		
B2	2623		
B3	2515		
B4	2403	2474	119
B5	3749	---	---

Table 9. 3. – Flexural rigidity of the beams.

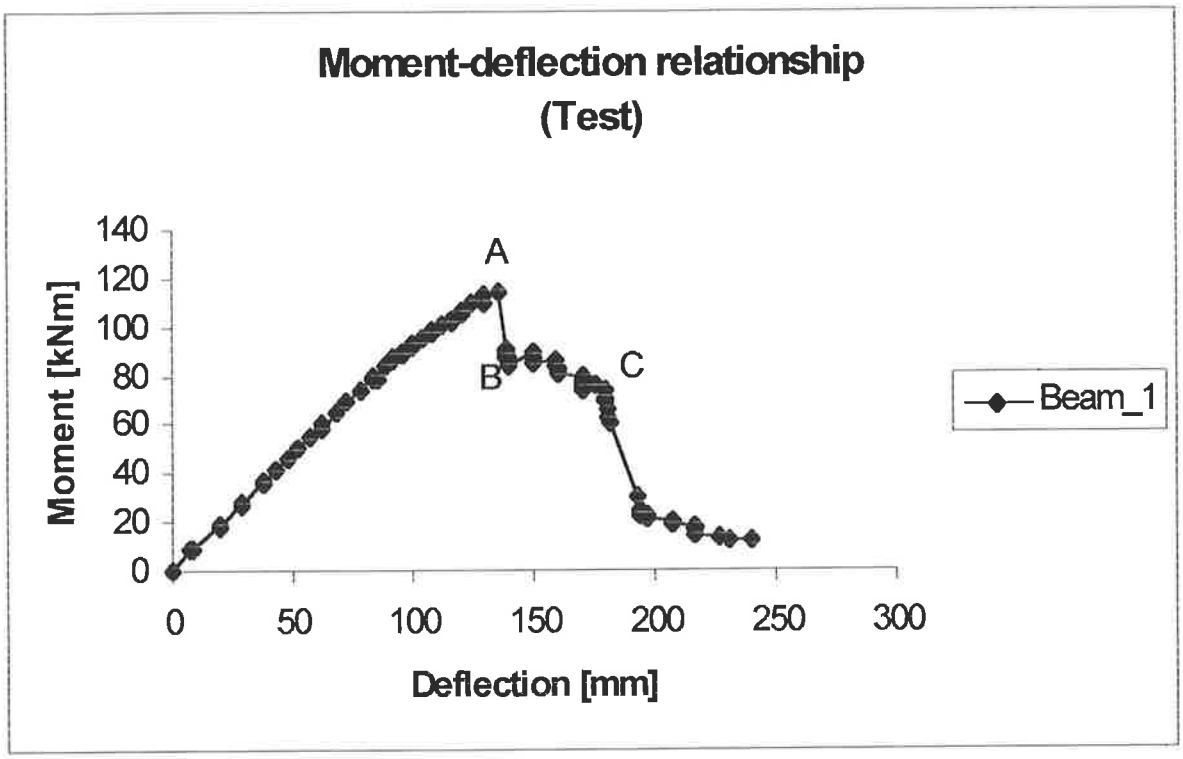

Figure 9.1. – Moment-deflection relationship of beam 1.

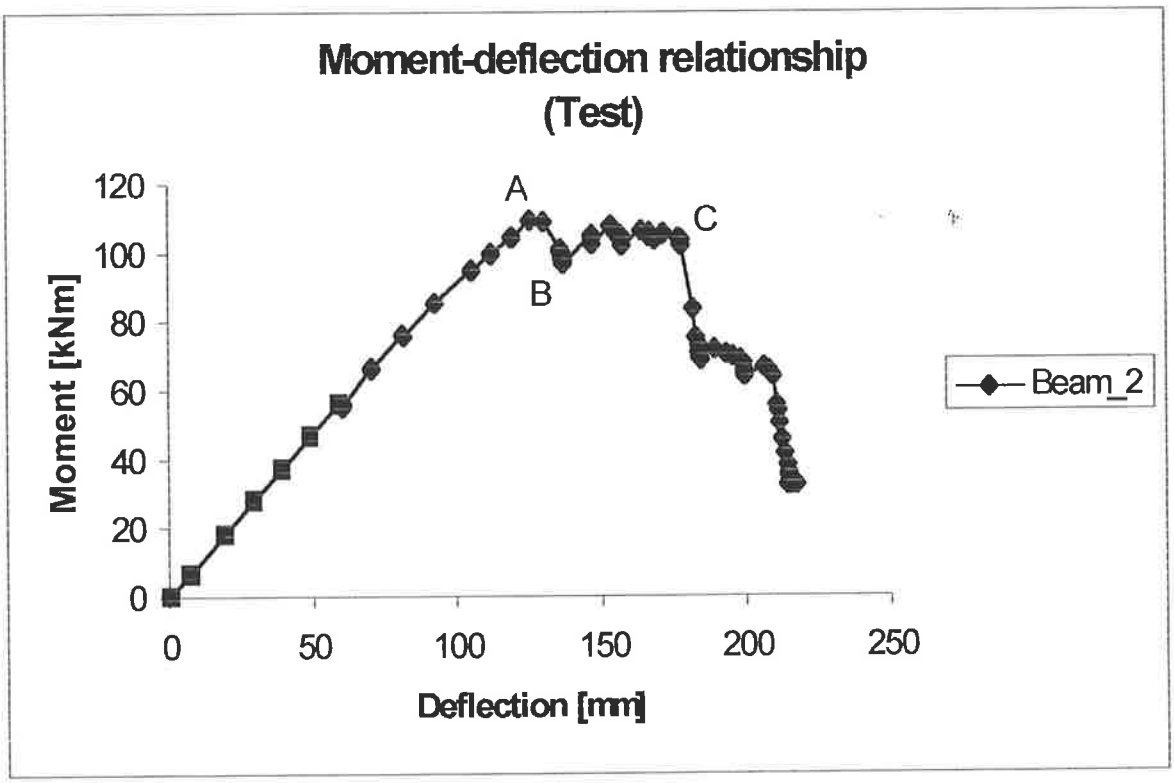

Figure 9.2. – Moment-deflection relationship of beam 2.

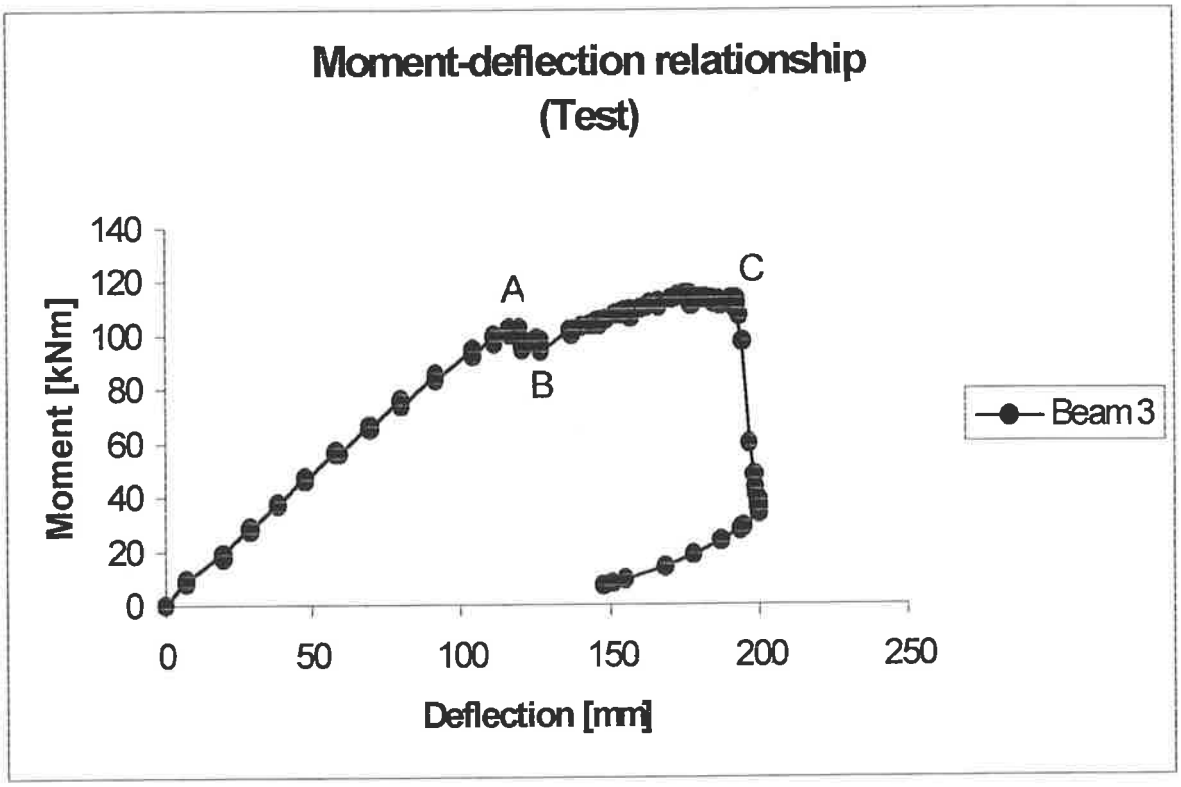

Figure 9.3. – Moment-deflection relationship of beam 3.

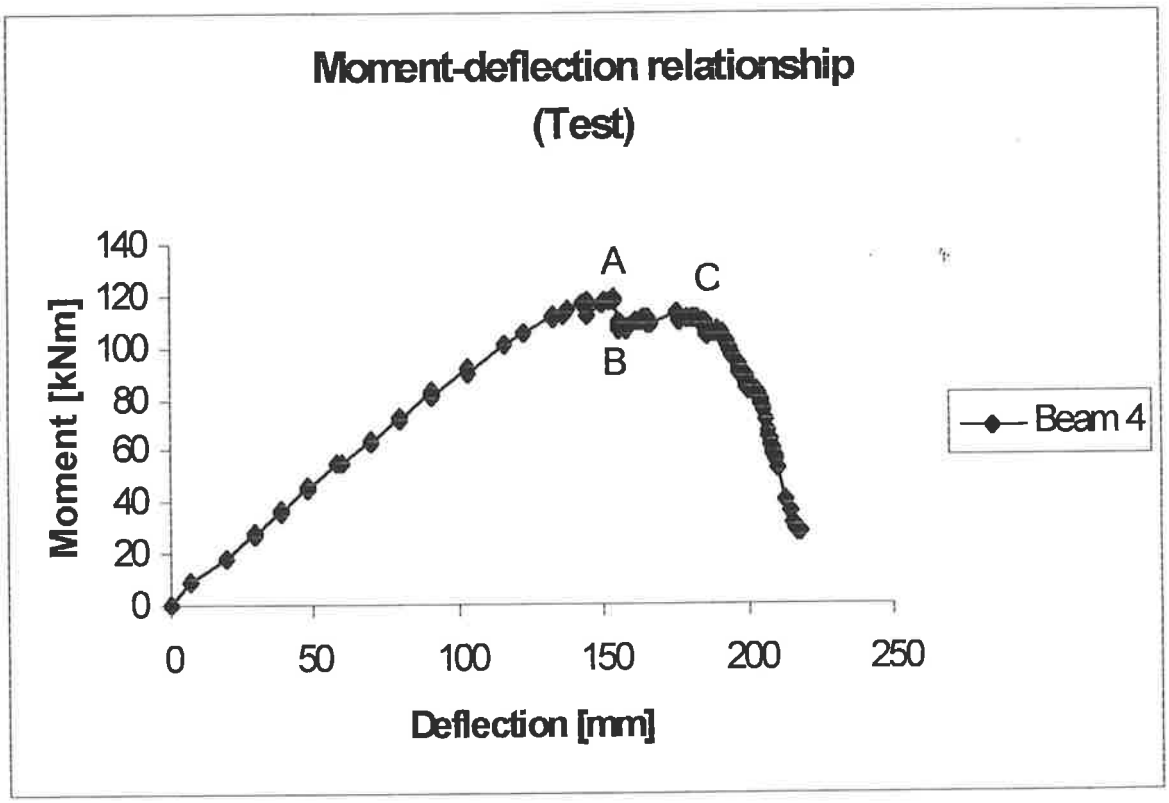

Figure 9.4. – Moment-deflection relationship of beam 4.

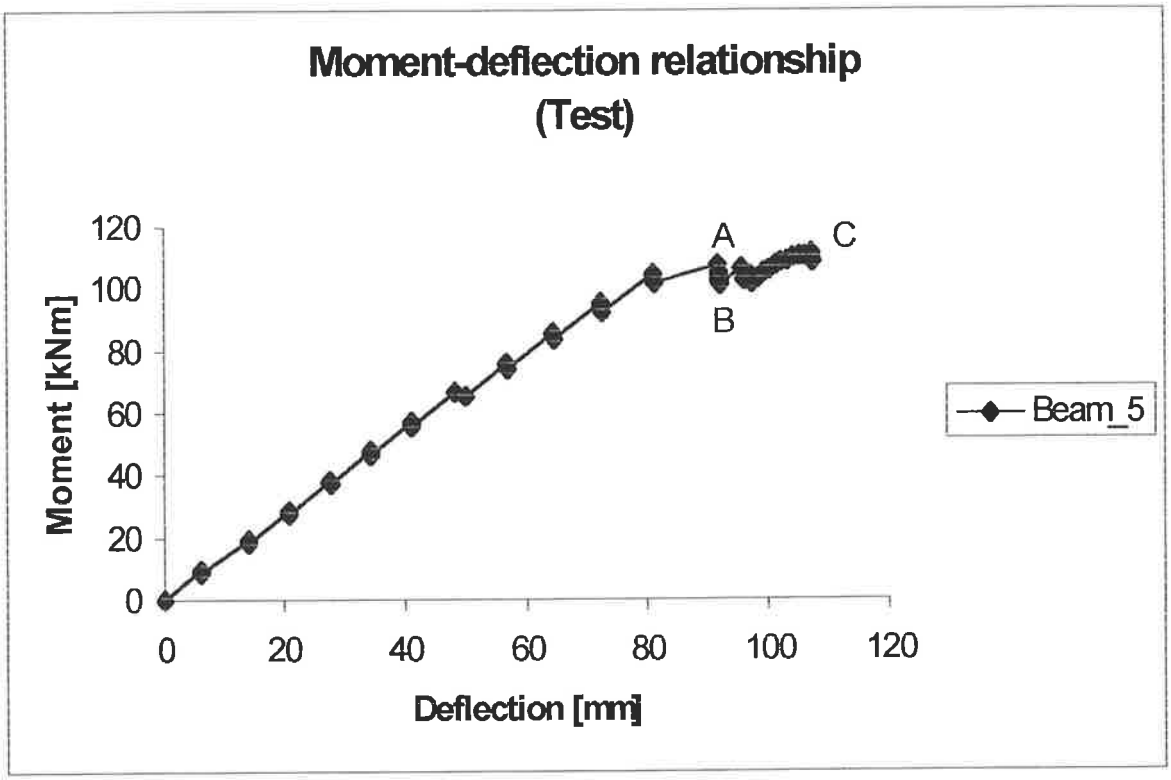

Figure 9.5. – Moment-deflection relationship of beam 5.

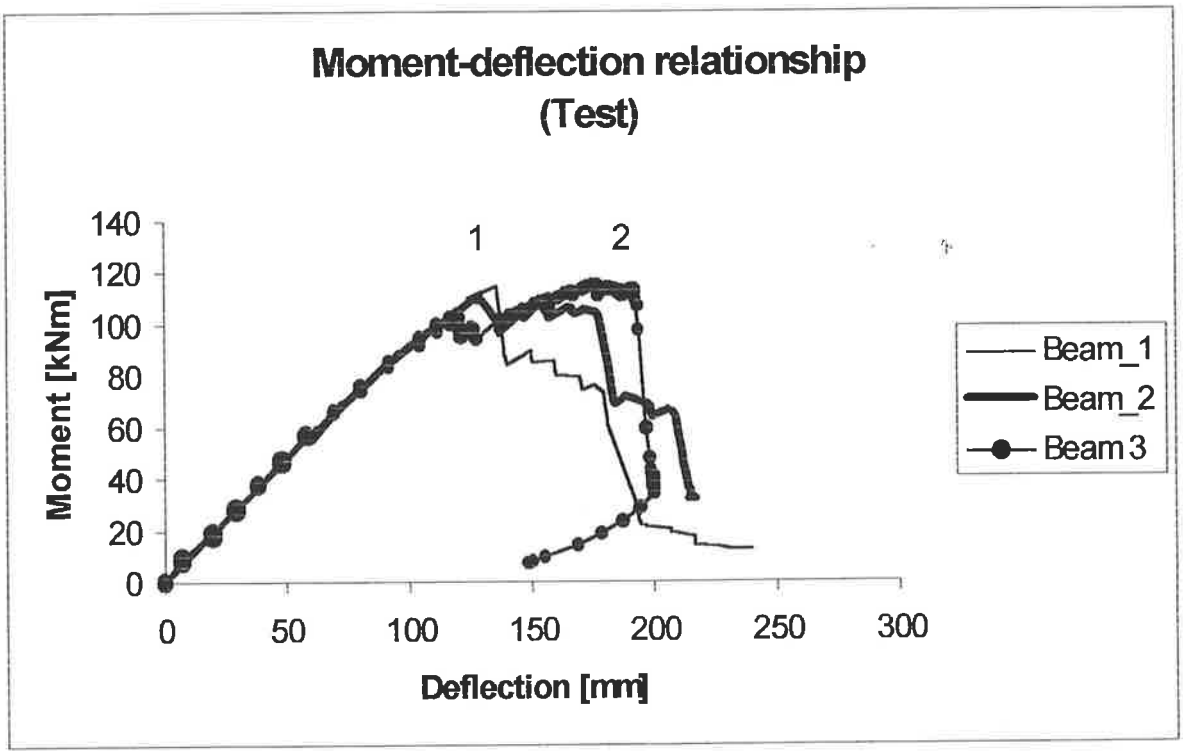

Figure 9.6. – Moment-deflection relationship of beams 1, 2 and 3.

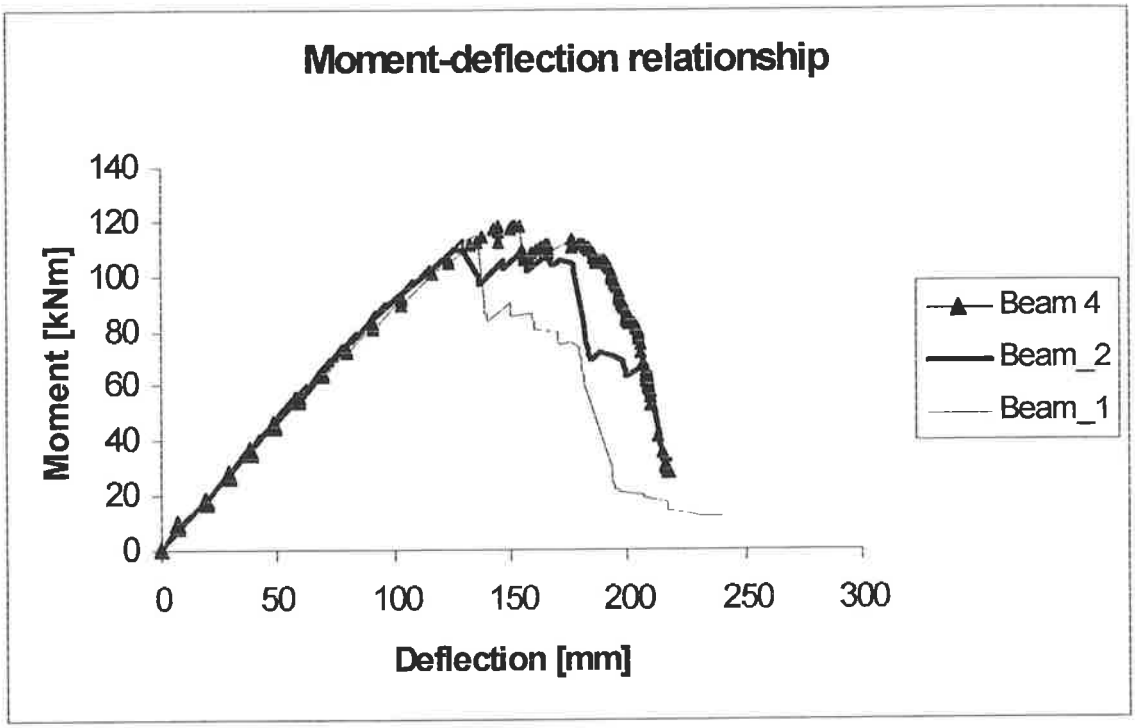

Figure 9.7. – Moment-deflection relationship of beams 1, 2 and 4.

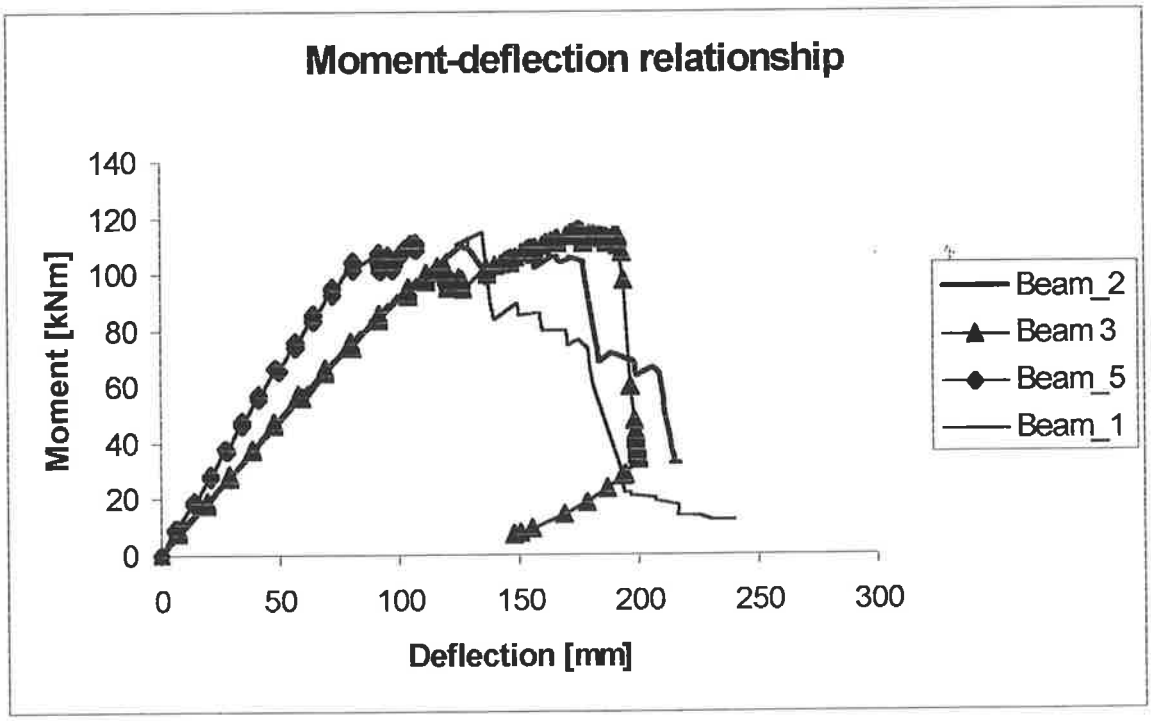

Figure 9.8. – Moment-deflection relationship of beams 1, 2, 3 and 5.

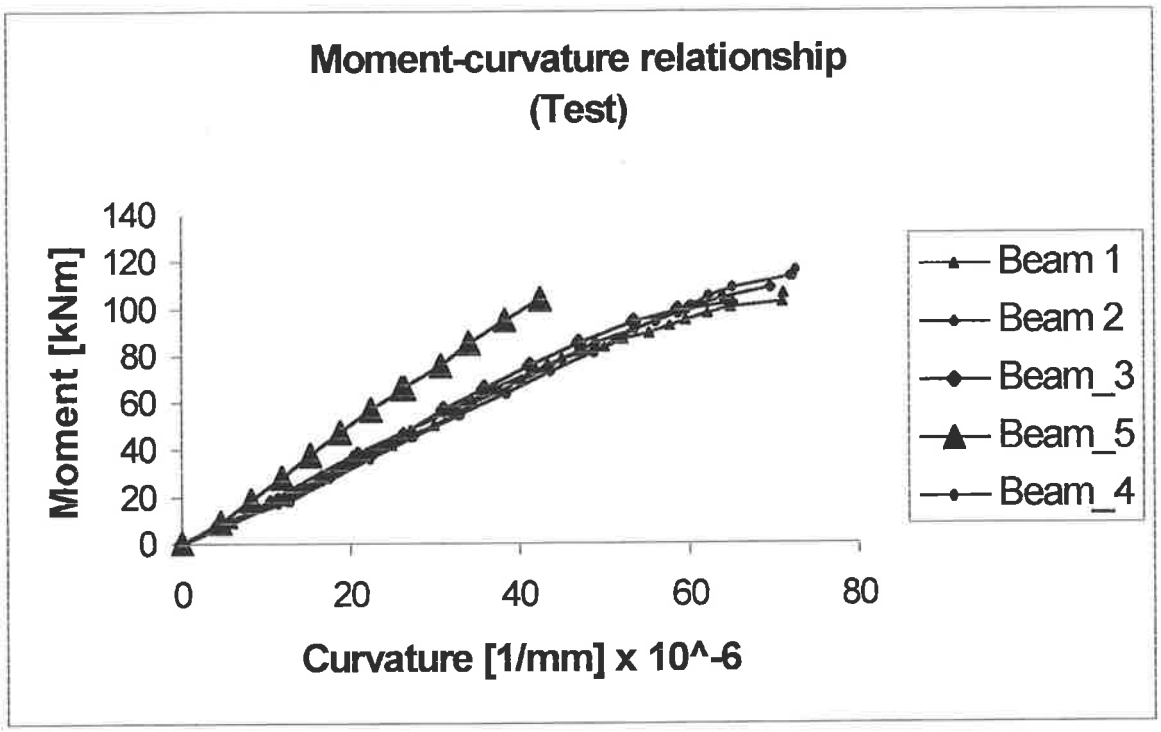

Figure 9.9. – Moment-curvature relationship of the 5 beam specimens.

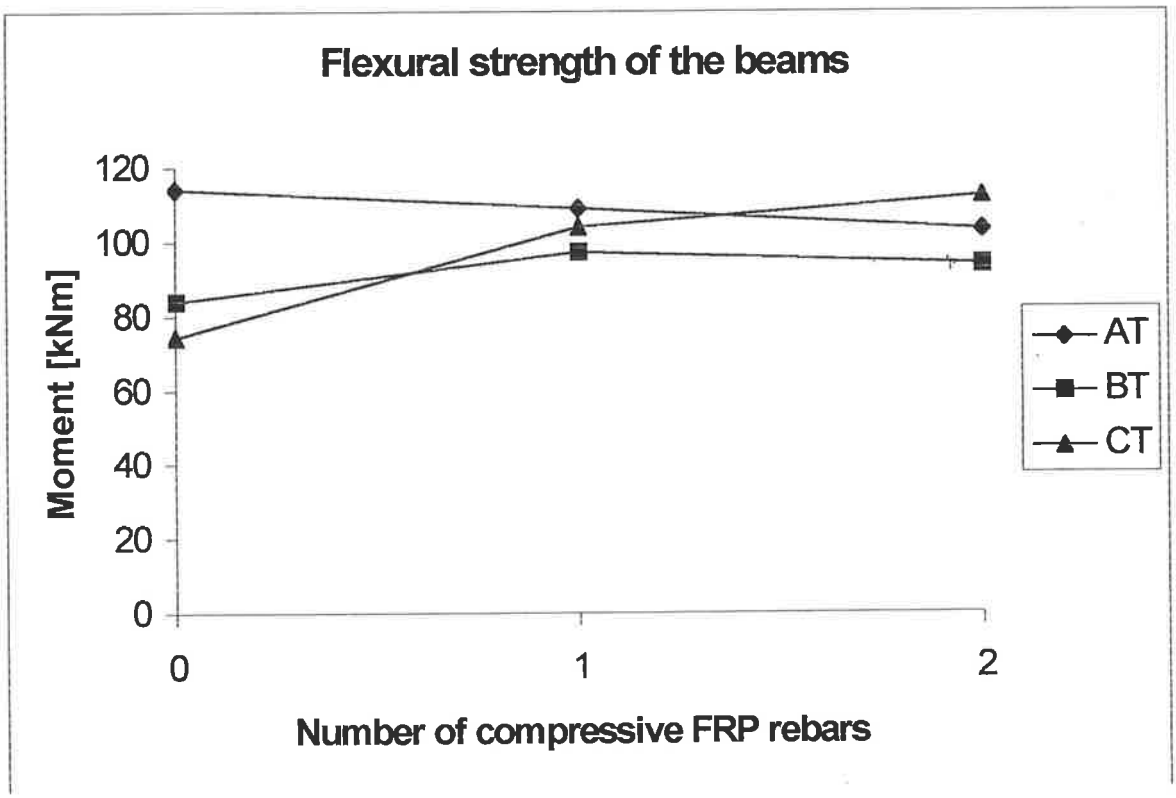

Figure 9.10. – Changes of moment in beams 1, 2 and 3 using the tests results.

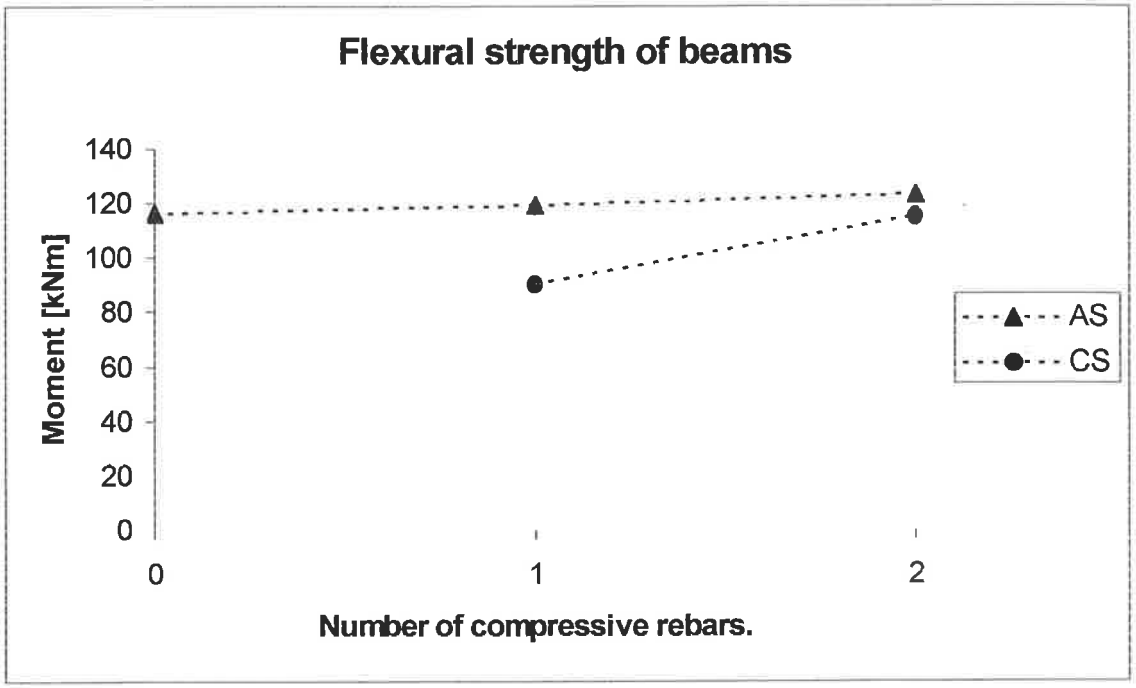

Figure 9.11. – Changes of moments of beams 1, 2 and 3 using the segmental analysis method.

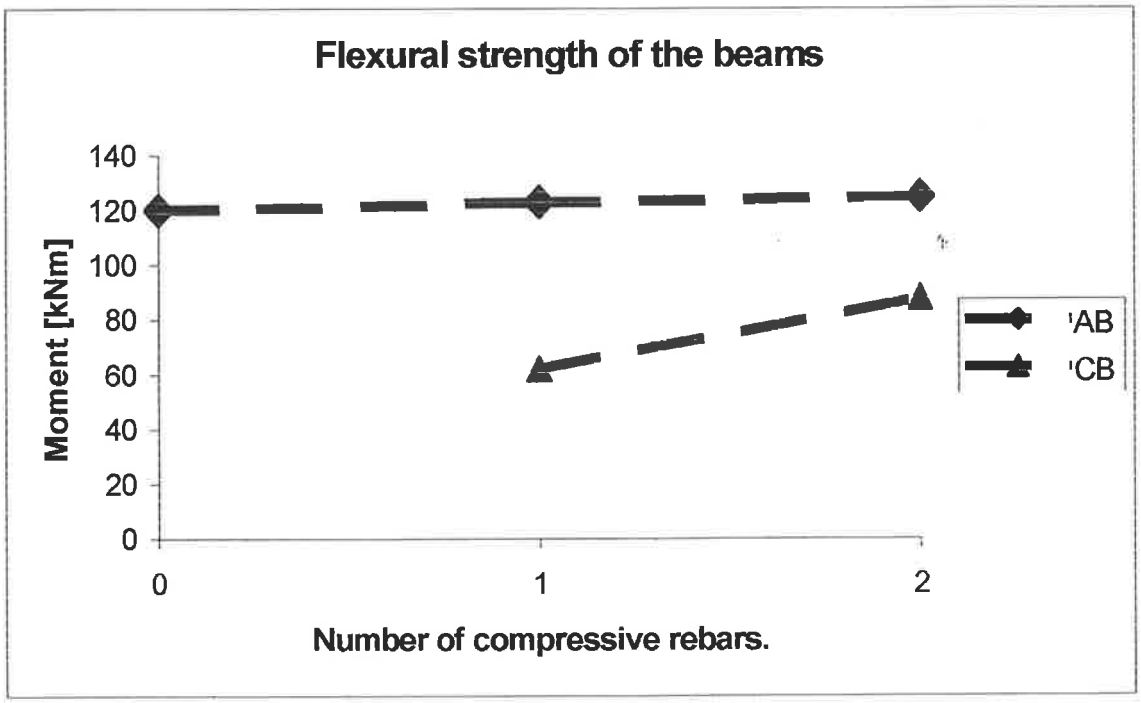

Figure 9.12. – Changes of moments in beams 1, 2 and 3 using the rectangular block of stresses analysis.

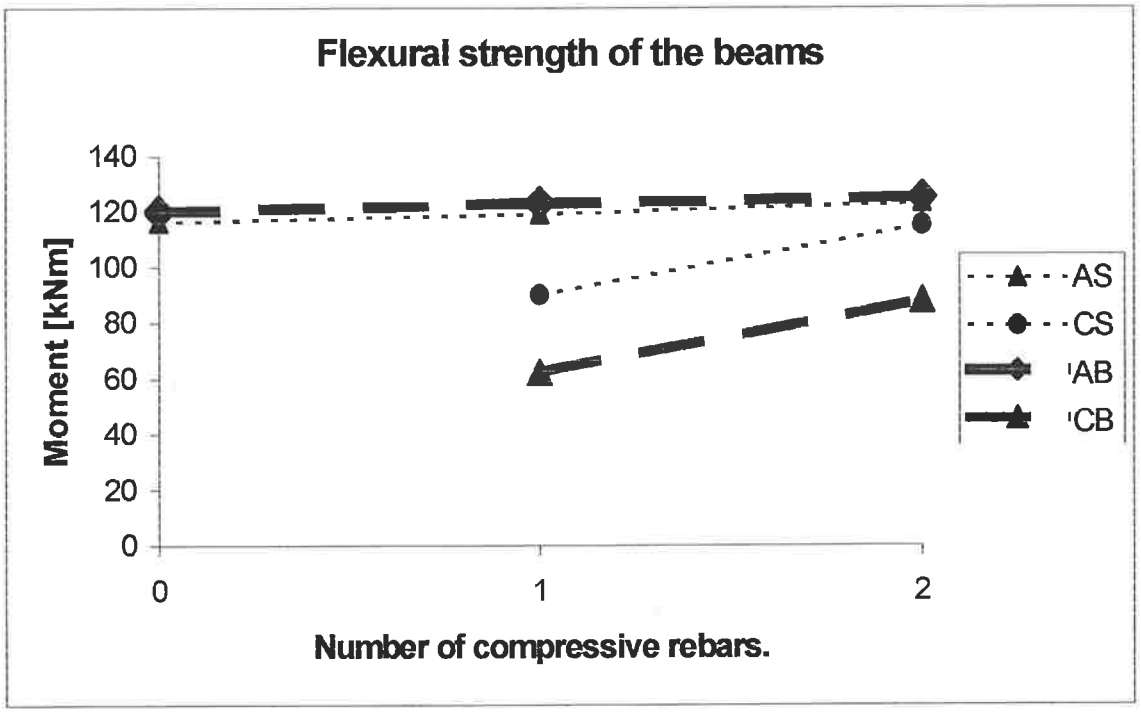

Figure 9.13. – Changes of moments of beams 1, 2 and 3 using both the segmental and the rectangular block of stresses analysis.

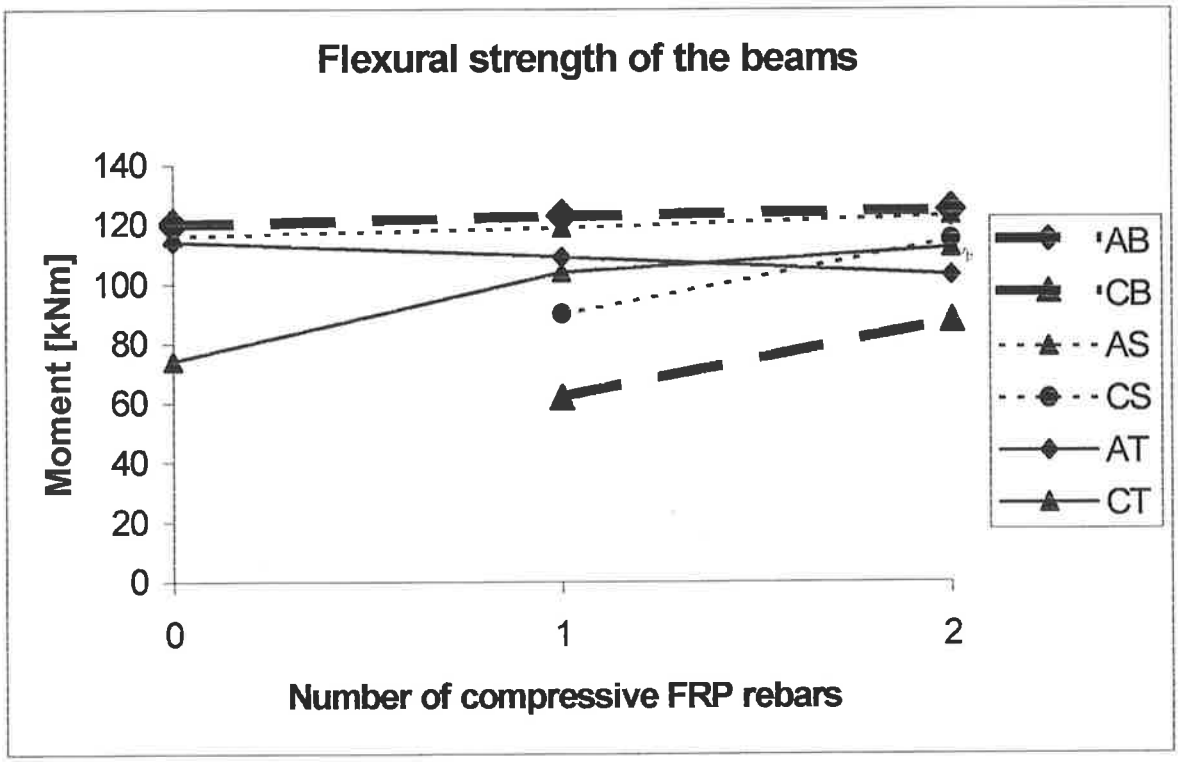

Figure 9.14. – Changes of moments in beams 1, 2 and 3 using the experimental results and the theoretical analyses.

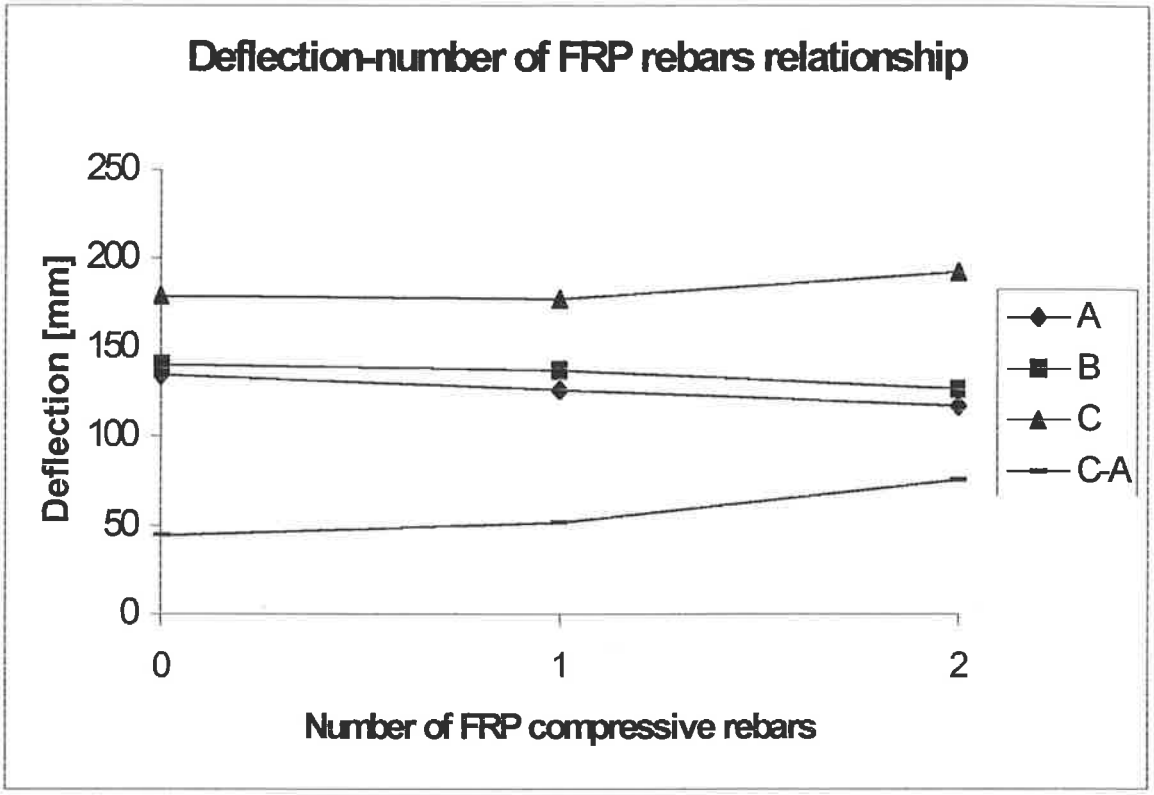

Figure 9.15. – Experimental plateau length of beams 1, 2 and 3.

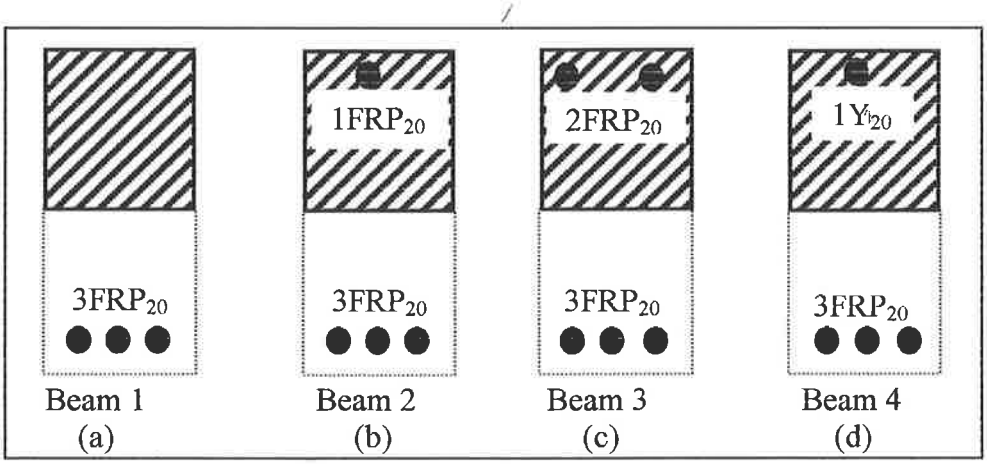

Figure 9.16. – Cross-sections of beams with different amount and type of compressive rebars.

Chapter 10 Conclusions

10.1 Introduction

The aim of the present study has been to investigate ductility of RC beams with FRP reinforcing bars. The work presented in this thesis has been extensive and many interesting problems have emerged during the time of the work. Important concepts have been looked at and interesting results have been found. In this chapter are listed some of the more relevant conclusions with regard to both the theoretical and experimental work.

10.2 Theoretical study

The following list presents a summary of the major theoretical studies contained within this research:

a) Two different methods have been used in the theoretical analysis of the flexural strength of the beams. One of the methods is a segmental analysis and the other is the usual rectangular block of stresses analysis.

b) A computer program has been developed to facilitate the manipulation of the mathematical algorithm of the segmental analysis method.

c) A mathematical model has been developed to facilitate the ductility analysis and design, by hand, of over reinforced concrete beams with FRP reinforcing bars using the rectangular block of stresses analysis method.

d) Computer simulations of the moment-curvature relationship of RC beams have been done for a variety of combinations of reinforcement of not only for FRP reinforcing bars but also steel rebars. In addition, a parametric study has been done to compare the behavior of beams in terms of ductility and to make the appropriate choice for the design of the beam specimens to be tested in the experimental work.

e) A good agreement has been found between the segmental analysis method and the rectangular block of stresses method when analyzing RC beams with FRP reinforcing bars.

10.3 Experimental results

Five RC beams were tested to failure to determine the mode of failure of the beams, and the following list presents a summary of the important findings from the experimental results:

a) Beam specimens without FRP reinforcing bars at the top showed a brittle failure due to the concrete crushing.

b) Beam specimens with steel rebars at the top, showed a brittle failure. Once the steel rebar at the top yielded, it did not compensate for the reduction in the strength of the crushed concrete. The failure of the steel rebar at the top of the beam was due to buckling.

c) Beams with FRP rebars at the top showed a good ductile behavior and therefore, good moment redistribution ability. The FRP rebars at the top of the beams attracted more load as the concrete crushed and, hence, took over from the crushed concrete describing a plateau whose length depends on the amount of FRP rebars at the top of the beams; the length of the plateau increased with the amount of FRP rebars at the top. The collapse of the beams with FRP rebars at top was due to fracture of the compressive rebars.

d) Increasing the amount of FRP rebars at the bottom of the beams increases the flexural rigidity of the beams, increases the strength slightly, but substantially reduces the ductility.

e) The failure of the compression FRP rebars at the top of the beams appear to be affected by stress concentration induced by the steel stirrups.

f) The failure of the tension FRP rebars at the bottom of the beams was due to splitting off the fibers of glass from the binding resin matrix. This occurred because there was no confinement of the fiberglass in the FRP rebars. None of the FRP rebars at the bottom of the 5 beam specimens fractured.

g) The Young's modulus of the reinforcing bars at the top of the beams influences significantly the occurrence of concrete crushing. In beams with steel reinforcement, the crushing of concrete was delayed by the steel rebars because the Young's modulus of the steel rebars is greater than the Young's modulus of the concrete. However, in beams with FRP compression reinforcement, crushing of the concrete occurred earlier because the Young's modulus of the FRP rebars is less than the Young's modulus of the concrete. (???).

References

1. – R. T Schwartz and H. S Schwartz. (editors, 1968). "Fundamental aspect of fiber reinforced plastic composites". John Wiley and Sons. pp vii.

2. – B. S. Benjamin (1969). "Structural design with plastics". Van Nostrand Reinhold Company. pp 1-2.

3. – Stephen W. Tsai (1968). "Strength theories of filamentary structures". Fundamental aspects of fiber reinforced plastic composites. Ed. R. T. Schwartz and H. S. Schwartz. Air Force Materials Laboratory. US. pp 311.

4. – Geralt Pickett (1968). "Elastic moduli of fiber reinforced plastic composites". Fundamental aspects of fiber reinforced plastic composites. Ed. R. T. Schwartz and H. S. Schwartz. Air Force. US. pp 13-27.

5. – W. Leissa, and W. E. Clausen. (1968). "Application of point matching to problems in micromechanics". Fundamental aspects of fiber reinforced plastic composites. Ed. R. T. Schwartz and H. S. Schwartz. Air Force. US. pp 29-44.

6. – H. T. Corten. (1968). "Influence of fracture toughness and flaws on the interlaminar shear strength of fibrous composites". Fundamental aspects of fiber reinforced plastic composites. Ed. R. T. Schwartz and H. S. Schwartz. Air Force. US. pp 89-107.

7. – F. W. Wendt. (1968). "Relationship between micromechanics and structural behavior of fiber reinforced plastic composites". Fundamental aspects of fiber reinforced plastic composites. Ed. R. T. Schwartz and H. S. Schwartz. Air Force. US. pp 109-128.

8. – James M Whitney. (1968). "Effects of constituent material properties on the stability of fiber reinforced composite plates". Fundamental aspects of fiber reinforced plastic composites. Ed. R. T. Schwartz and H. S. Schwartz. Air Force. US. pp 129-139.

9. – W. Rogers. (1968). "Structural design with composites". Fundamental aspects of fiber reinforced plastic composites. Ed. R. T. Schwartz and H. S. Schwartz. Air Force. US. pp 141-159.

10. – F. H. Guzzetta. (1968). " The adsorption of a cationic lubricant onto E-glass fibers". Fundamental aspects of fiber reinforced plastic composites. Ed. R. T. Schwartz and H. S. Schwartz. Air Force. US. pp 217-224.

11. – Robert L. Patrick and William S. Layne. (1968). "The role of water in interfacial interactions". Fundamental aspects of fiber reinforced plastic composites. Ed. R. T. Schwartz and H. S. Schwartz. Air Force. US. pp 225-236.

12. – Robert Wong. (1968). "Mechanism of coupling by silanes of epoxies to glass fibers". Fundamental aspects of fiber reinforced plastic composites. Ed. R. T. Schwartz and H. S. Schwartz. Air Force. US. pp 237-243.

13. – S. Sterman and J. G. Marsden. (1968). "Bonding organic polymers to glass by silane coupling agents". Fundamental aspects of fiber reinforced plastic composites. Ed. R. T. Schwartz and H. S. Schwartz. Air Force. US. pp 245-273.

14. – R. M. Gill. (1972). "Carbon fibres in composite materials". The Plastics Institute. England. pp 7-85.

15. – Ballinger (1992). "Development of fibre-reinforced plastic products for the construction market". Advanced composite materials in bridges and structures. K. W. Neale and P. Labossière, Editors. Canadian Society for Civil Engineering. pp 3.

16. – Gueritse (1992). "Durability criteria for non-metallic tendons in an alkaline environment". Advanced composite materials in bridges and structures. K.W. Neale and P. Labossiére, Editors. p 132.

17. – J. Larralde, and R. Silva-Rodriguez (1993). "Bond and slip of FRP rebars in concrete". Journal of Materials in Civil Engineering, ASCE. Vol 5, No. 1. pp 30–40.

18. – Nikola Deskovic, and Thanasis C. Triantafillou (1995). "Innovative design of FRP combined with concrete: short-term behavior". Journal of Structural Engineering. ASCE. Vol. 121. No. 7. pp 1069–1078.

19. – Nikola Deskovic, and Thanasis C. Triantafillou (1995). "Innovative design of FRP combined with concrete: long-term behavior". Journal of Structural Engineering. ASCE. Vol. 127. No. 7. pp 1079–1089.

20. – Akira Kobayashi, Masami Endoh, Hiroyuki Kuroda, and Howard Kliger (1995). "Use of carbon fiber tow sheet reinforcement for improved bridge capacity ratings in Japan". 40th International SAMPE Symposium. pp 513–521.

21. – Hamid Saadatmanesh, Mohammad R. Ehsani, and Limin Jin. "Repair of earthquake-damaged RC columns with FRP wraps". ACI Structural Journal. Technical Paper. Title 94–S20. pp 206–215.

22. – Amir Mirmiran, and Mohsen Shahawy (1997). "Behavior of concrete columns confined by fiber composites". Journal of Structural Engineering, ASCE. Vol 123, No. 5 pp 583–590.

23. – Tom Norris, Hamid Saadatmanesh, and Mohammad R. Ehsani. "Shear and flexural strengthening of RC beams with carbon fiber sheets". Journal of Structural Engineering, ASCE, Vol 123, No. 7. pp 903–911.

24. – L. C. Muszynski, and R. L. Sierakowski (1995). "Durability of carbon fiber reinforced plastics (CFRPs) as external reinforcement of concrete beams". 50th Annual Conference, Composites Institute, The Society of Plastics Industry, Inc. Session 4–C. pp1–4.

25. – Hamid Saadatmanesh, and Mohammad R. Ehsani (1991). "RC beams strengthened with GFRP plates, I: experimental study". Journal of Structural Engineering, ASCE. Vol 117 No. 11. pp 3417–3433.

26. – L. Javier Malvar (1995). "Tensile and bond properties of GFRP reinforcing bars". ACI Materials Journal. Vol 92, No. 3. pp 266–285.

27. – Saeed Daniali (1990). "Bond strength of fiber reinforced plastic bars in concrete". Serviceability and Durability of Construction Materials. – Proceedings of the First Materials Engineering Congress. Part (2). ASCE. pp 1182–1191.

28. – H. Shima, and T. Suga. "Local bond stress-slip relationship of braided aramid fiber bar". Building for the 21th Century, Y. C. Loo, Editor. Australia. pp 1041–1046.

29. – Benmokrane, O. Chaallal, and R. Masmoudi (1995). "Glass fiber reinforced plastic (GFRP) rebars for concrete structures". Construction and Building Materials. Volume 9 Number 6. pp 353–364.

30. – Vicki L. Brown and Charles L. Bratholomew (1993). "FRP reinforcing bars in reinforced concrete members". ACI Materials. Vol 90, No. 1. pp 34–39.

31. – Antonio Nanni (1993). "Flexural behavior and design of RC members using FRP reinforcement". Journal of Structural Engineering, ASCE. Vol 119 No. 11. pp 3344–3359.

32. – H. Saadatmanesh, and M. R. Ehsani (1991). "Fiber composite bar for reinforced concrete construction". Journal of Composite Materials. Vol 25. pp 188–203.

33. – Popovic, Sandor (1970). "A review of stress-strain relationships for concrete". Proceedings Vol. 67, No. 3. pp 243–248.

34. – Popovic, Sandor (1973). "A numerical approach to the complete stress-strain curve of concrete". Cement and Concrete Research, Vol. 3, No. 4. pp 583–599.

35. – Hognestad, E. (1951). "A study of combined bending and axial load in reinforced concrete members". Bull. Ser. No 399, University of Illinois Engineering Experimental Station, Champaign. Ill.

36. – Desayi, Prakash, and Krishman, S. (1964). "Equation for stress-strain curve of concrete". ACI Journal, Proceedings Vol. 81, No. 3. pp 345–350.

37. – Wang, P. T., Shah, S. P., and Naaman, A. E. (1978). "Stress-strain curve of normal and lightweight concrete in compression". ACI Journal, Proceedings, Vol. 75, No. 11. pp 603–611.

38. – T. H. Wee, M. S. Chin, and M. A. Mansur (1996). "Stress-strain relationship of high-strength concrete in compression". Journal of Materials in Civil Engineering, ASCE. Vol 8 No. 2. pp 70–76.

39. – Nicholaus Holkmann Olsen (1990). "Uniaxial stress-strain curves of high strength concrete". Department of Structural Engineering, Technical University of Denmark.

40. – Australian Standard AS 3600–1994. Concrete Structures. pag 67.

41. – Method for the determination of the static chord modulus of elasticity and Poisson's ratio of concrete specimens. Australia Standard 1012, Part 17–1976.

42. – Methods of testing concrete. Method 10: Method for the determination of indirect tensile strength of concrete cylinders ('Brazil' or splitting test). Australian Standard AS 1012.10 1985.

43. – Methods of testing concrete. Part 11–Method for the determination of the flexural strength of concrete specimens. Australian Standard 1012.11–1985.